Modelling and characterisation of antennas and propagation for body-centric wireless communication

Sani, Andrea

Modelling and Characterisation of Antennas and Propagation for Body-Centric Wireless Communication

Andrea Sani

A thesis submitted to the faculty of the University of London in partial fulfillment of the requirements for the degree of

Doctor of Philosophy

Electronic Engineering, Queen Mary, University of London
London E1 4NS, United Kingdom

April 2010

To my family

Abstract

Body-Centric Wireless Communication (BCWC) is a central point in the development of fourth generation mobile communications. The continuous miniaturisation of sensors, in addition to the advancement in wearable electronics, embedded software, digital signal processing and biomedical technologies, have led to a new concept of user-centric networks, where devices can be carried in the user's pockets, attached to the user's body or even implanted.

Body-centric wireless networks take their place within the personal area networks, body area networks and body sensor networks which are all emerging technologies that have a broad range of applications such as healthcare and personal entertainment. The major difference between BCWC and conventional wireless systems is the radio channel over which the communication takes place. The human body is a hostile environment from radio propagation perspective and it is therefore important to understand and characterise the effect of the human body on the antenna elements, the radio channel parameters and hence the system performance. This is presented and highlighted in the thesis through a combination of experimental and electromagnetic numerical investigations, with a particular emphasis to the numerical analysis based on the finite-difference time-domain technique.

The presented research work encapsulates the characteristics of the narrowband (2.4 GHz) and ultra wide-band (3-10 GHz) on-body radio channels with respect to different digital phantoms, body postures, and antenna types hence highlighting the effect of subject-specific modelling, static and dynamic environments and antenna performance on the overall body-centric network. The investigations covered extend further to include in-body communications where the radio channel for telemetry with medical implants is also analysed by considering the effect of different digital phantoms on the radio channel characteristics. The study supports the significance of developing powerful and reliable numerical modelling to be used in conjunction with

measurement campaigns for a comprehensive understanding of the radio channel in body-centric wireless communication. It also emphasises the importance of considering subject-specific electromagnetic modelling to provide a reliable prediction of the network performance.

Contents

Acknowledgement

My most sincere and deep gratitude goes to my supervisor Prof. Yang Hao, whose support, guidance and encouragement have given me the strength and confidence necessary for the development of the work. I would like also to thank Prof. Clive Parini for his positive and fruitful comments, and Mr. John Dupuy for his assistance in the experimental part of the work.

A special mention goes to my colleagues Dr. Akram Alomainy and Dr. Yan Zhao. Their friendship, knowledge, and willingness to help have facilitated not only my research, but every aspect of my PhD.

Many thanks also to the Engineering and Physical Research Council (EPSRC) for the financial support. I would like also to thank Prof. Peter Hall (University of Birmingham) for the fruitful discussions. Many appreciations to my colleagues Mr. Christos Argyropolus, Mr. Anestis Katsounaros, Mr. George Palikaras, Dr. Rob Foster, Dr. Themos Kallos, Mr. Max Munoz and Dr. Rostylav Dubrovka for having created such a pleasant atmosphere within the research group.

Above all, i would like to thank my family and my friends. Regardless of physical distance, their support and affection have always been with me.

Andrea Sani

London, April 2010

List of Publications

Journal Publications

1. A. Sani, Y. Zhao, Y. Hao, S-L Lee and G-Z Yang, "A Subject-Specific Radio Propagation Study in Wireless Body Area Networks", under review for *IEEE Antennas and Propagation Magazine*.

2. Q. Abbasi, A. Sani, A. Alomainy and Y. Hao "Ultra Wideband On-Body Radio Channel Characterisation and System-Level Modelling for Multiband OFDM Body-Centric Wireless Network" under review for *IEEE Microwave Theory and Techniques*

3. A. Sani, M. Rajab, R. Foster and Y. Hao "Antennas and Propagation of Implanted RFIDs for Pervasive Healthcare Applications", to appear in *Proceedings of the IEEE*, August 2010.

4. A. Sani, A. Alomainy and Yang Hao, "Numerical Characterization and Link Budget Evaluation of Wireless Implants Considering Different Digital Human Phantoms", *IEEE Transactions on Microwave Techniques and Theory, Biomedical Special Issue*, Vol. 57, Issue 10 (Part 2), October 2009, pp. 2605-2613,.

5. A. Sani, A. Alomainy, G. Palikaras, Y. Nechayev, Y. Hao, C. G. Parini, P. S. Hall, "Experimental Characterization of UWB On-Body Radio Channel in Indoor Environment Considering Different Antennas", *IEEE Transactions on Antennas and Propagation*, Vol. 58, Issue 1, January 2010, pp.238-241.

6. A. Sani, Y. Zhao, A. Alomainy, Y. Hao and C. G. Parini, "An Efficient FDTD Algorithm Based on Equivalence Principle for Analyzing On-Body Antenna Performance", *IEEE Transactions on Antennas and Propagation, Special Issue on Body-Centric Wireless Networks*, Vol. 57, Issue 4, Part 1, April 2009, pp. 1006-1014.

7. A. Alomainy, A. Sani, A. Rahman, J. Santas and Y. Hao, “Transient Characteristics of Wearable Antennas and Radio Propagation Channels for Ultra Wideband Body-Centric Wireless Communications”, *IEEE Transactions on Antennas and Propagation, Special Issue on Body-Centric Wireless Networks*, Vol. 57, Issue 4, Part 1, April 2009, pp. 875-884.

Conference Presentations

1. S-L Lee, M. Lerotic, A. Sani, Y. Zhao, J. Keegan, Y. Hao and G-Z Lee“Articulated Postures for Subject-Specific RF Simulations” to be presented at Body Sensor Networks (BSN10), Singapore, June 2010.

2. A. Sani, Y. Zhao, Y. Hao, S-L Lee and G-Z Yang “A Subject-Specific Numerical Study in UWB Body-Centric Wireless Communications” invited for presentation at European Conference on Antennas and Propagation (EUCAP) 2010, Barcelona, Spain, April 2010.

3. A. Sani, Y. Zhao, Y. Hao, S-L Lee and G-Z Yang “Subject-Specific Analysis of the On-Body Radio Propagation Channel Adopting a Parallel FDTD Code” invited for presentation at European Conference on Antennas and Propagation (EUCAP) 2010, Barcelona, Spain, April 2010.

4. Y. Zhao, A. Sani and Y. Hao “Subject-Specific Numerical Modelling for Body-Centric Wireless Communications”, Loughborough Antennas and Propagation Conference 2009 (LAPC09), September 2009.

5. Q. Abbasi, A. Sani, A. Alomainy and Y. Hao “Arm Movements Effect on Ultra Wideband On-Body Propagation Channels and Radio Systems” Loughborough Antennas and Propagation Conference 2009 (LAPC09), September 2009.

6. A. Alomainy, Q. H. Abbasi, A. Sani and Y. Hao, ” System-Level Modelling of Optimal Ultra Wideband Body-Centric Wireless Network ”, Asia Pacific Microwave Conference (APMC) 2009, Singapore, December 2009 (Invited Paper).

7. A. Sani, Y. Zhao, A. Alomainy, Y. Hao and C.G. Parini “Modelling of Propagation and Interaction Between Body-Mounted Antennas, and the Modelling

of Body-Centric, Context Aware Application Scenarios" IET seminar on Body-Centric Wireless Communications, London, April 2009.

8. A. Sani, A. Alomainy and Y. Hao "Effect of Various Human Body Tissue Models on Radiowave Propagation from a Bladder Wireless Implanted Source" Antennas and Propagation Society (AP-S) 2009, Charleston, USA, June 2009.

9. Y. Zhao, A. Sani, Y. Hao, S-L Lee and G-Z Yang "A Simulation Environment for Subject-Specific Radio Channel Modeling in Wireless Body Sensor Networks" Body Sensor Networks (BSN) 2009, Berkeley, California, USA, June 2009.

10. A. Sani, Y. Hao "Modeling of Path Loss for Ultrawide Band Body-Centric Wireless Communications" International Conference in Electromagnetism in Advanced Applications (ICEAA) 2009, Turin, Italy, September 2009.

11. A. Sani, A. Alomainy and Yang Hao, "Time Domain UWB Radio Channel Characterisation for Body-Centric Wireless Communications in Indoor Environment", IET seminar on wideband and ultrawide band systems and technologies, London, October 2008.

12. A. Sani, A. Alomainy and Y. Hao, "Effect of the Indoor Environment on the UWB On-Body Radio Propagation Channel" invited for presentation at European Conference on Antennas and Propagation (EUCAP) 2009, Berlin, Germany, March 2009.

13. A. Sani, A. Alomainy and Y. Hao, "Numerical Characterization of the Radiation from Implanted Wireless Sources Considering Different Digital Body Phantoms" invited for presentation at European Conference on Antennas and Propagation (EUCAP) 2009, Berlin, Germany, March 2009.

14. A. Sani, A. Alomainy, Y. Hao, "Characterisation of Ultra Wideband Wearable Antennas and Body-Centric Wireless-Networks in Indoor Environment", European Microwave Week (EuMW) 2008, Amsterdam, The Netherlands, October 2008.

15. A. Sani, A. Alomainy, J. Santas and Yang Hao, "Time Domain Characterisation of Ultra Wideband Wearable Antennas and Radio Propagation for Body-Centric

Wireless Networks in Healthcare Applications", The 5th International Workshop on Wearable and Implantable Body Sensor Networks (BSN 2008), Hong Kong, June 2008.

16. A. Sani, Y. Zhao and Y. Hao, "Analysis of on-body propagation channel using a hybrid technique combining the equivalence principle and FDTD", International Workshop on Antenna Technology 2008 (IWAT08), Chiba, Japan, March 2008.

17. A. Sani, Y. Zhao and Y. Hao, "Analysis of on-body antenna radiation pattern using a numerical technique based on equivalence principle and FDTD", Loughborough Antenna and Propagation Conference (LAPC) 2008, Loughborough, U.K., March 2008.

List of Abbreviations

ABC	Absorbing Boundary Condition
AWGN	Additive White Gaussian Noise
BAN	Body Area Network
BER	Bit Error Rate
BMI	Body Mass Index
BPSK	Binary Phase-Shift Keying
BCWC	Body-Centric Wireless Communications
CDF	Cumulative Distribution Function
CPW	Co-Planar Waveguide
C/No	Signal-to-noise ratio in dB/Hz
dBm	Decibels relative to 1mW
Eb/No	Energy per bit to noise power spectral density
ERP	Effective Radiated Power
EIRP	Effective Isotropic Radiated Power
EM	Electromagnetic
ETRI	Electronic & Telecommunications Research Institute
FCC	Federal Communications Commission
FDTD	Finite-Difference Time-Domain
FEM	Finite Element Method
FFT	Fast Fourier Transform
FIT	Finite Integral Technique
FR	Frequency Response
FR4	Flame Resistance 4
HSCA	Horn-shaped Self Complementary Antenna
IEEE	Institute of Electrical & Electronics Engineers
IFFT	Inverse Fast Fourier Transform

IR	Impulse Response
ISM	Industrial, Scientific and Medical
ITU	International Telecommunication Union
LOS	Line Of Sight
MICS	Medical Implant Communications Services
MoM	Method of Moments
MR	Magnetic Resonance
MS	MicroStrip
NLOS	Non Line-Of-Sight
PDF	Probability Density Function
PDP	Power Delay Profile
PICA	Planar Inverted Cone Antenna
PML	Perfect Matched Layer
RF	Radio Frequency
RMS	Root Mean Square
RSSI	Received Signal Strength Indicator
Rx	Receiver
SAR	Specific Absorption Rate
SNR	Signal-to-Noise Ratio
TM	Transverse Magnetic
TSA	Tapered Slot Antenna
Tx	Transmitter
UWB	Ultra Wide-Band
VNA	Vector Network Analyser
WMTS	Wireless Medical Telemetry System
WBAN	Wireless Body Area Network
WPAN	Wireless Personal Area Network

List of Figures

List of Tables

Chapter 1

Introduction

With the increasing average age of populations in the occidental world (see Fig. 1.1), and the associated rise of healthcare costs, the development of systems for freeing hospital resources is of particular interest in academic and industrial environments.

A continuous and remote diagnosis of a patient has been proposed [1, 2] by using a "smart" network, where data sets collected from various sensors are analysed in order to allow controlled administration of medicine, as well as the generation of emergency calls.

The major drawback of current body-worn systems is the use of wired communication, which is often undesirable because of the inconvenience to the user. Other connection methods have been proposed for alleviating this problem, including the use of smart textiles. Smart clothes imply the need for a special garment to be worn, which may conflict with the user's personal preferences [4]. With the increasing presence of wireless communications in our daily lives, body-centric wireless communications (BCWC) systems will be a focal point in the development of the fourth generation (4G) mobile communications system [5–7].

Body-centric wireless networks consist of a number of wireless sensors placed on the human body or in close proximity to it. These sensors are required to communicate

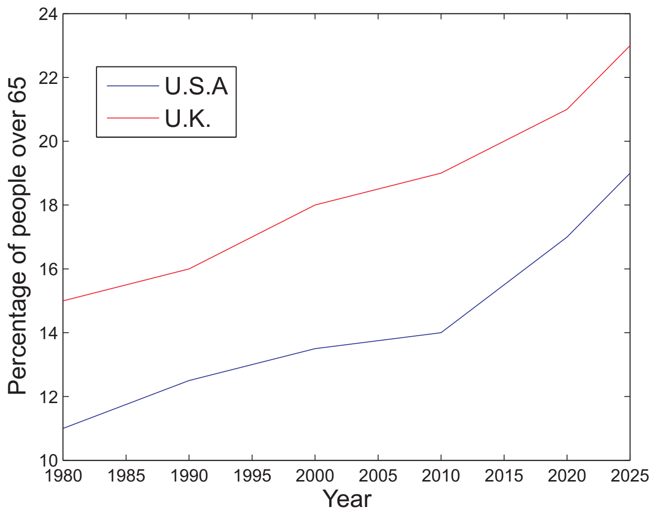

Figure 1.1: Percentage of people aged over 65 in UK and USA (reproduced from [3]).

with other on-body units, with external base stations, or with wireless implants.

The applications of BCWC vary from low-power low-data-rate communications in healthcare services, to high-data-rate networks used for personal entertainment. The concept of BCWC include wireless body area networks (WBANs), wireless personal area networks (WPANs) and body sensor networks (BSNs). A WPAN usually refers as the communication between the wearable device and off-body base units, while WBAN consists of several wireless sensor nodes scattered on the human body, communicating with an on-body base unit. The BSN is extended from the wireless sensor network (WSN), and mainly concerned with human physiological data acquisition and communication through a combination of bio-medical and wireless sensors. A very important subject related to BCWC is convergence, in which several functions, capabilities and technologies are merged into a single terminal that will embrace both local and global connectivity.

1.1 Motivations

The major difference between BCWC and conventional wireless systems is the radio channel over which the communication takes place. Since the human body is hostile in regards to attenuating, delaying and distorting the transmitted signal, the design of a power and spectrum efficient wireless system requires accurate analysis and understanding of the radio propagation channel including the human body. Furthermore, the characteristics of body-centric radio channel are subject-specific, and depend on many factors, such as the posture of the body, the frequency of operation and the antenna polarization. All these issues, if not accurately examined, can lead to increased transmission errors or, in extreme cases, loss of a marginal communication link. The design of body-worn and hand-held devices has many other aspects to take into account, including the safety for the user, the dimensions, and the cost.

For body-centric antennas, the presence of the human body in proximity of the radiating structure reduces the radiation efficiency due to electromagnetic absorption in body tissues, causes frequency detuning and radiation pattern distortion. The significance and nature of these effects are system-specific, and depending on the propagation environment, and the choice of antennas.

1.2 Research Objectivies and Challenges

Body-centric wireless networks should provide cost-effective solutions and guarantee the mobility and freedom desired by the users. Therefore the various components of the radio system should provide light weight and low power consumption to avoid short battery life and unwanted obtrusiveness to the user. One of the major issues in designing such a wireless system, is to understand the effect of the human body on the antenna, and on the radio propagation channel.

Measurement campaigns are a valid instrument for characterising the radio channel, and have been widely applied to derive statistical models applicable to the system design [8, 9]. However, since measurement campaigns are time consuming and hardly repeatable, they can not constitute a reliable reference for radio channel characterisation. Besides, for wireless implants, measurements can only be deployed adopting simplified homogeneous physical phantoms representing specific body tissues [10], and hence do not represent the true radio environment.

On the other hand, the recent progress in medical imaging technologies, together with the availability of large computing power, allows the development of homogeneous and inhomogeneous digital human phantoms which can be embedded in electromagnetic numerical codes [11, 12]. Such a numerical approach can provide a physical insight into the propagation mechanism, and overcomes most of the issues arisen by the use of measurement campaigns.

The aim of the research work presented in this thesis, is to analyse and characterise the antenna and the radio propagation in BCWC. This was done through a combination of numerical simulations and measurement campaigns, with a particular emphasis to the numerical analysis. The main objectives of the study include:

- Numerical investigation of the effect of different digital body phantoms, and body postures on the radio channel characteristics.
- Investigation of a novel numerical technique based on the equivalence principle for analysing the impact of different antennas on the on-body radio channel.
- Characterisation of the Ultra wide-band on-body radio channel with respect to different antenna types and propagation scenarios.
- Analysis of the radio channel for telemetry with medical implants.

According to the author's knowledge, the work based on the aforementioned objectives has not been done by others.

1.3 Organisation of the Thesis

Pursuing the introductory chapter, the rest of the thesis is organised as follows:

Chapter 2 introduces the allocation of the frequency spectrum for BCWC, and the main features of the IEEE 802.15 WPAN and WBAN standards, and of the medical implants communications services (MICS) standard. An overview of the main technologies available for BCWC, such as Bluetooth, ZigBee, and ultra wide-band (UWB) was also given.

Chapter 3 gives an introduction to antenna and radio propagation for BCWC. An exstensive literature review on the state-of-the-art in the development of body-worn and implanted antennas was provided. It also discusses the parameters ruling the radio propagation in multipath channels.

Chapter 4 illustrates the characteristics of the human body tissues and it describes the possible ways to model the body. An overview of the challenges in numerical modelling for BCWC was also given. The last part of the chapter was devoted to introduce the characteristics of the finite-difference time-domain (FDTD) technique.

Chapter 5 presents the numerical analysis of wearable antennas and on-body radio channel at the frequency of 2.4 GHz. The analysis is performed adopting the FDTD technique, and the effect of body posture, and the subject-specificity of the radio channel are investigated. It also presents a new technique based on the equivalence principle for analysing the radiation pattern of body-worn antennas, and investigating the impact of different antenna types on the radio channel characteristics.

Chapter 6 presents the characterisation of the UWB on-body radio channel. The radio channel has been studied adopting two different planar antennas presenting different characteristics, and considering their impact on the radio channel. It also presents a statistical analysis on the time delay characteristics of the channel including the effect of the body posture.

Chapter 7 studies the radiation characteristics of medical implants from different locations, and considering different digital phantoms. It also presents a link budget study for MICS applications where the trade-off between antenna size, data-rate, transmitted power and communication distance was analysed. The proposed link budget was studied for propagation in free space, and propagation in a room.

Chapter 8 provides a summary of the main contributions and findings of the study and concludes the accomplished work packages. It also introduces the potential future research activities.

References

[1] C. Otto, A. Milenkovic, C. Sanders, and E. Jovanov, "System architecture of a wireless body area sensor network for ubiquitous health monitoring," *Journal of Mobile Multimedia*, vol. 1, no. 4, pp. 307–326, 2006.

[2] J. Penders, B. Gyselinckx, R. Vullers, M. De Nil, S. Nimmala, J. Van de Molengraft, F. Yazicioglu, T. Torfs, V. Leonov, P. Merken, *et al.*, "Human++: from technology to emerging health monitoring concepts," in *Int. Workshop on Wearable and Implantable Body Sensor Networks (BSN 2008)*, 2008, p. 948.

[3] Y. Hao and R. Foster, "Wireless body sensor networks for health-monitoring applications," *Physiol. Meas.*, vol. 29, pp. R27–R56, Nov. 2008.

[4] "Internet resources, smart textiles offer wearable solutions using nanotechnology," *URL: http://www.fibre2fashion.com/news/*.

[5] The European IST-507102, "My personal adaptive global net (magnet)."

[6] S. Drude, "Requirements and Application Scenarios for Body Area Networks," in *Mobile and Wireless Communications Summit, 16th IST*, 2007.

[7] P. S. Hall and Y. Hao, *Antennas and Propagation for Body-Centric Wireless Communications*. Artech House, 2006.

[8] A. Fort, C. Desset, P. D. Doncker, and L. V. Biesen, "Ultra wideband body area propagation: from statistics to implementation," *IEEE Transactions on Microwave Theory and Technique*, vol. 54, no. 4, pp. 1820–1826, June 2006.

[9] Q. Wang, T. Tayamachi, I. Kimura, and J. Wang, "An on-body channel model for UWB body area communications for various postures," *IEEE Journal on Selected Areas in Communications*, vol. 57, no. 4, pp. 991–998, April 2009.

[10] J. Kim and Y. Rahmat-Samii, "Implanted antennas inside a human body: Simulations, designs, and characterizations," *IEEE Transactions on Microwave Theory and Techniques*, vol. 52, no. 8, pp. 1934–1943, August 2004.

[11] National Institute of Health National Library of Medicine (USA) Board of Regents, Bethesda, MD, Technical Report NIH 90-2197,1990,, "Electronic imaging: Board of regents," *http://www.brooks.af.mil/AFRL/HED/hedr/*.

[12] T. Nagaoka, S. Watanabe, K. Sakurai, E. Kunieda, S. Watanabe, M. Taki, and Y. Yamanaka, "Development of realistic high-resolution whole-body voxel models of japanese adult males and females of average height and weight, and application of models to radio-frequency electromagnetic-field dosimetry," *Phys. Med. Biol.*, vol. 49, no. 4, pp. 1–15, December 2003.

Chapter 2

Communication Standards for Body-Centric Wireless Networks

The IEEE 802.15 task group is responsible for the development of a standard for WPAN and WBAN. The chapter discusses the frequency allocation for BCWC, and introduces the main technologies considered by the standard, namely Bluetooth, ZigBee, and UWB, and discusses the medical implanted communication service (MICS) standard, devoted to the telemetry with medical implants.

2.1 Frequency Allocation for Body and Personal Area Networks

Wireless communications systems can operate in unlicensed portions of the spectrum. However, the allocation of unlicensed frequencies is not the same in every country. Table 2.1 lists the frequency bands allocated for WBANs and WPANs.

- **Medical implanted communication service (MICS)**: In '98, the ITU-R allocated the bandwidth 402-405 MHz for medical implants [1]. MICS devices can use up to 300 KHz of bandwidth at a time to accomodate future higher data rate communications.

Name	Band [MHz]	Max Tx Power[dBm EIRP]	Comments
MICS	402.0-405.0	-16	Worldwide
ISM	433.1-434.8	+7.85	Europe
ISM	868.0-868.6	+11.85	Europe
ISM	902.8-928.0	+36 w/ spreading	Not in Europe
ISM	2400.0-2483.5	+36 w/ spreading	Worldwide
ISM	5725.0-5875.0	+36 w/ spreading	Worldwide
WMTS	608.0-614.0	+10.8	US only
WMTS	1395.0-1400.0	+22.2	US only
WMTS	1427.0-1432.0	+22.2	US only
UWB	100.0-960.0	see Fig. 2.2	US only
UWB	3100.0-10600.0	see Fig. 2.2	US only

Table 2.1: Unlicensed frequencies available for WBANs and WPANs.

- **Industrial scientific and medical (ISM)**: these frequency bands were originally preserved internationally for the non-commercial use of the radio frequency spectrum. However, many are now used by commercial standards since government approval is not required. These frequency band, are allocated by the International Radio Communication Radio sector (ITU-R) [2]; and every country uses them differently, due to different regional regulations.

- **Wireless medical telemetry services (WMTS)**: the Federal Communication Commission (FCC) has allocated these frequency bands in the USA [3] for remote monitoring of patients' health; however, such frequency bands are not available in Europe.

- **Ultra wide-band (UWB)**: is possible to define an ultra wide-band a communication scheme whose spectral occupation is greater than 20%, or higher than 500 MHz. In UWB communications, extremely short pulses are transmitted and higher data rates can be achieved. The FCC authorized the unlicensed use of UWB in the range of 3.1 to 10.6 GHz.

2.2 WPAN Standards

A wireless personal area network (WPAN) is a network for interconnecting devices centered around an individual person's workspace - in which the connections are wireless. Typically, a wireless personal area network uses some technology that permits communication within about 10 meters - in other words, a very short range. In another usage, a WPAN is a technology that could enable wearable computing devices to communicate with other nearby computers and exchange digital information, using the electrical conductivity of the human body as a data network.

For short, medium and long-range communications, Bluetooth, Zigbee, UWB,Wireless LAN (Wi-Fi), WiMAX, GSM, GPRS, UMTS and satellite communication are available, allowing a wide coverage area and offering the possibility of ubiquitous worldwide wireless mobility [4].

In particular, the Bluetooth technology was the basis of a new family of standards, the IEEE 802.15 [5]. IEEE802.15 includes seven different task groups:

1. **IEEE 802.15.1** has derived a WPAN standard based on the Bluetooth specifications [6]. It includes a media access control-and physical layer specification.

2. **IEEE 802.15.2** addresses the issue of coexistence of WPANs with other wireless devices operating in unlicensed frequency bands such as wireless local area networks (WLAN).

3. **IEEE 802.15.3** was responsible for the development of a standard for high-rate (11 to 55 Mbit/s) communications. The task group **IEEE 802.15.3a** attempted to provide a higher speed UWB enhancement to the standard, for applications including imaging and multimedia. The task group **IEEE 802.15.3c** is developing a millimeter-wave-based alternative physical layer (PHY) for the existing 802.15.3 WPAN.

4. **IEEE 802.15.4** deals with low data rates but very long battery life (months or even years) and very low complexity. This standard is based on ZigBee technology [7].

5. **IEEE 802.15.5** is responsible for the specification of mesh networking for WPAN.

6. **IEEE 802.15.6** is focused on WBAN technologies. The goal is a low-power and low-frequency short-range wireless standard.

7. **IEEE 802.15.7** is chartered to write a standard for Visible Light Communications (VLC).

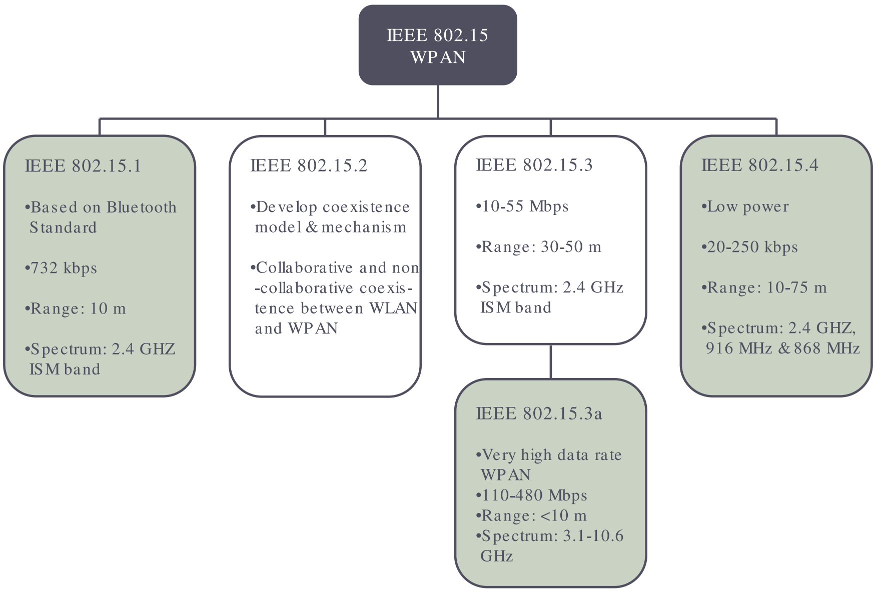

Figure 2.1: Organisation of IEEE802.15 Wireless PAN Group (*Reproduced from* [5])

Short-range devices and networks operate mainly in stand-alone configuration in home and office environments or large enclosed public areas, while their integration into the wireless wide-area infrastructure is still nearly non-existent. When designing future short-range wireless systems, the increasing pervasive nature of communications and computing must be accounted for. Developers and researchers alike assume that the new wireless systems will be the result of a comprehensive integration of existing and future wireless systems. The Bluetooth, ZigBee and UWB technologies are introduced and considered in this study, with UWB regarded as the most promising technology for high data rate and low-power systems.

2.2.1 Bluetooth

Bluetooth is an always-on, low power, short-range radio system for point-to-point and point-to-multi-point voice and data transfer. It operates in the 2.4 GHz ISM band, occupying 79 channels. The radio layer uses frequency hopping spread spectrum coding. The primary modulation method is Gaussian-shaped binary phase shift keying (BPSK). Bluetooth devices are divided into three classes, which specify the antennas output power [4]:

- Class 1 devices broadcast using up to 100 mW of power, the maximum range is approximately 100 m;

- Class 2 devices broadcast using up to 2.5 mW of power, the maximum range is approximately 10 m;
- Class 3 devices broadcast using up to 1 mW of power, and a maximum range of approximately 1 m;

Bluetooth can sustain a data rate of 1 Mbps at a distance of 10 m, and is intended to support an open-ended list of applications, including data, audio, graphics and even video [6], and it allows for the replacement of the many proprietary cables that connect one device to another with one universal short-range radio link. It also provides a universal bridge to existing data networks, a peripheral interface and a mechanism to form small private ad hoc groupings of connected devices away from fixed network infrastructures [8].

The Bluetooth system consists of a radio unit, a link control unit, and a support unit for link management and host terminal interface functions. The Host Controller Interface (HCI) provides the means for a host device to access Bluetooth hardware capabilities. Bluetooth provides support for three general application areas using short-range wireless connectivity [8]:

- Data and voice access points: Bluetooth facilitates real-time voice and data transmissions by providing effortless wireless connection of portable and stationary communication devices;
- Cable replacement: the technology eliminates the need for numerous, often proprietary cable attachments for connection of practically any kind of communication device. Connections are instant and are maintained even when devices are not within line of sight;
- Ad hoc networking: A device equipped with a Bluetooth radio can establish instant connection to another Bluetooth radio as soon as it comes into range;

2.2.2 ZigBee

ZigBee technology is a low data rate, low power consumption, low cost, wireless networking protocol targeted towards automation and remote control applications. ZigBee is expected to provide low cost and low power connectivity for equipment that needs battery life as long as several months to several years but does not require data transfer rates as high as those enabled by Bluetooth [4]. In addition, ZigBee can be implemented in mesh networks larger than is possible with Bluetooth. ZigBee-compliant wireless devices are expected to transmit 10-75 meters, depending on the RF environment and the power output consumption required for a given application, and will operate in the unlicensed RF worldwide (2.4 GHz global, 915 MHz Americas or 868 MHz Europe). The IEEE 802.15.4 physical layer uses direct sequence spread spectrum coding to minimize data loss due to noise and interference. The low band (868/915 MHz) physical layer uses BSPK modulation, whereas the 2.4 GHz physical layer uses offset quadrature phase shift keying (OQPSK). The data rate is 250 kbps at 2.4 GHz, 40 kbps at 915MHz and 20 kbps at 868MHz [4].

IEEE and the ZigBee Alliance have been working closely to specify the entire protocol stack. The IEEE 802.15.4 focuses on the specification of the lower two layers of the protocol (physical and data link layer). On the other hand, the ZigBee Alliance aims to provide the upper layers of the protocol stack (from network to the application layer) for interoperable data networking, security services and a range of wireless home and building control solutions, together with coordinated marketing of the standard, and advanced engineering for the evolution of the standard. This will assure consumers to buy products from different manufacturers with confidence that the products will work together.

IEEE 802.15.4 gives the specification of physical and data-link layers, by offering building blocks for different types of networking, known as star, mesh, and cluster tree [4]. Network routing schemes are designed to ensure power conservation, and low latency through guaranteed time slots. A unique feature of the ZigBee network layer is communication redundancy, eliminating single points of failure in mesh networks.

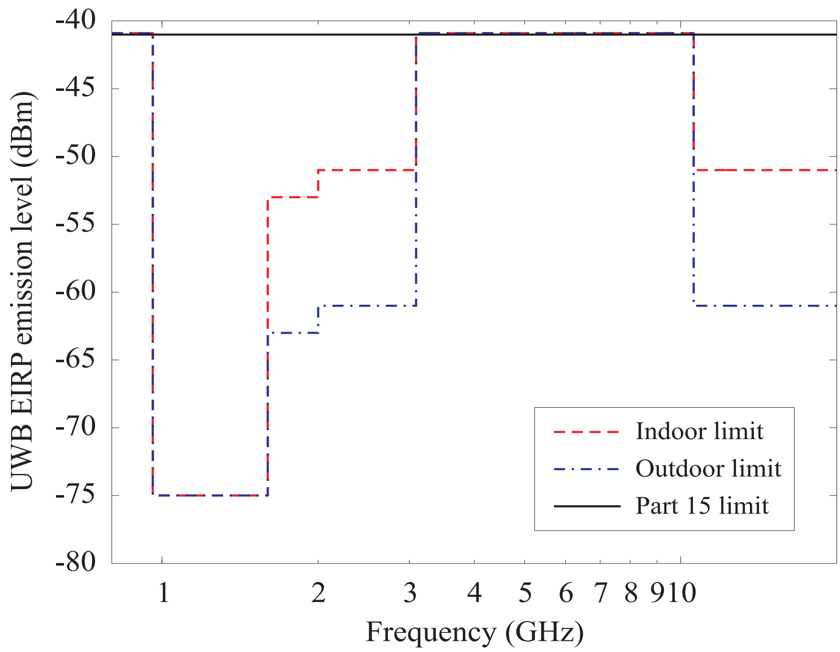

Figure 2.2: FCC Spectrum Mask for Transmissions by UWB Communication Devices (*Reproduced from* [10])

2.2.3 UWB Technology

The UWB is an innovative wireless technology which can transmit digital data over a wide frequency spectrum with very low power and at very high data rates. This technology can carry signals through many obstacles that usually reflect signals at more limited bandwidths and at higher power [9].

The FCC issued in April 2002 UWB Regulations, under Part 15 of the Commission's rules, permitting ultra-wideband intentional emissions subject to certain frequencies and power limitations that will mitigate interference risk to those sharing the same spectrum [10]. Figure 2.2 shows the allowed emission spectrum under Part 15 of the FCC's rules. UWB signals may be transmitted between 3.1 GHz and 10.6 GHz at power levels up to -41 dBm/MHz, with higher degree of attenuation required for the out of band region for outdoor communication.

The bandwidth of UWB systems, as defined by FCC in [10], is more than 20% of a center frequency or more than 0.5 GHz. Clearly, this bandwidth is much greater than the bandwidth used by any current communication technology. UWB implementations can directly modulate an impulse that has a very sharp rise and fall time, thus resulting in a waveform that occupies several GHz of bandwidth. Ultra-wideband communication systems modulate short duration (nanosecond) pulses to transmit and receive information. The pulses used in such systems have bandwidths of GHz range and a fractional bandwidth larger than 20% [11]. Fractional bandwidth is defined as

$$B_f = \frac{2(f_h - f_l)}{f_h + f_l} \cdot 100\% \tag{2.1}$$

where, f_h and f_l are the highest and lowest cut-off frequencies (-10 dB point) of a UWB pulse spectrum respectively. The large bandwidth of UWB signals provide robustness to jamming and have low probability of detection properties. UWB devices usually require low transmit power, due to the control over duty cycle, thus supporting a longer battery life for hand-held devices.

Typical UWB pulse waveforms used in the literature include rectangular, Gaussian and Gaussian monocycle [12, 13]. The rectangular pulse is a simple pulse; however, it has a large DC component, which makes it less appealing for modelling and analysis aspects. One of the most used pulse shapes is a Gaussian pulse, which can be expressed by

$$p(t) = \frac{1}{\sqrt{2\pi}\tau} e^{-\frac{1}{2}\left(\frac{t-t_0}{\tau}\right)^2} \tag{2.2}$$

where τ determines the width of the pulse and t_0 sets the center of the pulse. Commonly, derivatives of the Gaussian pulse in eq. 2.2 are applied to describe transmitted and received UWB pulses for characterization and modeling purposes. The first derivative of the Gaussian pulse (known as the Gaussian Monocycle) is given by

$$p_m(t) = A\left(\frac{t-t_0}{\tau^2}\right) e^{-\frac{1}{2}\left(\frac{t-t_0}{\tau}\right)^2} \tag{2.3}$$

where τ determines the monocycle pulse width, and A is the pulse amplitude. A useful representation of the pulse is the equivalent frequency spectrum, which is defined as

$$P_m(f) = A\sqrt{2\pi}(2\pi f\tau)e^{-\frac{1}{2}(2\pi f\tau)^2} \cdot e^{-j(2\pi f t_0 + 0.5\pi)} \tag{2.4}$$

The second derivative of the Gaussian pulse (derivative of the Monocycle) is also a popular pulse waveform used in literature and is given by

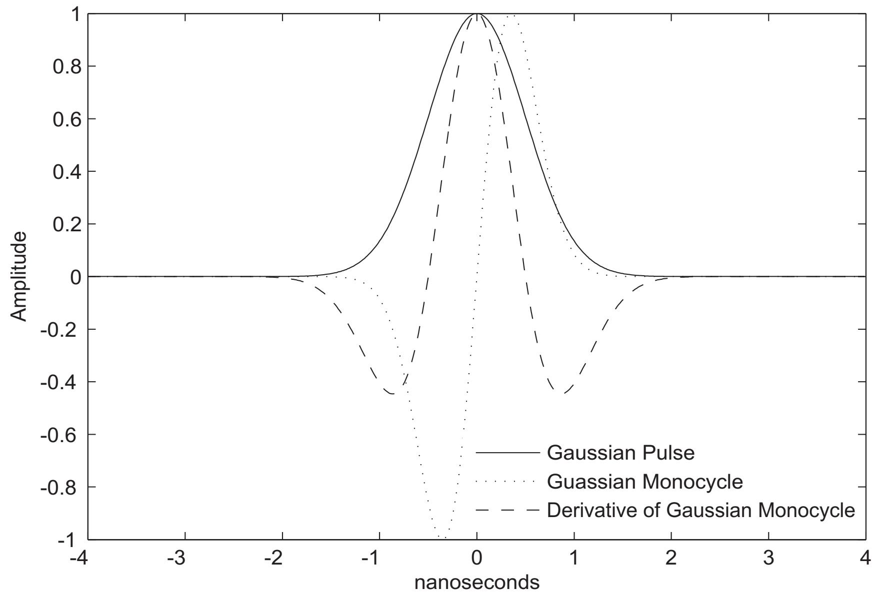

Figure 2.3: Normalised waveforms of a Gaussian pulse, Monocycle and Monocycle derivative for $\tau = 0.5$ ns.

$$p_{\delta m}(t) = A\left[1 - \left(\frac{t - t_0}{\tau^2}\right)^2\right] e^{-\frac{1}{2}\left(\frac{t-t_0}{\tau}\right)^2} \tag{2.5}$$

Figure 2.3 presents the pulses described above, for $\tau = 0.5$ ns and $t_0 = 0$ ns and the amplitude normalised to 1. The Gaussian monocycle and its derivative, do not have a DC component, which makes the radiation more efficient in comparison to rectangular pulses.

The UWB emission limit is set to the lowest level ever applied to any system, which means that the total power emission of a UWB system is in the milliwatt range, spread over several gigahertz of bandwidth. However, it is not merely the high data-rate and short range features that make UWB a suitable candidate for body-centric wireless networks: the regulatory limits on power emissions are actually complementary to the requirements for low-power consumption for most body-centric wireless network applications.

Ultra-Wideband Vs. Narrow Band

The UWB technology offers many advantages with respect to narrow band systems, such as:

- **higher data rate** due to their very wide bandwidth;
- **less power consumption**: the transmission of short nanosecond pulses, rather than continuous waveforms, allow pulse generators, amplifiers and receivers to not work continuously, but to be turned on for only a few nanoseconds in each repetition period. In addition, UWB systems can transmit at a much faster data rate compared with narrow band systems due to their wide bandwidth. The combination of high data rate and intermittent signal reduces average power consumption, and hence UWB radio chips can have smaller batteries;
- **less analog components** since it is possible to transmit and receive pulses without generating a carrier. This makes possible to achieve smaller chip sizes which is a very important feature in the context of small and low-cost WBANs;
- **robustness to multipath**: A typical problem in wireless communication is the multipath. In a typical complex indoor environment, the presence of many scatterers produce reflected signals which can cause a destructive interference on the direct signal (the received power decreases). In UWB, due to the short duration of pulses, it is easy to separate at the receiver the direct component from each single reflection, and hence is possible to achieve longer transmission range with the same power level.
- **higher sensibility in positioning systems** since the accuracy is proportional to the bandwidth of the emitted signal;
- **safer for the user** because of the very low peak power (-41 dBm). Besides, since in UWB systems short nanopulses are transmitted, the user is not continuously exposed to the radiation.

On the other hand, the design of wideband devices for a UWB transceiver is complex. The difficulty in having power efficient small UWB antennas, pulse shape distortions due to the filtering characteristics of the antenna and the communication channel, losses due to wideband matching and consumption of wideband low-noise amplifier are major challenges in implementing UWB front-end in portable devices [14]. In addition, UWB systems are sensitive to continuous wave jamming.

2.3 Towards the Standardization of WBAN

WBANs consist of a number of units placed inside or in proximity of the human body (such as in everyday clothing), and are a natural progression of the WPAN concept [5]. Also known as IEEE 802.15.6, WBAN is a low-frequency technology intended to endow a future generation of short-range electronics for exchanging information [15]. The advances in communication and electronic technologies have enabled the development of compact and intelligent devices has facilitated the introduction of such a network. Wireless communication within a WBAN may be based on an infrared, light, microwave radio and even near-field coupling through skin conduction. WBANs may communicate externally with other networks (which may themselves be WBANs), using one of a range of available wireless technologies.

A good real-world example of this technology in practice is a pacemaker that can alert, or be controlled by, a wristwatch by using wireless transmission. The military is also considering to use WBAN to reduce the probability of interference and eavesdropping in battle field communication. In the future, more complex body area networks are needed to provide the powerful computational functionalities required for high-data rate and broadband applications.

These requirements have led to increasing research and development activities in the area of WBAN applications for many purposes [16–19], with the main interests being healthcare, patient monitoring, and wearable computers.

The idea of a WBAN was initiated for medical purposes, in order to keep continuous records of patients' health at all times. Sensors are placed around the human body to measure specified parameters and signals in the body (e.g. blood pressure, ECG, sugar level, temperature, etc). As an extension to these sensors, base units can be deployed on or close to the human body to collect information or relay command signals to the various sensors in order to perform a desired operation. Figure 2.4 presents an illustration of WBAN applied in medical care services. Body area networks can be applied to many fields; some of its applications include [20][21]:

- Wearable audio - the central device is the headset, applying stereo audio and microphone, with connected devices including (but not limited to): cellular phone, MP3 player, PDA, CD audio player. [22]

- Assistance to emergency services, such as police, paramedics and fire fighters.
- Military applications, including soldier location tracking, image and video transmission and instant decentralised communications.
- Augmented reality to support production and maintenance.
- Access/identification systems by identification of individual peripheral devices.
- Navigation support in the car or while walking with reliable and efficient communication with existing technologies, such as GPS.
- Bio-Sensors for athletes' performance monitoring and enhancement to improve outcomes in major events.

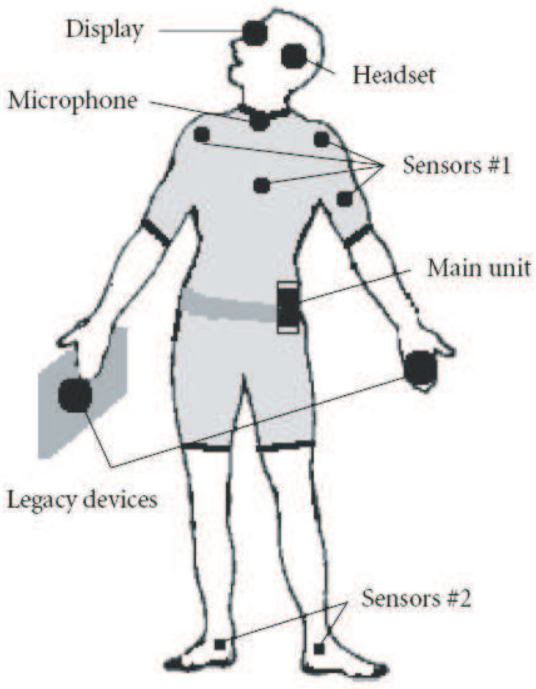

Figure 2.4: Envisioned WBAN and its possible components [23]

Currently, there is no specific standard for WBANs to operate among other available wireless consumer technologies, and the proposed standards for WPAN do not meet the medical (proximity to the tissues) relevant communication regulations for some application environments. Table 2.2 lists the features of the available technologies for WBAN. The IEEE 802.15.6 task group, is responsible for the development of a standard for WBANs, and the purpose of the group is to tackle the main challenges and constraints, such as power consumption and quality of service (QoS). The main

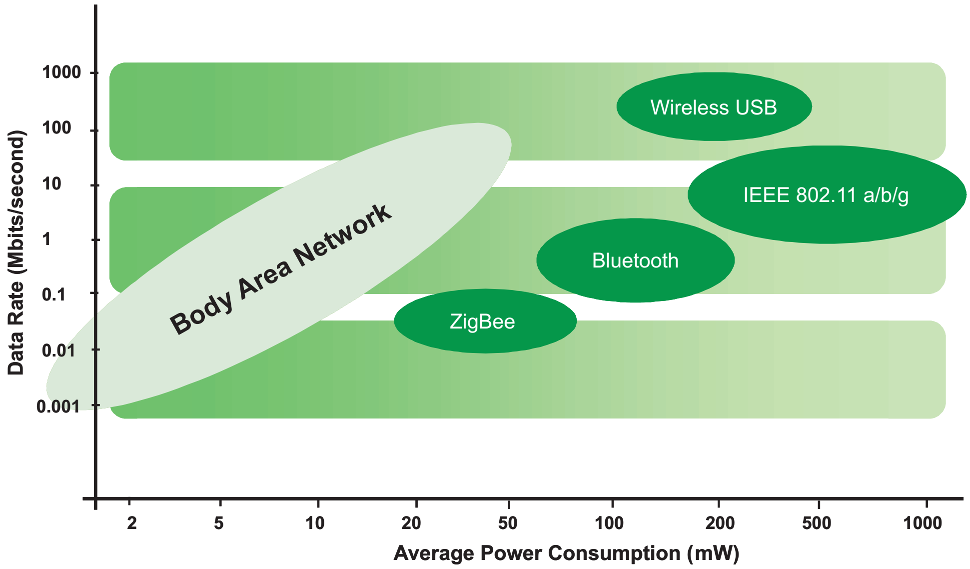

Figure 2.5: Targeted location of BAN among other existing wireless personal area network technologies with sustained data rate presented as a function of average power consumption (*Reproduced from* [22])

requirements of the initial study are the support for very low power devices and sensors, a target of less than 10% power consumption for communications compared to the total device and to have a single standard with a broad range of supported data rates Fig. 2.5.

WBANs, bring about a new set of challenges, such as scalability (in terms of data rate, power consumption and number of devices), integration of on/in/off-body networking, interference mitigation, coexistence, QoS, and ultra-low power protocols and algorithms. Moreover, effects on the human body have to be considered and several regulatory requirements have to be met. Two kinds of devices were indicated namely, class A for medical devices and class B for non-medical devices. The frequency bands of interest include the ISM bands, as well as frequency bands approved by medical and/or regulatory authorities in different countries. The task group concluded that (for low data rate applications) WBANs should operate on, inside or in the vicinity of the body with limited range (up to 2 metres). The channel model should include human body effects including radio wave absorption and underlying impact on the user's health. Moreover, an extremely low consumption power (0.1 to 1 mW) is required for the system, in addition to its capability of energy scavenging/battery-less operation. The standard should be designed to support scalable data rates (0.01 to 1,000 kbps, optional 10 Mbps); therefore the task group will possibly split the standard into class A for low data rate applications, and class B for high data rate communications.

	Medical	**Non-medical**	**Bandwidth**	**Data rate**
MICS (world wide)	Yes	No	$\leq$300 KHz	Low
WMTS (regional)	Yes	No	8.5 KHz-6 MHz	Medium
ISM (world wide)	Yes	Yes	Selectable	Medium
UWB (world wide)	Yes	Yes	>500 MHz	High

Table 2.2: Features of the available technologies for WBANs

2.4 MICS standard

The European Telecommunications Standards Institute (ETSI) developed the Medical Implant Communication Services (MICS) standard [24]. The ETSI document indicates two principal fields of application for the standard. The first one regards the communication between a base station and an implanted device. The second one is for telecommunication between medical implants within the same body.

The frequency band allocated is 402 MHz to 405 MHz. The maximum emission bandwidth for the complete session is 300 kHz, and in the case where the system uses separate frequencies for the up- and down-links, the two link bandwidths must not exceed 300 kHz. This implies that, in order to get high data throughput, a half-duplex scheme should be adopted, where only one device transmits at a time. However, most of the applications require the transmission of physiological data, and the uplink (from the implant to the base station) requires more bandwidth than the downlink. Note that, in the case of a half duplex solution the up- and down-link do not have to share the same frequency band. Separate RX and TX bands, each with a bandwidth of 300 kHz, may be used as long as they are not used simultaneously.

The 300 kHz bandwidth is an emission limit: the power at the band edges has to be 20 dB below the maximum level of the modulated output. The resolution bandwidth of the measurement should be 1 % of the emission bandwidth of the device under test. The maximum power limit is set to 25 μW Equivalent Radiated Power (ERP), i.e., the maximum field-strength in any direction should be equal to, or lower than, what a resonant dipole would give in its maximum direction at the same distance, with the dipole being fed with a signal of 25 μW. There is some confusion about the power level, as the ITU-R recommendation [25] sets a level of 25 μW EIRP, which equals a level 2.2 dB lower than the ERP level set in the ETSI MICS standard.

2.5 Summary

The chapter presented an overview of the communication standards developed by the IEEE 802.15 task groups for WPAN and WBAN. The main features of Bluetooth, ZigBee and UWB were briefly introduced, and it was highlighted that the UWB technology promises to be a suitable candidate for Body-Centric communications; its advantages over narrow band systems have been illustrated. The chapter then presented a description of the MICS standard which has been developed for the telemetry with medical implants.

References

[1] "Federal communications commission (FCC), code of federal regulations (CFR), title 47 part 95, MCIS band plan," *URL: http://www.fcc.gov*, March'03.

[2] "International telecommunications union-radiocommunications (ITU-R), radio regulations, section 5.138 and 5.150," *URL: http://www.itu.int/home*.

[3] "Federal communications commission (FCC), code of federal regulations (CFR), title 47 part 95, WMTS band plan," *URL: http://www.fcc.gov*, January'03.

[4] R. Foster and Y. Hao, "Wireless body sensor networks for health-monitoring applications," *Physiological Measurement*, vol. 29, no. 11, pp. 27–56, 2008.

[5] "IEEE 802.15,an international standards working group, IEEE 802.15," *URL: http://grouper.ieee.org/groups/802/15/*.

[6] "The bluetooth standard version 1b," *URL: http://www.bluetooth.com*.

[7] "IEEE802.15.4, wireless medium access control for low-rate medium acces control (MAC) and physical layer (PHY) specifications for low-rate wireless personal area networks (LR-WPANs)," 2003.

[8] B. T. Overview, *Nokia Forum*, vol. , Version 1.0, 2003.

[9] D. Porcino and W. Hirt, "Ultra-wideband radio technology: potential and challenges ahead," *IEEE Communications Magazine*, vol. 41, no. 7, pp. 66–74, July 2003.

[10] *FCC First Report and Order, Revision of the Part 15 Commission's Rules Regarding Ultra-Wideband Transmission Systems*, pp. 98–153, April 22, 2003.

[11] F. Dowla and F. Nekoogar, "Multiple access in ultra-wideband communications using multiple pulses and the use of least squares filters," *Radio and Wireless Conference, RAWCON*, pp. 211–214, 2003.

[12] R. A. Scholtz, "Multiple access with time-hopping impulse modulation," *Proceedings of IEEE MILCOM 1993*, pp. 447–450, 1993.

[13] L. Zhao and A. M. Haimovich, "Performance of ultra-wideband communications in the presence of interference," *IEEE Journal on Selected Areas in Communications*, vol. 20, no. 9, pp. 1684–1691, 2002.

[14] D. Barras, F. Ellinger, and H. J
"ackel, "A comparison between ultrawideband and narrowband transceivers," *Proc. TR-Labs/IEEE Wireless*, pp. 211–214, 2002.

[15] A. Alomainy, "Antennas and radio propagation for body-centric wireless networks," Ph.D. dissertation, Queen Mary, University of London, 2007.

[16] E. Jovanov, A. ODonnell-Lords, D. Raskovic, P. Cox, R. Adhami, and F. Andrasik, "Stress monitoring using a distributed wireless intelligent sensor system," *IEEE Engineering in Medicine and Biology Magazine*, vol. 22, no. 3, pp. 49–55, 2003.

[17] S. Matsushita, "A headset-based minimized wearable computer," *IEEE Intelligent Systems*, vol. 16, no. 3, pp. 28–32, May/June 2001.

[18] P. Lukowicz, U. Anliker, J. Ward, G. Troster, E. Hirt, and C. Neufelt, "AMON: a wearable medical computer for high risk patients," *Proceeding Sixth International Symposium on Wearable Computers 2002, Seattle*, pp. 133–134, October 2002.

[19] C. Kunze, U. Grossmann, W. Stork, and K. Muller-Glaser, "Application of ubiquitous computing in personal health monitoring systems," *Biomedizinische Technik: 36th Annual meeting of the German Society for Biomedical Engineering*, pp. 360–362, 2002.

[20] P. S. Hall and Y. Hao, *Antennas and Propagation for Body-Centric Wireless Communications*. Artech House, 2006.

[21] Z. N. C. (Editor), *Antennas for Portable Devices*. wiley & Sons, Inc., 2007.

[22] S. Drude, "Tutorial on body area networks - document: IEEE 802.15-06-0331," *IEEE P802.15 Working Group for Wireless Personal Area Networks (WPANs)*, 18 July 2006.

[23] M. G. Benedetto, T. Kaiser, A. Molisch, I. Oppermann, and D. Porcino, *UWB communication systems: a comprehensive overview*. Hindawi Publishing Corporation, 2006.

[24] European Telecommunications Standards Institute, "Electromagnetic compatibility and radio spectrum matters (ERM); radio equipment in the frequency range 402 MHz to 405 MHz for ultra low power active medical implants and accessories; part 1: Technical characteristics, including electromagnetic compatibility requirements, and test methods." *European Telecommunications Standards Institute, ETSI EN 301 839-1*, 2002.

[25] *International Telecommunication Union, Recommendation ITU-R SA.1346, 1998*, 1998.

Chapter 3

Basics of Antenna and Propagation for Body-Centric Wireless Communications

In this chapter, the recent developments in antenna design for WPAN/WBAN are discussed, as well as the fundamentals of radio propagation for body-centric wireless communications.

3.1 The Radio Link

The radio link can be represented as three distinct blocks, namely, the transmitting antenna (with transfer function $H_{Tx}(\omega)$), the radio channel (with transfer function $H_{Ch}(\omega)$), and the receiving antenna (with transfer function $H_{Rx}(\omega)$). Therefore, the receiving signal $S_{Rx}(\omega)$ can be defined as

$$S_{Rx}(\omega) = S_{Tx}(\omega)\, H_{Tx}(\omega)\, H_{Ch}(\omega)\, H_{Rx}(\omega) \tag{3.1}$$

where $S_{Tx}(\omega)$ is the input signal. The path gain, which is given by the ratio between received and transmitted power, can be calculated adopting the Friis transmission formula

$$PG = \frac{P_r(\omega)}{P_t(\omega)} = \left(1 - |\Gamma_t(\omega)|^2\right)\left(1 - |\Gamma_r(\omega)|^2\right) G_r(\omega) G_t(\omega) \left|\hat{\rho}_t(\omega) \cdot \hat{\rho}_r(\omega)\right|^2 \left(\frac{\lambda}{4\pi d}\right)^2 \tag{3.2}$$

where

- G_t is the peak gain of transmitting antenna;
- G_r is the peak gain of receiving antenna;
- P_t is the average input power of transmitting antenna;
- P_r is the average output power of receiving antenna;
- Γ_t is the return loss at the input of transmitting antenna;
- Γ_r is the return loss at the output of receiving antenna;
- $|\hat{\rho}_t \cdot \hat{\rho}_r|^2$ is the polarization matching factor between Tx and the output at Rx;
- λ is the wavelength at the operating frequency;
- d is the distance between transmitting and receiving antennas;

Often, the inverse of the path gain (path loss) is adopted.

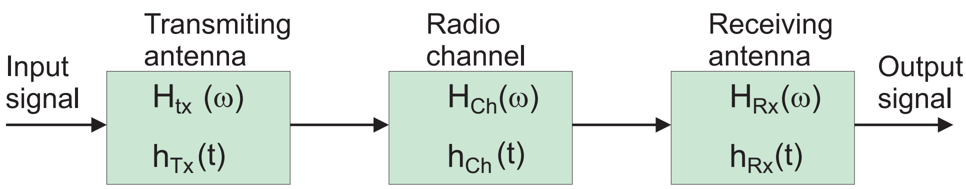

Figure 3.1: Block diagram representing the radio link.

In conventional mobile communications systems, between a mobile terminal and a base station, the variation in the channel is due to interference between multiple rays scattered from the local environment. In WBANs, in addition to the local scattering, significant changes in the channel are also due to the changes in posture of the body. Thus, characterisation of the radio channel needs to consider both the change in position of the mobile terminals, and for the change in geometry of the body [1].

Furthermore, the presence of the body, and its changes in posture, affect the radiation pattern, and the impedance of the antenna.

The aforementioned Friis transmission formula 3.2 is valid in the case of free space propagation, and when the receiver is located in the far-field region. In a scattered environment, the wave reaches the receiver through multiple paths and more complex path loss models need to be considered. For on-body communications, the scenario is even more complex, and the propagation is a combination of free space waves, reflections from body parts and surrounding scatterers, and creeping waves along the body surface. Moreover, the impedance matching and the antenna gain depend on many factors, such as its position on the body, and the separation distance between the antenna and the body. For all these reasons, the three blocks of Fig 3.1 are not independent anymore, and the antenna characteristics need to be included in the on-body radio channel.

3.2 Antennas for Body-Centric Wireless Communications

In BCWC, communications among on-body devices are required, as well as communications with external base stations, which therefore require antennas with different radiation characterisitcs. For the wireless BAN to be accepted by the majority of consumers, the radio system components, including the antenna, need to be somehow hidden, conformal to the body, small in size and light in weight. This requires a possible integration of these systems within everyone's daily clothes. The design of body-mounted antennas needs an accurate understanding of how the human body affects the behavior of the antenna in terms of frequency detuning, pattern modification and efficiency reduction. The general requirements for WBAN antennas are [1, 2]:

- low mutual influence between antennas and body for high radiation efficiency and low specific absorption rate (SAR);
- small size and low profile;
- polarization normal to the body surface for minimized link loss in on-body communications;

Many studies have been done on the operation of antennas located in close proximity of the body [3–6], as well as on the SAR [7, 8] and on the propagation on and off the body, for use in cellular networks [9].

The use of an antenna with a ground plane (e.g.microstrip patch) minimizes the absorption from the human body, although this kind of antenna presents a narrowband behavior. In [5], a parametric study to evaluate how the antenna-body spacing affects the antenna performance has been presented. The farther the antenna is from the body, the lower is the absorption from the human body. The use of a lossy material to keep this spacing is beneficial, as it leads to SAR reduction, since part of the power is dissipated in the lossy material rather than in the body tissues.

To enable the integration of wireless devices in garments, antennas made out of textile materials have been proposed [10–15]. In [14], a patch antenna integrated into protective clothing for fire-fighters was introduced. The antenna was printed on a flexible pad of foam, which is commonly used in protective clothing. In [11, 12, 16] narrowband antennas are printed above Electromagnetic Band Gap (EBG) structures to reduce the radiation towards the human body, and minimize the detuning effect. In [12], Langley *et al.* proposed a flexible dual-band patch antenna (2.45 and 5.5 GHz) printed on a EBG textile substrate made of felt (see Fig. 3.2). Results demonstrated that, introducing the EBG, the radiation into the body is reduced by over 10 dB, and the antenna gain is improved by 3 dB. However, the antenna is big in size (120 x 120 mm In [17], Scanlon *et al.*, presented a set of higher mode microstrip patch antennas operating at 2.45 GHz. The antennas are excited at the higher TM_{21} resonant mode which has the advantage of having a vertical monopole-like radiation pattern. In this way, despite a total antenna height of only $\lambda/20$, the on-body coupling performance is comparable to that achievable with a quarter wavelength monopole and significatively higher than that measured with a fundamental microstrip patch antenna. In [2] a cavity slot antenna is proposed for communication at 2.45 GHz. The polarization of the antenna is normal to the body, thus leading to minimized path loss in the on-body link and relatively high efficiency (50%) when it is body-mounted.

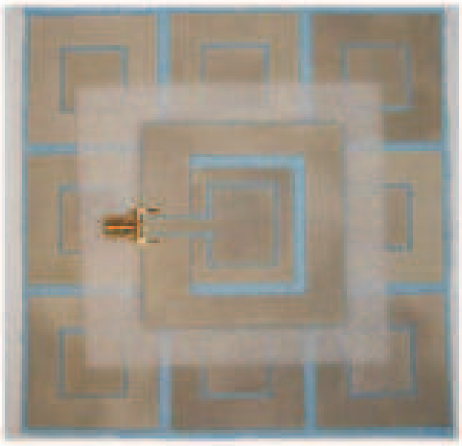

Figure 3.2: Picture of the dual band wearable antenna over an EBG substrate presented in [12].

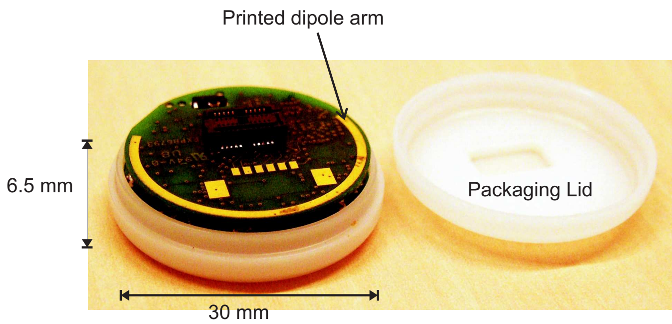

Figure 3.3: Picture of compact sensor antenna presented in [19].

In [18], a patch antenna on a ceramic substrate with a high dielectric constant and a planar inverted F-antenna operating at 868 MHz close to the human body were presented by Adel *et al*. Both antennas have good omni-directional directivity and dimensions significantly smaller than 1/10 of the wavelength. It was concluded that, by choosing a thicker substrate, the radiation efficiency can be improved; and that an improvement of the radiation properties could be accomplished by using a substrate with a lower dielectric constant combined with a shorter shorting strip between the two metal planes for the PIFA case.

In [19], Alomainy *et al*. presented a compact sensor antenna (printed dipole) for healthcare devices (see Fig. 3.3). A thorough numerical investigation of the antenna performance including full sensor details and the presence of the human body was performed. The results demonstrated that the power radiated from the compact embedded antenna is comparable to the one of an external monopole.

Salonen *et al.* has presented a flexible planar inverted F antenna (PIFA) that can be applied for smart clothing intended for use with wearable computers as part of WBAN [15]. In [20] a dual band button antenna for WLAN applications was presented. The antenna has the size of a standard metal button used in denim jeans, and can be easily integrated in clothes.

3.2.1 UWB Antennas for On-Body Applications

In UWB communications, the antennas are significant pulse-shaping filters. Any distortion of the signal in the frequency domain causes distortion of the transmitted pulse shape, thereby increasing the complexity of the detection mechanism at the receiver. Fundamental antenna parameters, such as impedance bandwidth, radiation patterns, half-power beam-width, antenna gain and total efficieny [21], should be considered in designing antennas for UWB radio; however, there are additional challenges for UWB antenna design.

When designing UWB antennas, group delay must be taken into account. If the phase is linear throughout the frequency range, the group delay will be constant and hence delivered pulses will be transmitted with no distortion in all directions. Any strong resonance at any frequency causes large group delay variation and thus causes much distortion in the pulse shape. So it is not reasonable to design ultra-wideband antenna with multiple deep resonance as far as pulse fidelity is concerned. UWB antennas require a constant return loss across the whole bandwidth of operation. A very wide operational fractional bandwidth of UWB systems makes the design and evaluation of antennas more difficult than in narrowband systems [22–24].

For more specific applications, such as WBANs, the antenna design becomes more complicated than for simple free-space operation scenarios, due to the complex human body medium presence. Most examples in the literatures consider the antennas as part of the propagation system and apply common and widely available antenna types to characterise the channel. Two different UWB antennas with different radiation characteristics were presented in [25]. The two antennas are shown in Fig. 3.4; the first antenna is a printed horn-shaped self complementary antenna (HSCA), and the second is vertical planar inverted cone antenna (PICA). The HSCA is tangentially polarised (respect to the body), while the vertical PICA is vertically polarised. As shown in [25], antennas with different radiation characteristics lead to different channel parameters. In particular, the use of a vertically polarized UWB monopole, rather than a planar antenna, reduces the attenuation but increases the time spread of the signal. Therefore, it was concluded that the hybrid use of different antennas can improve the channel performances. However, such antennas are relatively big and not conformal to the body, and the aim of the authors was to demonstrate the effect of different antenna types on the UWB on-body radio channel.

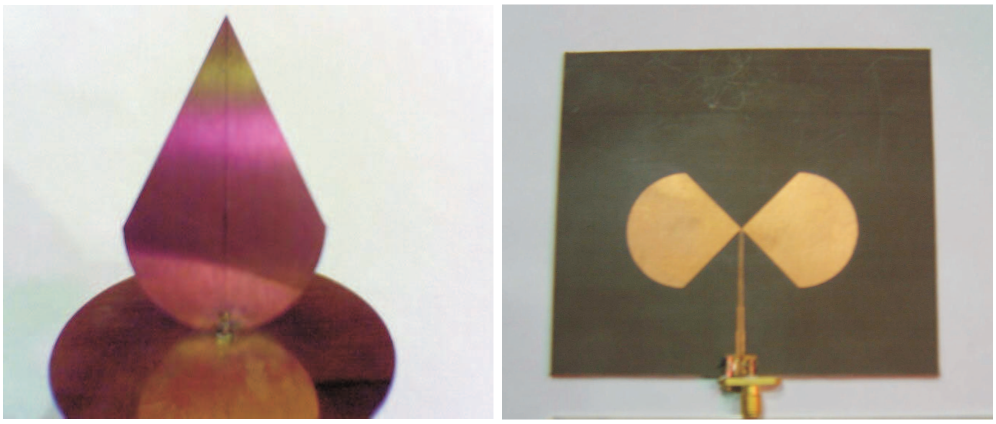

(a) Vertical planar inverted cone antenna (PICA).

(b) Printed horn-shaped self complementary antenna (HSCA).

Figure 3.4: The two UWB antennas proposed in [25].

In [26], Chen *et al.* proposed three different microstrip-fed wearable UWB antennas. Such antennas were designed to operate in the lower UWB frequency band (3-5 GHz), and they present different radiation characteristics. Chen *et al.* proposed a novel diversity antenna with two different radiating elements providing different and symmetric coverage regions.

In [27], Klemm *et al.* presented time-domain characteristics of an aperture-stacked patch antenna for UWB body-worn devices through numerical modelling. Both frequency and time domain characteristics of the proposed antenna are analysed and discussed with regards to applicability in wearable computing. Three different modes were investigated: transmit, receive and two antennas mode (where one antenna is transmitting and the other is receiving in free space), with a Gaussian pulse excitation. The spatial and impulse performance of the antenna was studied by obtaining fidelity of pulses radiated in different directions in comparison to a reference pulse. High fidelity values suggested that the antenna is a good candidate for UWB wireless body area network.

Promwong *et al.* used a three-antenna method to characterise the UWB transfer function of two antennas with one placed on the human body. The measurement results are then used to evaluate the extended Friis transmission formula used for calculating transmission gain [28]. The biconical antenna is used for transmitting and the Skycross antennas for receiving. Both transmitted waveform and matched filter system are used to characterise the antenna with the extended Friis formula.

A discussion of the main parameters affecting UWB antennas and how they can be applied to WBAN applications is presented in the following sections.

Radiation and Pulse Fidelity

For UWB antennas, an additional criterion has to be taken into account, which is the frequency variations of the antenna radiation patterns. This criterion is considered essential in designing suitable UWB antennas as due to the large relative bandwidth of UWB antennas, the variations of the antenna pattern over the considered frequency range are more significant. In addition, the emission rules for UWB radiation specify that the power spectral density must be limited in each possible direction. The regulations enforce a limit on the emitted power in the frequency-angle domain [29].

UWB antennas' impulse responses affect the actual system design with respect to actual bandwidth and time domain signal shape. The impulse response of an UWB antenna is also direction-dependent, which urges the introduction of a spatial root-mean-square (RMS) delay spread similar to the classical delay spread of the radio propagation channel. The enclosed energy level in radiated signals (also in received signals) by a specified time window is often used in describing UWB antenna time domain performance [30]. This leads to time spread being defined as a ratio between the lengths of 99% of energy level of radiated pulse and the source pulse. It discloses how much the energy of the radiated pulse is spread compared to the input pulse.

Consistency of radiated pulse shape is a critical issue in UWB antenna performance. It is helpful to have a measure of the energy radiated and a measure of fidelity for a given input waveform, when describing UWB antennas. A correlation between the transmitted, or received, waveform and a template is used to assess how an antenna affects a waveform and to quantify the level of distortion.

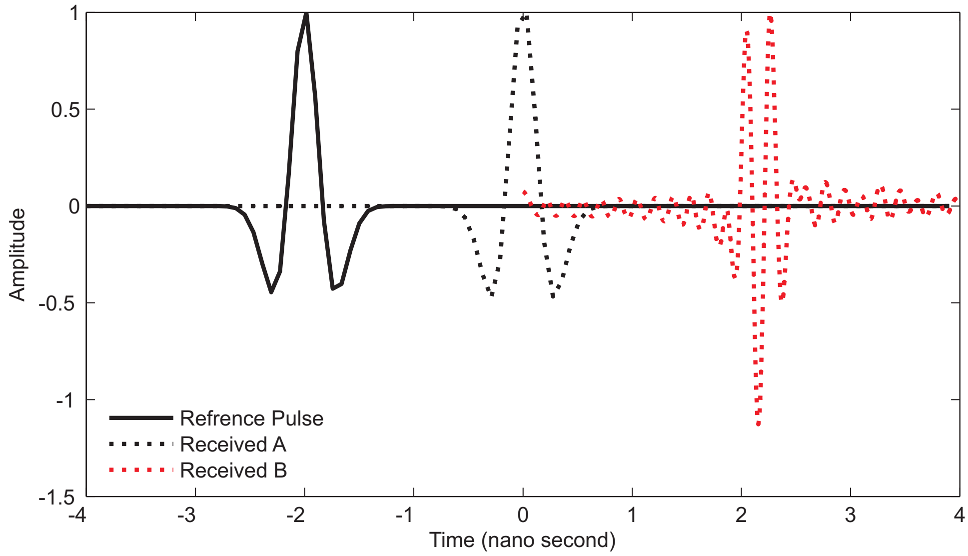

Figure 3.5: Examples of transmitted UWB pulses to illustrate pulse fidelity concept. Fidelity of reference pulse compared to Received A is 100% and compared to Received B is 85% to demonstrate that fidelity compares pulse shape only regardless of pulse amplitude and phase offsets.

A fidelity parameter involving the auto-correlation of the difference of the time domain transmitted field and a template function is described by Lamensdorf *et al.* in [31]. In certain UWB transceivers, correlation detection is applied to recover sent data correctly and introducing a correlation pattern involving the cross-correlation between the transmitted/received signal and the template function would provide an excellent measure for antenna performance. Descriptors of energy patterns are useful for specific applications where signal level varies depending on system parameters and propagation environments.

In time-domain formulation, the fidelity between waveforms $x(t)$ and $y(t)$ is generally defined as a normalised correlation coefficient [31, 32],

$$F = \max_{\tau} \left[\frac{\int_{-\infty}^{\infty} x(t).y(t-\tau) \cdot dt}{\sqrt{\int_{-\infty}^{\infty} |x(t)|^2 \cdot dt \int_{-\infty}^{\infty} |y(t)|^2 \cdot dt}} \right] \tag{3.3}$$

where $x(t)$ and $y(t)$ are normalized by their energy, respectively and the fidelity is the maximum integration by varying time delay τ. Figure 3.5 illustrates the definition of pulse fidelity characterisation.

In practice, signal fidelity is calculated for a given direction in space in order to fully characterise the spatial radiation properties of an antenna. The fidelity depends not only on the antenna characteristics, but also on the excitation pulse; thus, it is also a system-dependent parameter.

3.2.2 Antennas for Medical Implants

The recent developments in nanotechnology, and microelectromechanical systems, allow the development of implantable sensors for improving the life for many patients [1]. Much work, is being done in the development of new sensors, however much less work has been done in the radio interface. Since implantable antennas are placed inside lossy tissues with high permittivities, their design is different from the one used in conventional on-body systems. In some cases, such as pacemakers, antennas that conform to the shape of the sensor have been developed. There are some differences between implanted and classical wire antennas. Since the antenna is immersed in a lossy material, the wave is attenuated as it propagates along the wire. The phase velocity of the traveling wire is much smaller than the free space, as it is reduced of a factor equal to the square root of the relative permittivity of the tissue in which it is immersed. If the antenna is surrounded with a low permittivity insulation layer, the phase velocity increases, therefore the electrical length of the antenna is reduced. On the other hand, since the lossy matter is removed from the region of the strongest near-field, the loss per unit length is reduced. Some analytical results on the effect of the insulation layer on the losses, were presented in [33] considering a simple Hertzian dipole in a lossy sphere, and in [34], the effect of a silicone insulation layer on the input impedance of the antenna was studied.

An example of antenna conformal to the case of the sensor is the circumference antenna [1]. Such an antenna is of a monopole type, where the circular wire is mounted around the edge of the pacemaker case, and the case acts as a ground plane. An alternative is the circular planar inverted F antenna (PIFA), where the wire is replaced by a plate.

A microstrip antenna can be placed on the large flat surface of a typical implant. These antennas consist of a dielectric slab with the ground plane on one side, and the radiating structure on the other side. In [35–39] spiral and meandered microstrip PIFA antennas for medical implants have been developed (see Fig. 3.6). Such antennas are printed on a substrate with relative permittivity of 10.2, and, in order to insulate the radiating element from the tissue, they are covered by a superstrate with same characteristics of the substrate.

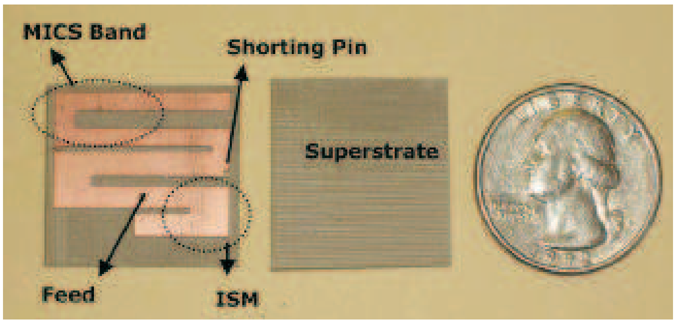

Figure 3.6: Picture of the dual band implantanble PIFA antenna operating at 402 and 2400 MHz (MICS and ISM bands) proposed in [37].

In [40], it was proposed a novel antenna design for an ingestible biotelemetric capsule system. The proposed structure is a meandered dipole conformal to the shape of a capsule. In [41] three dimensional folded dipole antennas as a data-telemetry in a dual-unit retinal prosthesis to restore partial vision to the blind were proposed (see Fig. 3.7). The performance of the two-dimensional and three-dimensional antennas

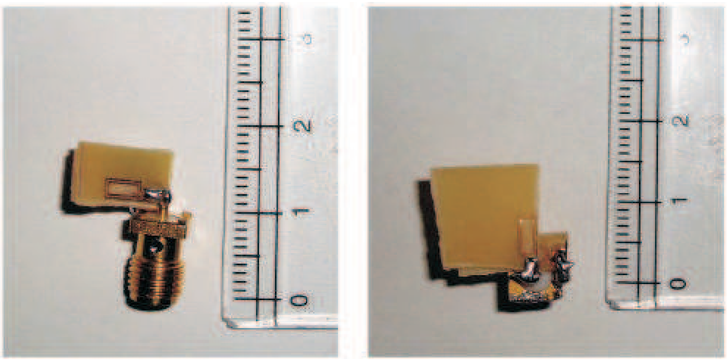

Figure 3.7: Picture of the three dimensional folded dipoles proposed in [41].

were compared in simulations and experimentally by considering an eye phantom. Three dimensional designs are explored in an effort to reduce the planar footprint size in comparison to its two dimensional equivalent. Results show that three-dimensional antennas can provide larger bandwidth while being physically smaller than the correspondent two-dimensional ones, thus providing larger channel capacity that could lead to a system with an increased number of stimulating electrodes.

3.3 Radio Channel Characterisation

In order to design a power-efficient system for personal communication environments, it is important to provide reliable models of the radio propagation channel. The case is even more complex when it comes to on-body channel characterisation, due to the unpredictable and dynamic nature of the problem. Before arriving at the receiver, the wave interacts with several obstacles, such as walls, furniture and body parts. The electromagnetic wave can be reflected, diffracted or penetrate in such objects and multiple waves arrives at the receiver. To ensure satisfactory performance of a wireless communication system, it is important to characterise the radio propagation channel; propagation models have been developed as a suitable alternative, but mostly complementary solution to measurement campaigns [42]. The existing models can be classified into two major classes:

- statistical models;
- deterministic propagation models.

Statistical models depend on measurement data, while deterministic propagation models are based on electromagnetic wave propagation theory. Examples of deterministic modelling are ray-tracing and full-wave electromagnetic numerical techniques such as the finite-difference time-domain (FDTD) technique.

Channel models that accurately describe the signal available at the receiver are crucial for communication system designers. However, if the model is extremely complex and difficult to use in analysis or implement in simulation, the model is of limited use to a designer, due to restricted physical and computational resources to evaluate potential system choices. Variations and fluctuations in received signal levels in any wireless network are usually considered in a short observation interval or a long observation interval. Different propagation measurement setups have been presented in the literature to characterise the radio channel. The measurement techniques can be generally characterised as time domain measurements, and frequency domain measurements [43–47]. These two techniques are the bases for many other radio propagation sounders commonly used in characterising wideband radio channels for indoor, outdoor and body-area network scenarios [48–50]. In time domain measurements (see Fig. 3.8a), a digital oscilloscope is used to receive the signal; it is relatively easy to detect multipath compnents if their delay in respect to the direct component is greater than the UWB pulse duration. Channel measurements can also be performed using a vector network analyser (VNA) in the frequency domain, (see Fig. 3.8b). The antennas are connected to the ports of the VNA and a sweep of discrete frequency tones, which include the S-parameters of the wireless channel, is taken by the VNA. S_{21} measures the transmission from one antenna to the other, and it represents the overall channel frequency response ($H(\omega)$). To note that $H(\omega)$ is the overall frequency response and it includes the effect of the two antennas and of the radio channel. Analyzing both magnitude and phase of S_{21} enable a transition to the time domain simply applying an Inverse Discrete Fourier Transform (IDFT).

One of the disadvantages of the frequency domain method is the restriction applied on measurement area freedom, since both transmit and receive antennas are connected to the same VNA; however, such problems can be avoided by the use of ultra low-loss long cables and applying advance calibration techniques.

3.3.1 Transient and Spectral Characterization of Multipath Channels

The effects of the wireless channel are commonly modelled by a linear filter where the received signal is given by,

$$r(t) = s(t) \otimes h(t) + n(t) \tag{3.4}$$

where $s(t)$ is the transmitted signal, $h(t)$ is the channel impulse response and $n(t)$ is complex-valued additive Gaussian noise. The channel impulse response changes as a function of time-spatial variation due to the motion of the transmitter, receiver or changes in the channel. The channel response is modelled as a linear filter with a complex-valued low-pass equivalent impulse response, and the channel response at the time t is given by

$$h(\tau, t) = \sum_{k=1}^{K} a_k(t)\delta(\tau - \tau_k)e^{j\theta_k(t)} \tag{3.5}$$

where δ is the Dirac delta function, K is the number of resolvable multipath components, τ_k are the delays of the multipath components, a_k are the path amplitude values and θ_k are the path phase values.

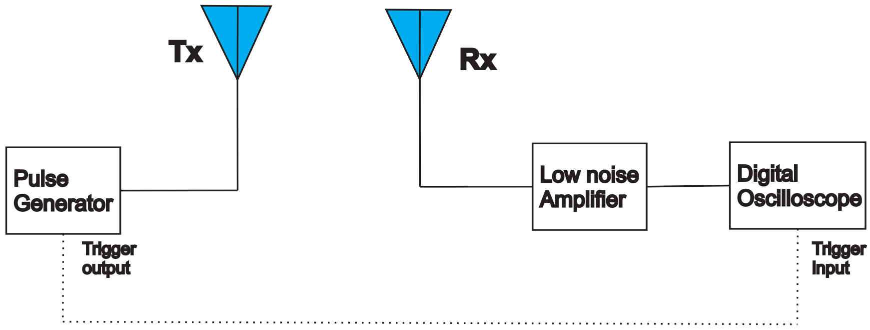

(a) Time domain method

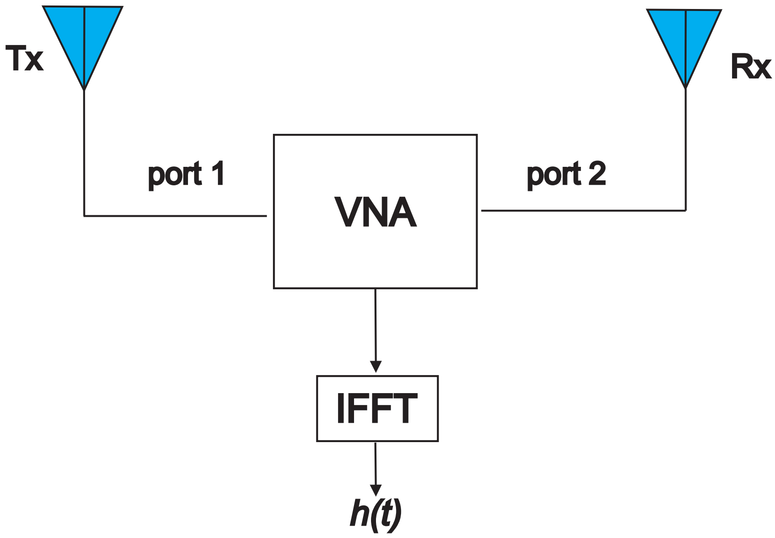

(b) Frequency domain method

Figure 3.8: Radio propagation measurement techniques for Indoor communication [43]

The power delay profile (PDP) is the squared magnitude of the impulse response, defined as

$$P(\tau, t) = h(\tau, t)h^*(\tau, t) = \sum_{k=1}^{K} a_k^2 \delta(\tau - \tau_k) \tag{3.6}$$

The radio channel is usually characterised by the first and second central moment of the PDP respectively the mean excess delay and the RMS delay spread, and by the maximum excess delay. Mean excess delay τ_m and RMS delay spread τ_{rms} (which can be used as a figure of merit for estimating data rates for multipath channels) describe the time dispersive properties of the channel. The mean excess delay is given as [43]

$$\tau_m = \frac{\sum_k a_k^2 \tau_k}{\sum_k a_k^2} \tag{3.7}$$

and the RMS delay spread is defined as,

$$\tau_{rms} = \sqrt{\frac{\sum_k a_k^2 \tau_k^2}{\sum_k a_k^2} - (\tau_m)^2} \tag{3.8}$$

where a_k are the multipath amplitudes and τ_k are the multipath delays relative to the first arriving multipath component. Most textbooks define the average PDP (APDP) which is a statistical average of several measurements taken over a small area, expressed as

$$\overline{P(\tau,t)} = E\{h(\tau,t)h^*(\tau,t)\} \tag{3.9}$$

The Fourier transform of the APDP is known as the spaced frequency correlation function can be expressed as

$$R(\Delta f) = \mathcal{F}\{\overline{P(\tau,t)}\} = \mathcal{F}\{E[h(\tau,t)h^*(\tau,t)]\} = E[H(f,t)H^*(f+\Delta f,t)] \tag{3.10}$$

where $H(f,t)$ is the Fourier transform of the channel impulse response. The expectation is taken over an area where $H(f,t)$ can be considered wide-sense stationary. The parameter $R(\Delta f)$ represents the expectation of the complex frequency domain channel response auto-correlation function, and can be used to represent the spectrum variation of a wireless channel. Increasing the frequency separation (Δf) leads to a decrease in the auto-correlation. The coherence bandwidth B_c is defined as the frequency range over which the channel does not distort the signal. Such parameter is inversely proportional to the RMS delay ($B_c \propto 1/\tau_{rms}$), and it is defined as the part of the spectrum with autocorrelation $R(\Delta f)$ greater than a certain value of acceptable correlation (a typical value is 0.5). This parameter is important to characterize the frequency selectivity of the channel. If B_c is much larger than the the bandwidth of the signal, all components will be equally treated by the channel and we refer to fluctuations in the signal level as flat fading. Otherwise, if B_c is much smaller than the signal bandwidth, we refer to this as frequency-selective fading. In the case of flat fading, the communication system is called a narrowband system, while in case of frequency selective fading is called wideband system. Similarly to the definition of the coherence bandwidth, it is possible to define the coherence time T_c as the expected time interval over which the channel can be considered time-invariant. The coherence time can be used to characterize the rapidity of the fading. The spaced time correlation is defined as

$$R(\Delta t) = E[h(f,t)h^*(f,t+\Delta t)] \tag{3.11}$$

It specifies the expected correlation between the channel responses to a sinusoid at frequency f at the instant t, and $t + \Delta t$. If T_c is much greater than the duration of the signal, we refer to this as slow fading: the channel does not change its fading characteristics during the propagation of the signal, which will not be distorted by this kind of fading. Alternatively, if T_c is much smaller than the duration of the signal, we refer to this as fast fading: the channel characteristics will change several times during the propagation of the signal, thus leading to distortion of the pulse.

Path Loss and Large Scale (Slow) Fading

One of the most important aspects of statistical characterization is the derivation of a model describing the fluctuations of the received signal with respect to the distance. Models of this kind are called large-scale propagation models and the output of these models is usually the estimation of the path loss at a certain distance. The path loss represents the attenuation of the signal and it is defined as

$$PL = \frac{P_r}{P_t}, \tag{3.12}$$

where P_r and P_t are received and transmitted power respectively. Prediction of the average received signal strength at a given distance from the transmitter has been traditionally applied in obtaining radio channel models. Path loss is usually examined using the Friis transmission formula, which provides a means for predicting the received power. The formula in general predicts that signal power will decrease at a rate of frequency squared (which has little effect on narrowband systems) and the square of separation distance between transmitter and receiver. The free space path loss for a communication distance d is given by [43]

$$PL(d) = \frac{G_t G_r \lambda^2}{(4\pi d)^2 L} \tag{3.13}$$

where G_t and G_r are the transmitter and receiver antenna gain, respectively. The distance between the transmitter and receiver is defined by d and L is the system loss (not related to propagation and is equal to 1 for lossless environments, e.g. free space).

Many theoretical and measurement-based studies presented in the literature have shown that the average received signal decreases logarithmically with distance (for both indoor and outdoor environments) [43, 44, 51, 52]. Therefore, the average path loss for a distance d between transmitter and receiver is expressed as,

$$PL(d) \propto \left(\frac{d}{d_0}\right)^{\gamma} \quad for \;\; d \geq d_0 \tag{3.14}$$

where γ is the path loss exponent that indicates the rate at which the path loss increases with distance and d_0 is a reference distance set in measurement and normally set to 1 m for indoor channels, while for on-body channel characterisation is usually set to 0.1 m [25]. The average path loss can be represented in dB as

$$PL_{dB}(d) = PL_{dB}(d_0) + 10\gamma \log\left(\frac{d}{d_0}\right) \tag{3.15}$$

which leads to the average received power represented as,

$$P_r(d) = P_r(d_0)\left(\frac{d}{d_0}\right)^{\gamma} \tag{3.16}$$

The path loss observed at any given point will deviate from this average value due to variations in the environment as reported in [43] and this variation has been shown to follow a lognormal distribution in many measurements. Therefore, the average path loss can be represented as:

$$PL_{dB}(d) = PL_{dB}(d_0) + 10\gamma \log\left(\frac{d}{d_0}\right) + X_{\sigma} \tag{3.17}$$

where X_{σ} is a zero-mean Gaussian distributed random variable with standard deviation σ, both values in dB.

In UWB systems the path loss is obtained by averaging the received power across the band for the specified number of sweeps taken with reference value of 1 m and was calculated by,

$$PL(d) = \frac{1}{NK}\sum_{i=1}^{N}\sum_{j=1}^{K}|H(f_i, x_j; d)|^2 \tag{3.18}$$

where $H(f_i, x_j; d)$ is the frequency response of the channel, which represents the received power relative to the transmitted power per frequency component. N represents the number of frequency components f measured in the channel, K is the number of sweeps defined by x and d is the separation distance between transmit and receive antennas.

Small-Scale (Fast) Fading

In addition to modelling the channel large-scale behaviour, it is necessary to consider small-scale effects on the received signal. Small-scale statistics describes variation of the channel over an area or period of time where the channel can be considered wide-sense stationary. Due to the constructive or destructive interference of the received paths, the received power has a fast and significant variation around the average path loss; we refer to this as small-scale channel fading. The amplitude of the fading can follow different distributions, such as Rice, Rayleigh, Nakagami, Log-normal, and Weibull. The Rician distribution is usually applied to model line of sight (LoS) channels. In this case, random multipath components are superimposed to a dominant signal, so that the received signal is the combination of a fixed deterministic component and some scattered components with stochastic amplitude and phase. If it is not a LOS channel, it is not possible to identify a dominant component, and the amplitude of the signal is modelled by the Rayleigh distribution.

Both Rayleigh and Rice distributions are applied to channels with a large number of unresolved multipath components, such as in the narrow-band case. However, in UWB channels more flexible empirical distributions are used to describe the path amplitude within a delay interval. The Nakagami and Weibull distributions have been applied to model the small-scale fluctuations of UWB indoor channels [53]. The lognormal distribution has been usually applied to model the large-scale fluctuations, however, in [54] it was shown that the lognormal provides a good fit for the small-scale fading in UWB on-body radio channel.

3.4 Radio Channel Characterisation for Body-Centric Wireless Communications

The human body is an uninviting and often hostile environment for the propagation of a wireless signal. For the design of a power and spectrum efficient wearable wireless system, it is important to understand and characterize the on-body radio channel [1].

Many channel models were derived for the wireless communication radio channels in WLAN, and more recently in WPAN, and have been applied for radio system designs [55, 56]. Over the past few years the interest has moved towards the channel characterization in WBAN, where both, transmitter and receiver, are worn by the user. In this complex scenario the signal could arrive to its destination through penetration inside the body, diffraction and scattering from body parts and surrounding scatterers. The narrowband on-body radio channel have been extensively analyzed [6, 49, 57–59]. In [58], a channel model for body area network at 400, 900, and 2400 MHz was derived from numerical simulation. It was shown that electromagnetic waves propagate around the body via two paths, penetration through the body, and creeping waves around the body surface. However, it was shown that the penetration suffers of high losses compared to the creeping wave, and that such attenuation increases with frequency. The on-body channel large-scale fading at 2.45 GHz was statistically investigated in [57], and it was demonstrated that the variation of the path gain in the on-body channel is a non-stationary process and can not be accurately modelled adopting a simple statistic distribution. Hall *et al.*, considered several representative on-body links and performed the measurements in different environments, and the results demonstrated that the statistic of the channel is associated with the nature of the body movements and it is environment-dependant. It was shown that, outdoors and in the car, Nakagami and Rician (or Rayleigh) distributions prevail because the movements were restricted to either walking or operating the car (see Fig. 3.9), and, therefore, probability of shadowing was small. Indoors and in the anechoic environment, where activities were more diverse and severe shadowing events were likely to be frequent, gamma or lognormal distributions are more suitable.

Many efforts were made to characterize the UWB on-body radio channel [25, 54, 60–64].

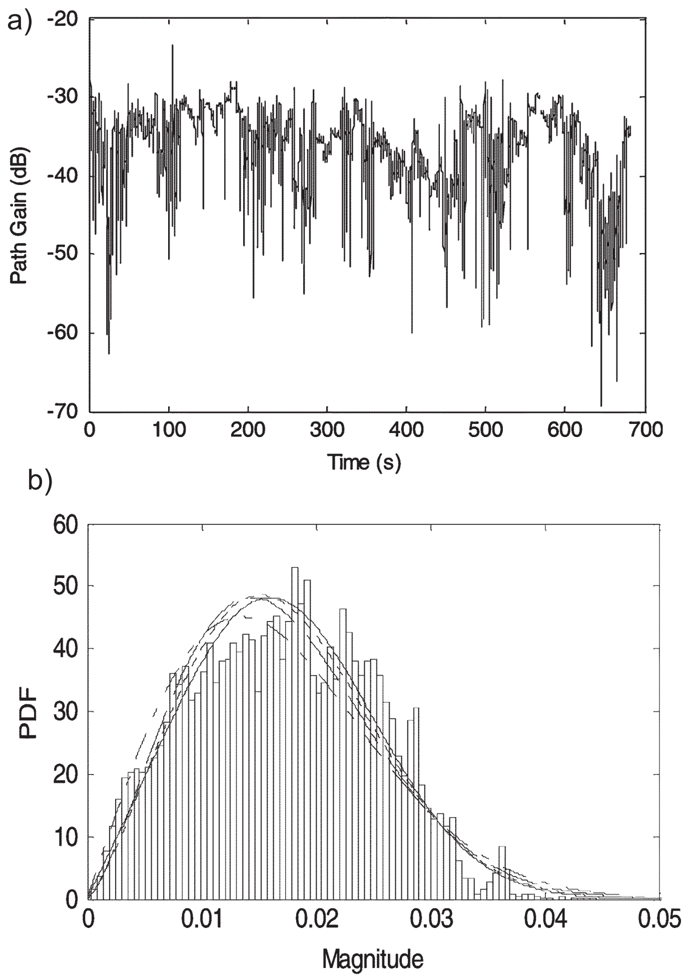

Figure 3.9: Variation with time (a), and probability density function (b) of the path gain for the belt-to-wrist channel for measurements in the car (reproduced from [57]).

The propagation of the electromagnetic wave around the body was simulated numerically and measured in [54, 65] in order to introduce a UWB-WBAN radio channel model. The propagation channel was investigated in the band 3GHz - 6GHz, and it was shown that the radiated signal is diffracted around the torso rather than passing through it. Fort *et al.* performed measurements of propagation around the body taken outdoors in an open space with only initial diffracted waves and the ground reflections were observed [54]. Frequency domain measurement technique with two commercial meander line antennas were used to determine channel transfer function. The path loss model for radio channel around the body from both simulation and measurement results was given by [61],

$$PL_{dB}(d) = 50.5dB + 7.4 \cdot 10log(d/0.1) \tag{3.19}$$

in addition, Fort *et al.* presented the BAN channel model for propagation on the front of the torso, which is given by,

$$PL_{dB}(d) = 44.6dB + 3.1 \cdot 10log(d/0.1) \tag{3.20}$$

Fort *et al.* has also proposed a procedure for measuring body area propagation in an indoor environment, where the body area channel included an initial cluster of components diffracting around the body, followed by subsequent clusters of components reflecting off surrounding objects in the room. Components diffracting around the body were best described by a high path loss exponent and correlated lognormal variables [54, 61], as predicted from the basic radio propagation theory in non-reflecting environments. The authors presented a generalised radio channel model for body area network communication in UWB band based on frequency domain measurements and commercially available antennas. Only static radio channels are considered for standing still scenarios with arm swinging applied; however, frequency domain measurements still require static channels for the sweeping duration and the system model provided is more scenario specific rather than generic [54, 66].

In [63], Wang *et al.* proposed a channel model which is a modified version of the one proposed by Saleh-Valanzuela for radio propagation in indoor environment [45]. Such UWB model, was proposed for some representative body links, and it is based on a set of dispersive-FDTD simulations. Wang *et al.* concluded that one cluster is sufficient for describing the PDPs of the five on-body links considered. It was also shown that the PDP decays exponentially with the time, however, no reflections from the surrounding environment were considered. In [25], a measurement campaign was performed using two pairs of different antennas exhibiting different radiation characteristics. Even if the antennas used are big and hence not practical, they are suitable to investigate the impact of different polarisation on the radio channel characteristics. In particular, a printed horn shaped self complementary antenna (HSCA) and a vertical version of the printed PICA (see Fig.3.4) were used. The measurements were carried out investigating six different links, and including several body postures, and results demonstrated the impact of the antenna radiation pattern on the received power. For HSCA,

$$PL_{dB}(d) = 86.5 + 10 \cdot (4.4) \cdot log\left(\frac{d}{d_0}\right) \quad for\ 40cm \leq d \leq 100cm \tag{3.21}$$

and for PICA as,

$$PL_{dB}(d) = 70.3 + 10 \cdot (2.7) \cdot log\left(\frac{d}{d_0}\right) \quad for\ 40cm \leq d \leq 100cm \tag{3.22}$$

where γ=4.4 and 2.7 are the path loss exponents for HSCA and PICA models, respectively. Figure 3.10 presents the measured values and modelled path losses as a function of distance for both antenna cases.

If an antenna with polarization normal to the body is used (vertical PICA), results demonstrated a reduction of path loss exponent, and hence an improvement in the radio link performance. However, such antenna is not practical, since it is not conformal to the body surface. In the analysis presented so far, the antennas adopted in the measurements were big and hence not practical. The effect of considering a miniaturised antenna on the radio propagation channel characteristics have not been presented. Besides, no emphasis was given to the subject-specificity of the on-body radio channel.

Less effort was put in characterising the radio channel for telemetry with wireless implants. The radiation characteristics of ingested sources were numerically investigated in [67] at VHF and UHF bands. Chirwa *et al.* [67] demonstrated that there is

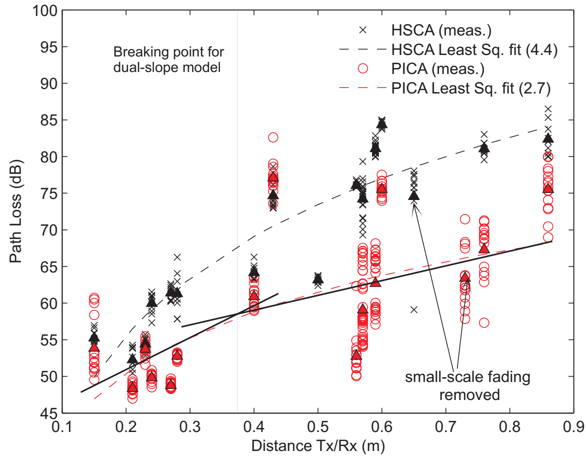

Figure 3.10: Measured and modelled path loss for HSCA and PICA on-body channels as function of distance in metres (Triangles represent the path loss averaged with small-scale fading removed at each scenario specified by distance, reproduced from [42].

a Gaussian-like relationship between the radiation intensity outside the body and the operating frequency. Johansson *et al.* [68] studied the link budget between an external base station and the wireless implant, and demonstrated the possibility of achieving communication with implants within very limited power levels and very low data rate. In [69] Alomainy *et al.* presented the numerical and experimental investigation of the biotelemetry radio channel and wave attenuation in human subjects with wireless implants. The path gain variation for communication between the implant and an external receiver in close vicinity of the subject was also analysed and modelled as a function of the communication distance. However, the effect of different human body subjects on the radiation characteristics and the overall performance of wireless implants has not been presented.

3.5 Summary

The chapter discussed the basics of antennas and radio propagation for BCWC. A literature review on wearable antennas highlighted the need of developing compact and conformal antennas, and understand their behavior when placed in proximity of the human body.

Furthermore, the human body, is a hostile environment for the propagation of electromagnetic waves, and, for the design of a power efficient system, the on-body radio channel needs to be fully characterized. Several features need to be encountered, such as the dynamic nature of the body, the effect of the indoor environment, and the subject-specificity of the radio channel.

Such tasks can be accomplished either experimentally or numerically. In the first case, measurements are performed adopting physical phantoms or real subjects, while in the second case, digital body phantoms embedded in numerical electromagnetic codes are used. The parameters governing the radio propagation in multipath environments are introduced, and the last part of the chapter is devoted to a literature review on the state-of-the-art on radio channel characterisation BCWC.

References

[1] P. S. Hall and Y. Hao, *Antennas and Propagation for Body-Centric Wireless Communications*. Artech House, 2006.

[2] N. Haga, K. Saito, M. Takahashi, and K. Ito, "Characteristics of cavity slot antennas for body-area networks," *IEEE Transactions on Antennas and Propagation*, vol. 57, no. 4, pp. 837–843, 2009.

[3] H. R. Chuang and W. T. Chen, "Computer simulation of the human-body effects on a circular-loop-wire antenna for radio-pager communications at 152, 280, and 400 MHz," *IEEE Transactions on Vehicular Technology*, vol. 46, no. 3, pp. 544–559, 1997.

[4] P. Salonen, Y. Rahmat-Samii, and M. Kivikoski, "Wearable antennas in the vicinity of human body," *IEEE Antenna and Propagation Society Symposium*, vol. 1, pp. 467–470, June 2004.

[5] A. Alomainy, Y. Hao, and D. M. Davenport, "Parametric study of wearable antennas with varying distances from the body and different on-body positions," *IET Seminar on Antenna and Prpagation for Body-Centric Wireless Communications, London UK*, April 2007.

[6] A. Alomainy, Y. Hao, A. Owadailly, C. G. Parini, P. S. Hall, and C. C. Costantinou, "Statistical analysis and performance evaluation for on-body radio propagation with microstrip patch antennas," *IEEE Transactions on Antenna and Propagation*, vol. 55, no. 1, pp. 245–248, January 2007.

[7] B. Sinha, "Numerical modelling of absorption and scattering of EM energy radiated by cellular phones by human arms," *IEEE Region 10 International Conference on Global Connectivity in Energy, Computer, Communication and Control, New Delhi, India*, vol. 2, pp. 261–264, December 1998.

[8] J. Wang, O. Fujiwara, S. Watanabe, and Y. Yamanaka, "Computation with a parallel FDTD system of human-body effect on electromagnetic absorption for portable telephone," *IEEE Transactions on Microwave Theory and Techniques*, vol. 52, no. 1, pp. 53–58, January 2004.

[9] K. I. Ziri-Castro, W. G. Scanlon, and N. E. Evans, "Indoor radio channel characterization and modeling for a 5.2-GHz bodyworn receiver," *IEEE Antennas and Wireless Propagation Letters*, vol. 3, no. 1, pp. 219–222, 2004.

[10] P. Salonen and Y. Rahmat-Samii, "Textile antennas: effects of antenna bending on input matching and impedance bandwidth," *IEEE Aerospace and Electronic Systems Magazine*, vol. 22, no. 3, pp. 10–14, 2007.

[11] S. Zhu and R. Langley, "Dual-band wearable antennas over EBG substrate," *Electronics Letters*, vol. 43, no. 3, pp. 141–142, 2007.

[12] ——, "Dual-band wearable textile antenna on an EBG substrate," *IEEE Transactions on Antennas and Propagation*, vol. 57, no. 4, pp. 926–935, 2009.

[13] C. Hertleer, A. Tronquo, H. Rogier, L. Vallozzi, and L. Van Langenhove, "Aperture-coupled patch antenna for integration into wearable textile systems," *IEEE antennas and wireless propagation letters*, vol. 6, 2007.

[14] C. Hertleer, H. Rogier, L. Vallozzi, and L. van Langenhove, "A textile antenna for off-body communication integrated into protective clothing for firefighters," *IEEE Transactions on Antennas and Propagation*, vol. 57, no. 4, pp. 919–925, 2009.

[15] P. Salonen and J. Rantanen, "A dual-band and wide-band antenna on flexible substrate for smart clothing," *27th Annual Conference of the IEEE Industrial Electronics Society*, 2001.

[16] J. Kim and Y. Rahmat-Samii, "Exterior antennas for wireless medical links: EBG backed dipole and loop antennas," *Antennas and Propagation Society International Symposium, IEEE*, 2005.

[17] G. Conway and W. Scanlon, "Antennas for over-the-body-surface communication at 2.45 GHz," *IEEE Transactions Antennas and Propagation*, vol. 57, no. 4, pp. 844–855, 2009.

[18] H. Adel, R. Wansch, and C. Schmidt, "Antennas for a body area network," *IEEE Antennas and Propagation Society International Symposium, 2003*, vol. 1, pp. 471–474, June 2003.

[19] A. Alomainy, Y. Hao, and F. Pasveer, "Numerical and experimental evaluation of a compact sensor antenna for healthcare devices," *IEEE Transactions on Biomedical Circuit and Systems*, vol. 1, no. 4, pp. 242–250, December 2007.

[20] B. Sanz-Izquierdo, F. Huang, and J. Batchelor, "Covert dual-band wearable button antenna," *Electronics Letters*, vol. 42, no. 12, pp. 668–670, 2006.

[21] W. L. Stutzman and G. A. Thiele, *Antenna Theory and Design*. John Wiley & Sons, Ltd., 1998.

[22] K. Y. Yazdandoost and R. Kohno, "Ultra wideband antenna," *IEEE Communications Magazine*, vol. 42, no. 6, pp. S29–S32, June 2004.

[23] P. R. Foster, "UWB antenna issues," *IEE Seminar on UWB Communications, London, UK*, July 2004.

[24] H. G. Schantz, "Introduction to ultra-wideband antennas," *IEEE Conference on Ultra Wideband Systems and Technologies*, pp. 1–9, November 2003.

[25] A. Alomainy, Y. Hao, C. G. Parini, and P. S. Hall, "Comparison between two different antennas for UWB on-body propagation measurements," *IEEE Antennas and Wireless Propagation Letter*, vol. 4, no. 1, pp. 31–34, December 2005.

[26] T. P. See and Z. N. Chen, "Expermiental characterization of UWB antennas for on-body communications," *IEEE Transctions on Antennas and Propagation*, vol. 57, no. 4, pp. 866–874, April Apr. 2009.

[27] M. Klemm and G. Troster, "Characterisation of an aperture-stacked patch antenna for ultra-wideband wearable radio systems," *15th International Conference on Microwaves, Radar and Wireless Communications, 2004*, vol. 2, pp. 395–398, May 2004.

[28] S. Promwong, W. Hachitani, G. S. Ching, and J. Takada, "Characterization of ultra-wideband antenna with human body," *Internationa Symposium on Communications and Information Technology (ISCIT 2004), Sapporo, Japan*, pp. 1213–1217, October 2004.

[29] *FCC First Report and Order, Revision of the Part 15 Commission's Rules Regarding Ultra-Wideband Transmission Systems*, pp. 98–153, April 22, 2003.

[30] T. Zasowski, F. Althaus, M. Stager, A. Wittneben, and G. Troster, "UWB for noninvasive wireless body area networks: channel measurements and results," *Proceedings of IEEE Conference on Ultra Wideband Systems and Technologies, Reston, Virginia*, vol. 55, no. 1, pp. 285–289, November 2003.

[31] D. Lamensdorf and L. Susman, "Baseband-pulse-antenna techniques," *IEEE Antennas and Propagation Magazine*, vol. 36, no. 1, February 1994.

[32] J. S. McLean, H. Foltz, and R. Sutton, "Pattern descriptors for UWB antennas," *IEEE Transactions on Antennas and Propagation*, vol. 53, no. 1, January 2005.

[33] F. Merli, B. Fuchs, and A. K. Skrivervik, "Influence of insulation for implanted antennas," *European Conference on Antennas and Propagation*, pp. 196–199, 2009.

[34] R. Warty, M. Tofighi, U. Kawoos, and A. Rosen, "Characterization of implantable antennas for intracranial pressure monitoring: Reflection by and transmission through a scalp phantom," *IEEE Transactions on Microwave Theory and Techniques*, vol. 56, no. 10, pp. 2366–2376, 2008.

[35] J. Kim and Y. Rahmat-Samii, "Implanted antennas inside a human body: Simulations, designs, and characterizations," *IEEE Transactions on Microwave Theory and Techniques*, vol. 52, no. 8, pp. 1934–1943, August 2004.

[36] P. Soontornpipit, C. M. Furse, and Y. Chung Chung, "Design of implantable microstrip antenna for communication with medical implants," *IEEE Transactions on Microwave Theory and Techniques*, vol. 52, no. 8, pp. 1944–1951, August 2004.

[37] T. Karacolak, A. Z. Hood, and E. Topsakal, "Design of a dual-band implantable antenna and development of skin mimicking gels for continuous glucose monitoring," *IEEE Transactions on Microwave Theory and Technique*, vol. 56, no. 4, pp. 1001–1008, April 2008.

[38] J. Kim and Y. Rahmat-Samii, "Planar inverted-F antennas on implantable medical devices: Meandered type versus spiral type," *Microwave and Optical Technology Letters*, vol. 48, no. 3, pp. 567–572, 2006.

[39] T. Karacolak, R. Cooper, and E. Topsakal, "Electrical properties of rat skin and design of implantable antennas for medical wireless telemetry," *IEEE Transactions on Antennas and Propagation*, vol. 57, no. 9, pp. 2806–2812, 2009.

[40] P. M. Izdebski, H. Rajagopalan, and Y. Rahmat-Samii, "Conformal ingestible capsule antenna: a novel chandelier meandered design," *IEEE Transactions on Antennas and Propagation*, vol. 57, no. 4, pp. 900–909, 2009.

[41] M. S. Soora, K. Gosalia, M. S. Humayun, and G. Lazzi, "A comparison of two and three dimensional dipole antennas for an implantable retinal prosthesis," *IEEE Transactions on Antenna and Propagation*, vol. 56, no. 3, pp. 622–629, March 2008.

[42] A. Alomainy, "Antennas and radio propagation for body-centric wireless networks," Ph.D. dissertation, Queen Mary, University of London, 2007.

[43] T. S. Rappaport, *Wireless Communications: Principle and Practice*. Prentice-Hall, 1999.

[44] H. Hashemi, "The indoor radio propagation channel," *Proceedings of IEEE*, vol. 81, no. 7, pp. 943–968, 1993.

[45] A. Saleh and R. A. Valenzuela, "A statistical model for indoor multipath propagation," *IEEE J. Selected Areas Commun*, vol. JSAC-5, no. 3, pp. 128–137, February 1987.

[46] H. Suzuki, "A statistical model for urban radio propagation," *IEEE Transactions on Communications*, vol. 25, no. 7, pp. 673–680, July 1977.

[47] M. Z. Win and R. A. Scholtz, "Impulse radio: how it works," *IEEE Communications Letters*, pp. 36–38, February 1998.

[48] I. S. Kovacs, G. Pedersen, P. Eggers, and K. Olesen, "Ultra wideband radio propagation in body area network scenarios," *in ISSSTA Proceedings*, pp. 102–106, 2004.

[49] S. L. Cotton and W. Scanlon, "A statistical analysis of indoor multipath fading for a narrowband wireless body area network," *IEEE 17th International Symposium on Personal, Indoor and Mobile Radio Communications*, pp. 1–5, September 2006.

[50] D. Neirynck, *Channel Characterisation and Physical Layer Analysis for Body and Personal Area Network Development*. Ph.D Thesis, University of Bristol, November 2006.

[51] S. R. Saunders, *Antennas and Propagation for Wireless Communication Systems*. John Wiley & Sons, Ltd., 2004.

[52] ——, *Antennas and Propagation for Wireless Communication Systems, 2nd Edition*. John Wiley & Sons, Ltd., 2007.

[53] C. Chong and S. Yong, "a Generic statistical-based UWB channel model for high-rise apartments ," *IEEE Transactions on Antennas and Propagation*, vol. 53, no. 8, pp. 2389–2399, 2005.

[54] A. Fort, C. Desset, P. D. Doncker, and L. V. Biesen, "Ultra wideband body area propagation: from statistics to implementation," *IEEE Transactions on Microwave Theory and Technique*, vol. 54, no. 4, pp. 1820–1826, June 2006.

[55] J. Karedal, A. J. Johansson, F. Tufvesson, and A. F. Molisch, "A measurement-based fading model for wireless personal area networks."

[56] S. L. Cotton and W. Scanlon, "Characterization and modeling of the indoor radio channel at 868 MHz for a mobile bodyworn wireless personal area network," *IEEE Antennas and Wireless Propagation Letters*, vol. 6, pp. 51–55, 2007.

[57] Z. H. Hu, Y. I. Nechayev, Y. Hao, C. C. Costantinou, and P. S. Hall, "Measurements and statistical analysis of on-body channel fading at 2.45 GHz," *IEEE Antennas and Propagation Letter*, vol. 6, pp. 612–615, 2007.

[58] J. Ryckaert, P. D. Doncker, R. Meys, A. de Le Hoye, and S. Donnay, "Channel model for wireless communication around human body," *IEE Electronics Letters*, vol. 40, no. 9, pp. 543–544, April 2004.

[59] S. L. Conway, G. A. Conway, and W. G. Scanlon, "A time-domain approach to the analysis and modelimg of on-body propagation characteristics using synchronized measurements at 2.45 GHz," *IEEE Transctions on Antennas and Propagation*, vol. 57, no. 4, pp. 943–955, April 2009.

[60] A. Alomainy and Y. Hao, "UWB on-body radio propagation and system modelling for wireless body-centric networks," *IEEE Antennas and Propagation Society International Symposium 2006*, pp. 2173–2176, July 2006.

[61] A. Fort, P. D. Doncker, and L. V. Biesen, "An ultra wideband channel model for communication around the body," *IEEE Journal on selcted area of comms*, vol. 24, no. 4, pp. 927–933, April 2006.

[62] T. Zasowski, F. Althaus, M. Stager, A. Wittneben, and G. Troster, "UWB for noninvasive wireless body area networks: channel measurements and results," *IEEE Conference on Ultra Wideband Systems and Technologies*, November 2003.

[63] Q. Wang, T. Tayamachi, I. Kimura, and J. Wang, "An on-body channel model for UWB body area communications for various postures," *IEEE Journal on Selected Areas in Communications*, vol. 57, no. 4, pp. 991–998, April 2009.

[64] Y. Chen, J. Teo, J. Y. Lai, E. Gunawan, K. Low, C. Soh, and P. Rapajic, "Cooperative communications in ultra-wideband wireless body area networks: Channel modeling and system diversity analysis," *IEEE Journal on Selected Areas in Communications*, vol. 27, no. 1, pp. 5–16, January 2009.

[65] A. Fort, C. Desset, J. Ryckaert, P. D. Doncker, and L. V. Biesen, "Ultra wideband body area channel model," *International Conference on Communications, ICC05, Seoul, South Korea*, May 2005.

[66] A. F. Molisch, D. Cassioli, C.-C. Chong, S. Emami, A. Fort, B. Kannan, J. Karedal, J. Kunisch, H. G. Schantz, K. Siwiak, and M. Z. Win, "A comprehensive standardized model for ultrawideband propagation channels," *IEEE Transactions on Antennas and Propagation*, vol. 54, no. 11, pp. 3151–3166, 2006.

[67] L. C. Chiwra, P. A. Hammond, S. Roy, and D. R. S. Cumming, "Electromagnetic radiation from ingested sources in the human intestine between 150 MHz and 1.2 GHz," *IEEE Transactions on Biomedical Engineering*, vol. 50, no. 4, pp. 484–492, April 2003.

[68] A. J. Johansson, "Performance of a radiolink between a base station and a medical implant utilizing the MICS standard," *26th EMBS Conference*, 2004.

[69] A. Alomainy and Y. Hao, "Modeling and characterization of the biotelemetric radio channel from ingested implants considering organ contents," *IEEE Transactions on Antennas and Propagations*, vol. 57, no. 4, pp. 999–1005, 2009.

Chapter 4

Electromagnetic Properties and Modelling of the Human Body

In studying the interaction of electromagnetic waves with the body, it is very important to understand the electromagnetic properties of the body tissues. To develop on-body antennas, and to study the on-body radio channel, characterisation of the human body is necessary. This can be done either with physical phantoms, or with numerical phantoms imported in numerical electromagnetic codes. The chapter discusses the properties of the body tissues, and the challenges in numerical modelling for BCWC.

4.1 Modelling of the Human Body

To understand the interaction of electromagnetic waves with the human body, it is most important to have knowledge of the electromagnetic properties of the body tissues. The human body is an irregularly shaped, stratified dielectric medium, with properties that vary significantly with tissue type and frequency. To investigate the radio propagation, and to analyze the performance of antennas in vicinity or inside the tissues, modelling of the body is necessary.

Such a task can be accomplished either experimentally or numerically. In the first case, physical phantoms made from solid, liquid or gel materials are adopted, while in the second, numerical body phantoms embedded in numerical electromagnetic codes are used.

4.1.1 Electrical Proprieties of Human Body Tissues

The electrical properties of biological tissues have been of interest for over a century for many reasons. Due to the large amount of electronic devices in our daily lives, the understanding of the electromagnetic waves propagation inside the human body has received an increasing attention. In addition, the determination of the pathways of current flowing through the body is very important in the analysis of a wide range of biomedical applications, such as electrical stimulation and the diagnosis and treatment of various physiological conditions with weak electrical currents [1].

To characterize the response of a tissue to electromagnetic waves, conductivities σ (S/m) and relative permittivities ϵ_r of the tissues are needed. The human body is a complex, irregular, and stratified dielectric object; the characterization of its tissue proprieties is very complicated, since the parameters depend on the polarization and frequency of the applied field. Human body tissues are, in general, lossy materials, for which it is possible to define a complex-valued relative permittivity:

$$\varepsilon_r = \varepsilon_r' - j\varepsilon_r'' \tag{4.1}$$

where $\varepsilon_r' = \varepsilon_r$, and $\varepsilon_r'' = \sigma/(\omega\varepsilon_0)$ (ω is the angular frequency).

Figure 4.1 shows measured permittivity data for a number of human tissues at different frequencies. The conductivity values are presented in Fig.4.2. The results are obtained from a compilation presented in [2, 3] that covers a wide range of different body tissues and provides the appropriate dielectric values at each desired frequency. In order to well understand the EM propagation in a media, an important parameter to take into account is the skin depth (δ), which is given by:

$$\delta = \frac{1}{\sqrt{\pi \, \mu \, f \, \sigma}} \tag{4.2}$$

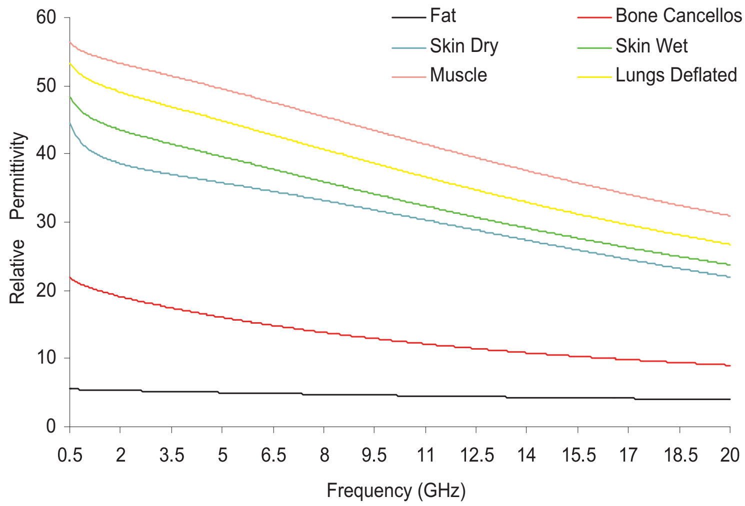

Figure 4.1: Measured data of human tissue permittivity [2] for various tissue types, reproduced from [4].

where μ is the permeability of the media and f the frequency. The decline in current density versus depth is known as the skin effect and the skin depth is a measure of the distance over which the current falls to 1/e of its original value. At lower frequencies, the permittivity is relatively high and the conductivity low; the EM wave can propagate through the human body. At higher frequencies, the lossy effect is higher, so the skin depth decreases. In wireless implants, the use of lower operation frequencies (e.g: 400 MHz) is therefore recommended.

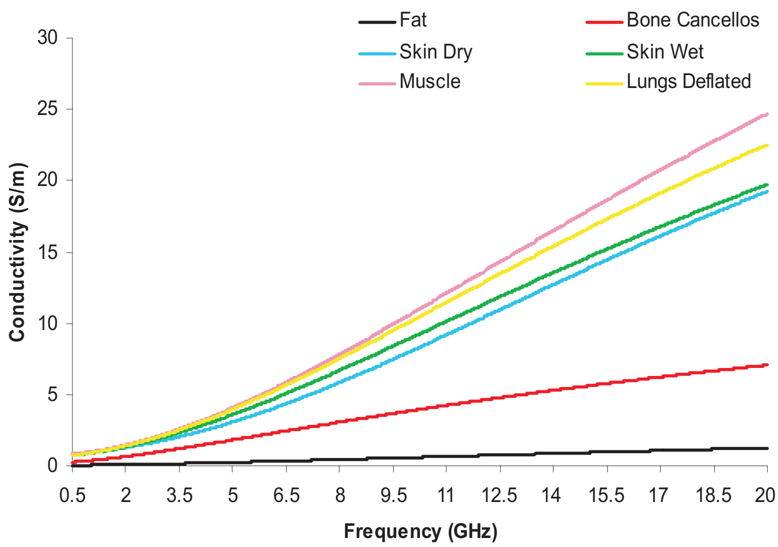

Figure 4.2: Measured data of human tissue conductivity [2] for various tissue types, reproduced from [4].

4.1.2 Physical Phantoms

A physical phantom is a physical model simulating the characteristics of biological tissues, and it is used to investigate the interaction between body tissues and the electromagnetic fields. Such phantoms have been extensively used in medical research for testing the effect of the electromagnetic radiation on health, as well as in the development of medical diagnosis and treatment, such as X-ray and magnetic resonance imaging [5]. More recently, with the advent of mobile phones, phantoms have been used to test the safety of such devices, and to ensure that the level of specific absorption rate (SAR) is below the acceptable limit.

Phantoms can be classified regarding to their frequency range, the body tissue that they represent, or the final state of the phantom, which can be solid (dry), solid (wet), semi-solid (gel), or liquid [5]. Liquid phantoms are used for measuring the SAR value, measuring the electric field inside the phantom with a probe. These phantoms have a form of a thin shell with a shape of a human head or a whole body. As indicated in [6], for frequencies in the range 0.8-3 GHz, the permittivity of the shell should be less than 5, the loss tangent less than 0.05, and the thickness should be 2.0$\pm$2mm. Such a shell is filled with a liquid approximating the dielectric properties of the human body. Most recipes for this liquid are based on de-ionized water, to which sugar is added to control the permittivity of the solution and salt to adjust the conductivity [7]. This type of phantom is easy to fabricate and it allows the recording of the field distribution inside the liquid; however, it has some disadvantages, such as the limited frequency range over which the liquid represents the tissues and the electrical properties of the shell.

The latter problem can be avoided by adding coagulants to the liquid solution, to create a solid (wet) or semisolid (gel) phantom which is capable of self-shaping. In [7], Guy presented a recipe to make a gel phantom and, based on such a recipe, Ito *et al* have developed a self-shaping phantom [9]. In [8], a three layer semisolid phantom (composed of skin, fat and muscle tissues) was developed in order to investigate the radiation characteristics of an implanted antenna (see Fig.4.3). These phantoms have the advantage of covering a wider frequency range than the liquid ones, but are suitable only to represent high-water content tissues (muscle, and brain). A problem with all of the wet phantoms, is the degradation over time, mainly due to a loss of water.

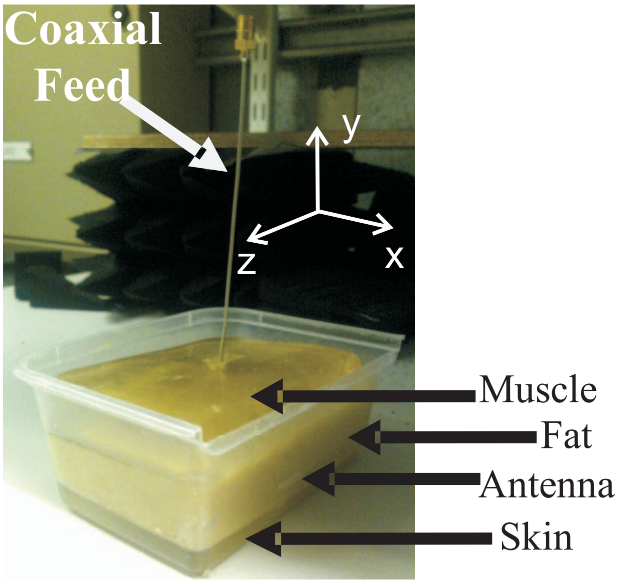

Figure 4.3: Picture of the three layer semisolid phantom proposed in [8]

If the internal distribution of the electric field is not of interest, a solid (dry) phantom can be adopted. Such phantoms have been used to measure the SAR on the surface of the body, and are the best suited for analyzing the propagation around the body. Furthermore, they can accurately represent the inhomogeneous structure of the human body. In [10], a mixture of graphite powder and ceramic was used, while in [11] a composition of silicone rubber and carbon fiber was used. Such phantoms have good mechanical characteristics, and, since they do not contain water, they do not degrade over time. On the other hand, the manufacture process require more advanced and complicated procedures, with respect to the liquid or semisolid phantoms.

4.1.3 Numerical Phantoms

A wide variety of phantoms have been used for theoretical analysis and numerical simulations. In theoretical studies, simplified shapes are used to model the body. However, for accurate modeling of the radio propagation, it is necessary to use more realistic numerical phantoms composed of many voxels. In FDTD simulations, the objects can be modelled using their material properties, e.g. permittivity, permeability and conductivity etc. Their values change with locations in space. Regular objects such as spheres, cylinders and cubes can be mathematically defined in space and easily represented in the FDTD domain. However complex objects such as the human body are often difficult to model and sometimes approximated by basic geometries [12]. However, for realistic simulations, proper human body models need to be created and imported to the FDTD domain. The recent progress in medical imaging technologies, together with the availability of large computing power, allows the development of homogeneous and inhomogeneous whole-body models based on magnetic resonance (MR) images. A high spatial resolution (voxel size of 1 mm^3) whole-body model named Hugo was proposed in [13]. The model classifies over 40 different types of tissues, and, is based on data from the visible human project dataset at the U.S. National Library of Medicine. This data was obtained on a 38-year-old cadaver, 1.86 m in height and 90 kg in weight (see Fig 4.4(c)). In [14], Nagaoka et al. developed two whole-body models (voxel size of 2 mm^3) of Japanese male and female, in which over 50 types of tissues are classified. The male model was based on the image of a 22-year-old, 1.73 m tall and weighed 65 kg (see Fig 4.4(b)); and the 22-year-old female was 1.60 in height and 53.0 kg in weight (see Fig 4.4(a)).

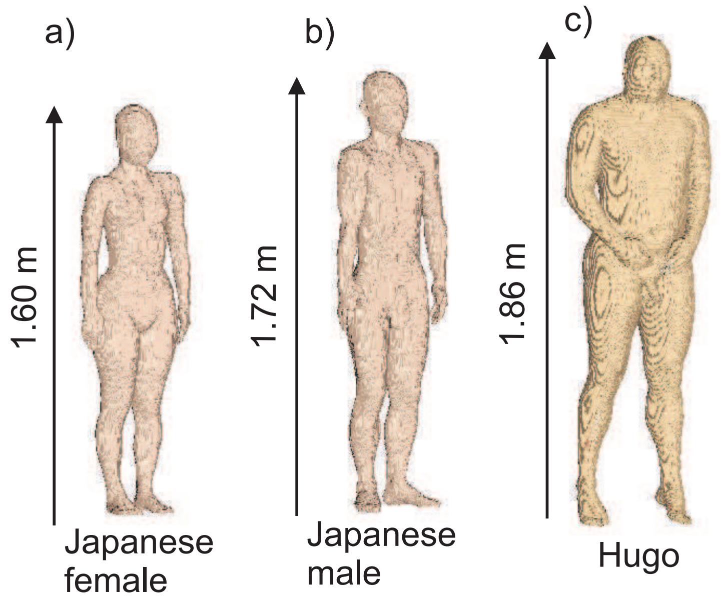

Figure 4.4: 3D models of the digital phantoms: (a) Japanese female; (b) Japanese male; (c) HUGO.

These phantoms can be easily imported in the cubic mesh of the FDTD code since at each cubic voxel is associated a value of permittivity and conductivity. However, data regarding the electrical properties of the internal organs are obtained by sectioning cadavers, and hence, the development of inhomogeneous phantoms is a complex process. This kind of phantom is necessary for certain applications such as the analysis of wireless implants, and for evaluating the distribution of the SAR inside the body. However, when studying the on-body radio channel at microwave frequencies, since the skin depth is small (due to the high losses), the internal composition of the body does not play a major role. This allows the use of realistic-shaped homogeneous phantoms (usually made of muscle tissue), which have the big advantage that can be easily developed by segmenting the images given by MR scans. In [15], Lee *et al.* used subject specific MR data of the whole body from eight subjects (four male and four female, mean age 27.0). To cover the entire body, the images were acquired section by section, moving the scanner bed after each acquisition to allow the volume of interest to sit in the middle of the scanner. Based on the MR images, a tetrahedral surface was generated. Since volume meshes are required in FDTD simulations, a voxelizer tool [16] is used to convert surface meshes into volume ones. Figure 4.5 shows the three dimensional images of six of the eight homogeneous digital phantoms developed in [15].

4.2 Numerical Modelling for On-Body Applications.

Since radio propagation in body-centric communications is a complex problem, an analytical solution can be found only if the problem is simplified. Numerical simulations, even if computationally more intensive that an analytical approach, can provide a physical insight into the propagation mechanism and accurate solutions [5]. Several numerical techniques are available, and each of them has its own advantages and drawbacks.

The Uniform Theory of Diffraction (UTD) is based on geometric optics and diffraction theory. It requires that the objects considered in the simulation are large compared to the wavelength, and assumes that all waves are locally planar, so that the Ray Tracing (RT) method can be adopted. Reflection and penetration are the basic phenomena when interaction between propagating waves and the surrounding environment occurs. The calculation of the diffraction from wedge and corner structures is unique in UTD. The inclusion of diffraction is essential to guarantee the continuity

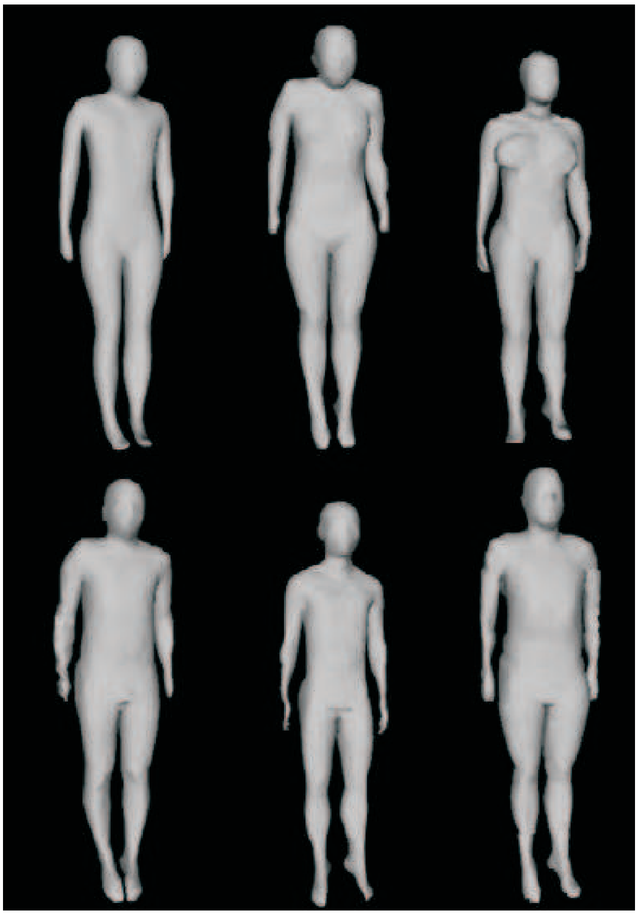

Figure 4.5: The 3D images of six of the subjects considered in [15]. The six models are based on the whole body MR images of three females (top) and three males (bottom).

of the fields. The RT technique has been extensively used to model indoor and outdoor radio channels in mobile communications. It can be used to accurately predict the received signal strength and the power delay profile (PDP). In [17] the UTD was applied to the study of the effect of the human body in the indoor radio propagation. Simulations were performed at 10.5 GHz, and the results demonstrated that at that frequency the human body can be approximated by a conducting cylinder. In [18], the UWB on-body radio channel was studied with a hybrid RT/UTD technique, and the human body was modeled as conducting spheres and cylinders representing the different body parts. The propagation around the body was studied; the RT technique was used together with the generalized Fermat principle to find a surface diffracted ray path, while the UTD surface diffraction coefficients were used for calculating the received signal strength. The problem of UTD and RT, is that the human body shape and composition need to be drastically simplified, and hence, they are not suitable for the analysis of the on-body radio channel at low RF frequencies.

The method of moments (MoM) technique, introduced by Harrington [19], is very efficient when applied to the analysis of wire structures and to the study of the scattering from metallic objects. In [20, 21] the MoM was used to investigate the effect of the human body on small loop antennas in pager systems. In [20], the human body was approximated as a reflecting surface, while in [21] a crude squared model of the human body was adopted. In a more recent paper [22], the MoM was adopted to analyse the performance of a body-worn diversity antenna, and a realistic homogeneous body model, provided by the commercial software FEKO ™ was used. However, this technique is not effective for modelling arbitrarily shaped structures. Moreover, since it requires the knowledge of the Green's function in every media, it is not suitable for inhomogeneous objects such as the human body.

The finite element method (FEM) is based on the decomposition of the electromagnetic domain into a number of elements of various shapes (usually tetrahedral), and it is well-suited to the modelling of curved structures. However, it has the disadvantage of having the highest computational complexity. The majority of the papers analyzing the effect of the human body in the EM radiation, adopts the Finite-difference time-domain (FDTD) technique. This technique, proposed by Yee in 1966 [23], is based on the direct solution of the time-domain versions of Maxwell's equations, and it is the most suitable technique for modeling the propagation of the electromagnetic waves inside and around the human body.

Since the early '90s, it has been applied to the study of the SAR in mobile communications [24]. At an early stage, crude models of the human body, like spheres and cylinders were used [25], while nowadays, realistic digital body phantoms are available. The FDTD has been widely used to the study of the radiation from implanted devices [26, 27], and to evaluate the behavior of body-worn antennas [28]. To account for the changes in the dielectric properties of the body with frequency, dispersive and subband FDTD codes have been developed [18, 29, 30].

The FDTD can be easily applied to the modelling of inhomogeneous structures, and it has the big advantage of having an O(N) computer complexity, while MoM and FEM have an O(N^2) complexity. Furthermore, since it is a time-domain technique, wideband results can be obtained with a single simulation.

On the other hand, like every numerical techniques, it suffers from a few weaknesses [5]. First, it requires the entire domain to be meshed in cells which are small compared to the wavelength. To take into account small geometric features, the cells need to be small, and hence computational time and memory required drastically increase. Especially in body-centric communications, where we are dealing with an electrically very large object, this is a big issue and it is necessary the development of a parallel code running on a cluster of computers. Another problem of the FDTD, is in the analysis of structure with sharp edges, where to accurately model the edge it is necessary to have a very fine mesh and a small time step, and hence the complexity of the computation increases. In the majority of the analysis presented so far, and in [12, 30, 31] computational models based on the FDTD were developed aiming to provide a physical insight of on-body radio channel, however, a single-cell Hertzian dipole was used as an excitation source, and hence it is not a true representation of body-worn antennas.

If practical antennas are considered in the on-body radio channel, a much higher spatial resolution is needed to accurately encounter small geometrical features in the antenna. This, in turn, increases the computation time and the memory requirements if a uniform mesh scheme is used. Although the use of a non-uniform mesh and a subgriding scheme in FDTD can be applied, it may result in spurious solutions or even suffer from instability for the sub-griding scheme [32]. It is also possible to combine the FDTD with other numerical schemes, for example, the frequency domain Method of Moments (FD-MoM) to increase numerical efficiency. In [33, 34], the equivalence principle has been used to divide the original problem into two sub-problems: the radiating element, ideally, a metallic structure is modeled using the MoM, while the surrounding environment using the FDTD.

In [35, 36], a time domain MoM (TD-MoM) is used to analyze the antenna in order to improve the numerical efficiency in ultra wideband analysis. The MoM technique, which requires the knowledge of the Green's function of every medium interested, is suitable to analyze pure metallic structures, but is not feasible to analyze planar antennas printed on dielectric substrate. A way of modelling sources in the FDTD domain is according to the Huygen's principle: "A given distribution of electric and magnetic fields on a closed surface drawn about the antenna structure can be cancelled by placing a suitable distribution of electric and magnetic current sheets $(\mathbf{J}, \mathbf{M})$ flowing on the closed surface", where $\hat{n} \times \mathbf{H} = \mathbf{J}$ is the electric current density, $\mathbf{E} \times \hat{n} = \mathbf{M}$ is the magnetic current density and $\hat{n}$ is the unit normal vector of an artificial surface Σ [35]. Hence, the radiation computed from the electric and magnetic current sheets is identical to the radiation which might be produced by the original source inside the closed surface. Knowing the fields produced by the source antenna on Σ, the real source can be replaced by the artificial surface Σ with fictitious sources lying on it. This technique has been implemented in this work and it will be explained in details in the next chapter.

4.3 Fundamentals of the FDTD Method

Maxwell Equations Classical electromagnetic theory is based on Maxwell equations: the electric and magnetic fields $\mathbf{E}$ and $\mathbf{H}$ are related to the electric and magnetic flux densities **D**, **B** and the electric and magnetic current densities **J** and **M** by

$$\begin{aligned}
\nabla \times \mathbf{E} &= -\frac{\partial \mathbf{B}}{\partial t} - \mathbf{M}, &(4.3)\\
\nabla \times \mathbf{H} &= \frac{\partial \mathbf{D}}{\partial t} + \mathbf{J}, &(4.4)\\
\nabla \cdot \mathbf{D} &= \rho, &(4.5)\\
\nabla \cdot \mathbf{B} &= 0. &(4.6)
\end{aligned}$$

Using the constitutive equations which relate fields to the properties of the medium, given by

$$\begin{aligned}
\mathbf{D} &= \varepsilon \mathbf{E}, &(4.7)\\
\mathbf{B} &= \mu \mathbf{H}, &(4.8)\\
\mathbf{J} &= \sigma \mathbf{E}, &(4.9)\\
\mathbf{M} &= \sigma^* \mathbf{H}, &(4.10)
\end{aligned}$$

where ε is the electric permittivity (farads/metre), μ is the magnetic permeability (henrys/metre), σ is the electric conductivity (siemens/metre), and σ^* is the magnetic resistivity (ohms/metre). For an isotropic medium with no charges ($\rho = 0$), the equations (4.3) and (4.4) relative to a free source point, are expressed in a cartesian coordinate system (x, y, z) as

$$\begin{aligned}
\frac{\partial E_x}{\partial t} &= \frac{1}{\varepsilon}\left(\frac{\partial H_z}{\partial y} - \frac{\partial H_y}{\partial z} - \sigma E_x\right),\\
\frac{\partial E_y}{\partial t} &= \frac{1}{\varepsilon}\left(\frac{\partial H_x}{\partial z} - \frac{\partial H_z}{\partial x} - \sigma E_y\right),\\
\frac{\partial E_z}{\partial t} &= \frac{1}{\varepsilon}\left(\frac{\partial H_y}{\partial x} - \frac{\partial H_x}{\partial y} - \sigma E_z\right),\\
\frac{\partial H_x}{\partial t} &= \frac{1}{\mu}\left(\frac{\partial E_y}{\partial z} - \frac{\partial E_z}{\partial y} - \sigma^* H_x\right),\\
\frac{\partial H_y}{\partial t} &= \frac{1}{\mu}\left(\frac{\partial E_z}{\partial x} - \frac{\partial E_x}{\partial z} - \sigma^* H_y\right),\\
\frac{\partial H_z}{\partial t} &= \frac{1}{\mu}\left(\frac{\partial E_x}{\partial y} - \frac{\partial E_y}{\partial x} - \sigma^* H_z\right). &(4.11)
\end{aligned}$$

Note that $\varepsilon = \varepsilon_r \varepsilon_0$ and $\mu = \mu_r \mu_0$, and for free space, ($\varepsilon_r = 1$, $\mu_r = 1$, $\sigma = 0$), $\varepsilon_0 = 8.854 \times 10^{-12}$ F/m and $\mu_0 = 4\pi \times 10^{-7}$ H/m.

Finite Difference and the Yee Algorithm The use of the finite difference method (FDM) to solve differential equations can be traced back to the 1910s by L. F. Richardson for weather forecasting [37, 38]. It was also used by A. Thom [39] in the 1920s, under the title "the method of squares", to solve non linear hydrodynamic equations. The finite difference technique is based upon approximations which permit replacing differential equations by finite difference equations. These finite difference approximations relate the value of the dependent variable at a point in the solution region to the values at some neighboring points. Thus, a finite difference solution basically involves three steps: (1) dividing the solution region into a grid of nodes; (2) approximating the given differential equation by finite difference equivalent that relates the dependent variable at a point in the solution region to its values at the neighboring points; (3) solving the difference equations subject to the prescribed boundary conditions and/or initial conditions.

In 1966, Kane S. Yee originated a set of finite-difference equations for the time dependent Maxwell's curl equations (4.3) and (4.4) for the case of lossless materials $\sigma = 0$ and $\sigma^* = 0$ [23]. A space point (m_x, m_y, m_z) in a uniform, rectangular lattice is denoted as

$$(m_x, m_y, m_z) = (m_x \Delta x, m_y \Delta y, m_z \Delta z), \tag{4.12}$$

where Δx, Δy and Δz are lattice space increments in x, y and z directions, respectively. Any function of space and time is evaluated as

$$\mathbf{F}^n(m_x, m_y, m_z) = \mathbf{F}(m_x \Delta x, m_y \Delta y, m_z \Delta z, n\Delta t), \tag{4.13}$$

and its space and time partial derivatives are set up to central-difference approximations as

$$\frac{\partial \mathbf{F}^n(m_x, m_y, m_z)}{\partial x} = \frac{\mathbf{F}^n(m_x + \frac{1}{2}, m_y, m_z) - \mathbf{F}^n(m_x - \frac{1}{2}, m_y, m_z)}{\Delta x} + \text{order}(\Delta x^2), \tag{4.14}$$

$$\frac{\partial \mathbf{F}^n(m_x, m_y, m_z)}{\partial t} = \frac{\mathbf{F}^{n+\frac{1}{2}}(m_x, m_y, m_z) - \mathbf{F}^{n-\frac{1}{2}}(m_x, m_y, m_z)}{\Delta t} + \text{order}(\Delta t^2), \tag{4.15}$$

where Δt is the time discretisation interval (or time step). Yee positioned the components of **E** and **H** at half-step intervals around a unit cell (see Fig. 4.6). The **E** and **H** fields are evaluated at alternate half-time steps, giving effectively central-difference

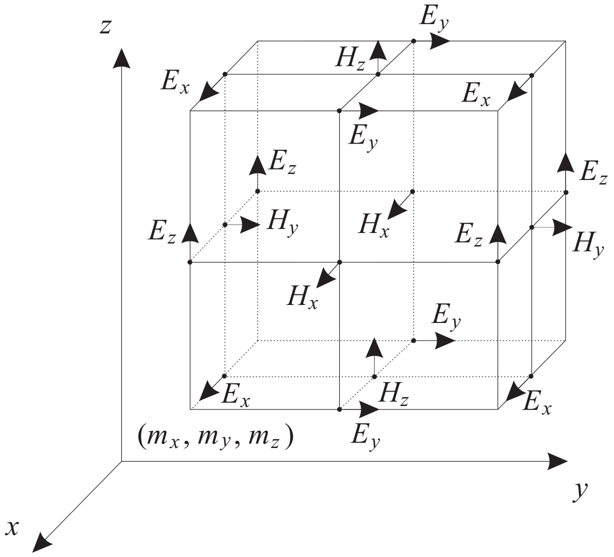

Figure 4.6: Position of the electric and magnetic field vector components about a cubic unit cell of the Yee space lattice.

expressions for both the space and time derivatives. If the components of **E** are calculated at $n\Delta t$, where n is any non-negative integer, the components of **H** are then calculated at $(n+\frac{1}{2})\Delta t$. Applying the above rules, the system of equations (4.11) provides the finite-difference time-stepping expressions for electric and magnetic field components. For example, the updating equations for the E_x and H_x components are

$$\begin{aligned} E_x\big|^{n+1}_{m_x+\frac{1}{2},m_y,m_z} &= E_x\big|^{n}_{m_x+\frac{1}{2},m_y,m_z} \\ &+\frac{\Delta t}{\varepsilon_{m_x,m_y,m_z}}\left(\frac{H_z\big|^{n+\frac{1}{2}}_{m_x+\frac{1}{2},m_y+\frac{1}{2},m_z}-H_z\big|^{n+\frac{1}{2}}_{m_x+\frac{1}{2},m_y-\frac{1}{2},m_z}}{\Delta y}\right. \\ &\left.-\frac{H_y\big|^{n+\frac{1}{2}}_{m_x+\frac{1}{2},m_y,m_z+\frac{1}{2}}-H_y\big|^{n+\frac{1}{2}}_{m_x+\frac{1}{2},m_y,m_z-\frac{1}{2}}}{\Delta z}\right), \end{aligned} \tag{4.16}$$

$$\begin{aligned} H_x\big|^{n+\frac{1}{2}}_{m_x,m_y+\frac{1}{2},m_z+\frac{1}{2}} &= H_x\big|^{n-\frac{1}{2}}_{m_x,m_y+\frac{1}{2},m_z+\frac{1}{2}} \\ &+\frac{\Delta t}{\mu_{m_x,m_y,m_z}}\left(\frac{E_y\big|^{n}_{m_x,m_y+\frac{1}{2},m_z+1}-E_y\big|^{n}_{m_x,m_y+\frac{1}{2},m_z}}{\Delta z}\right. \\ &\left.-\frac{E_z\big|^{n}_{m_x,m_y+1,m_z+\frac{1}{2}}-E_z\big|^{n}_{m_x,m_y,m_z+\frac{1}{2}}}{\Delta y}\right). \end{aligned} \tag{4.17}$$

The complete derivation procedure can be found in [40]. In the updating equations, H fields are computed for $t = (n + \frac{1}{2})\Delta t$ from the E field components at integer multiples of Δt. Therefore all H fields at a time step $(n + \frac{1}{2})\Delta t$ can be calculated from their previous values at $(n - \frac{1}{2})\Delta t$, E fields at $n\Delta t$ and vice versa. This method is also known as the staggered *leapfrog* time stepping scheme.

Because of the staggered arrangement of the vector field components in the grid and the leapfrog updating scheme, all finite difference terms for the derivatives in Maxwell equations are centred approximations. A Taylor series analysis shows that the Yee algorithm on a grid with constant mesh steps is second-order accurate both in space and time [40].

The maximum time step $\Delta t_{\max}$ for stable operations can be determined as [40]

$$\Delta t_{\max} \leq \frac{1}{c\sqrt{\frac{1}{(\Delta x)^2} + \frac{1}{(\Delta y)^2} + \frac{1}{(\Delta z)^2}}}, \tag{4.18}$$

where c is the maximum speed of light for all materials in the grid.

Most applications of the Yee algorithm, such as scattering problems or antenna analysis, require an unbounded open space for their accurate simulation. Since the available computer resources are in any case limited, the computation domain must be truncated with a so-called absorbing boundary condition (ABC), which simulates the behaviour of open space, i.e. which permits outbound waves to leave the grid without reflecting any energy back into it. In all the simulations presented in this thesis, a ten cell perfectly matched layer (PML) ABC has been adopted [41].

4.3.1 Dispersive FDTD

Current and emerging technological applications, such as body-centric communications, involve interactions of electromagnetic waves with material having frequency-dispersive dielectric properties. FDTD methods for incorporating the dispersive characteristics of biological tissues have been developed. These techniques have different computational complexity, ranging from the simple single-pole Debye model, to the more computationally complex Cole-Cole model [42]. For a Debye medium, the relative permittivity is expressed as

$$\varepsilon(\omega) = \varepsilon_\infty + \sum_{p=1}^{P} \frac{\Delta\varepsilon_p}{1 + j\omega\tau_p} \tag{4.19}$$

where ε_∞ is the relative permittivity at infinite frequency, $\Delta\varepsilon_p$ is the change in relative permittivity due to the Debye pole, and τ_p is the pole relaxation time. If a high number of poles is used, the algorithm results more accurate, but computationally more complex. The parameters of the Debye model can be extracted from the measured data by applying a fitting technique as explained in [43]. Table 4.1 shows the parameters of the two-pole Debye model used to fit the muscle tissue properties in the range 3-10 GHz.

ε_∞	4
$\Delta\varepsilon_1$	44.67
$\Delta\varepsilon_2$	14.92
τ_1	$0.0664 \cdot 10^{-10}$
τ_2	$0.7007 \cdot 10^{-10}$

Table 4.1: Parameters of the two-pole Debye model used to fit the dielectric properties of the muscle tissues in the frequency range 3-10 GHz.

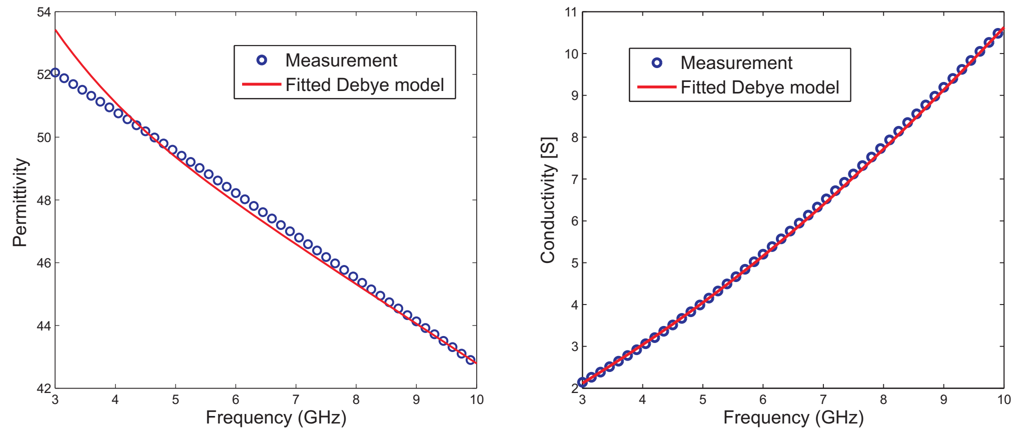

Figure 4.7: Comparison between the dielectric properties represented with a two-pole debye model and the ones measured in [3]; the tissue represented is the muscle.

Figure 4.7 shows the comparison between the measured dielectric properties [42], and the ones given by the 2-pole Debye model. The tissue considered is the muscle, and results demonstrated an acceptable accuracy of the 2-pole Debye model in representing the frequency-dependency of the body tissues. The update equations for the electric and magnetic fields are derived as in [29, 44]. Applying eq. 4.7 the displacement vector **D** can be expressed as

$$\mathbf{D}(\omega) = \varepsilon_0 \frac{\varepsilon_s + j\omega(\varepsilon_{s1}\tau_2 + \Delta\varepsilon_{s2}\tau_1) - \omega^2\tau_1\tau_2\varepsilon_\infty}{1 + j\omega(\tau_1 + \tau_2) - \omega^2\tau_1\tau_2} \tag{4.20}$$

where $\varepsilon_{si} = \Delta\varepsilon_i + \varepsilon_\infty$, and $\varepsilon_s = \varepsilon_{s1} + \varepsilon_{s2} - \varepsilon_\infty$. Applying the fourier transform to (4.20), it is possible the following time domain relation

$$\tau_1\tau_2\frac{\partial^2\mathbf{D}}{\partial t^2} + (\tau_1 + \tau_2)\frac{\partial\mathbf{D}}{\partial t} + \mathbf{D} = \varepsilon_0\left[\varepsilon_s E + (\varepsilon_{s1}\tau_2 + \varepsilon_{s2}\tau_1)\frac{\partial\mathbf{E}}{\partial t} + \varepsilon_\infty\tau_1\tau_2\frac{\partial^2\mathbf{D}}{\partial t^2}\right] \tag{4.21}$$

Such an equation, can be written in a differential form, and the final update equations are shown only for the x-component in eq. 4.22-4.23. The magnetic field is updated as in the conventional FDTD scheme, the displacement vector **D** and the electric field **E** are updated as following

$$\begin{aligned} D_x|^{n+1}_{m_x+\frac{1}{2},m_y,m_z} &= D_x|^{n}_{m_x+\frac{1}{2},m_y,m_z} \\ &\quad + \frac{\Delta t}{\varepsilon_{m_x,m_y,m_z}}\left(\frac{H_z|^{n+\frac{1}{2}}_{m_x+\frac{1}{2},m_y+\frac{1}{2},m_z} - H_z|^{n+\frac{1}{2}}_{m_x+\frac{1}{2},m_y-\frac{1}{2},m_z}}{\Delta y}\right. \\ &\quad \left. - \frac{H_y|^{n+\frac{1}{2}}_{m_x+\frac{1}{2},m_y,m_z+\frac{1}{2}} - H_y|^{n+\frac{1}{2}}_{m_x+\frac{1}{2},m_y,m_z-\frac{1}{2}}}{\Delta z}\right) \end{aligned} \tag{4.22}$$

$$\begin{aligned} &\left[\alpha_0 + \frac{\alpha_1}{\Delta t} + \frac{\alpha_2}{\Delta t^2}\right] E_x|^{n+1} = \left[\frac{2\alpha_2}{\Delta t^2} + \frac{\alpha_1}{\Delta t} - \alpha_0\right] E_x|^{n} - \frac{\alpha_2}{\Delta t^2} E_x|^{n-1} \\ &+ \left[\beta_0 + \frac{\beta_1}{\Delta t} + \frac{\beta_2}{\Delta t^2}\right] D_x|^{n+1} + \left[\beta_0 - \frac{\beta_1}{\Delta t} - \frac{2\beta_2}{\Delta t^2}\right] D_x|^{n} + \frac{\beta_2}{\Delta t^2} D_x|^{n-1} \end{aligned} \tag{4.23}$$

where

$$\begin{aligned} \alpha_0 &= (\varepsilon_s\varepsilon_0)/2, \quad \alpha_1 = \varepsilon_0(\varepsilon_{s1}\tau_2 + \varepsilon_{s2}\tau_1), \quad \alpha 2 = \varepsilon_0\varepsilon_\infty\tau_1\tau_2 \\ \beta_0 &= 1/2, \qquad \beta_1 = \tau_1 + \tau_2, \qquad \beta_2 = \tau_1\tau_2 \end{aligned} \tag{4.24}$$

The z and y components are updated in a similar way. In this formulation the values of **E** are used to calculate **H** using (4.17); then **H** is used to calculate **D** adopting (4.22), and finally **D** is used to calculate **E** adopting (4.23) for the following time step, after which the process is repeated for the next time step and so on [29].

4.4 Summary

Modelling of the human body is a necessary task for studying the interaction between human body tissues and EM waves. This task can be accomplished by developing physical phantoms, or numerical digital phantoms to be embedded in EM codes. The chapter illustrates the electromagnetic properties of the body tissues, and discusses state-of-the-art and major challenges in numerical modelling for BCWC. The main features of the FDTD technique were illustrated, since it is the most suitable for modelling the human body, and it has been used throughout the development of this work.

References

[1] N. P. D. Milavcic and F. X. Hart, *Wiley Encyclopedia of Biomedial Enginnering*. John Wiley & Sons, Ltd., 2006.

[2] "Calculation of the dielectric properties of body tissues," *Institute for Applied Physics, Italian National Research Council, http://niremf.ifac.cnr.it/tissprop/*.

[3] C. Gabriel and S. Gabriel, "Compilation of the dielectric properties of body tissues at RF and microwave frequencies," 1999, www.brooks.af.mil/AFRL/HED/hedr/reports/dielectric/Title/Title.html.

[4] A. Alomainy, "Antennas and radio propagation for body-centric wireless networks," Ph.D. dissertation, Queen Mary, University of London, 2007.

[5] P. S. Hall and Y. Hao, *Antennas and Propagation for Body-Centric Wireless Communications*. Artech House, 2006.

[6] M. Kanda, M. Ballen, S. Salins, C. Chou, and Q. Balzano, "Formulation and characterization of tissue equivalent liquids used for RF densitometry and dosimetry measurements," *IEEE Transactions on Microwave Theory and Techniques*, vol. 52, no. 8 Part 2, pp. 2046–2056, 2004.

[7] A. Guy, "Analyses of electromagnetic fields induced in biological tissues by thermographic studies on equivalent phantom models," *IEEE Transactions on Microwave Theory and Techniques*, vol. 19, no. 2, pp. 205–214, 1968.

[8] A. Sani, M. Rajab, R. Foster, and Y. Hao, "Antennas and propagation of implanted RFIDs for pervasive healthcare applications," *Accepted for publication in the Proceeding of the IEEE*.

[9] K. Ito, K. Furuya, Y. Okano, and L. Hamada, "Development and characteristics of a biological tissue-equivalent phantom for microwaves," *Electronics and Communications in Japan (Part I: Communications)*, vol. 84, no. 4, 2001.

[10] H. Tamura, Y. Ishikawa, T. Kobayashi, and T. Nojima, "A dry phantom material composed of ceramic and graphite powder," *IEEE Transactions on Electromagnetic Compatibility*, vol. 39, no. 2, pp. 132–137, 1997.

[11] Y. Nikawa, M. Chino, and K. Kikuchi, "Soft and dry phantom modeling material using silicone rubber withcarbon fiber," *IEEE Transactions on Microwave Theory and Techniques*, vol. 44, no. 10 Part 2, pp. 1949–1953, 1996.

[12] Y. Zhao, Y. Hao, A. Alomainy, and C. Parini, "Ultra wide- band body area channel model," *IEEE Transaction on Microwave Theory and Techniques*, vol. 54, no. 4, pp. 1827–1835, April 2006.

[13] X. Xu, T. Chao, and A. Bozkurt, "VIP-Man: an image-based whole-body adult male model constructed from color photographs of the visible human project for multi-particle Monte Carlo calculations," *Health Physics*, vol. 78, no. 5, p. 476, 2000.

[14] T. Nagaoka, S. Watanabe, K. Sakurai, E. Kunieda, S. Watanabe, M. Taki, and Y. Yamanaka, "Development of realistic high-resolution whole-body voxel models of japanese adult males and females of average height and weight, and application of models to radio-frequency electromagnetic-field dosimetry," *Phys. Med. Biol.*, vol. 49, no. 4, pp. 1–15, December 2003.

[15] S.-L. Lee, M. Lerotic, A. Sani, Y. Zhao, J. Keegan, Y. Hao, and G.-Z. Yang, "Articulated postures for subject-specific RF simulations," in *Body Sensor Networks 2010, BSN 2010.*, June 2010.

[16] "Binvox 3D mesh voxelizer," http://www.cs.princeton.edu/∼min/binvox/.

[17] M. Ghaddar, L. Talbi, T. Denidni, and A. Sebak, "A conducting cylinder for modeling human body presence in indoor propagation channel," *IEEE Transactions on Antennas and Propagation*, vol. 55, no. 11 Part 1, pp. 3099–3103, 2007.

[18] Y. Zhao, Y. Hao, A. Alomainy, and C. Parini, "UWB on-body radio channel modeling using ray theory and subband FDTD method," *IEEE transactions on microwave theory and techniques*, vol. 54, no. 4 Part 2, pp. 1827–1835, 2006.

[19] R. Harrington, *Field computation by moment methods*. Wiley-IEEE Press, 1993.

[20] K. Ito, I. Ida, and M. Wu, "Body effect on characteristics of small loop antenna in pagersystems," in *IEEE Antennas and Propagation Society International Symposium, 1992. AP-S. 1992 Digest. Held in Conjuction with: URSI Radio Science Meeting and Nuclear EMP Meeting.*, 1992, pp. 1081–1084.

[21] H. Chuang and W. Chen, "Computer simulation of the human-body effects on a circular-loop-wire antenna for radio-pager communications at 152, 280, and 400 MHz," *IEEE Transactions on Vehicular Technology*, vol. 46, no. 3, pp. 544–559, 1997.

[22] D. Psychoudakis, G. Lee, C. Chen, and J. Volakis, "Body-worn diversity antennas for squad area networks (SAN)," *URSI General Assembly*, 2008.

[23] K. S. Yee, "Numerical solution of initial boundary value problems involving Maxwell's equations in isotropic media," *IEEE Trans. Antennas Propgat.*, vol. 14, no. 3, pp. 302–307, 1966.

[24] J. Chen and O. Gandhi, "Currents induced in an anatomically based model of a human forexposure to vertically polarized electromagnetic pulses," *IEEE Transactions on Microwave Theory and Techniques*, vol. 39, no. 1, pp. 31–39, 1991.

[25] J. Toftgard, S. Hornsleth, and J. Andersen, "Effects on portable antennas of the presence of a person," *IEEE Transactions on Antennas and Propagation*, vol. 41, no. 6, pp. 739–746, 1993.

[26] W. G. Scanlon, N. E. Evans, and Z. McCresh, "RF performance of a 418 MHz radio telemeter packaged for human vaginal placement," *IEEE Transactions on Biomedical Engineering*, vol. 44, no. 5, pp. 427–430, May 1997.

[27] W. Xia, K. Saito, M. Takahashi, and K. Ito, "Performaces of an implanted cavity slot antennas embedded in the human arm," *IEEE Transactions on Antennas and Propagation*, vol. 57, no. 4, pp. 894–899, 2009.

[28] N. Haga, K. Saito, M. Takahashi, and K. Ito, "Characteristics of cavity slot antennas for body-area networks," *IEEE Transactions on Antennas and Propagation*, vol. 57, no. 4, pp. 837–843, 2009.

[29] O. Gandhi, B. Gao, and J. Chen, "A frequency-dependent finite-difference time-domain formulation forgeneral dispersive media," *IEEE Transactions on Microwave Theory and Techniques*, vol. 41, no. 4, pp. 658–665, 1993.

[30] Q. Wang, T. Tayamachi, I. Kimura, and J. Wang, "An on-body channel model for UWB body area communications for various postures," *IEEE Journal on Selected Areas in Communications*, vol. 57, no. 4, pp. 991–998, April 2009.

[31] A. Fort, C. Desset, J. Ryckaert, P. De-Doncker, L. V. Biesen, and S. Donnay, "Ultra wideband body area channel model," *ICC Proceedings, Seoul, Korea*, 2005.

[32] P. Monk and E. Suli, "Error estimates for yee's method on non-uniform grids," *IEEE Trans. Magn.*, vol. 30, pp. 3200–3203, 1994.

[33] Z. Huang, K. R. Demarest, and R. G. Plumb, "An FDTD/MoM hybrid technique for modelling complex antennas in the presence of heterogeneous grounds," *IEEE Transactions on Geoscience and Remote Sensing*, vol. 37, no. 6, pp. 2692–2698, November 1999.

[34] R. A. Abd-Alhameed, M. A. Mangoud, and P. S. Excel, "Broadband antenna respaonse using hybrid technique combining frequency domain MoM and FDTD," *11th International Conference on Antennas and Prooagation. UMIST. Manchester. U.K.*, 17-20 April 2001.

[35] A. R. Bretones, R. Mittra, and R. G. Martin, "A hybrid technique combining the method of moments in time domain and FDTD," *IEEE Microwave and Guided Wave Letters*, vol. 8, no. 8, pp. 281–283, August 1998.

[36] W. G. Scanlon, S. Cascino, and P. Russo, "Hybrid method for time-domain analysis of wire antennas embedded in a scattering dielectric medium," *Antennas and Propagation, 2001. Eleventh International Conference on (IEE Conf. Publ. No. 480)*, vol. 2, pp. 861–865, 2001.

[37] L. F. Richardson, "The approximate arithmetical solution by finite differences of physical problems involving differential equations, with an application to the stresses in a masonry dam," *Phil. Trans. R. Soc. London Ser. A*, vol. 210, pp. 307–357, 1910.

[38] ——, *Weather Prediction by Numerical Process*. Cambridge University Press, 1922.

[39] A. Thom and C. J. Apelt, *Field Computations in Engineering and Physics*. London: D. Van Nostrand, 1961.

[40] A. Taflove, *Computational Electrodynamics: The Finite Difference Time Domain Method*. Norwood, MA: Artech House, 1995.

[41] J.-P. Berenger, "A perfectly matched layer for the absorption of electromagnetic waves," *J. Computat. Phys.*, vol. 114, no. 2, pp. 185–200, 1994.

[42] S. Gabriel, R. Lau, and C. Gabriel, "The dielectric properties of biological tissues: III. Parametric models for the dielectric spectrum of tissues," *Physics in medicine and biology*, vol. 41, no. 11, pp. 2271–2294, 1996.

[43] M. Mrozowski and M. Stuchly, "Parameterization of media dispersive properties for FDTD," *IEEE Transactions on Antennas and Propagation*, vol. 45, no. 9, pp. 1438–1439, 1997.

[44] T. Wuren, T. Takai, M. Fujii, and I. Sakagami, "Effective 2-debye-pole FDTD model of electromagnetic interaction between whole human body and UWB radiation," *IEEE Microwave and Wireless Components Letters*, vol. 17, no. 7, pp. 483–485, 2007.

Chapter 5

Numerical Modelling of Wearable Antennas and Radio Channel at 2.4 GHz

The design of a spectrum and power efficient on-body communication system, requires an accurate understanding of the radio channel characteristics, task that in the past have been mainly accomplished through experiments [1–7]. However, experiments are expensive and time-consuming. On the other hand, the propagation of electromagnetic waves inside or around the human body is a complex problem, which can not be treated analytically. This chapter presents a numerical investigation of the radio propagation in WBAN at 2.4 GHz adopting a parallel version of the FDTD technique. The effect of the body posture and the subject-specificity of the radio channel have been addressed. This chapter, also presents a technique based on the equivalence principle for analysing the performance of body-worn antennas.

5.1 Homogeneous vs. Inhomogeneous Phantom

In order to characterise on-body radio channel and wearable antennas, realistic digital phantoms need to be included in the numerical analysis as discussed in Chapter 4. The development of inhomogeneous phantoms, classifying several internal organs, is a complicated process where data regarding the internal composition of the body are obtained by sectioning a cadaver [8]. This kind of phantom is necessary for certain applications such as the analysis of medical implants, and for evaluating the distribution of the SAR inside the body. However, when studying the on-body radio channel at microwave frequencies, since the skin depth is small (due to the high losses), the internal composition of the body does not play a major role. This allows the use of realistic-shaped homogeneous phantoms (usually made of muscle tissue), which have the big advantage that can be easily developed by segmenting the images given by a single MRI scan.

In this analysis, the results obtained adopting a homogeneous phantom, are compared to those obtained with a stratified phantom. The FDTD simulations are carried out at 2.4 GHz with a cell size $dx = dy = dz = 3$ mm. The stratified phantom adopted is the body model of a Japanese male (22-year-old, 1.73 m tall and weighed 65 kg), in which over 50 types of tissues are classified [9]. The electrical properties of the principal human tissues at 2.4 GHz are listed in Table 5.1.

Two different cases of homogeneous models have been analysed. In the first, the properties of the muscle tissues are considered ($\varepsilon_r = 53.6$, $\sigma = 1.77$ S/m at 2.45 GHz), while in the second a tissue called 2/3 muscle is used ($\varepsilon_r = 35.4$, $\sigma = 1.19$ S/m at 2.45 GHz). Such a tissue model represents a sort of "average tissue", and it has been extensively used in evaluating the performance of medical implants [11].

Figure 5.1 shows the distribution of the electric field sliced horizontally on the plane of the transmitter. It is possible to note a good agreement between homogeneous and inhomogeneous case.

The transmitting antenna is placed on the left side of the waist, and eight representative on-body links have been considered as shown in Fig.5.2. Table 5.2 lists the values of received power (for each link) obtained adopting the homogenous phantoms

	2.4 GHz		
Tissue	σ (S/m)	ϵ_r	δ **(mm)**
Aorta	1.40	42.59	24.86
Bladder	0.67	18.03	33.83
Blood	2.50	58.35	16.41
Body Fluid	2.44	68.24	18.14
Bone	0.79	18.61	29.43
Grey Matter	1.77	48.99	21.15
White Matter	1.19	36.23	27.05
Breast Fat	0.13	5.16	90.76
Fat	0.10	5.29	119.56
Gall Bladder	2.02	57.68	20.10
Gland	1.93	57.27	21.00
Heart	2.22	54.92	17.95
Kidney	2.39	52.86	16.37
Liver	1.65	43.12	21.30
Lung Deflated	1.65	48.45	22.59
Lung Inflated	0.79	20.51	30.73
Muscle	1.71	52.79	22.79
Pancreas	1.93	57.27	21.00
Prostate	2.13	57.63	19.12
Skin Dry	1.44	38.06	22.96
Skin Wet	1.56	42.92	22.47
Spleen	2.20	52.55	17.70
Stomach	2.17	62.24	19.49
Tendon	1.64	43.21	21.44
Testis	2.13	57.63	19.12

Table 5.1: Electric properties of specific human tissues used within the visible man model at 2.4 GHz [10] (σ is the tissue conductivity, ϵ_r is the dielectric constant and δ is the penetration depth in mm)

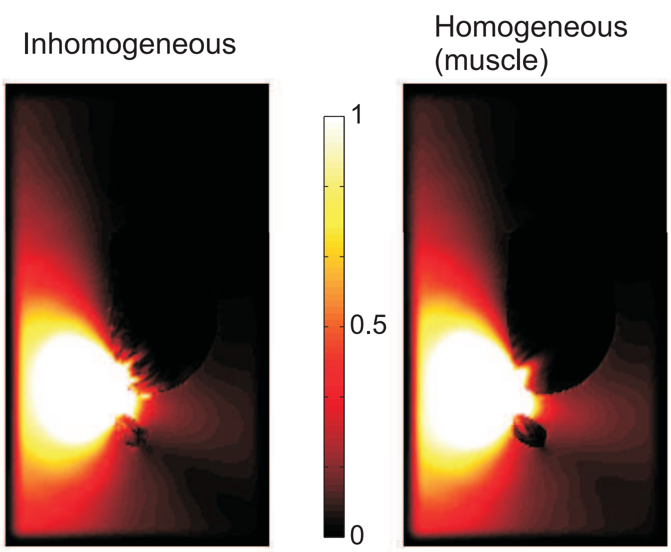

Figure 5.1: Normalised amplitude of the electric field sliced on the plane of the transmitter

Figure 5.2: Location of the transmitter and of the eight on-body receivers.

RX	Muscle	2/3 Muscle
Left ear	+1.0	+1.6
Right ear	-2.4	-1.7
Left chest	+2.9	+1.6
Right chest	+2.9	+2.5
Left wrist	+1.6	+2.0
Right wrist	-2.0	-2.6
Left ankle	+2.4	+2.4
Right ankle	-2.8	-1.4

Table 5.2: Received power (in dB) for the homogeneous case; the values have been normalised to the ones obtained adopting the inhomogeneous digital phantom. The transmitting antenna was placed on the left side of the waist.

with respect to the values obtained in the inhomogeneous case. The maximum difference between homogeneous and inhomogeneous phantoms, is 2.9 dB for the muscle case, and 3.4 dB for the 2/3 muscle case. The conclusion of this analysis is that a homogeneous phantom made of muscle tissue is suitable for modeling the on-body radio channel at 2.4 GHz. As explained in the previous chapter, the development of homogenous phantoms is relatively easy (compared with inhomogeneous phantoms); thus allowing a thorough numerical analysis where the impact of different digital phantoms and human body postures on the radio channel can be considered.

5.2 Path Loss Characterisation Including Different Body Postures

The changes in body posture significantly affect the propagation paths and cause large variation in path loss [12]. The impact of different body postures on the radio channel is studied by considering eight body postures when the subject is standing and sitting down; and considering four different positions of the arms. The details of the postures are illustrated in Fig. 5.3. The transmitting antenna is placed on the left side of the waist, and eight different receiver positions are considered (as shown in Fig. 5.2). The homogeneous digital phantom adopted in the simulations has a height of 1.75 m and weights 73 kg. The transmitter is a Hertzian dipole parallel to the body surface (along z direction), and the settings of the FDTD simulations are the same described in section 5.1.

In indoor wireless communications, the path loss is usually modelled as a linear function of the logarithmic distance as explained in section 3.3.1. Such a model has been widely used also for modelling the large scale path loss in on-body communications [2, 13], and it provides a reasonably good fit to the simulated data as shown in Fig.5.4. The path loss is modelled as

$$PL_{dB} = 24.2 + 10 \cdot 3.2 \cdot \log(d/0.1) + N(0, 64.3) \tag{5.1}$$

the path loss exponent is obtained applying a least square fit on the measured data (see Fig. 5.4), and it is found to be γ=3.2. The reference distance d_0 has been

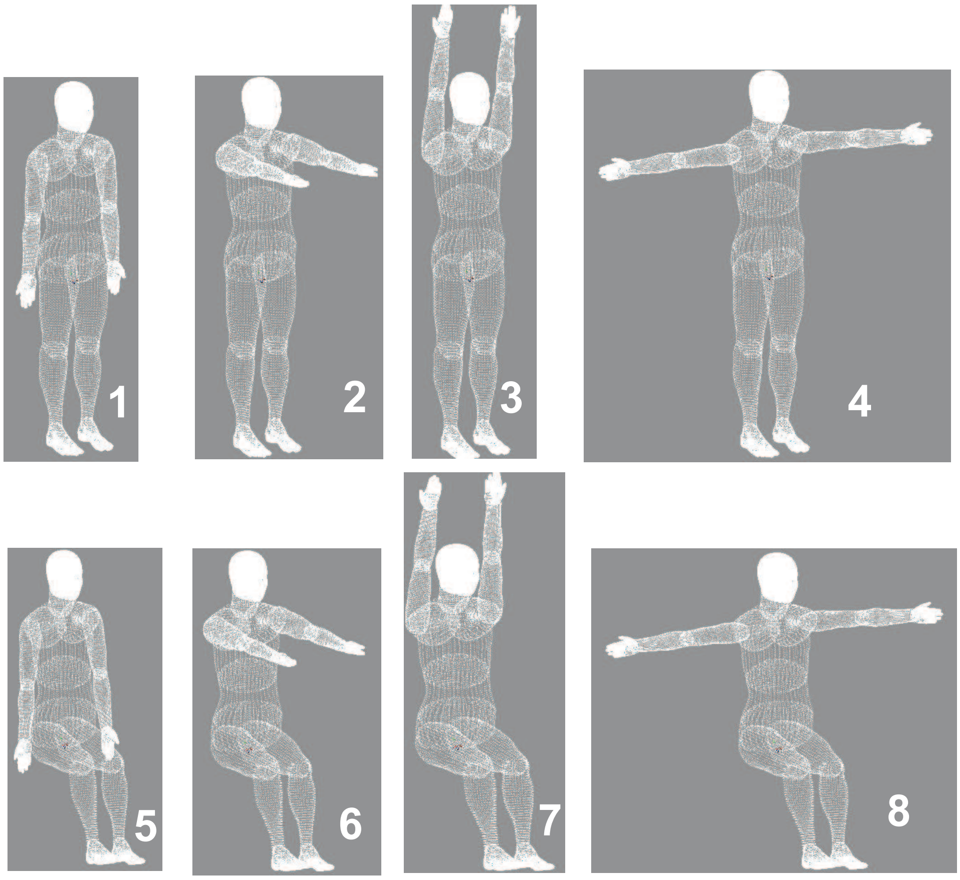

Figure 5.3: Illustration of the eight postures analysed.

set to 0.1 m as explained in section 3.3.1. The shadowing factor χ is a zero-mean normal distribution with variance σ^2=84.6. The simulated results are compared to experimental data obtained performing measurements on a candidate with similar size to the digital phantom adopted. A pair of printed monopoles (with polarisation tangential to the human body) is used to measure the path loss. There is a reasonable agreement between experimental and simulated data, and the measured path loss can be modeled as

$$PL_{dB} = 26 + 10 \cdot 3.6 \cdot \log(d/0.1) + N(0, 85.6) \tag{5.2}$$

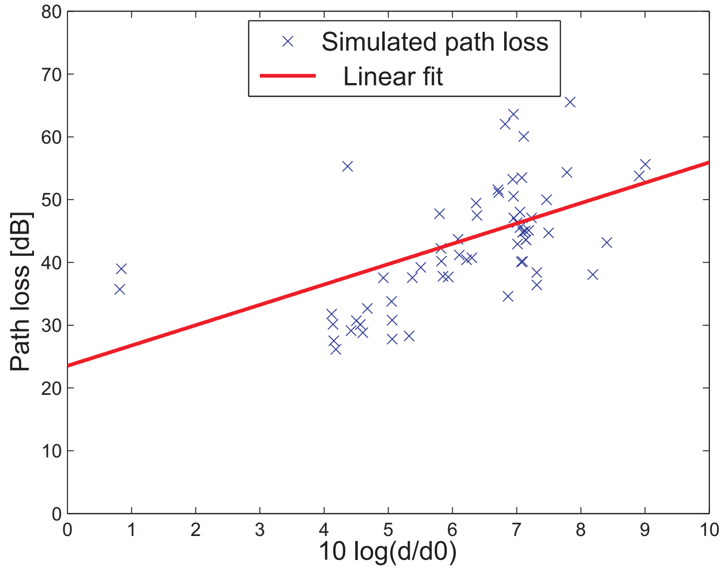

Figure 5.4: Simulated and modeled path loss obtained considering the eight different postures.

In addition to modeling the path loss as a function of the distance, it is very interesting to investigate the changes in the received power with respect to different body postures.

Figure 5.5(a) shows the variation of the path loss for the receivers 1 to 4, while Fig. 5.5(b) considers the receivers 5 to 8. It is important to note that the values are normalised to the maximum received power obtained for each link. For the receiver 1, located on the left ear, the received power is minimum for the postures 2 and 6 (-20 and -27 dB respectively); in these cases, the left arm stretched in front of the body constitutes an obstacle for the propagation of the signal. The maximum power is received for the posture 8, case in which arms stretched laterally do not interfere with the propagation of the signal. An opposite trend is found for the receiver 2 (placed on the right ear). In

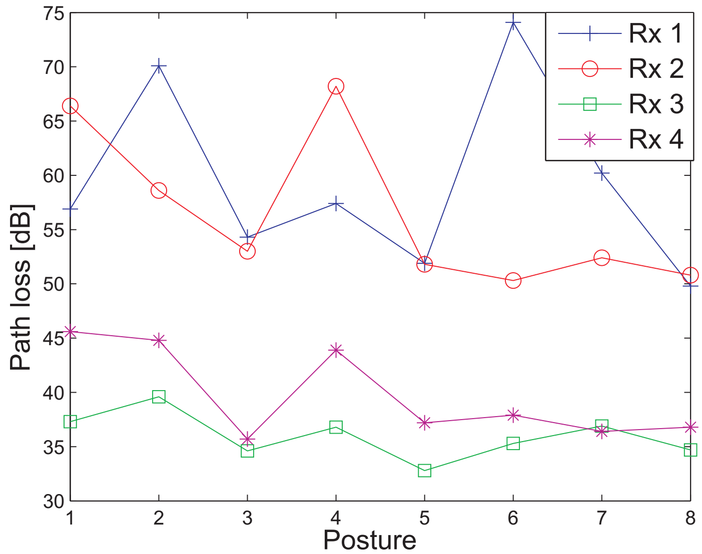

(a) Receivers 1-4

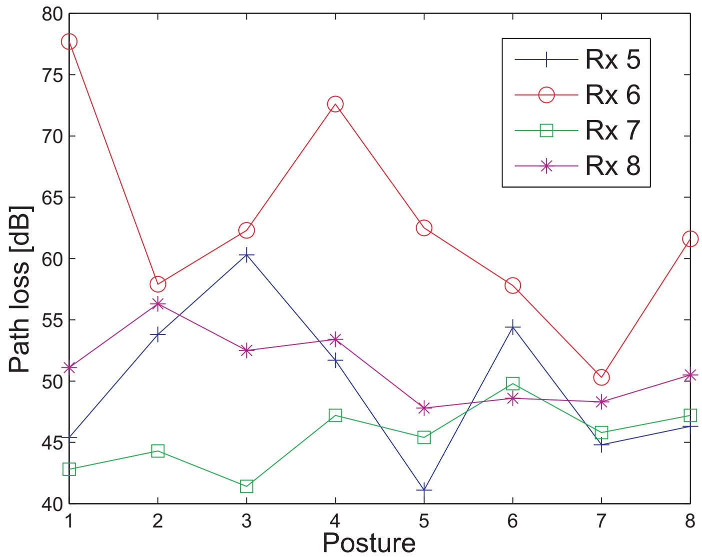

(b) Receivers 5-8

Figure 5.5: Variation of the path loss for selected Rx/Tx positions with the different postures.

this case, when the arms are stretched in front of the body, there is still LOS between transmitter and receiver, and the reflections from the arms enforce the signal, which has a maximum for the posture 6.

For the receivers 3 and 4 (placed on the chest), since there is always LOS between transmitter and receiver, the links are less affected by changes in posture and position of the arms. In the belt-to-left wrist link (receiver 5) the minimum power is received when the subject is standing with the arms stretched above the head (posture 3), and this is due to the increased communication distance. The peak power is found for the position 5, for which the reflections form the legs (the subject is sitting) lead to a higher value of received power. Different results are found for the receiver 6 (placed on the right wrist). In such case, the weakest signal is received for the postures 1 and 4 (-29 and -22 dB respectively). The arms stretched along the body (for the posture 1), and stretched laterally (for the posture 4), lead to clear situation of NLOS between transmitter and receiver, and hence to a minimum value of received power.

Finally, for the two links belt-to-ankle (receivers 7 and 8) the position of the arms do not affect much the propagation of the signal. When the subject is sitting down, the communication distance is shorter, however this effect is partially compensated by the obstruction caused by the legs. For the left ankle case a higher level of power is recorded when the subject is standing (posture 1 to 4), while for the right ankle case, the signal power is found to be higher when the subject is sitting down. Please note that for all simulations, the effect of the ground was not taken into account.

The variations in posture cause signficant changes in the received power level. For example, for the receivers on the right ear and on the right wrist (receivers 2 and 6 respectively), there is a difference of more than 12 dB between postures 1 and 5 (subject standing still and subject sitting down respectively). In particular, when the subject is sitting down the power is increasing, and this is due to the fact that the power reflected by the legs enforces the received signal at the receivers. However, such effect is not evident for the receivers placed on the left ear and on the left wrist (receivers 1 and 5 respectively), where the reflections from the legs do not lead to a significant increase in received power (only 3-4 dB). It is very hard to provide a physical explanation for the propagation mechanism in on-body communications, since the signal at the receiver is a combination of direct wave, reflections and diffractions from different body parts, and surface and creeping waves propagation along the body surface. All these different contributions could recombine in phase or out of phase, and a minimum change in the position of the reciver can lead to significant fading in the received power level. By performing several simulations including different postures, it is possible to quantify the fading caused by the changes in posture thus providing useful information for the system designers.

In conclusion, for particular links such as waist-to-wrist and waist-to-head, the changes in posture (especially the position of the arms) can lead to path loss variations up to 30 dB, similarly to what was experimentally demonstrated in [1].

5.3 Subject-Specific Study of the On-Body Radio Channel

In addition to the changes in posture, also the size of the body causes large variations in the path loss. A subject-specific radio propagation study in WBAN is performed by characterising the path loss for nine different digital phantoms of different size and gender.

5.3.1 Digital Phantoms Adopted in the Simulations

A total of nine subjects are considered in this study: five females and four males. Heights and weights of the phantoms are listed in Table 6.8, together with the body mass indices (BMIs) and the chest and waist circumferences.

	F01	F02	F03	F04	F05	M01	M02	M03	M04
Height (m)	1.55	1.60	1.65	1.66	1.80	1.67	1.76	1.78	1.80
Weight (kg)	52	50	52	55	75	56	73	87	85
BMI	21.6	19.5	19.1	20.0	23.1	20.1	23.6	27.5	26.2
Waist (cm)	68.8	67.0	66.2	72.7	81.9	67.1	82.6	91.0	84.2
Chest (cm)	96.9	79.4	80.7	85.6	107.9	82.1	91.3	101.1	98.4

Table 5.3: The dimensions of nine subjects scanned using MRI and used in FDTD simulations (F – Female, M – Male).

The subjects are scanned using magnetic resonance imaging (MRI) and a surface tetrahedral mesh is generated for each subject. However, since volume meshes are required in FDTD simulations, a voxelizer tool [14] has been used to convert the surface meshes into cubic volumetric ones. Figure 5.6 shows three dimensional images, and cross sections (at the height of stomach) of the nine voxelized subjects.

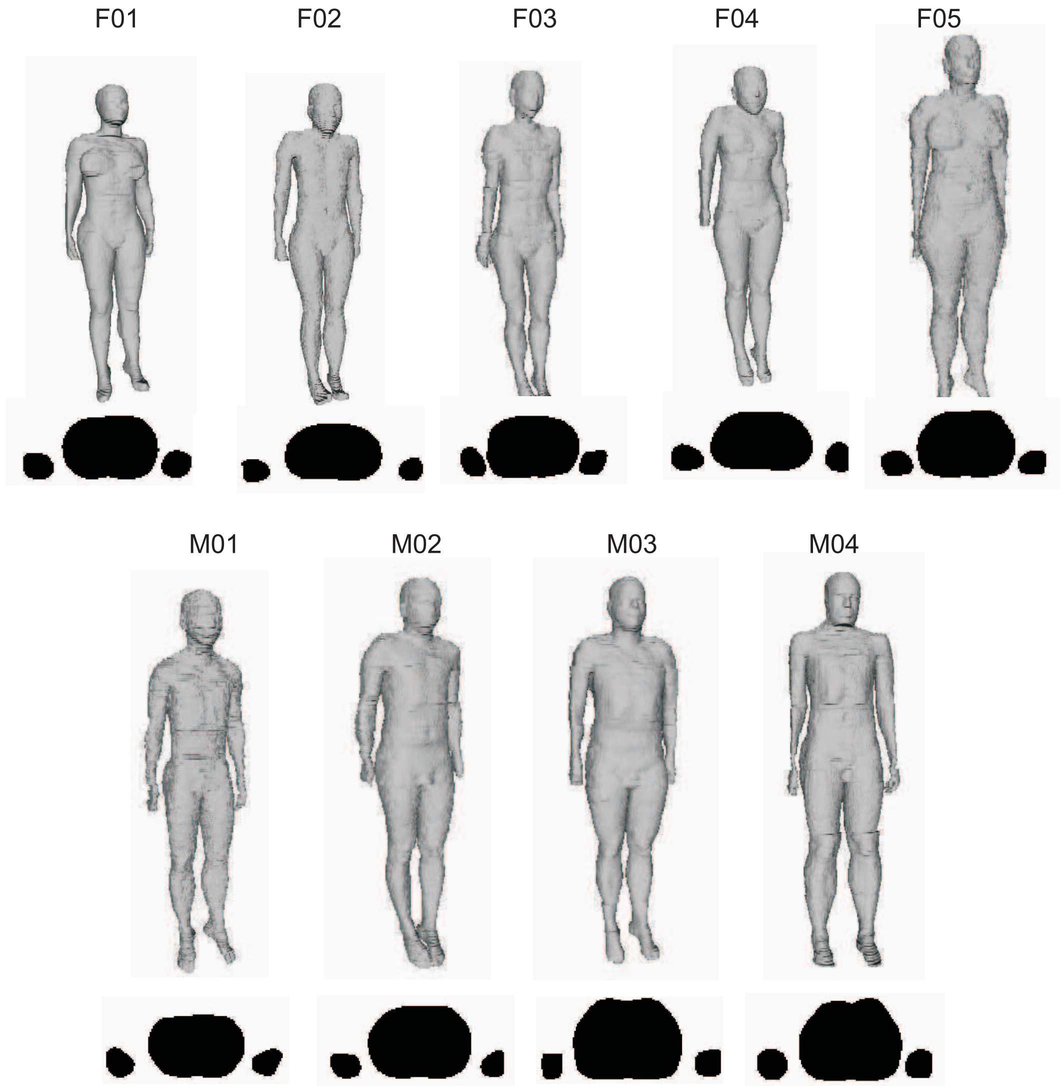

Figure 5.6: Three dimensional images, and cross sections at the height of stomach of the nine voxelized subjects.

5.3.2 Path Loss Characterisation

The impact of different digital phantoms on the radio channel characteristics is studied by considering eight representative on-body links (listed in Table 5.4). The transmitting source is a Hertzian dipole parallel to the body surface (along z direction) placed on the left side of the waist. The settings of the FDTD simulations are the same described in section 5.1. Table 5.4 lists the values of path loss obtained for the different digital phantoms. For the receivers placed on the ears and on the chest, it is possible to note that the path loss is higher for taller subjects with a larger curvature radius at the trunk such as F05 and M04. For shorter subjects with a smaller value of BMI (such as F03 and M02), the path loss is found to be 6-10 dB lower. For the receivers on the wrists and on the ankles, the variation of path loss between the different models is found to be higher (up to 15 dB). However, such values depend on the position of the arms and the legs during the MR scan, and hence can not be directly related to the phantoms' anatomical features

RX	F01	F02	F03	F04	F05	M01	M02	M03	M04
Left ear	60.9	58.2	67.3	67.9	69.4	59.7	64.3	63.0	69.0
Right ear	67.1	66.2	68.3	71.5	69.1	60.2	64.7	66.7	70.3
Left chest	34.5	36.2	41.4	42.3	44.5	35.3	38.8	43.8	45.4
Right chest	41.6	40.1	46.5	43.8	49.7	41.4	44.6	43.6	46.7
Left wrist	43.6	41.5	40.1	43.8	50.2	47.1	43.3	56.9	47.3
Right wrist	65.7	70.8	69.1	69.5	75.2	52.2	59.5	67.5	58.7
Left ankle	43.5	42.8	55.1	50.0	47.9	42.4	48.3	52.3	49.4
Right ankle	53.7	52.6	61.2	58.9	60.1	54.4	57.1	66.9	55.2

Table 5.4: Path loss (in dB) of the on-body links for the nine digital phantoms considered. The transmitting antenna is placed on the left side of the belt.

The path loss is also characterised for propagation along the trunk as a function of the communication distance. The transmitting antenna is located on the left side of the waist, and the received power is sampled on several locations (over a hundred) on the front part of the trunk. In order to model the path loss as a linear function of the logarithmic distance (equation 3.17), a least square fit is performed on the simulated data.

	F01	F02	F03	F04	F05	M01	M02	M03	M04
γ	2.3	2.3	2.7	2.4	2.9	2.6	2.5	3.1	3.0
σ [dB]	3.8	4.0	6.0	3.9	4.1	4.5	3.9	4.8	3.8

Table 5.5: Path loss exponent and standard deviation of the shadowing factor for the nine subjects (F – Female, M – Male).

In general, the comparison between simulations and measurements of Fig. 5.7 shows good agreement which validates the numerical simulation. However, the measured data is more spread comparing with the simulated one, and this may be due to the cable effect which are not taken into account in numerical simulations. Despite this

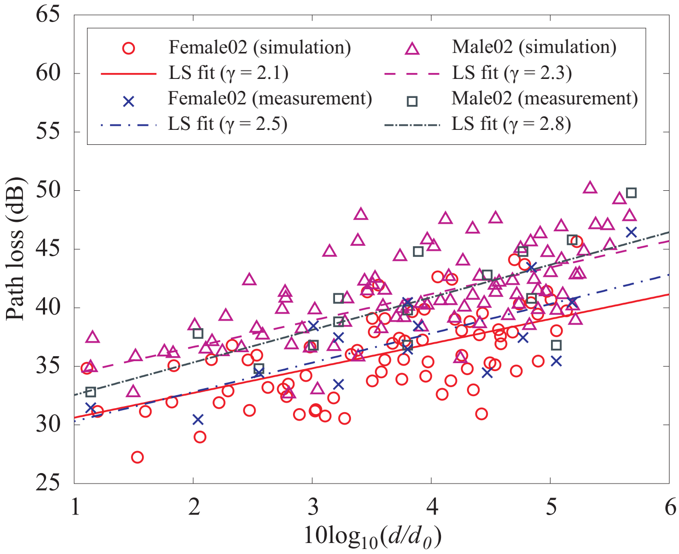

Figure 5.7: The comparison between measurements and simulations of the on-body path loss (against distance) for subjects Female01 and Male01.

fact, the path loss exponent from simulations and measurements shows good agreement. Table 5.5 lists the values of path loss exponent, and standard deviation of the shadowing factor, obtained for the nine digital phantoms. The results show that the exponent is generally increasing with the body size. In the case of subjects with a low value of BMI such as F01 and F02, the subject presents a very small curvature radius of the trunk, and hence there is LOS between transmitter and receiver, and the path loss exponent is $\gamma = 2.3$, which is close to the free space value. For subjects with higher curvature radius of the trunk (such as F05), the wave reaches the receiver through creeping wave propagation, thus leading to higher value of exponent (γ=2.9). A similar conclusion can be drawn for the male phantoms, where subjects with higher BMI (and hence with a larger curvature radius at the trunk), such as M03 and M04 have a path loss exponent greater than 3.0.

5.4 Implementation of the Equivalence Principle in FDTD

In an electromagnetic point of view the human body can be seen as an irregular, stratified, lossy, and frequency dependant dielectric object located in proximity of an antenna. An analytical approach to such electromagnetic problem is possible only after drastic simplification: in the human body (e.g: considering an homogenous cylindric of lossy material), and in the antenna (modeling ideal sources instead of real antenna structures). As highlighted in the previous chapter, if practical wearable antennas are considered in the on-body radio channel, a much higher spatial resolution is needed to accurately encounter small geometrical features in the antenna. In this thesis, to overcome this, a solution based on the equivalence principle is proposed. The proposed technique [15] begins with a division of the original problem into two sub-problems as shown in Fig. 5.8.

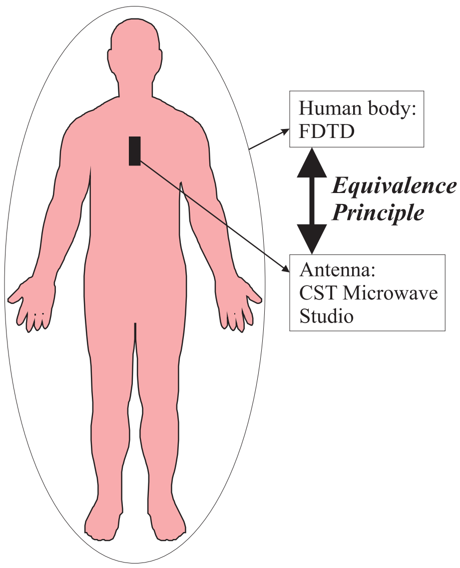

Figure 5.8: The numerical problem is split in two sub-problems: the antenna is analyzed in free space with CST Microwave Studio^{TM}, the human body is modeled with FDTD, the equivalence principle is used to interface the two computational domains.

The antenna is analyzed in free space using CST Microwave Studio^{TM}; near-fields on a closed surface surrounding the antenna are recorded. The human body is modeled in FDTD using the HUGO digital human phantom [16]. Near fields obtained from the CST simulation, are used as an input in the form of electrical and magnetic surface currents to the FDTD code [17].

5.4.1 Field Equivalence Principle: Huygen's Principle

The field equivalence principle is a principle by which actual source (e.g. an antenna) is replaced with equivalent sources. These virtual sources are said to be "equivalent within a region" because they produce the same fields of the original problem in that region. Such principle was introduced by Schelkunoff in 1936 [18], and is a rigorous formulation of Huygen's principle [19]. With this principle the fields outside an imaginary surface are obtained by placing over the closed surface suitable electric and magnetic current densities which satisfy the boundary conditions. This currents produce zero fields inside the surface, and outside they have to induce the same fields of the original problem. The formulation is exact, although it requires an integration over the closed surface, and the degree of accuracy depends on the knowledge of the tangential fields over the closed surface. In most applications the surface is chosen to be for most of it coincident with the metallic part of the structure, so that the tangential electric field is null, and the physical area of integration drastically decreases.

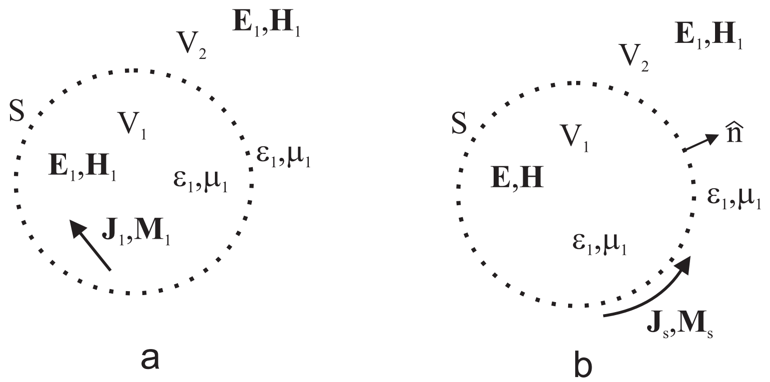

Figure 5.9: (a) Original problem; (b) equivalent problem

The equivalence principle is developed considering a radiating source $(\mathbf{J}_1, \mathbf{M}_1)$ which radiates fields $\mathbf{E}_1, \mathbf{H}_1$ everywhere as shown in Fig. 5.9(a). A closed surface S surrounding the source is chosen (shown dashed in Fig. 5.9(a)). The volume inside the surface is denoted from V_1, while V_2 is the volume outside S. The task is to replace the original problem, by an equivalent one producing the same fields $\mathbf{E}_1, \mathbf{H}_1$ in V_2. An equivalent problem is shown in Fig. 5.9(b). The original sources $(\mathbf{J}_1, \mathbf{M}_1)$ are removed, and it is assumed that there exist fields $\mathbf{E}, \mathbf{H}$ inside S, and $\mathbf{E}_1, \mathbf{H}_1$ outside. These fields to exist must satisfy the boundary conditions on S, thus on the boundary must exist the equivalent sources:

$$\mathbf{J}_s = \hat{n} \times (\mathbf{H}_1 - \mathbf{H}) \tag{5.3}$$

$$\mathbf{M}_s = (\mathbf{E}_1 - \mathbf{E}) \times \hat{n} \tag{5.4}$$

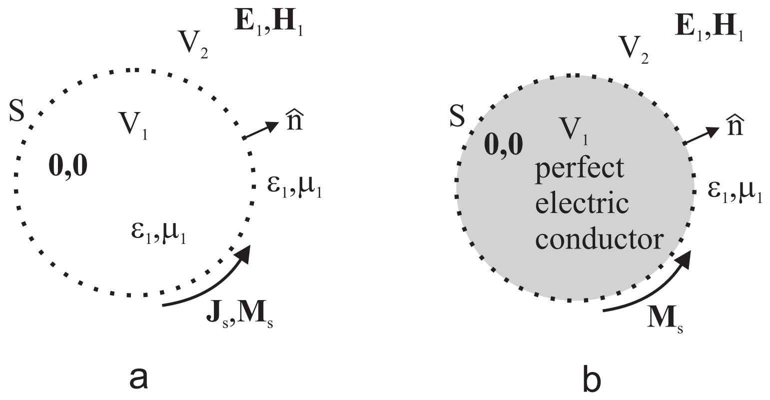

Figure 5.10: (a) Original problem; (b) equivalent problem

These surface currents are said to be equivalent only within V_2, because they produce the equivalent fields only outside S. Since the fields $\mathbf{E}, \mathbf{H}$ within the surface can be anything (is not the region of interests), it can be assumed to be null as shown in Fig. 5.10(a). This form of the equivalence principle is known as Love's equivalence principle [20], and the equivalent currents are equal to:

$$\mathbf{J}_s = \hat{n} \times \mathbf{H}_1 \tag{5.5}$$

$$\mathbf{M}_s = \mathbf{E}_1 \times \hat{n} \tag{5.6}$$

Since the value of the fields within S are null, cannot be disturbed if the medium property are changed. If we assume to fill S with perfect electric conductor (PEC), the electric source $\mathbf{J}_s$, which is tangential to the surface, is short circuited from the PEC. Thus the equivalent problem become the one illustrated in Fig. 5.10(b), where only magnetic currents radiate. The final problem is the radiation of magnetic sources above of a perfect conductor object, which is analytically solvable only after approximation about the nature of the surface.

5.4.2 Description of the Numerical Technique

The numerical problem is divided into two: the antenna is first analyzed in free space with CST Microwave Studio$^{\text{TM}}$ and a virtual box surrounding the antenna is set (as shown in Fig. 5.11) at which near fields are sampled at the steady state for the desired frequency. Different from [17], in which indoor propagation scenarios were considered, the radiation pattern calculated with CST Microwave Studio$^{\text{TM}}$ cannot be directly applied to on-body propagation, the radiation pattern must be modified due to back-scattering and energy absorption when the antenna is placed close to the human body. The distance *d* (as shown in Fig. 5.11) represents the spacing between the antenna and the human body, hence its value has to be small when the antenna is body-worn, and it depends on the FDTD spatial discretization. Secondly, the recorded field components are converted into surface currents, to be used as an excitation source for the FDTD code [21] to evaluate on-body antennas and radio channels.

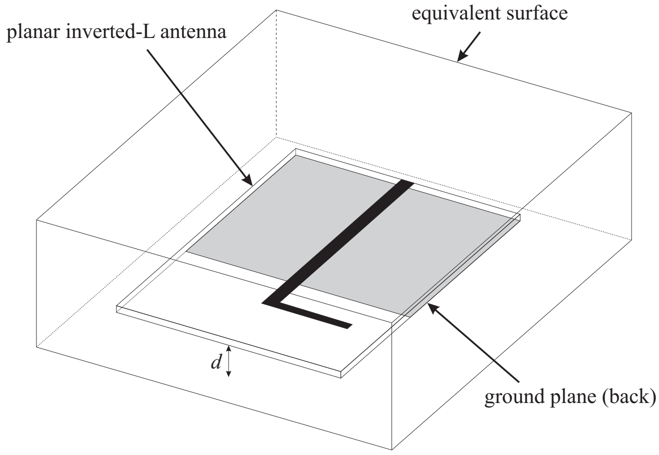

Figure 5.11: Equivalent surface surrounding the antenna: fields on this box are recorded; the distance d between the antenna and the face of the box in proximity of the human body has to be small.

FDTD Formulation with the Equivalence Principle

The FDTD is based on a direct solution to Maxwell curl equations where the differential operator is approximated with the central finite differences:

$$\begin{cases} \nabla \times \mathbf{E} = -\mu \dfrac{\partial \mathbf{H}}{\partial t} - \mathbf{M} \\ \nabla \times \mathbf{H} = \varepsilon \dfrac{\partial \mathbf{E}}{\partial t} + \sigma \mathbf{E} + \mathbf{J} \end{cases} \tag{5.7}$$

where $\mathbf{E}, \mathbf{H}$ are electric and magnetic fields, μ is the permeability, ε the permittivity, $\mathbf{J}, \mathbf{M}$ are electric and magnetic current density, and σ is the electric conductivity. The fields on the equivalent surface, calculated with CST Microwave studio$^{\text{TM}}$, are converted in surface currents using the relations:

$$\mathbf{J} = \widehat{n} \times \mathbf{H} \tag{5.8}$$

$$\mathbf{M} = \mathbf{E} \times \widehat{n} \tag{5.9}$$

where $\widehat{n}$ is the normal vector to the surface. The electric surface currents **J** are used to update the electric field, while the magnetic surface currents **M** are used to update the magnetic field as explained in [21]. Example iteration equations for electric and magnetic fields can be found in (5.10)-(5.14). i, j, k indicate the position on the spatial grid, the superscript n represents the time step index, $\Delta x, \Delta y, \Delta z$ are the spatial discretization along x, y, and z directions respectively, and Δt is the time step. For the electric field:

$$\begin{aligned} E_x^{n+1}(i,j,k) = C(i,j,k)E_x^n(i,j,k) + \\ +K_y(i,j,k)[H_z^{n+1/2}(i,j+1,k) - H_z^{n+1/2}(i,j,k)] + \\ +K_z(i,j,k)[H_y^{n+1/2}(i,j,k) - H_y^{n+1/2}(i,j,k+1)] - \\ -(\Delta t/\varepsilon_0)J_x^{n+1/2}(i,j,k) \end{aligned} \tag{5.10}$$

$$C(i,j,k) = \frac{1 - \frac{\Delta t \sigma(i,j,k)}{2\varepsilon_0 \varepsilon_r(i,j,k)}}{1 + \frac{\Delta t \sigma(i,j,k)}{2\varepsilon_0 \varepsilon_r(i,j,k)}} \tag{5.11}$$

$$K_m(i,j,k) = \frac{\frac{\Delta t}{2\varepsilon_0 \varepsilon_r(i,j,k)}}{1 + \frac{\Delta t \sigma(i,j,k)}{2\varepsilon_0 \varepsilon_r(i,j,k)}} \frac{1}{dm} \tag{5.12}$$

with $m = x, y$, or z.
And for the magnetic field:

$$\begin{aligned} H_x^{n+1/2}(i,j,k) = H_x^{n-1/2}(i,j,k) + \\ +Q_y(i,j,k)[E_z^n(i,j-1,k) - E_z^n(i,j,k)] + \\ +Q_z(i,j,k)[E_y^n(i,j,k) - E_y^n(i,j,k-1)] + \\ +(\Delta t/\mu_0)M_x^n(i,j,k) \end{aligned} \tag{5.13}$$

where:

$$Q_m = \frac{\Delta t}{\mu_0 dm} \tag{5.14}$$

with $m = x, y$, or z.

Total-Field/Scattered-Field Implementation

In the classic Equivalence Principle, for the exterior region, only far field information is of interest, and hence the equivalent surface currents are set only to radiate outwards the enclosed surface, and both the electric and magnetic fields inside the surface are always assumed to be zero. However, if the surface current source radiates in proximity of an object (e.g. the human body), the usual condition that sets zero fields inside the equivalent surface prevents the reflected field entering the surface, hence causing inaccuracy in FDTD simulations. To alleviate such a problem, we apply the total-field/scattered-field method within two different FDTD domains:

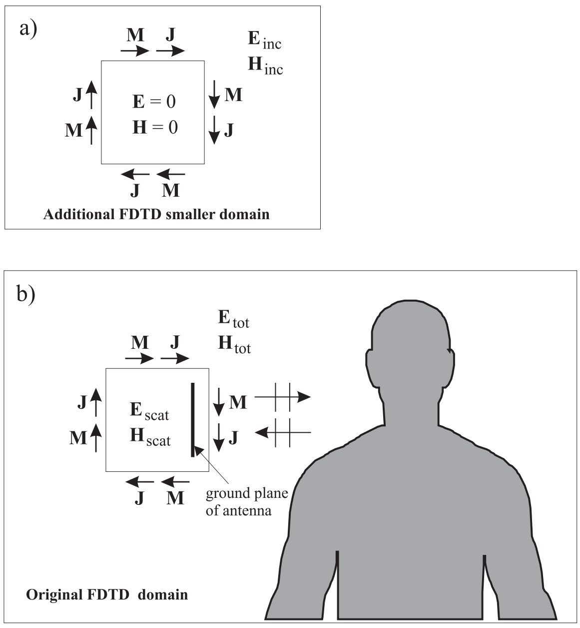

Figure 5.12: (a) Additional smaller FDTD domain: equivalent currents radiate in the free space; (b) Original FDTD domain: radiation of equivalent sources in presence of the human body.

- Domain A (see Fig. 5.12(a)) containing only the equivalence surface in the free space.

- Domain B (see Fig. 5.12(b)) where surface currents radiate in the presence of the human body.

For both cases, the box size and current density of the virtual source are same. Inside one iteration, the following operations are implemented:

1. Fields are updated in the Domain A. The equivalent currents ($\overline{J}, \overline{M}$) only radiate outwards the surface, and electric and magnetic fields are forced to zero inside the equivalent surface (as shown in Fig. 5.12(a)), in order to calculate the incident field components ($\overline{E}_{inc}, \overline{H}_{inc}$).

2. Fields are updated in Domain B. The equivalent currents ($\overline{J}, \overline{M}$) radiate outwards and inwards the equivalent surface. The fields obtained ($\overline{E}_{tot}, \overline{H}_{tot}$) are a combination of incident fields (radiation of the equivalent currents) and back-scattered fields from the human body ($\overline{E}_{scat}, \overline{H}_{scat}$).

3. In the original domain, the electric field components on the surface boundary are modified according to the following relation:

$$\overline{E}_{scat} = \overline{E}_{tot} - \overline{E}_{inc}|_{\Omega} \tag{5.15}$$

   Where Ω represents the equivalent surface surrounding the antenna. At each time step, the electric field components, calculated from Domain A ($\overline{E}_{inc}$), are subtracted from the electric field components calculated in the Domain B ($\overline{E}_{tot}$) to allow only the back-scattered fields to propagate inside the equivalent surface. If there are no objects near the equivalent surface, the fields are zero inside hence the Equivalence Principle is satisfied.

Figure 5.13(b) shows the locations of one of the six faces of the equivalent surface, specifically, the one with its normal towards the outside surface $-\widehat{y}$. Such surfaces are aligned with the magnetic field components. In the Domain B, the electric field components (indicated by solid gray arrows in Fig.5.13(b)) are modified inside the surface with those values of the same components just outside the equivalent surface which are obtained from the simulation of Domain A. Only the field components tangential to the surface are required to be modified, for example, inside the surfaces normal to *x*-direction, E_y and E_z are modified; inside the surfaces normal to *y*-direction, E_x

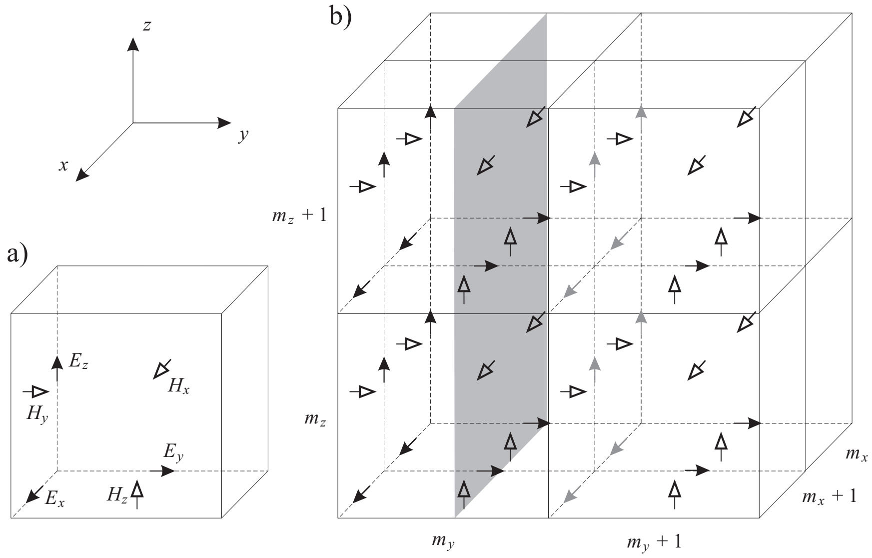

Figure 5.13: (a) Three-dimensional (3-D) FDTD lattice cell: solid arrows denote the electric field components and hollow arrows denote magnetic field components. (b) Demonstration of the total-field/scattered-field boundary for the Equivalence Principle. The shaded surface is the equivalent surface with normal $-\widehat{y}$ and the gray arrows indicate the modified electric field components on the surface.

and E_z are modified; and inside the surfaces normal to z-direction, E_x and E_y are modified.

Figure 5.14 shows the magnitude of the electric field considering the radiation of an inverted L antenna (see Fig. 5.20(a)) in proximity of the human body. In Fig. 5.14(a) fields are forced to zero inside the box; while in Fig. 5.14(b), back-scattered fields are considered inside the box as explained above.

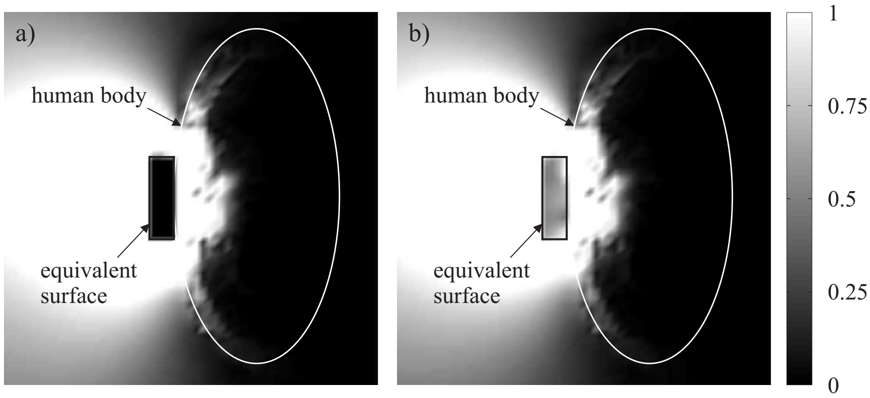

Figure 5.14: (a) Normalised magnitude of the electric field for the classic equivalence principle for the exterior problem; (b) Magnitude of the electric field considering the back scattered energy inside the equivalent surface.

To further increase numerical accuracy of the equivalence principle, multiple reflections between the body-worn antennas and human body has to be taken into account. For example, when a body-worn microstrip-fed antenna is characterized in the presence of a human body, a metallic sheet with the same size as the antenna ground plane is placed inside the equivalent box (see Fig. 5.12(b)). This would induce multiple reflections that are similar to those between the antenna and the body surface.

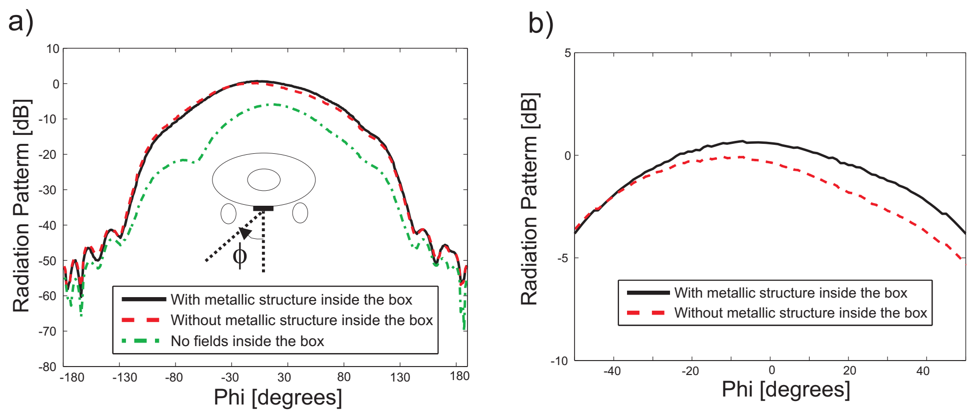

Figure 5.15: (a) Effect of the total-field scattered-field implementation on the on-body antenna radiation pattern. (b) Effect of modeling the antenna ground plane inside the equivalent box on the antenna pattern.

Figure 5.15(a) shows the importance of implementing the total-field scattered-field technique. It is noted that if the field is set to zero inside the equivalent surface (dash-dot line), large error is introduced in the calculation of the radiation pattern (about 15 dB). The introduction of a metallic sheet (representing the antenna ground plane) inside the box, causes a variation on the antenna pattern of around 1-2 dB (see Fig. 5.15(b)).

5.5 Wearable Antennas for 2.4 GHz ISM Band

Different planar antenna types are presented in this section and analysed to investigate the effect of human body presence on their characteristics. Although their dimensions are large compared to acceptable sizes for practical wearable devices, they provide an understanding of body effects on antenna operation and radio propagation modeling.

The antennas are numerically investigated using the equivalence principle based FDTD technique illustrated in the previous section. The human model applied is the commonly available HUGO male model developed by the US Air Force [16]. Figure 5.16 shows the permittivity and the conductivity values of the digital phantom sliced vertically at the frequency of 2.4 GHz.

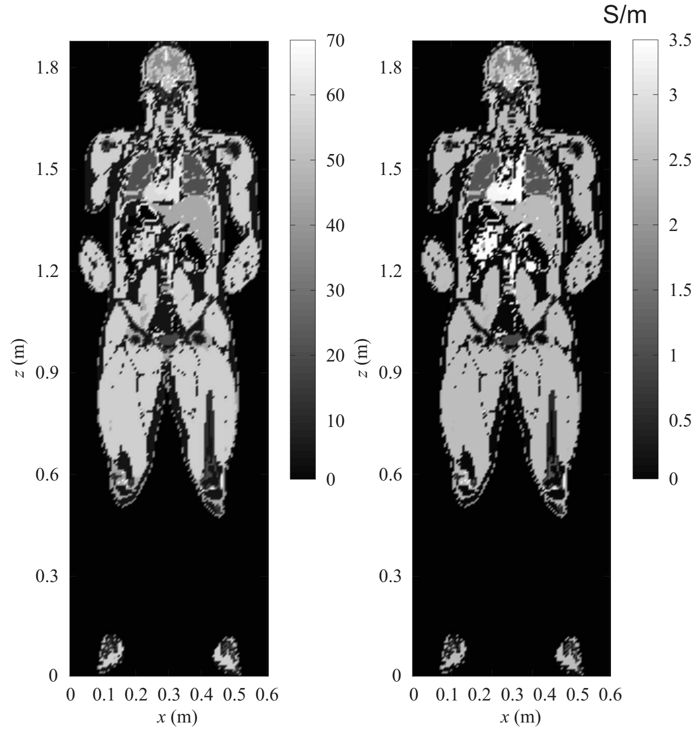

Figure 5.16: Permittivity and conductivity (respectively left and right) of the HUGO body model sliced vertically at 2.4 GHz.

FDTD simulations are carried out in 3D with a cell size $dx = dy = dz = 3$ mm. The radiation pattern has been evaluated in free space and in presence of the human body with the antenna placed in proximity of the body trunk (see Fig. 5.17). Radiation patterns calculated from the proposed method have been validated with measurement results.

5.5.1 Microstrip Patch Antenna

The antenna is a conventional rectangular patch which is printed on a RT/Duroid substrate of thickness $t = 1.5324$ mm and permittivity $\varepsilon_r = 3$. The patch is fed with a 50Ω transmission line and a quarter wavelength impedance transformer. Dimensions are given in Fig. 5.18(a). The reflection coefficients of the antenna in free space and on-body are shown in appendix B. Figures 5.18(b) and (c) show a good match between simulated and measured results in both of free space and on-body. The shielding

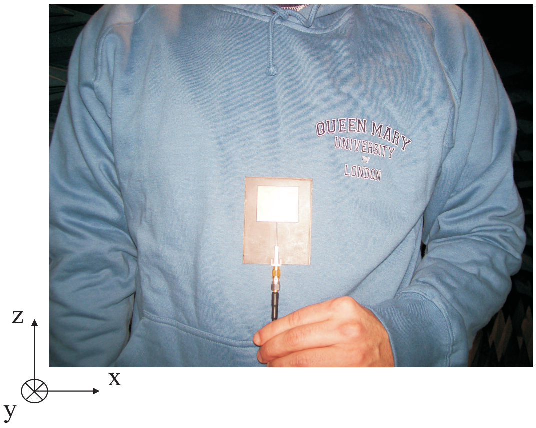

Figure 5.17: Position of the antenna for on-body measurements.

effect provided from the metallic ground plane minimize the absorption of the energy by the human body, and hence the on-body radiation pattern (Fig. 5.18(c)) is slightly distorted from that in free space (Fig. 5.18(b)).

5.5.2 Planar Monopole Antenna

The planar monopole is printed on a board with a thickness of $t = 1.6$ mm and permittivity $\varepsilon_r = 4.6$. It has a microstrip line feed with impedance 50 Ω to guarantee a good match. The antenna dimensions are given in Fig. 5.19(a), and the reflection coefficients of the antenna (in free space and on-body) are shown in appendix B. Figures 5.19(b), 5.19(c), show the radiation pattern in free space and on-body respectively. The omni-directional pattern is strongly modified when the antenna is placed on-body. Differently from the microstrip patch, the small size of the ground plane does not provide full shielding, and hence the effect of the human body in terms of wave absorption and reflection is visible with a front-to-back ratio of around 30 dB as shown in Fig. 5.19(c). At 2.4GHz, the human tissues are very lossy, the energy present on the opposite side of the human body (respect to the antenna) is mainly propagating through creeping wave around the trunk.

5.5.3 Planar Inverted L Antenna

The inverted L antenna is a modified monopole (bent monopole) aiming for antenna size reduction and omni-directional radiation. The antenna is printed on FR4 board

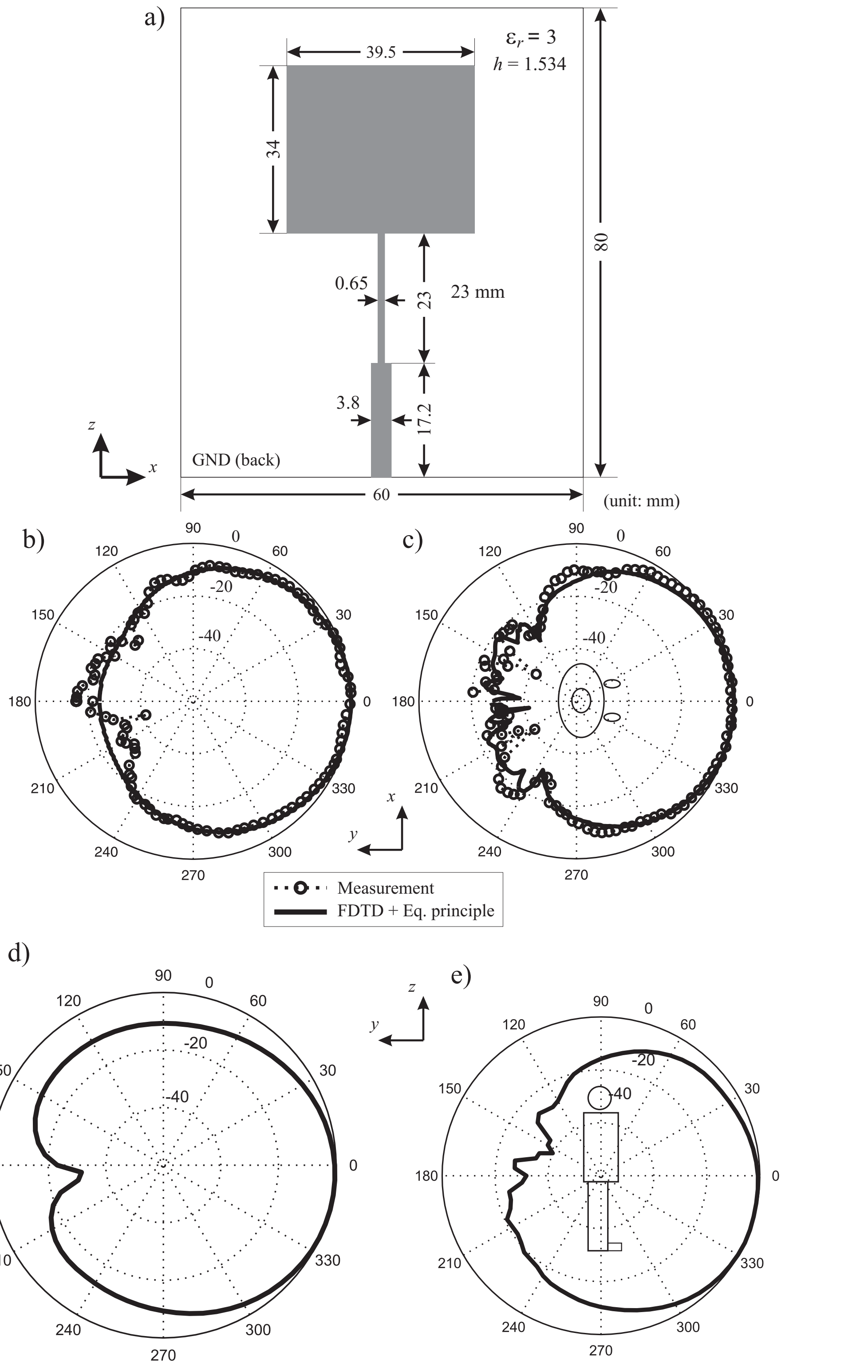

Figure 5.18: (a) Patch antenna and relative dimensions, (b) Comparison between simulated and measured radiation pattern on the azimuth plane in free space, (c) On-body radiation pattern on the azimuth plane; (d) Free space radiation pattern on the elevation plane; (e) On-body radiation pattern on the elevation plane.

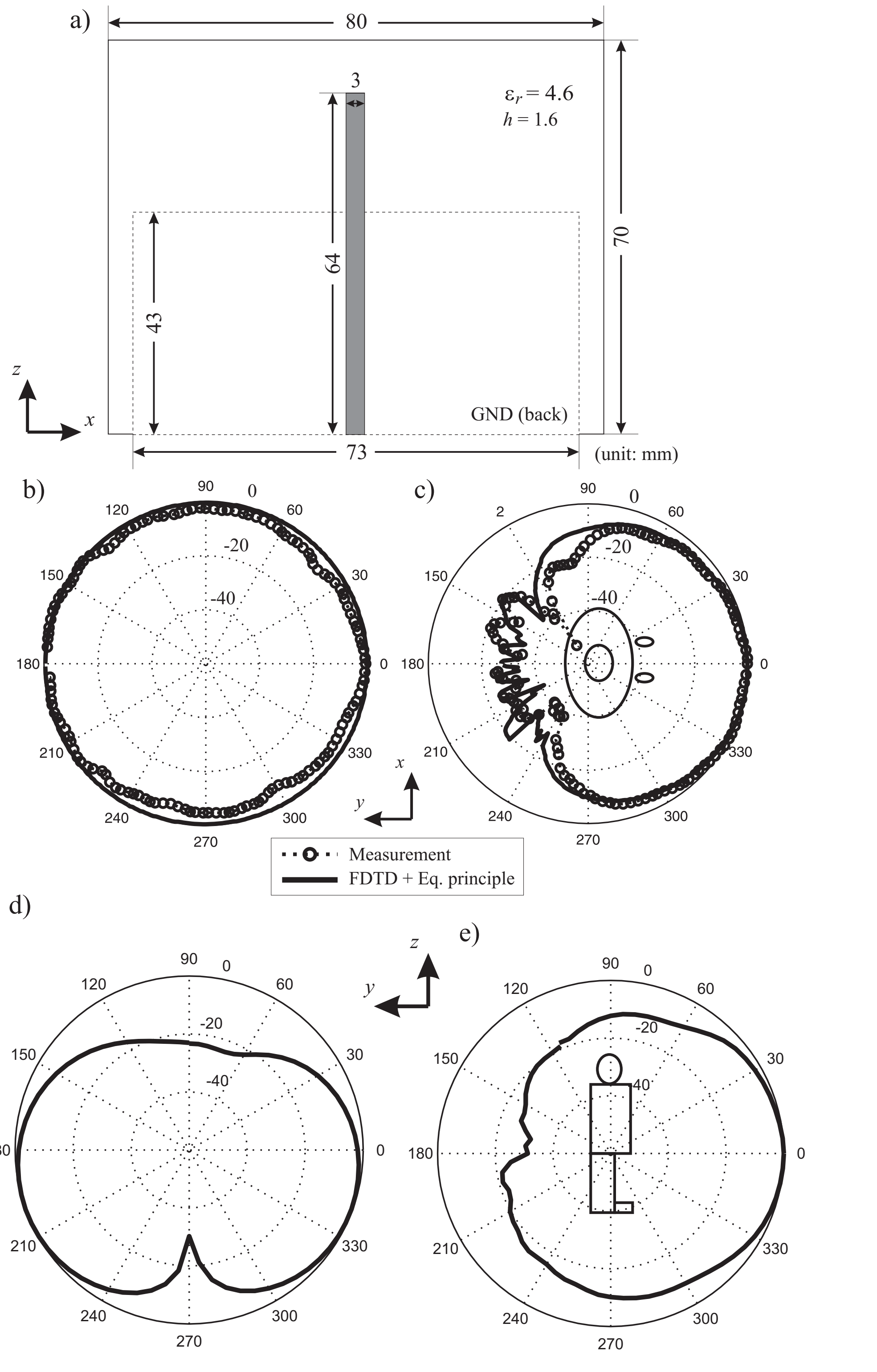

Figure 5.19: (a) Monopole antenna and relative dimensions; (b) Comparison between simulated and measured radiation pattern on the azimuth plane in free space; (c) On-body radiation pattern on the azimuth plane; (d) Free space radiation pattern on the elevation plane; (e) On-body radiation pattern on the elevation plane.

with substrate thickness $t = 1.6$ mm and permittivity $\varepsilon_r = 4.6$ and the antenna dimensions are given in Fig. 5.20(a). The reflection coefficients of the antenna in free space and on-body are shown in appendix B. Figures 5.20(b), and 5.20(c) show a good match between simulated and measured patterns. As for the planar monopole, the on-body distortion is significant, and the front-to-back ratio is around 30 dB (as shown in Fig. 5.20(c)). The use of a monopole like antenna (instead of a patch), increases the operational bandwidth, however, the high absorption from the human body reduce drastically the radiation efficiency (approximately 50% reduction [22]).

5.6 Effect of Different Antennas on the Path Loss Along the Body Torso.

The variation of the path loss with the communication distance is evaluated by placing the transmitting antenna on the bottom part of the trunk, and moving the receiver probe along the torso in various positions as shown in Fig. 5.21. The path loss for a communication link, can be modeled as a linear function of the logarithmic distance adopting (3.15).

In [23], a flat uniform dielectric phantom has been used to model the human body torso and the exponent γ has been estimated to be around $3.5-4$ at 2.4 GHz when transmitting and receiving antenna are both placed less than $\lambda/10$ away from the phantom. In reality, the human body torso presents a curvature along both the longitudinal and horizontal directions, and hence the use of flat or cylindrical uniform dielectric phantoms can lead to an inaccuracy in the estimation of path loss exponent. In [24], the path loss exponent was found to be $\gamma = 3.23$ for propagation along the torso. In this work, the effect of body-worn antenna types on the radiowave propagation along the torso is investigated adopting the previously described numerical code based on the equivalence principle. Figure 5.22 shows the simulated path losses with linear fitting curves. The slope of each line represents the path loss exponent γ, for three proposed body-worn antennas and for a Hertzian dipole (parallel to the body surface), respectively. Results have proven that the antenna radiation pattern has a significant influence on the on-body propagation channel as shown in table 5.6, in particular, it is possible

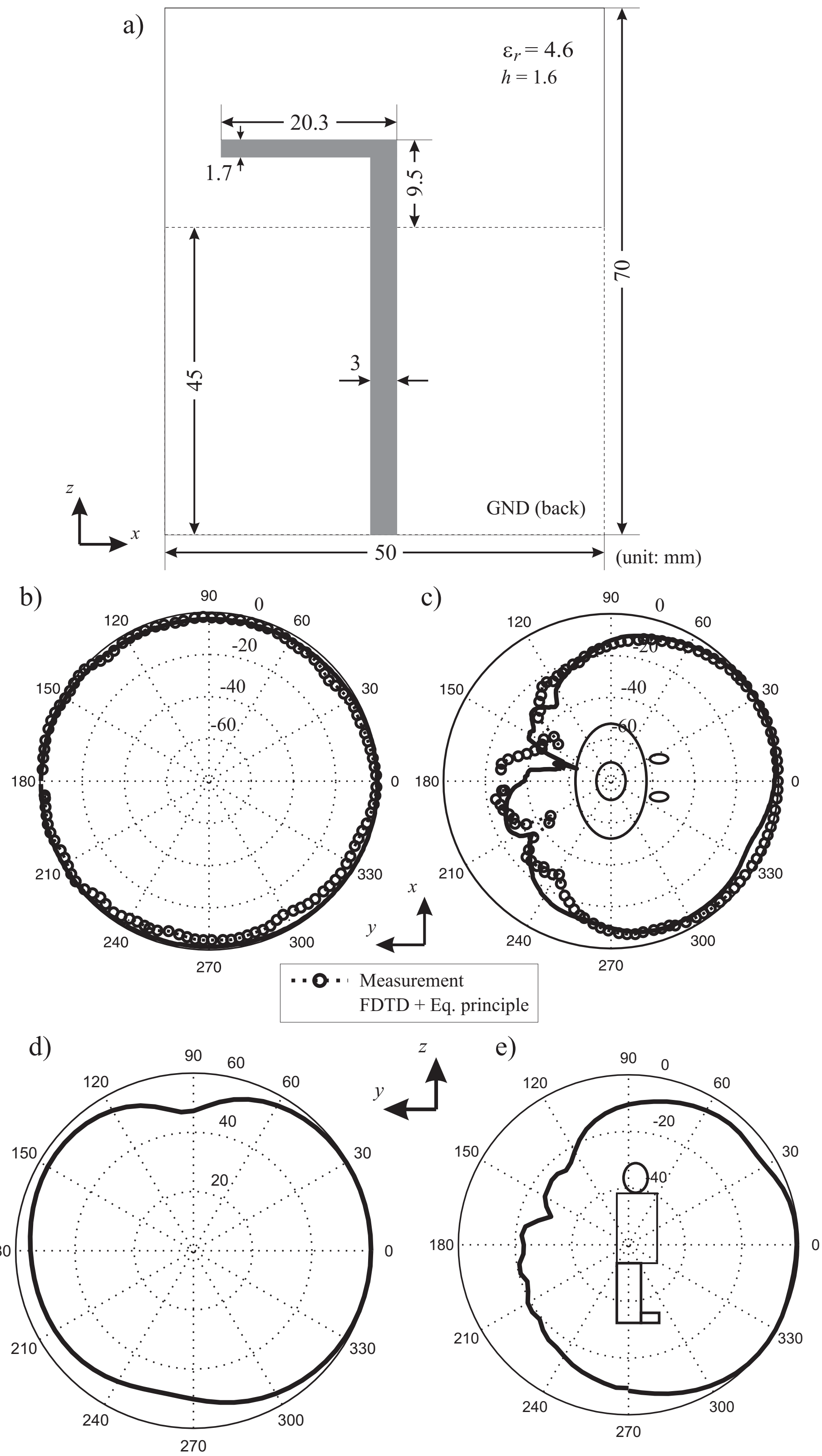

Figure 5.20: (a) Inverted L antenna and relative dimensions; (b) Comparison between simulated and measured radiation pattern on the azimuth plane in free space; (c) On-body radiation pattern on the azimuth plane; (d) Free space radiation pattern on the elevation plane; (e) On-body radiation pattern on the elevation plane.

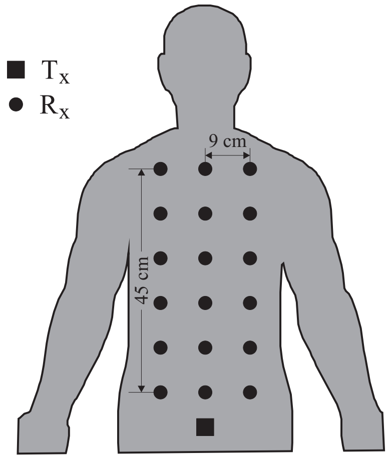

Figure 5.21: Proposed scenario: the transmitting antenna is placed on the bottom part of the trunk, the receiving probe is moved along the trunk.

to appreciate in Fig. 5.22 that the use of a more directive antenna for on-body communications produces path loss data more spread around the linear fit. For the setup proposed in Fig. 5.21 it is possible to consider the antenna radiation pattern as a function which weight the path loss, the more directive the antenna it is, the less the linear relation between $PL[dB]$ and $\log(d/d_0)$ is valid. Table 5.6 lists the simulated exponent γ, its values agree with the ones reported in [23]. The inverted L antenna is quite omni-directional in all planes and the exponent obtained is $\gamma = 3.6$, which is the closest to $\gamma = 3.9$, for the Hertzian dipole (parallel to the human body). The simulated path loss results for the monopole antenna (Fig. 5.22(b)) are the most spread around the average path loss (higher value of σ), as the antenna has a more directive beam on the elevation plane (plane $z - y$), and on the plane tangential to the body (plane $z - x$) if compared with the other two antennas.

Tx antenna	γ	σ [dB]
Rectangular Patch	3.29	4.5
Inverted L	3.62	4.9
Printed Monopole	4.25	6.6
Hertzian Dipole	3.90	4.7

Table 5.6: Calculated values of γ, and standard deviation σ of the normally distributed shadowing factor.

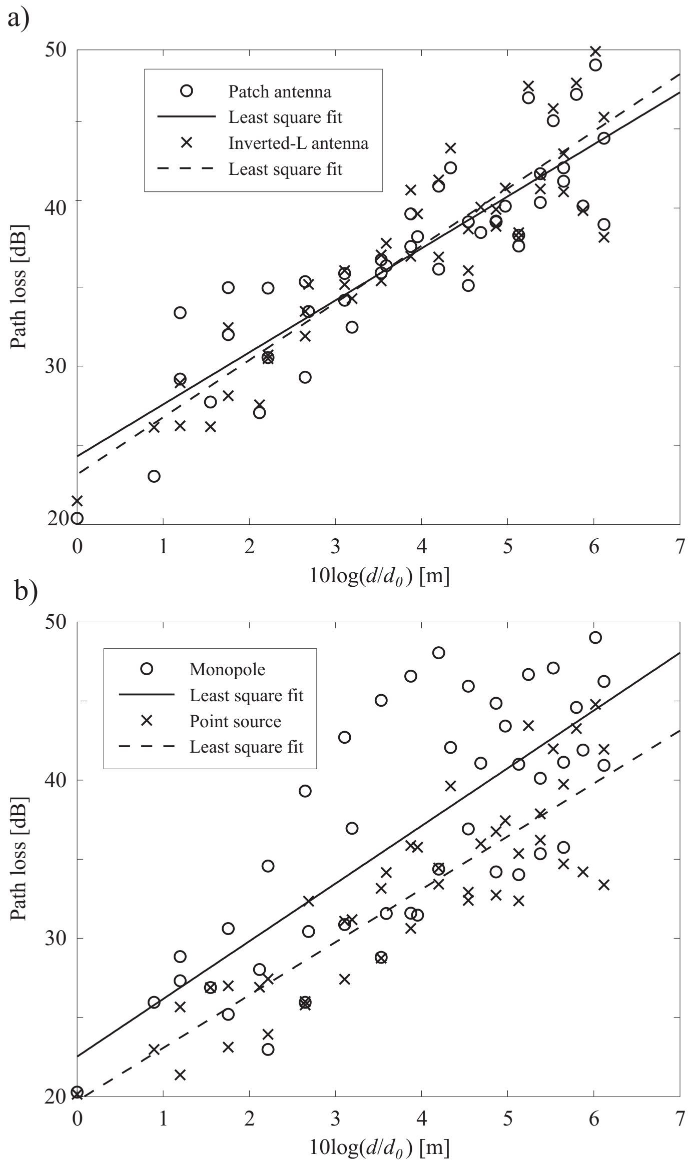

Figure 5.22: Variation of the path loss with the transmitter-receiver distance using different transmitting antenna: (a) Patch and Inverted L, (b) Monopole and Point Source.

5.7 Summary

Prediction of the received power in body-centric networks is of extreme importance for designing a power efficient system. With the increasing amount of computational resources available (such as computer clusters), is now possible to model the human body adopting numerical phantoms embedded in numerical electromagnetic solvers. The chapter introduced the numerical analysis of the on-body radio propagation adopting the FDTD technique. It was demonstrated that for on-body communications at 2.4 GHz, the internal composition of the human body does not play a major role, thus allowing the use of homogeneous digital phantoms for the analysis. When two nodes are located on the body, the body posture affects the propagation paths causing significative path loss variations. This was investigated by simulating eight representative scenarios, in which emphasis was given to the position of the arms. Results demonstrated that the changes in posture can lead to a significant variation (up to 30 dB) in the received power. The chapter also addressed the impact of different digital phantoms on the radio channel characterisitcs. Nine digital phantoms (five females and four males) obtained with MR scanning on real human candidates were considered, and the results demonstrated that different body sizes and shapes can lead to different path loss models, and hence to different system performance.

In the last part of the chapter, a technique for including the radiation characteristics of practical antennas on the on-body radio channel was presented. Since wearable antennas are small, in order to accurately encounter small features, a high spatial resolution is needed. This can be overcame by adopting the equivalence principle where the physical antenna is replaced by equivalent currents representing its radiation properties. The proposed technique has been applied to evaluate the impact of three different planar antennas on the radio channel.

References

[1] Y. Nechayev, P. Hall, C. C. Constantinou, Y. Hao, A. Owadally, and C. Parini, "Path loss measurements of on-body propagation channels," *in Proc.2004 International Symposium on Antennas and Propagation Sendai, Japan*, pp. 745–748, August 2004.

[2] A. Alomainy, Y. Hao, C. G. Parini, and P. S. Hall, "Comparison between two different antennas for UWB on-body propagation measurements," *IEEE Antennas and Wireless Propagation Letter*, vol. 4, no. 1, pp. 31–34, December 2005.

[3] A. Alomainy, Y. Hao, X. Hu, C. G. Parini, and P. S. Hall, "UWB on-body radio propagation and system modelling for wireless body-centric networks," *IEE Proceeding Communications Special Issue on Ultra Wideband Systems, Technologies and Applications*, vol. 153, no. 1, February 2006.

[4] P. S. Hall, Y. Nechayev, Y. Hao, A. Alomainy, M. R. Kanarudin, C. C. Constantinou, R. Dubrovka, and C. G. Parini, "Radio channel characterisation and antennas for on-body communications," *in Proc. Loughborough Antennas and Propagation Conference*.

[5] Y. Hao, A. Alomainy, P. S. Hall, Y. I. Nechayev, C. G. Parini, and C. C. Constantinou, "Antennas and propagation for body centric wireless communications," *IEEE/ACES International Conference on Wireless Communications and Applied Computational Electromagnetics, Honolulu, Hawaii*, 3-7 Apr. 2005.

[6] A. Alomainy, Y. Hao, A. Owadally, C. G. Parini, Y. I. Nechayev, C. C. Constantinou, and P. S. Hall, "Statistical analysis and performance evaluation for on-body radio propagation with microstrip patch antennas," *IEEE/ACES International Conference on Wireless Communications and Applied Computational Electromagnetics, Honolulu, Hawaii*, 3-7 Apr. 2005.

[7] A. Fort, C. Desset, J. Ryckaert, P. D. Doncker, L. V. Biesen, and P. Wambacq, "Characterization of the ultra wideband body area propagation channel," *International Conference on Ultra-WideBand, ICU'05, Zurich*, September 2005.

[8] X. Xu, T. Chao, and A. Bozkurt, "VIP-Man: an image-based whole-body adult male model constructed from color photographs of the visible human project for multi-particle Monte Carlo calculations," *Health Physics*, vol. 78, no. 5, p. 476, 2000.

[9] T. Nagaoka, S. Watanabe, K. Sakurai, E. Kunieda, S. Watanabe, M. Taki, and Y. Yamanaka, "Development of realistic high-resolution whole-body voxel models of japanese adult males and females of average height and weight, and application of models to radio-frequency electromagnetic-field dosimetry," *Phys. Med. Biol.*, vol. 49, no. 4, pp. 1–15, December 2003.

[10] C. Gabriel and S. Gabriel, "Compilation of the dielectric properties of body tissues at RF and microwave frequencies," 1999, www.brooks.af.mil/AFRL/HED/hedr/reports/dielectric/Title/Title.html.

[11] J. Kim and Y. Rahmat-Samii, "Implanted antennas inside a human body: Simulations, designs, and characterizations," *IEEE Transactions on Microwave Theory and Techniques*, vol. 52, no. 8, pp. 1934–1943, August 2004.

[12] P. S. Hall and Y. Hao, *Antennas and Propagation for Body-Centric Wireless Communications*. Artech House, 2006.

[13] A. Fort, P. D. Doncker, and L. V. Biesen, "An ultra wideband channel model for communication around the body," *IEEE Journal on selcted area of comms*, vol. 24, no. 4, pp. 927–933, April 2006.

[14] "Binvox 3D mesh voxelizer," http://www.cs.princeton.edu/∼min/binvox/.

[15] A. Sani, Y. Zhao, A. Alomainy, Y. Hao, and C. Parini, "An efficient FDTD algorithm based on the equivalence principle for analyzing on-body antenna performace," *IEEE Transactions in Antenna and Propagation*, vol. 57, no. 4, pp. 1006–1014, 2009.

[16] National Institute of Health National Library of Medicine (USA) Board of Regents, Bethesda, MD, Technical Report NIH 90-2197,1990,, "Electronic imaging: Board of regents," *http://www.brooks.af.mil/AFRL/HED/hedr/*.

[17] Y. Zhao, Y. Hao, and C. G. Parini, "FDTD characterization of UWB indoor radio channel including frequency dependant antenna directivities," *IEEE Antennas and Wireless Propagation Letters*, vol. 6, pp. 191–194, 2007.

[18] A. Schelkunoff, "Some equivalence theorems of electromagnetics and their applications to radiation problems," *Bell Syst. Tech. J.*, vol. 15, pp. 92–112, 1936.

[19] C. Huygens, "Traite de lumiere," Leyden,1960.

[20] A. E. H. Love, "The integration of the equations of propagation of electric waves," *Philos. Trans. R. Soc. London, Ser.*, vol. 197, pp. 1–45, 1901.

[21] L. Talbi and G. Y. Delisle, "Finite difference time domain characterization of indoor radio propagation," *PIER 12*, pp. 251–275, 1996.

[22] A. Alomainy, "Antennas and radio propagation for body-centric wireless networks," Ph.D. dissertation, Queen Mary, University of London, 2007.

[23] L. Roelens, S. V. den Bulcke, W. Joseph, G. Vermeeren, and L. Martens, "Path loss model for wireless narrowband communication above flat phantom," *IET Electronics Letters*, vol. 42, no. 1, 5th Jan. 2006.

[24] E. Reusens, W. Joseph, G. Vermeeren, and L. Martens, "On-body measurements and characterization of wireless communication channel for arm and torso of human," *4th International Workshop on Wearable and Implantable Body Sensor Networks (BSN 2007), Aachen, Germany*, 264-269.

Chapter 6

Ultra Wide-Band for Body-Centric Wireless Communications

The UWB technology has attracted much attention and experienced considerable growth over the past few years. In 2002, the Federal Communication Commission (FCC) [1] has allocated the spectrum from 3.1 to 10.6 GHz for unlicensed UWB communication applications. One of the most promising areas of UWB applications is the body-centric wireless communication, where the wireless connectivity between body-centric units is provided through the deployment of light-weight and compact UWB antennas [2–4]. The chapter presents the analysis of two planar UWB antennas for wearable applications, discussing their radiation characteristics, and their ability in preserving the pulse shape. In particular, a miniaturised tapered slot antenna (TSA) is proposed. Such an antenna shows a significant size reduction and improved time delay behavior making it an ideal candidate for UWB-BCWC systems. Experimental characterisation of the UWB on-body radio channel parameters including different antennas was performed, and the effect of the movements of the body was addressed. The presented results can be used to predict the performance of UWB wireless systems for body-centric applications.

6.1 UWB Wearable Antennas

In a UWB radio system, the antenna plays a more important role than it does for a conventional narrow-band system. In such a system, the antenna behaves like a filter in both spatial and frequency domains and tends to introduce signal distortion and degradation [5, 6]. Unlike its narrow-band counterpart, the design of a UWB antenna is determined not only by its return loss characteristics but also by its ability to preserve the pulse shape as it employs the unorthodox carrier-free modulation in impulse radio systems. Antennas for UWB systems are required to have very broad impedance bandwidths, stable and constant channel transfer responses. Ordinary wide-band antennas will cause distortion to transmitted short pulses since they radiate various components from different parts and hence experience sever frequency-dependent changes in their phase centers, e.g. log-periodic and spiral antennas [7, 8]. Any strong resonance at any frequency of the UWB antenna response causes large group delay variation and thus causes distortion in the pulse shape which in turn affects the pulse fidelity factor of the antenna performance. In this analysis, a novel miniaturised coplanar waveguide (CPW) fed tapered slot antenna (TSA) for ultra-wideband applications [9] is proposed in addition to a modified CPW-fed planar inverted cone antenna (PICA) for cross-referencing [10, 11].

6.1.1 Planar Inverted Cone Antenna

The CPW-fed PICA [10–12] consists of two elements; the top element (planar cone) and bottom rectangular-shaped ground plane (incorporating a CPW feed), Fig. 6.1. The antenna is fabricated on RT/Duroid substrate with thickness h=1.524 mm, relative permittivity ε_r=3, and loss tangent $\tan(\delta)$=0.0013. The total size of the antenna is 47.5$\times$ 50 mm^2 which is around $0.48\lambda_0 \times 0.5\lambda_0$ in electrical length, where λ_0 is the free space wavelength at 3 GHz.

The return loss response of the PICA is shown in Fig. 6.2. The figure illustrates that the antenna has excellent impedance matching across the UWB band with reflection coefficient below -10 dB in the band 3 - 12 GHz. For the on-body measurements, the antenna is located on the center of the trunk, and it is placed directly on a tight cotton jumper worn by the human subject, with a thickness of around 3 mm and material

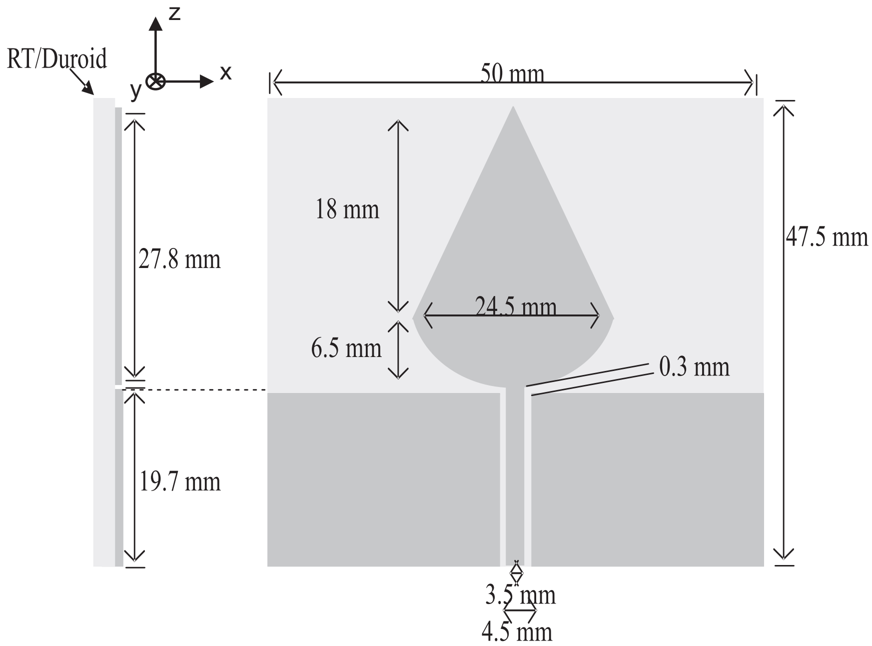

Figure 6.1: Dimensions and geometry of the designed CPW-fed planar inverted cone antenna (PICA) [10–12]

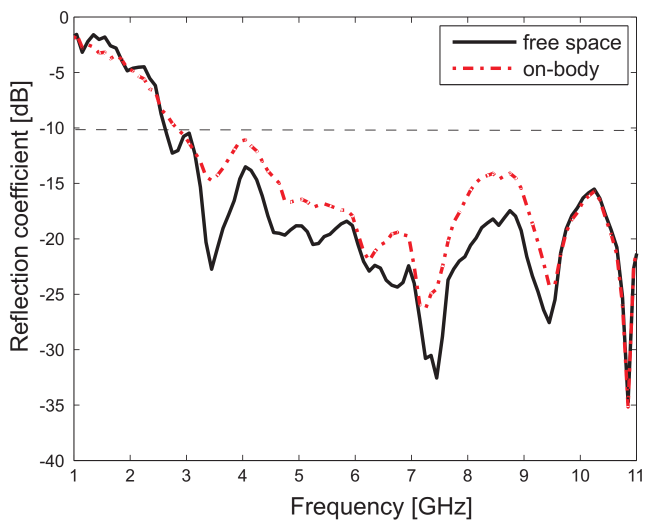

Figure 6.2: Measured return loss of both proposed antennas; on-body measurements were done placing the antenna on a tight cotton jumper with a thickness of 3mm worn by the human subject and oriented with radiating elements (XY plane) parallel to the body and facing outward.

permittivity of around 1.6; the main radiating elements ($x-y$ plane) are parallel to the human body and facing outward. As shown in Fig. 6.2 antenna has a good impedance matching even when placed on the human body.

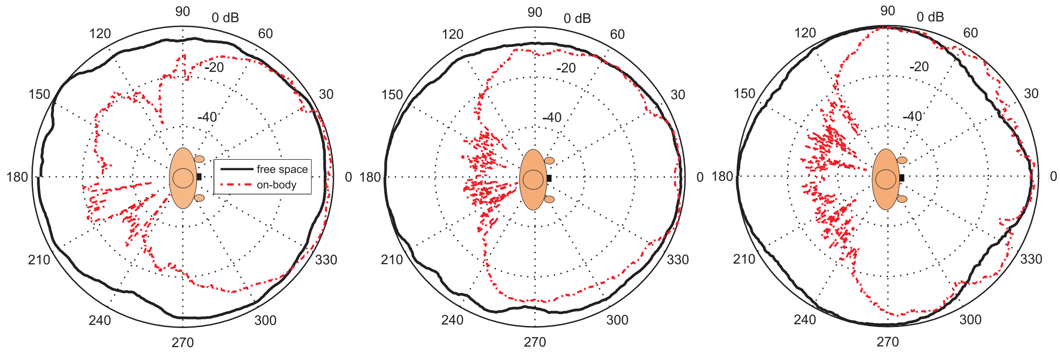

(a) plane $x-y$ at 3 GHz (b) plane $x-y$ at 6 GHz (c) plane $x-y$ at 9 GHz

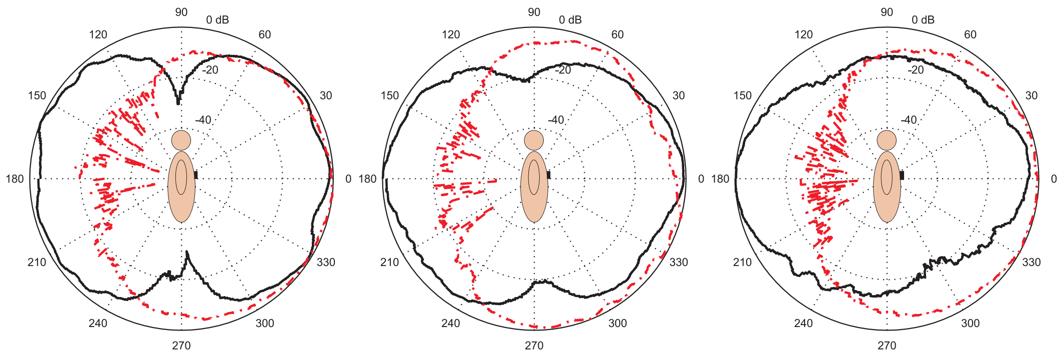

(d) plane $y-z$ at 3 GHz (e) plane $y-z$ at 6 GHz (f) plane $y-z$ at 9 GHz

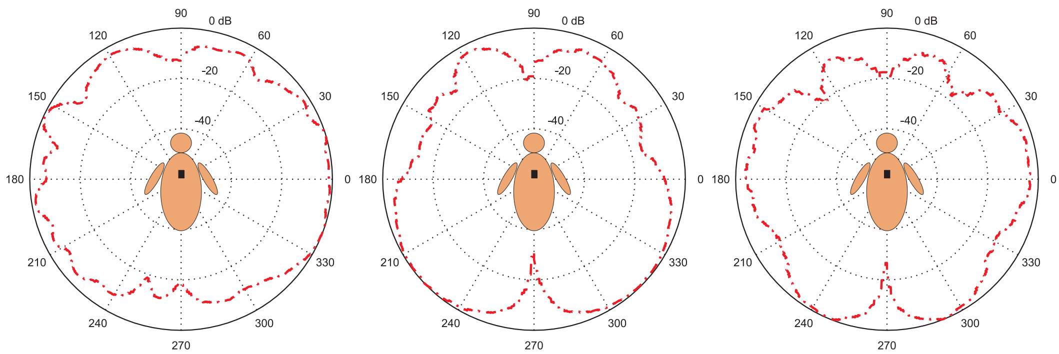

(g) plane $x-z$ at 3 GHz (h) plane $x-z$ at 6 GHz (i) plane $x-z$ at 9 GHz

Figure 6.3: Normalised radiation patterns of the PICA in free space (black solid line) and on-body (red dash-dot line).

The radiation patterns have been measured at 3, 6, and 9 GHz, and the results show a monopole like pattern across the whole frequency band (see Fig. 6.3). In free space, the pattern is reasonably omnidirectional on the azimuth plane ($x-y$ plane), but it presents a null along the z direction, suggesting that the orientation of the antenna needs to be adapted to the context.

The on-body radiation performance is also investigated by placing the antennas on the center of the human trunk and repeating the pattern measurements for the specified frequencies as shown in Fig. 6.3. Due to the presence of the lossy human body tissues (with increased conductivity at high frequencies), the omni-directional radiation pattern is distorted, and the antenna front-to-back ratio is significantly increased to 25-40 dB. Furthermore, the presence of the body makes the radiation pattern more stable across the UWB frequency band. The gain has been simulated for the antenna in free space, and when placed on a homogeneous phantom made of muscle. A two-pole Debye model has been used to represent the frequency dispersion of the muscle tissues across the UWB frequency band (as explained in 4.3.1). Figure 6.4 shows the peak gain of the PICA as a function of the frequency. In free space, the gain ranges from 2.7 to 5 dBi. While in free space the peak gain is always in broadside direction (x=0 and z=0), when the antenna is body-worn, the wave reflected from the body may be recombined in phase with the direct one in a different direction, and hence the direction of the peak gain changes with frequency and it is slightly tilted with respect to the free space case. When placed on the body, the directivity of the antenna increases because the wave is reflected from the body, while the efficiency decreases due to tissue absorption. The peak gain increases respect to the free space case, and it ranges from 2.8 to 7.8 dBi.

Pulse Fidelity

To investigate both frequency domain and transient antenna characteristics, the free space channel between two identical antennas set side-by-side (most appropriate setting for WBAN applications of the proposed printed antenna) and face-to-face is measured at different angular orientations, namely 0^0, 45^0 and 90^0, when the distance between the antennas is 50 cm as shown in Fig. 6.5.

The antennas are connected to a vector network analyser (Hewlett Packard 8720ES-VNA) to measure the transmission response (S21) with port I and port II of the VNA serving as transmit and receive nodes, respectively. Two cables of length 3 meters are used to connect the antennas to the analyser ports. Measurements have been done in

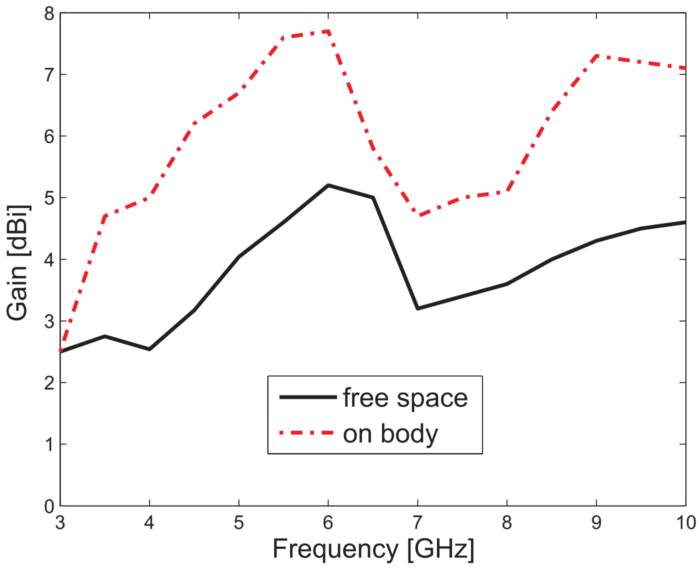

Figure 6.4: Simulated free space and on-body gain as a function of the frequency

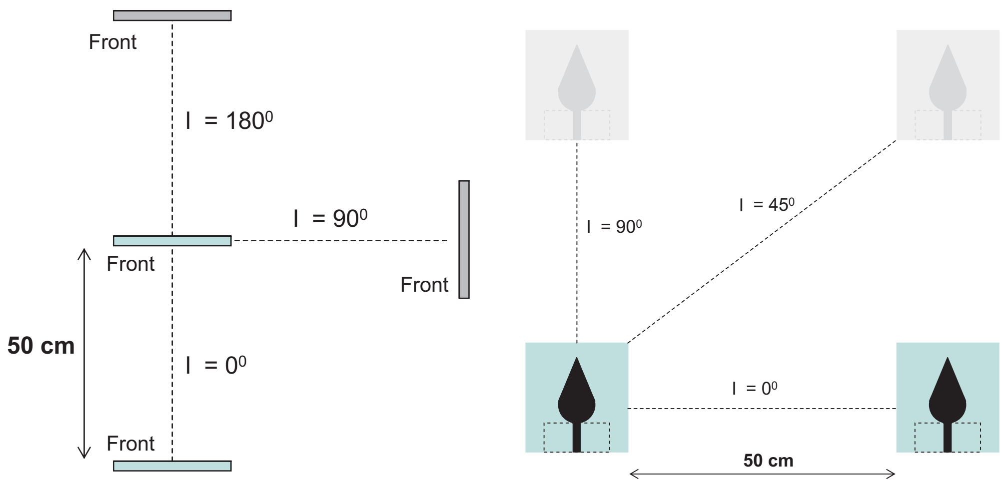

(a) Face-to-Face

(b) Side-by-Side

Figure 6.5: Antenna transfer functions measurement setup with two identical antennas (PICA and tapered slot antenna) in free space with distance of 50 cm between the antennas with different orientations

the anechoic chamber to eliminate multipath reflections from surrounding scatterers. The VNA is set on the response mode in the range 3-9 GHz with intervals of 3.75 MHz, at a sweep rate of 800 ms. Magnitude and phase of each frequency component are recorded.

In this study the chosen distance between the antennas is 0.5 meter which is 5 times the wavelength at the lower frequency in the band (3 GHz). Thus, the interaction between the antennas is minimal and most of the distortion in frequency channel responses is due to impedance mismatch and inherent radiation properties of the antenna. The time domain responses of the free space radio channel with the antennas are obtained by direct application of IFFT on the measured real frequency responses S_{21} [7].

In UWB communications, specifically impulse radio systems, a correlation between the transmitted or received waveform and a template is often used to assess how the system affects a waveform and quantify the level of pulse distortion. A fidelity parameter involving the cross-correlation between the time domain transmitted field and a template function is described by Lamensdorf *et al.* [13], and it was defined in eq. 3.3. For many applications, fidelity analysis is applied to investigate the preservation of pulse shape (not amplitude) with respect to space and time. Usually a pattern is defined which is simply the normalized correlation coefficient of the electric field with the template, as a function of direction [13–16].

The choice of template function is not restricted to a specific reference pulse or stringent requirements [15]. The template function in fidelity analysis can be the transmitted pulse, input pulse or transmitted pulse in a reference direction (usually maximum radiation density direction) and the latter is the case chosen in this study since the main interest is to evaluate the UWB antennas performance in space as part of the radio propagation channel (the whole system) [13–15]. The impulse response when both antennas are set face-to-face (maximum density direction at 0^0), Fig. 6.5(a) is set to be the template pulse. The correlation with pulses radiated and received at various angles is experimentally evaluated using two identical antennas [8, 16]. The aim of this analysis is to investigate the performance of the antenna as a spatial filter, however, as explained in section 3.2.1, the antenna is also acting as a time filter, thus distorting the transmitted pulse. To evaluate the performance of the antenna as a time filter, a time domain measurement setup (adopting a UWB pulse generator and a digital oscilloscope) is needed, and this is out of the scope of this thesis.

Figure 6.6(a) shows the impulse responses in the band 3 GHz to 9 GHz for the PICA case when the antennas are set side-by-side, as shown in Fig. 6.5(b). The fidelity values for the measured band are 91.25% and 82.98% for 45^0 and 90^0, respectively, with the response at 0^0 set as a reference. The results show good transient performance of the antenna at different orientations.

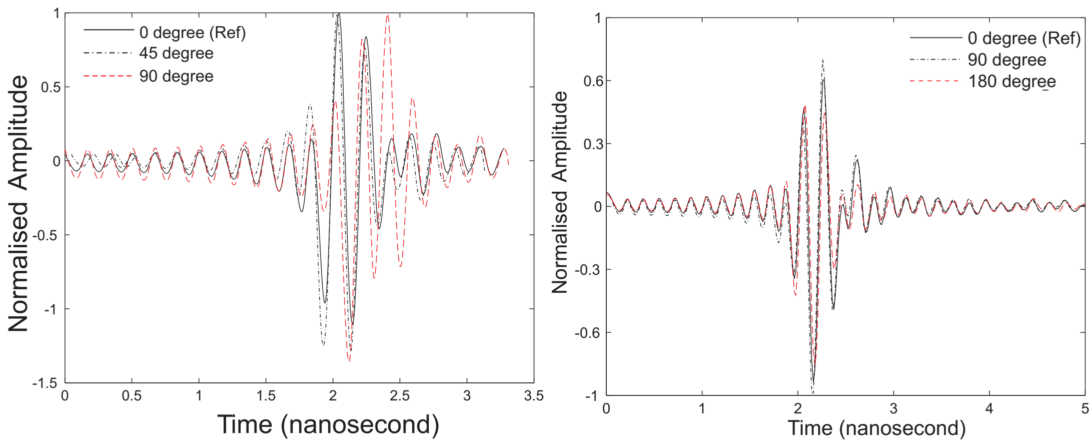

(a) Side-by-Side

(b) Face-to-Face

Figure 6.6: Normalised Impulse responses of the measured channel of two PICAs in the band 3GHz-9GHz at different angular orientations.

In addition, Fig. 6.6(b) shows face-to-face channel impulse responses at various angular directions for two PICAs. The fidelity of the system impulse response at different directions with reference to the response at 0^0 (when the antennas are facing each other) is 91.7% and 95.07% for 90^0 and 180^0, respectively. The antenna performance is also evaluated by comparing responses obtained for side-by-side and face-to-face configurations. Fidelity of 85.4% is obtained which is considerably sufficient performance for the proposed applications, considering the short communication distance between the body-centric network devices.

6.1.2 Tapered Slot Antenna

A far as the design of a UWB antenna is concerned, a broadband impedance matching network is needed and it can be achieved by employing two tapered radiating slots at the end of the CPW feeding line [17] by gradually varying the feed-gap [18] and with the help of a pair of tapered radiating slots [19]. A proposed tapered slot antenna (TSA) is proposed using a similar approach to [17]. The antenna is fabricated on RT/Duroid board (with parameters the same as those used for the PICA antenna), Fig. 6.7. The total antenna size is 27×16 mm^2 which is around $0.27\lambda_0 \times 0.16\lambda_0$ in electrical length, where λ_0 is the free space wavelength at 3GHz. The TSA is designed to allow for the smooth transition of line impedance. The ratio of semi-major to semi-minor axis within the design is the most significant parameter to affect the impedance matching [17].

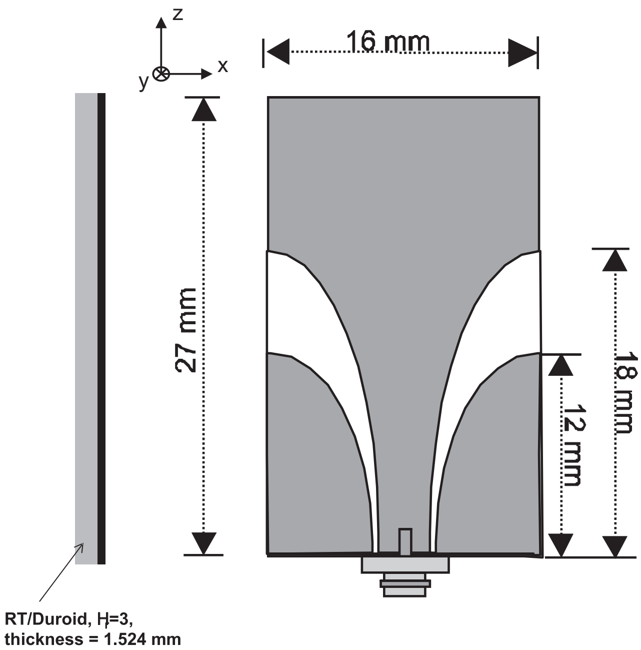

Figure 6.7: Dimensions and geometry of the designed CPW-fed tapered slot antenna (TSA).

The reflection coefficient of the TSA is below -10dB in the band 3 - 11.5 GHz as shown in Fig. 6.8. The antenna seems to preserve good impedance bandwidth even when placed on the human body with slight detuning in lower frequency band due to reduction in size and also absence of ground plane.

The radiation pattern has been measured at 3, 6, and 9 GHz (see Fig. 6.9). The free space radiation patterns are expected to be similar to the PICA ones. However, especially at the lower frequency, the radiation of the TSA seems to be more directional. The on-body radiation characteristics of the TSA are comparable to the PICA ones, apart from a slightly more directive pattern (especially on the $x - z$ plane).

Figure 6.10 shows the gain of the TSA as a function of the frequency. In free space,

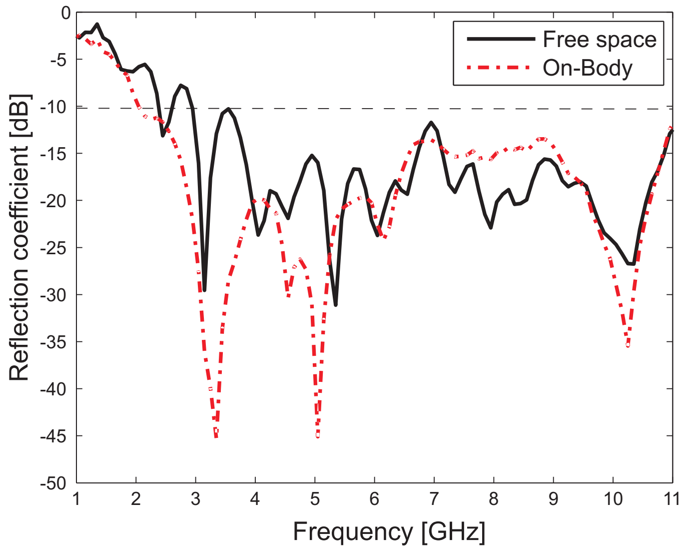

Figure 6.8: Measured return loss of the TSA antenna; on-body measurements are done placing the antenna on a tight cotton jumper with thickness of 3mm worn by the human subject and oriented with radiating elements ($x - y$ plane) parallel to the body and facing outward.

the gain ranges from 2.0 to 4.2 dBi, while on-body the values are in the range 2.8-7.5 dBi, and hence comparable with the values obtained for a bigger antenna such as the PICA. In free space, the peak gain is in broadside direction. However, as explained for the PICA case, the direction of the on-body peak gain is slightly tilted respect to the free space case.

Pulse Fidelity

Figure 6.11(a) shows the impulse responses in the band 3-9 GHz when the antennas are set side-by-side. The fidelity values for the measured band 3-9 GHz are 96.04% and 72.43% for 45^0 and 90^0, respectively, which are slightly degraded compared to those for the PICA, bearing in mind that the tapered slot antenna has a significant size reduction. As for the case of the PICA, the impulse response at various angular directions is analysed for two identical pairs facing each other with one antenna oriented as shown in Fig. 6.5(a). The fidelity of the impulse response at different directions (with reference to the response at 0^0 when the antennas are facing each other) is 91.06% and 95.35% for 90^0 and 180^0, respectively. Fidelity of 77.1% is obtained when comparing side-by-side and face-to-face scenarios.

Fidelity studies of commonly used antennas such as monopoles and resistively

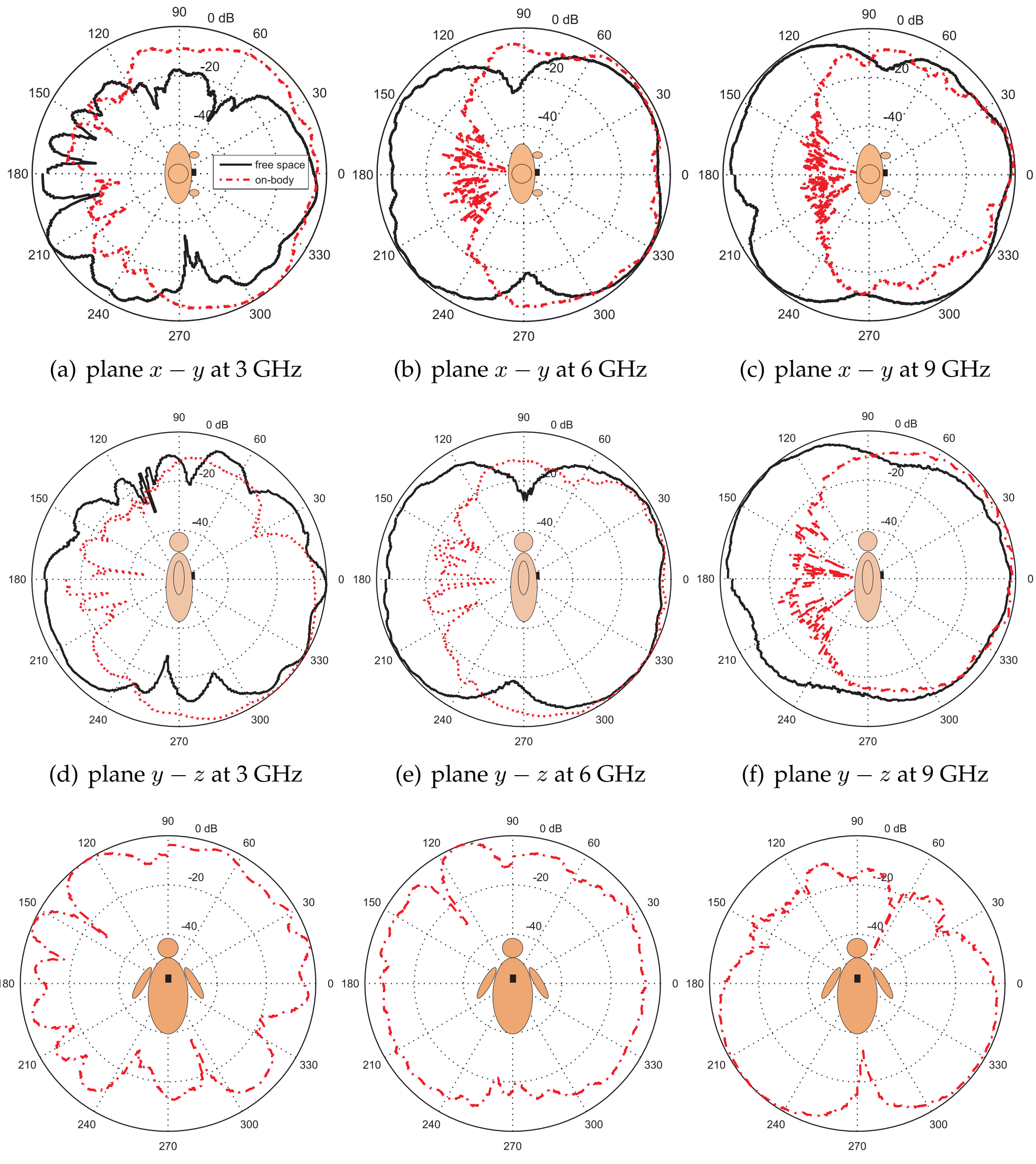

(a) plane $x - y$ at 3 GHz (b) plane $x - y$ at 6 GHz (c) plane $x - y$ at 9 GHz

(d) plane $y - z$ at 3 GHz (e) plane $y - z$ at 6 GHz (f) plane $y - z$ at 9 GHz

(g) plane $x - z$ at 3 GHz (h) plane $x - z$ at 6 GHz (i) plane $x - z$ at 9 GHz

Figure 6.9: Normalised radiation patterns of the TSA in free space (black solid line) and on-body (red dash-dot line).

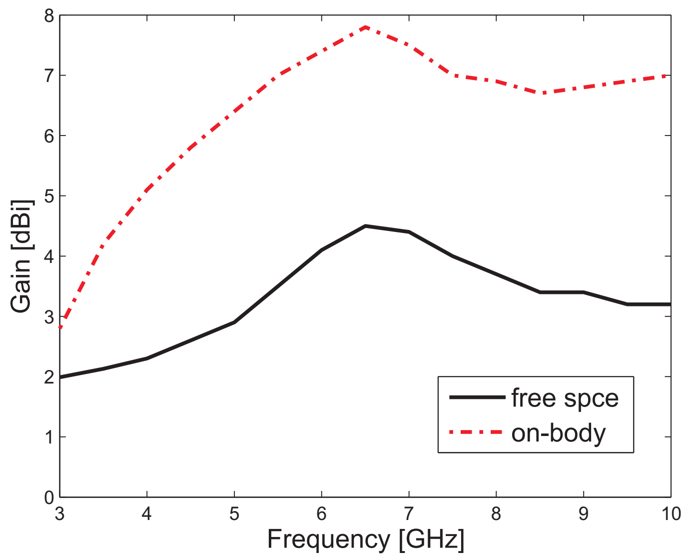

Figure 6.10: Free space and on-body gain as a function of the frequency.

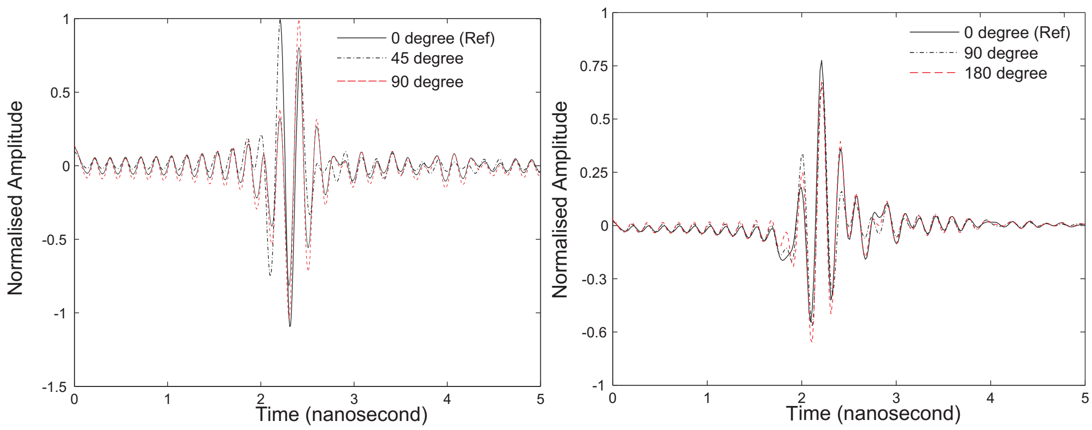

(a) Side-by-Side

(b) Face-to-Face

Figure 6.11: Normalised Impulse responses of the measured channel of two tapered slot antennas in the band 3GHz-9GHz at different angular orientations.

loaded dipoles presented in [13–16, 20] has shown that a spatially averaged fidelity factor as low as 70 % is often deduced. In wireless BAN specific study presented in [14], a value of 76-99% is derived for fidelity when numerically comparing input pulse to a transmitted pulse for various antenna types. This indicates that the acceptable minimum value for fidelity is application and environment specific. In the study presented here, the average values obtained for PICA and TSA (around 86%) is considered sufficient for the indoor body-centric wireless communication application when considering 99% of energy windowed pulse [14, 15]. In order to determine a specific threshold fidelity factor for generic application (or even for body-centric networks), further evaluations and more in depth system-level analysis is required. The TSA presents similar radiation characteristics compared with the PICA, with a significant size reduction that makes it an ideal candidate for BANs. However for on-body applications, the behavior of the antenna as a part of the on-body radio channel needs to be investigated.

6.2 Radio Propagation for UWB Body-Centric Wireless Networks in Indoor Environment

In order to characterise the UWB on-body radio channel, a frequency domain measurement setup is applied (see Fig.3.8(a)). Measurements are first performed in the anechoic chamber to eliminate multipath reflections from the surrounding environment, and then repeated in the Body-Centric Wireless Sensor Lab, located at Queen Mary, University of London to consider the effect of the indoor environment in the on-body radio propagation channel. The sensor lab (see Fig. 6.12) is a dense multipath environment including hospital and office furniture. The measurements are performed on an average sized male, with a height of 1.75 m and a weight of 73 Kg.

Figure 6.13 shows the location of the two antennas during the measurements, the transmitting one is placed on the left side of the belt, while the receiver is moved along the front part of the body. Thirty-three different positions are measured (on the chest, legs and arms) to ensure sufficient data collection for channel characterization and modelling. To eliminate the coupling effect between the two antennas we ensure a minimum distance of 10 cm between transmitting and receiving antenna (corresponding

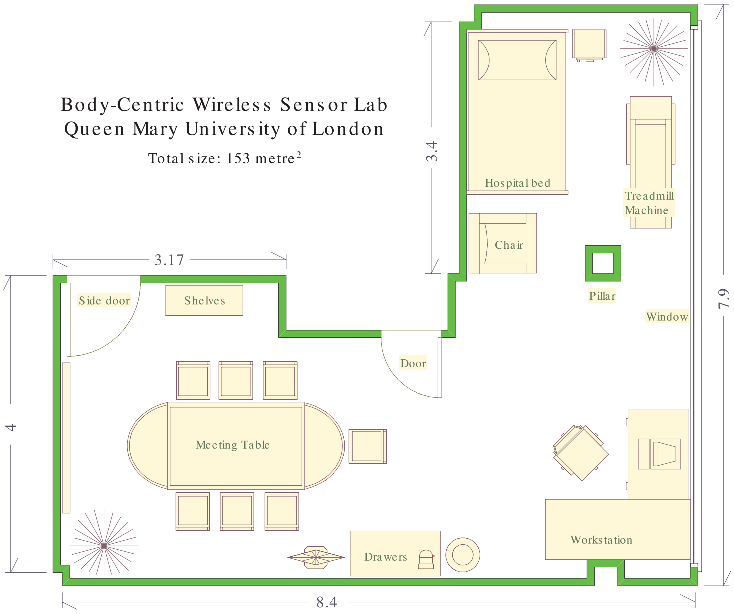

Figure 6.12: Layout of the Body-Centric Sensor Lab, at Queen Mary, University of London.

to one free space wavelength at the minimum frequency frequency of 3 GHz).

6.2.1 Path Loss Characterisation

The path loss, can be modeled as a function of the distance between transmitter and receiver using the eq. 3.17. A least square fit is performed on the measured data to evaluate the average path loss, and the path loss exponent is given by the slope of the curve obtained.

The exponent is 3.9 for the PICA and 3.0 for the TSA (see Fig. 6.14). When measurements are performed in the indoor environment, the reflections from the surrounding scatterers increases the received power, causing reduction of the path loss exponent. A reduction of 33% is experienced for the PICA case ($\gamma = 2.6$), and 13% for the TSA ($\gamma = 2.6$). The PICA having a more omnidirectional radiation than the TSA, is more affected from the multipath reflections, and the exponent reduction is more significant. The values of γ agree with the ones presented in [21], where it was found $\gamma = 3.3$ in free space, and $\gamma = 2.7$ in the office environment. The shadowing factor is a zero mean, normally distributed statistical variable and it takes into account of the deviation of the measurements from the calculated average path loss (see Fig. 6.15).

In the anechoic chamber the standard deviation of the normal distribution is $\sigma =$

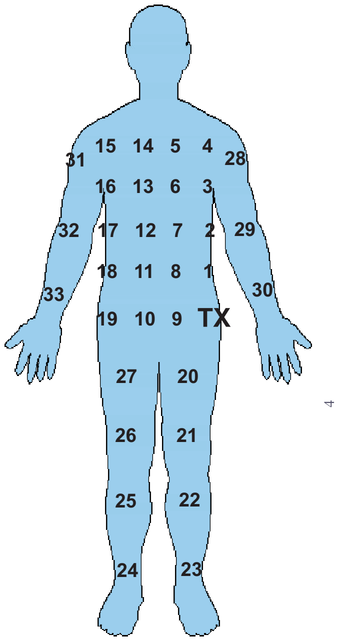

Figure 6.13: Location of the transmitting antenna and position of the 33 receiver.

6.8 for the PICA, and $\sigma = 8.2$ for the TSA. For the measurement setup proposed, the antenna radiation pattern is a function which weight the path loss: the more directive the antenna is, the more spread the data are, and this explains the higher value of σ for the TSA case. In the indoor environment, the values of σ are 8.0 and 6.7, respectively for PICA and TSA. In such scenarios, the reflections from surrounding scatterers are the main contributors to the deviation from the average path loss. This effect is more significant in the PICA case, where the radiation is more omni-directional.

6.2.2 Transient Characterisation

The time domain dispersion of the received signal strongly affects the capacity of UWB systems [22]. This effect is characterized by the first central moment (mean excess delay τ_m), and the square root of the second order central moment (root mean square τ_{RMS}) of the Power Delay Profile (PDP)

Channel impulse responses are calculated based on the measured frequency transfer functions which consist of 1601 frequency points using windowing and IDFT. The time domain results for both measurement sets are compared for evaluation. The time domain window can detect multipath signals separated up to 267 ns, with a resolution of 55 ps. Power delay profiles (PDP) are produced by averaging all impulse responses,

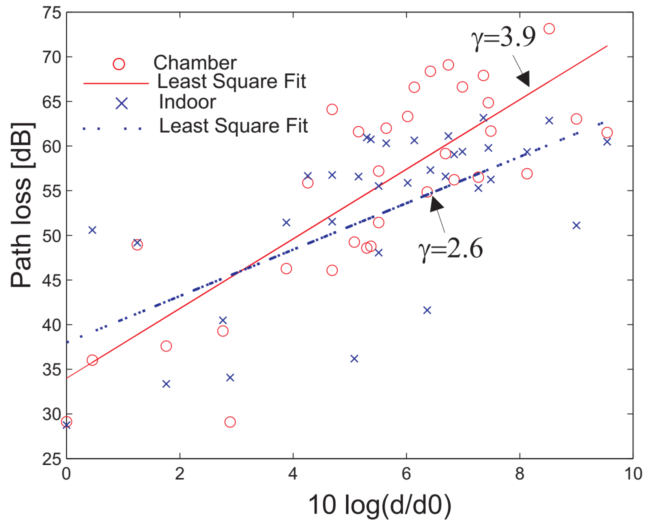

(a) PICA

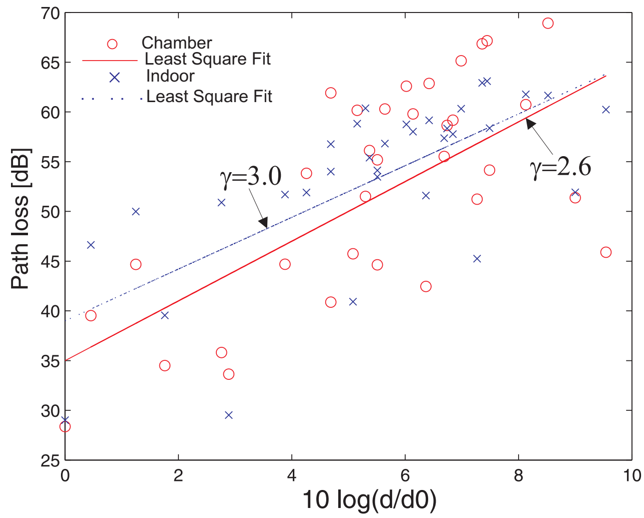

(b) TSA

Figure 6.14: Path Loss of the measured channel: a least square fit has been performed on the measured data.

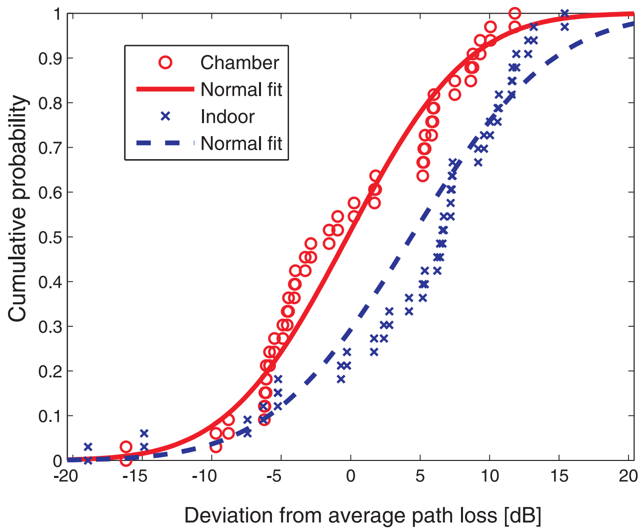

(a) CPW-fed planar inverted cone antenna

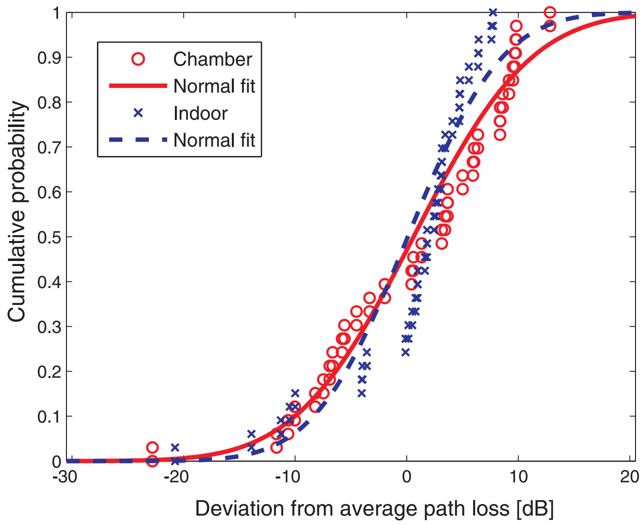

(b) Tapered slot CPW-fed antenna

Figure 6.15: Deviation of measurements from the average path loss fitted to a normal distribution; (a) CPW-fed PICA and (b) CPW-fed tapered slot antenna.

considering only samples with the signal level higher than a selected threshold, and observing their delay respect to the peak sample (the direct pulse). Three different threshold levels are considered: 20, 25 and 30 dB below the peak power.

The Akaike information criteria is a method widely used to evaluate the goodness of a statistical fit [23]. The second order AIC (AIC_c) is defined as:

$$AIC_c = -2\log_e(L) + 2K + \frac{2K(K+1)}{n-K-1} \tag{6.1}$$

Where L is the maximized likelihood, K is the number of parameters estimated for that distribution, n is the number of samples of the experiment. The criterion is applied to evaluate the goodness of five different distributions commonly used in wireless communications that seem to provide the best fittng for our measurements, namely: normal, lognormal, Nakagami, Weibull, and Rayleigh. They are all two parameters distributions (K=2), except the Rayleigh (K=1). Smaller value of AIC_c means better statistical model, and the criterion is used to classify the models from the best to the worse. To facilitate this process the relative AIC_c is considered and results are normalised to the lowest value obtained:

$$\Delta_i = AIC_{c,i} - min(AIC_c) \tag{6.2}$$

A zero value indicates the best fitness. In this analysis, two different antennas are compared. Furthermore the effect of the receiver sensitivity (the threshold applied to calculate the PDP) on the statistical model is considered. For both parameters analysed, the best case ($\Delta_i = 0$), is found for the TSA in the anechoic chamber adopting a less sensitive receiver (threshold -20 dB).

	Normal		**Log-Normal**		**Nakagami**		**Weibull**		**Rayleigh**	
Chamber	**PICA**	**TSA**	**PICA**	**TSA**	**PICA**	**TSA**	**PICA**	**TSA**	**PICA**	**TSA**
Th. -20 dB	38.2	21.0	14.8	7.8	12.6	0	13.0	2.8	52.0	32.9
Th. -25 dB	41.0	19.4	30.8	16.4	26.8	8.8	27.8	10.4	44.4	18.7
Th. -30 dB	52.4	17.6	44.0	16.8	41.1	11.4	40.6	11.8	46.7	10.9
Indoor	**PICA**	**TSA**	**PICA**	**TSA**	**PICA**	**TSA**	**PICA**	**TSA**	**PICA**	**TSA**
Th. -20 dB	69.0	39.4	61.4	36.2	52.0	28.8	54.4	29.6	77.3	36.9
Th. -25 dB	69.2	43.4	63.2	37.5	54.5	34.2	57.8	33.8	70.5	36.5
Th. -30 dB	69.0	46.2	64.2	39.2	59.0	37.6	60.2	37.0	67.5	37.7

Table 6.1: Akaike criterion applied to the RMS spread delay

	Normal		Log-Normal		Nakagami		Weibull		Rayleigh	
Chamber	**PICA**	**TSA**	**PICA**	**TSA**	**PICA**	**TSA**	**PICA**	**TSA**	**PICA**	**TSA**
Th. -20 dB	49.8	40.4	7.8	0	17.8	10.0	16.6	5.4	56.4	48.7
Th. -25 dB	50.2	39.0	20.4	6.4	26.2	14.2	24.0	10.6	54.9	41.3
Th. -30 dB	50.4	38.2	27.8	10.0	34.0	17.4	32.2	14.4	52.2	35.7
Indoor	**PICA**	**TSA**	**PICA**	**TSA**	**PICA**	**TSA**	**PICA**	**TSA**	**PICA**	**TSA**
Th. -20 dB	85.2	55.8	62.2	45.0	61.4	42.0	60.8	40.6	93.5	55.2
Th. -25 dB	85.4	58.8	66.6	49.0	65.2	46.6	64.8	46.4	90.0	53.9
Th. -30 dB	85.5	60.0	69.2	50.6	67.2	49.0	69.1	49.0	88.1	54.1

Table 6.2: Akaike criterion applied to the Mean excess delay

When measurements are performed in indoor environment, more scattered components are considered, and the statistical model is less accurate (higher value of Δ_i) than the anechoic chamber case. As shown in Table 6.1, 6.2, the receiver sensitivity (the threshold applied) affects the statistical model. Using a less sensitive system (threshold -20 dB), less reflected components are taken into account, and the model obtained is more deterministic. Comparing the two antennas, the TSA, being more directive, collects less secondary components, thus producing a better statistical model. To fit the RMS calculated data, the Nakagami distribution is the best. For the mean excess delay, the lognormal is clearly the best in the anechoic chamber, while Nakagami and Weibull produce a slight advantage in the indoor case.

RMS Delay

The root mean square spread delay (τ_{RMS}) is a crucial parameter for multipath channels because it imposes a limit to the data rate achievable [24]. Figure 6.16 shows the cumulative distribution of the RMS delay fitted to a Nakagami distribution. Table 6.3 shows average value and standard deviation (respectively μ and σ) of the distribution for each case. The TSA, due to its more directional radiation, seems to be less affected from the reflections from human body and surrounding environment, and it presents lower average and data less spread than the PICA. When measurements are performed in indoor environment, the multipath effect produces higher spread delay. The PICA, having more omnidirectional radiation, is more affected from the scattering caused by surrounding scatterer, and the increment is more significative. Furthermore using a more sensitive receiver, more secondary components are considered, and the average value of the spread delay is higher.

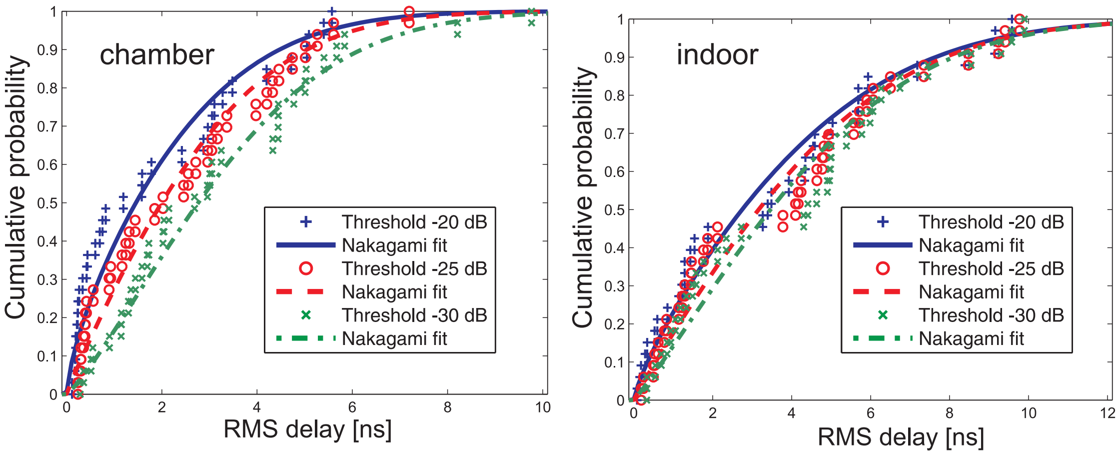

(a) PICA

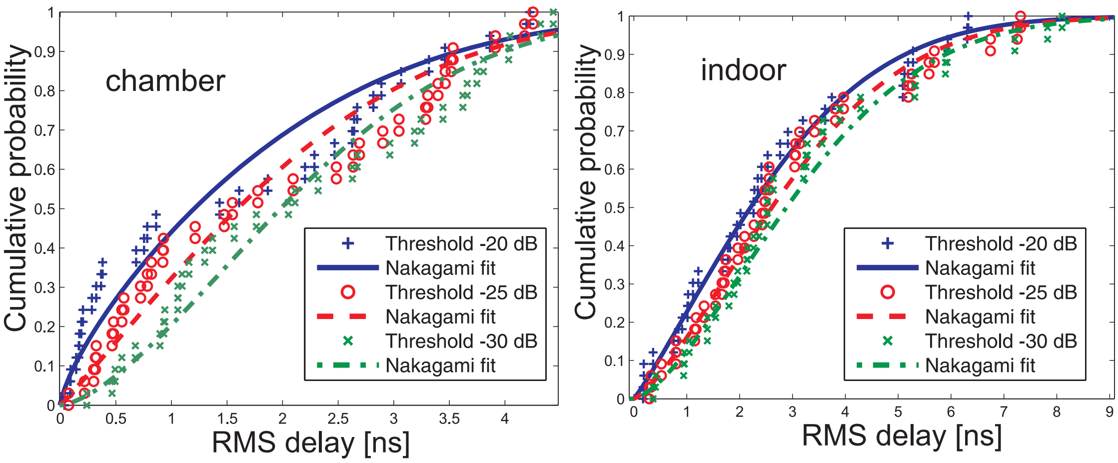

(b) TSA

Figure 6.16: Cumulative distribution of the RMS spread delay fitted to a Nakagami distribution; (a) CPW-fed PICA and (b) CPW-fed tapered slot antenna.

RMS delay	**Chamber**		**Indoor**	
PICA	μ	σ	μ	σ
Th. -20 dB	2.00	1.94	3.58	2.03
Th. -25 dB	2.47	1.94	3.88	3.00
Th. -30 dB	3.12	2.12	4.13	3.02
TSA	μ	σ	μ	σ
Th. -20 dB	1.61	1.43	2.11	3.12
Th. -25 dB	1.86	1.42	2.32	3.09
Th. -30 dB	2.18	1.34	2.45	2.93

Table 6.3: Average value and standard deviation of the Nakagami distributions applied to fit the RMS delay measured values.

Mean Excess Delay

Figure 6.17 shows the cumulative distribution of the mean excess delay fitted with a lognormal distribution. In Table 6.4 are reported average value and standard deviation for each case. Conclusions are similar to the ones drawn for the RMS delay: using a TSA less reflected components are collected and the mean excess delay has lower mean and standard deviation.

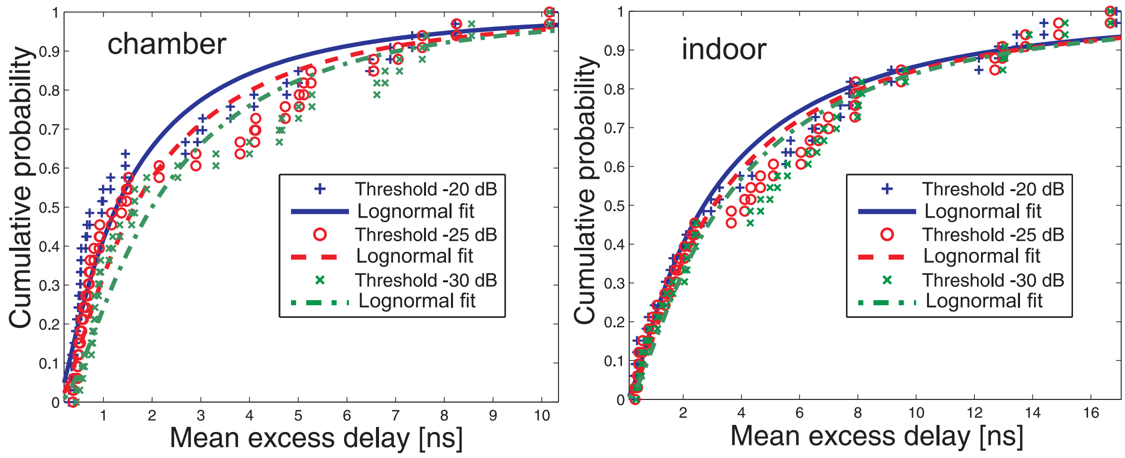

(a) PICA

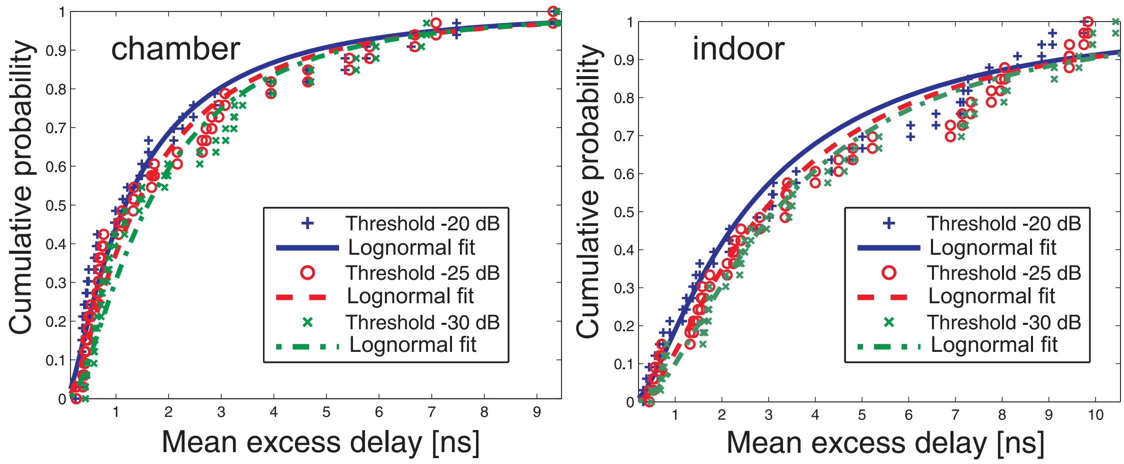

(b) TSA

Figure 6.17: Cumulative distribution of the mean excess delay fitted to a Lognormal distribution; (a) CPW-fed PICA and (b) CPW-fed tapered slot antenna.

Pulse Fidelity

The pulse fidelity is calculated adopting the eq. 3.3, and using as a reference pulse, the one obtained when both antennas are set face-to-face in free space as explained in

	Chamber		Indoor	
PICA	μ	σ	μ	σ
Th. -20 dB	2.44	4.04	5.69	10.50
Th. -25 dB	2.91	4.32	5.96	10.13
Th. -30 dB	3.24	4.13	6.14	9.72
TSA	μ	σ	μ	σ
Th. -20 dB	2.12	3.24	4.23	5.71
Th. -25 dB	2.34	3.15	4.52	5.30
Th. -30 dB	2.48	2.92	4.62	5.05

Table 6.4: Average value and standard deviation of the Lognormal distributions shown in Fig. 6.17

Section 6.1.1. Figure 6.18 shows the fidelity value obtained for the thirty-three receiver considered. The PICA seems to better preserve the pulse shape, the mean fidelity is 85.36% in the anechoic chamber, and 84.88% in indoor environment, while for the TSA the mean values are respectively 81.30 % and 76.41%. However, even for the TSA the average fidelity is above 70%, and hence acceptable for short range communications.

6.3 Effect of the Body Movements on the UWB On-Body Radio Channel

In the analysis presented so far, the radio channel in the measurements was considered to be static. However, the changes in body postures during normal activities lead to significant changes in the radio channel as demonstrated in the previous chapter for narrowband systems at 2.4 GHz. While performing movements, the transmitter and receiver may alter their position from LoS to non LoS, and the distance between transmitter and receiver and the relative orientation of the antennas can be modified. Moreover, the antenna input impedance and even its radiation characteristics (pattern and gain) can be affected by the movements. All these changes on the radio channel introduce a significant fading on the received signal, which, if not accurately considered, could lead to a marginal loss of communication. In this work, a set of measurements is performed while the human candidate is carrying out several pre-defined movements. Measurements are first performed in the anechoic chamber to eliminate multipath reflections from the surrounding environment, and then repeated in the Body-Centric Wireless Sensor Lab (see Fig. 6.12) to consider the effect of the indoor environment on

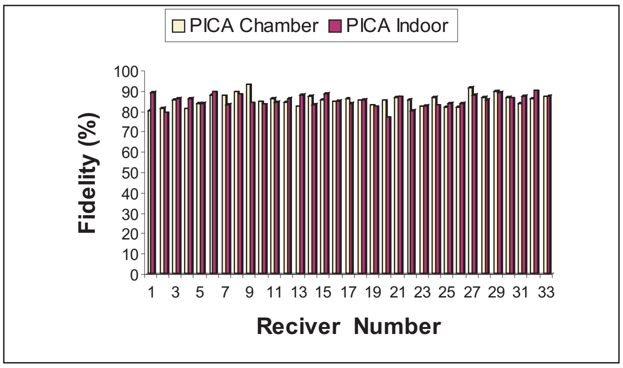

(a) CPW-fed planar inverted cone antenna

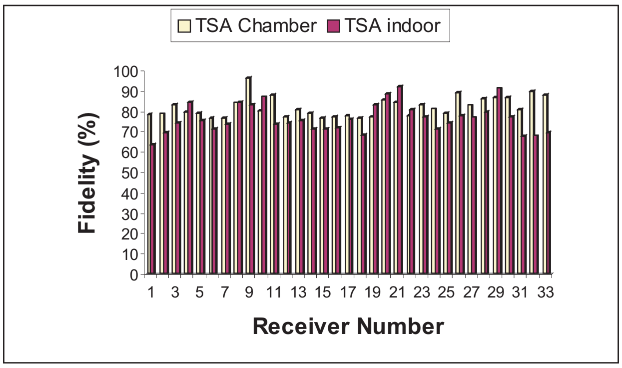

(b) Tapered slot CPW-fed antenna

Figure 6.18: Calculated pulse fidelity for measurements in the anechoic chamber and in indoor environment: (a) CPW-fed PICA and (b) CPW-fed tapered slot antenna.

the on-body radio propagation channel. The transmitting antenna is placed on the left side of the belt. Four different receiver locations are considered as shown in Fig.6.19, namely: the right ear (Rx1), the right chest(Rx2), the right wrist (Rx3), and the right ankle (Rx4). Two TSA antennas are used as transmitting and receiving antennas, and over eighty measurements are recorded for each link.

Considering the short communication distance, the electromagnetic energy propagates from the transmitter to the receiver in few nanoseconds, and hence the channel can be considered static in such period of time. It is therefore a safe assumption recording ”snapshots” of each movement, and, in order to do that, the candidate is maintaining the same position for the entire duration of the sweep (800 ms). The PDP are produced by considering only samples with level above -25 dB (respect to the maximum sample), and observing their delay respect to the peak sample. To enable prediction and modelling of the time delay parameters, the measured data are fitted to empirical statistical models. For the belt-to-wrist link, four different body movements are performed:

- Arm along the body moving to the side to form 90^0 with the body and returning back to initial position (Fig. 6.19).
- Arm along the body moving forward to the front so the arm forms 90^0 with the body trunk and return back to initial position.
- Arm is placed straight in front of the body, moving from the left to the right in front of the body and returning to the initial position.
- Random arm and body movements.

For the belt-to-ear link, three different body movements are performed:

- Head moved from the left to the right clockwise and anti-clockwise.
- Body from standing still to leaning forward and return in the initial position.
- Random arm and body movements.

For the belt-to-chest case the following movements are performed:

- From body standing still to leaning forward and return in the initial position.

- Movement of the torso clockwise and anti-clockwise.
- Random arm and body movements.

For the belt-to-ankle case, measurements are taken while the subject is pacing up and down, and including random body and arm movements.

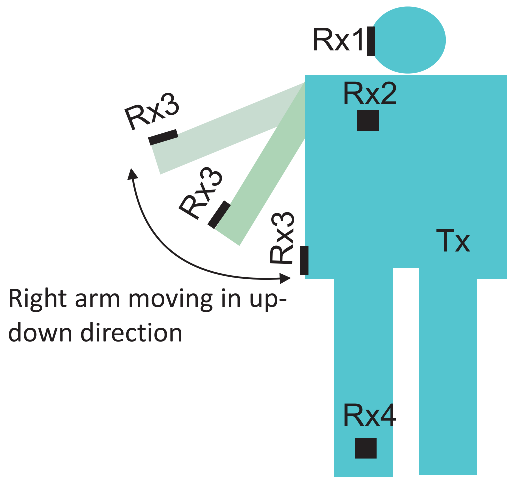

Figure 6.19: Location of the transmitter, and position of the receiver for the four different cases analyzed.

6.3.1 Path Loss Characterisation

The path loss, which is given by the ratio between transmitted and received power, is directly calculated from the measured data, averaging over the measured frequency transfers at each frequency point [25]. When the receiver is moving with respect to the transmitter, the changes in relative distance and orientation lead to a variation of the signal strength. Figure 6.20 shows the variation of the path loss when the arm is moving from straight along the body to extended in front of the candidate, and return in the initial position. While the arm is moving, the distance between transmitter and receiver is increasing, and so is the path loss. The same trend can be seen observing the channel impulse responses of Fig. 6.21, where the level of the peak decreases with the movement of the arm.

The time variation of the path loss, (averaged over the measured frequency) is compared to several well known distributions adopting the Akaike Criterion [23], and results demonstrate that the normal distribution provides the best fitting for most of the cases analysed.

This supports what explained in [24], namely that the long-term variations in the received power due to shadowing and changes in communication distance are usually lognormally distributed (normally in dB units). Figure 6.22 shows the cumulative distribution of the path loss for the measurements in the anechoic chamber. Table 6.5 lists average value (μ) and standard deviation (σ) of the modelled path loss.

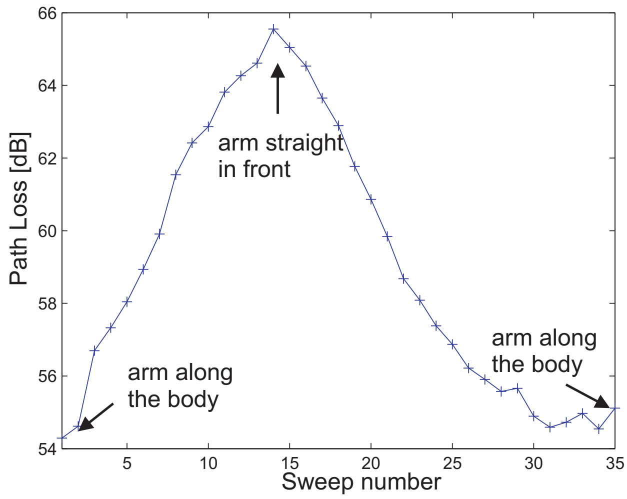

Figure 6.20: Variation of the path loss for the belt-to-wrist link, while the subject is moving the arm from straight along the body to extended in front and return in the initial position.

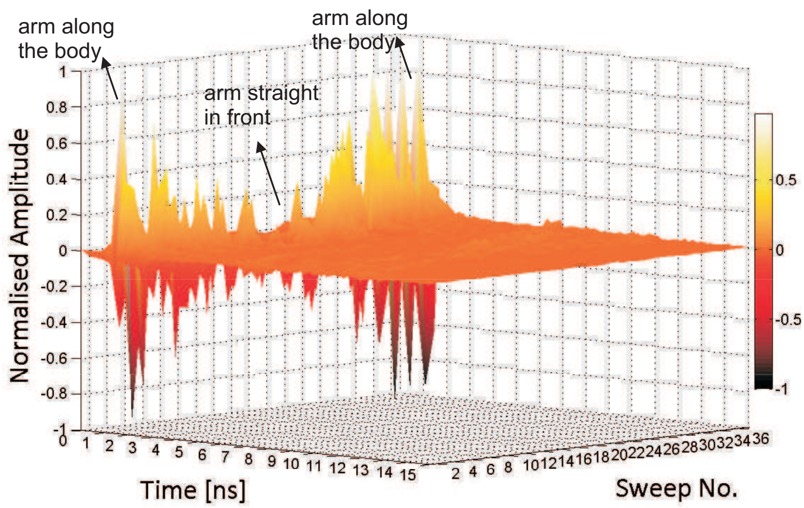

Figure 6.21: Measured time domain channel impulse responses while the subject is moving the arm as explained in Fig. 6.20

In the anechoic chamber, the lowest average path loss is found when the receiver is on the wrist. In such case, the communication distance is in general shorter, and, while

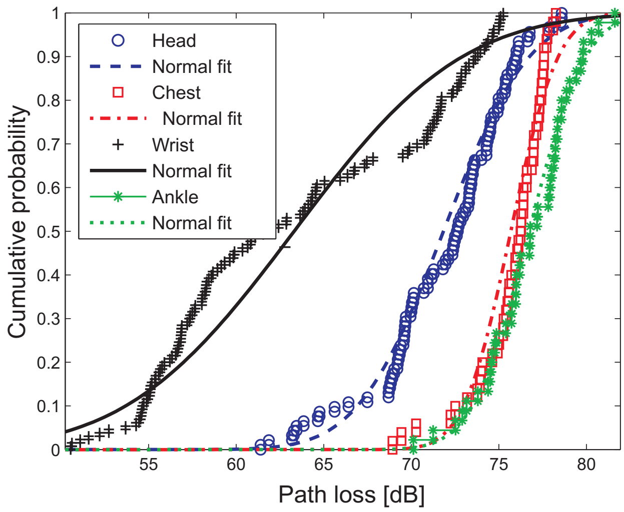

Figure 6.22: Cumulative distribution of the path loss for the measurements in the chamber, the measured data are fitted to a normal distribution.

	Chamber		Indoor	
Rx	μ	σ	μ	σ
Head	71.8	3.8	81.6	2.5
Chest	75.7	1.4	65.8	2.4
Wrist	63.3	7.5	74.7	8.1
Ankle	76.7	2.5	69.9	3.3

Table 6.5: Average and standard deviation of the modelled path loss.

the arm is moving, in some cases there is a clear LOS between transmitter and receiver. However, such link is the most affected by changes in distance and relative orientation between the two antennas, and the data are mostly spread around the average value (highest value of σ). Figure 6.22 also shows the low accuracy of the statistical fit for the wrist case, while in the other cases, the normal distribution represents the variation of the path loss well. For the wrist case, the path loss is in the range 50-71 dB, and for the head case the range is 60-75 dB. The variation of the path loss is lower than the one found in chapter 5 for a narrowband system (the variation was found to be 30 dB for the wrist case, and 25 dB for the head case). This is due to the inherent frequency diversity of UWB systems. In other words, since the power is averaged across the UWB frequency spectrum, such a system is less affected by the narrowband fading caused by the reflections from the different body parts. Table 6.5 demonstrates that the belt-to-chest, and belt-to-ankle links are the less affected by the movements performed, and hence they have the smallest value of σ. When the measurements are performed in the sensor lab, the multipath reflections lead to an increase of μ and σ for the belt-to-head and belt-to-wrist link, and to a decrease for the remaining links.

6.3.2 Time Delay Characterisation

The channel impulse responses have been calculated based on the measured frequency transfer functions which consist of 1601 frequency points using windowing and Inverse Discrete Fourier Transform (IDFT). The applied time window can detect received multipath components up to 267 ns with 55 ps of resolution. The average power delay profile (APDP) is calculated averaging the impulse response (at each time step) over all the measured postures, and it is shown in Fig. 6.23. The signal is expected to decay exponentially with time (linearly in dB units). However, not in every case, the power is concentrated in a single cluster. Especially when the receiver is on the wrist, two clusters with almost equal peak power and significative delay can be identified; the first has its maximum amplitude at 3 ns, while the second has its maximum at 9 ns. This confirms that this link is the most affected by the body movements and hence the APDP is more spread in time. A similar conclusion can be drawn for the ankle receiver, where a second cluster can be identified (possibly due to the reflections from the ground), however, the relative delay between the two cluster is approximately 1.5

ns, four times smaller than the one found for the belt-to-wrist link. For the other two cases, the most of the power is concentrated in a single cluster whose power tends to decay exponentially with time.

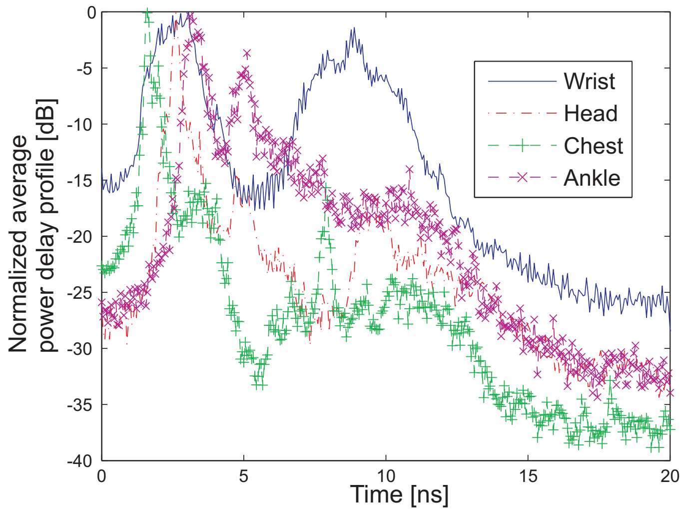

Figure 6.23: Average power delay profile for all the links measured.

RMS Delay

The root mean square spread delay (τ_{RMS}) is a crucial parameter for multipath channels since it imposes a limit to the data rate achievable [24]. The goodness of different statistical distributions in fitting the data have been evaluated. For the case of study, the lognormal distribution provides the highest likelihood among a wide set of distributions. Similarly to the statistic of the path loss, a lower likelihood is found for the belt-to-wrist case (see Fig. 6.24).

	Chamber		**Indoor**	
Rx	μ	σ	μ	σ
Head	4.4	3.6	6.1	2.7
Chest	4.2	1.9	7.6	3.4
Wrist	2.0	3.5	7.8	1.9
Ankle	3.3	2.6	6.0	1.7

Table 6.6: RMS delay

Table 6.6 lists average value and standard deviation of the lognormal distributions used to model the RMS delay. In the anechoic chamber, where only the reflections from the body parts are considered, the delay is found to be higher for the belt-to-head and

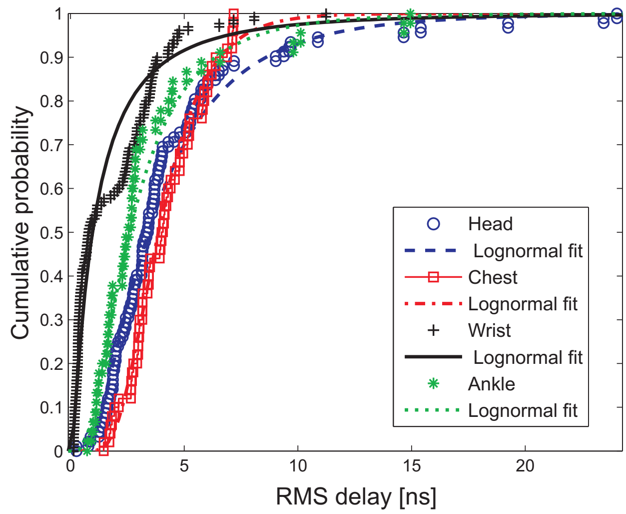

Figure 6.24: Cumulative distribution of the RMS delay for the measurements in the chamber, the measured data are fitted to a lognormal distribution.

belt-to-chest links. When measurements are performed in the lab, the reflections from the surrounding scatterers lead to a higher delay, and such effect is more significative for the wrist receiver. This is due to the fact that the in the setup considered the wrist receiver is closer to the wall, and while moving laterally, such distance is further reducing, and hence more multipath reflections are collected.

Mean Excess Delay

Similarly to the RMS delay, the lognormal distribution provides the highest likelihood in modeling the mean excess delay. Figure 6.25 shows the distribution of the mean delay for the anechoic chamber case.

	Chamber		**Indoor**	
Rx	μ	σ	μ	σ
Head	3.4	2.8	6.6	3.2
Chest	2.5	0.9	8.0	1.7
Wrist	1.8	2.2	9.6	3.7
Ankle	2.6	1.3	7.2	2.6

Table 6.7: Mean delay

Table 6.7 lists average value and standard deviation of the Lognormal distributions used to model the mean delay. Conclusions are similar to the ones drawn for the RMS delay.

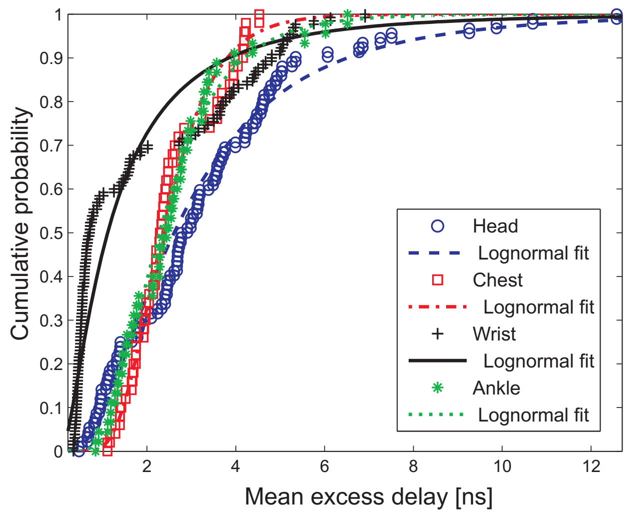

Figure 6.25: Cumulative distribution of the mean excess delay for the measurements in the chamber, the measured data are fitted to a lognormal distribution.

6.4 Numerical Study of the UWB On-Body Radio Channel

The characteristics of the UWB on-body radio channel have been analysed adopting the dispersive FDTD technique. As explained in section 4.3.1, the frequency-dispersion of the human body tissues has been represented by a two-pole Debye model.

6.4.1 Path Loss Characterisation Including Different Body Postures

The impact of different body postures on the radio channel was investigated by considering ten body postures when the subject is standing and sitting down; and considering five different positions of the arms. The details of the postures, together with the positions of transmitter and receivers are illustrated in Fig. 6.26. The transmitting antenna is placed on the left side of the waist, and eight different receiver positions are considered (as shown in Fig. 6.26). The homogeneous digital phantom adopted in the simulations has a height of 1.75 m and weights 73 kg. The transmitter is a Hertzian dipole parallel to the body surface (along z direction), and the excitation source is a gaussian monocycle pulse with bandwidth 3-9 GHz. The FDTD cell size is $\Delta x = \Delta y = \Delta z = 1$ mm (corresponding to 6 cells per wavelength inside the body at the upper frequency of 10 GHz).

The fields at the receiver locations are recorded and converted in the frequency

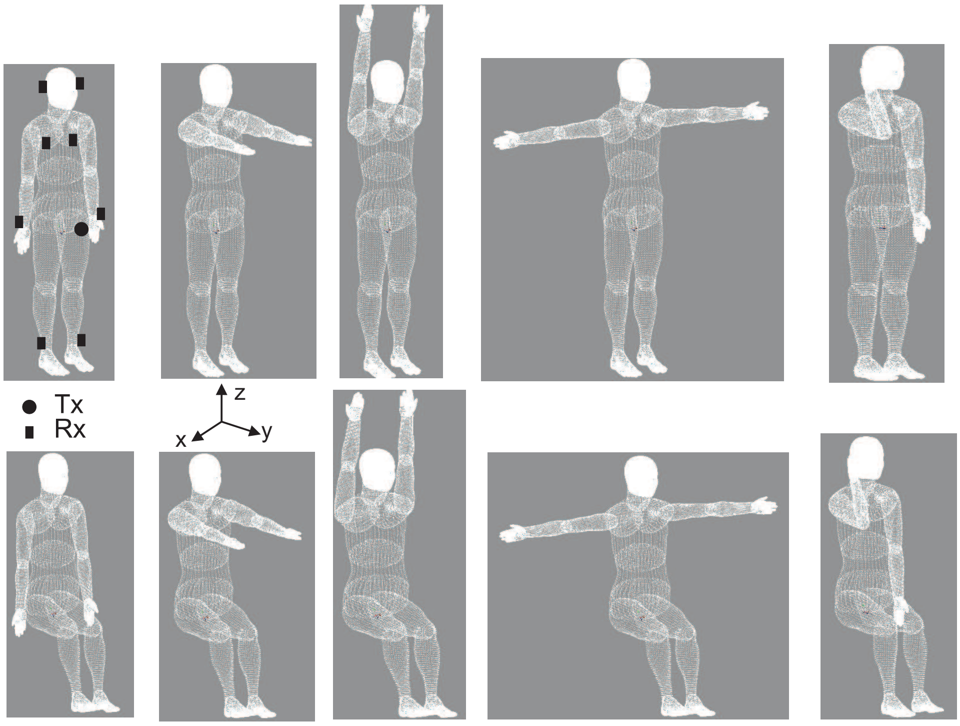

Figure 6.26: Illustration of the ten postures analysed. The transmitter is placed on the left side of the waist, and eight representative on-body links are considered.

domain by applying FFT. The path loss is then calculated by averaging over the frequency band (3-9 GHz), and can be modelled as a linear function of the logarithmic distance (eq. 3.17) as

$$PL_{dB} = 25 + 10 \cdot 4.0 \cdot \log(d/0.1) + N(0, 95.6) \tag{6.3}$$

The path loss exponent is obtained applying a least square fit on the measured data (see Fig. 5.4(a)), and it is found to be γ=4.0. The shadowing factor χ is a zero-mean normal distribution with variance σ^2=95.6. The simulated results are compared to measurements performed on a candidate with similar size than the digital phantom adopted. Two identical HSCA antennas (see Fig. 3.4) are used in the measurement campaign. Such an antenna has a polarisation parallel to the human body like the Hertzian dipole adopted in the simulations. The path loss exponent is found to be $\gamma = 4.4$ [26], and hence comparable with the calculated one.

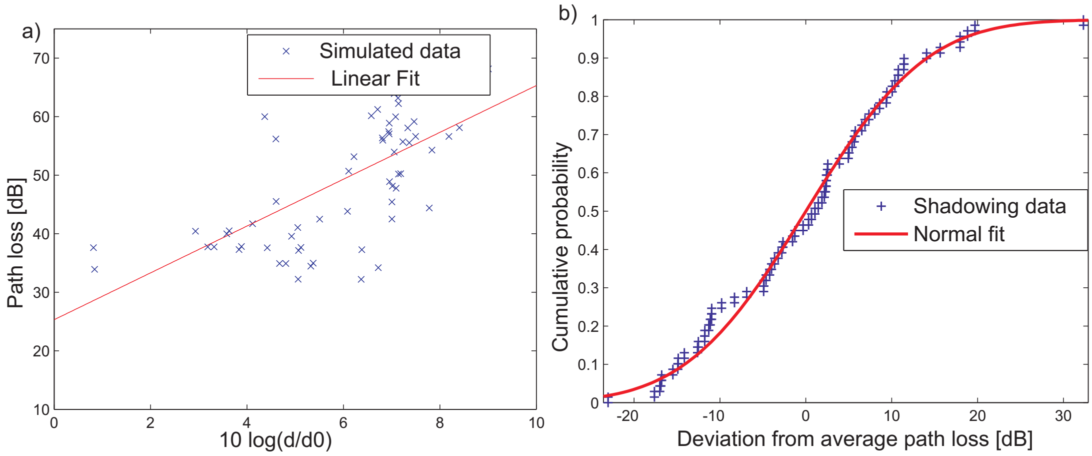

Figure 6.27: Simulated and modeled path loss obtained considering the ten different postures; (a) path loss as a function of the communication distance, (b) deviation from the average path loss (shadowing factor).

6.4.2 Subject-Specific UWB On-Body Radio Channel

Similarly to what has been done in chapter 5, the subject-specificity of the UWB on-body radio channel is investigated by considering the nine digital phantoms of Fig. 5.6.

Figure 6.28 shows the received pulses in the links left waist-to-right ear (top), and left waist-to-right wrist for the models F01 and F05. Since F05 is much taller and bigger in size than F01 (see Table 6.8), the communication distance is greater, and so it is the delay of the received pulse. For the ear receiver case, the reflections from the body parts do not affect much the signal propagation, and the received pulse is less spread in time than in the wrist receiver case. In the latter, there is not a LoS between transmitter and receiver, and the signal reaches the receiver through creeping wave propagation and scattering from the body parts.

The path loss is characterised for propagation along the trunk by placing the transmitting source (Hertzian dipole) on the left side of the waist. The received waveform is recorded at several locations (over fifty) on the front part of the trunk, and converted in the frequency domain. The path loss at each location is then calculated by averaging the received power across the whole frequency band (3-9 GHz). A linear fit is performed on the simulated data, and the path loss is modelled as a linear function of the logarithmic distance adopting 3.17.

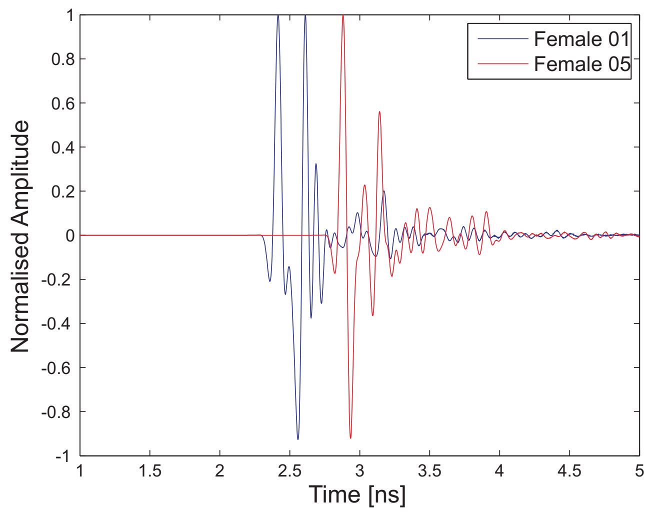

(a) Ear

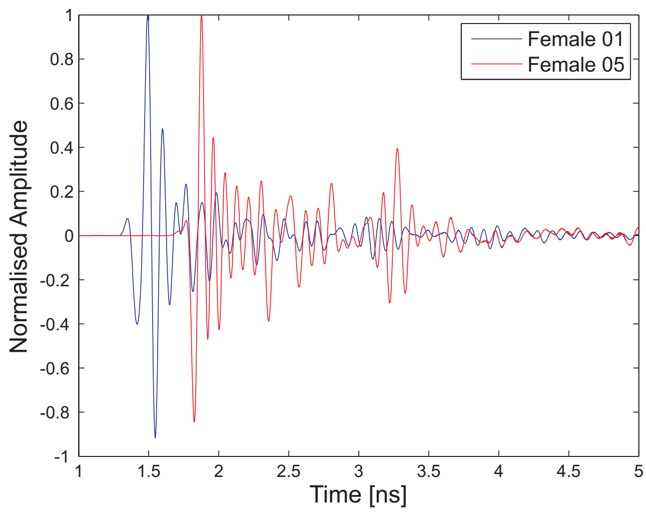

(b) Wrist

Figure 6.28: Normalised received pulse for the model Female 02, and Female 05. The waist-to-right ear (top) and waist-to-right wrist (bottom) links were considered.

	F01	F02	F03	F04	F05	M01	M02	M03	M04
γ	2.7	2.9	3.2	2.8	3.5	3.0	3.2	3.4	3.6
σ [dB]	4.0	4.2	5.8	4.7	5.5	5.7	4.6	6.0	5.7

Table 6.8: Parameters of the modelled path loss for the nine digital phantoms. The parameter γ is the path loss exponent, and σ is the standard deviation of the normally distributed shadowing factor.

Table 6.8 lists the values of path loss exponent γ obtained for the different models. The conclusions are similar to the ones drawn in the previous chapter for a narrow-band system. The values of γ are ranging from 2.7 (F01) to 3.6 (M04). In particular, it can be noted that subjects smaller in size (such as F01, F02 and M01) have a smaller curvature radius at the waist, and hence they present a lower value of γ. The simulated results are compared to the measured data performed on a subject with same dimensions than the model M02. The path loss is characterised by considering thirty different receivers placed on the body trunk, and by adopting a pair of planar PICA antenna in addition to two TSA antennas. For the PICA case, it is found γ=4.2 and σ=11.9 dB, while for the TSA it is found γ=3.5 and σ=10.7 dB. For the TSA case, the exponent is quite similar to the simulated one (γ=3.2), while for the PICA case the exponent is found to be higher than the calculated one, thus supporting that γ depends on the radiation characteristics of the antenna used. It is important to note that the shadowing factor is more spread in the measured cases, and this may be due to the effect of the cables used to connect the antennas to the VNA. The values of γ are higher than the ones found at 2.4 GHz, and this is due to the higher losses of the body tissues in the UWB frequency band.

6.5 Summary

UWB is one of the key emerging technologies, targeted for short-range low-power and high-data-rate applications. Its low transmit power requirements allow longer battery life, and hence it is suitable for wearable units.

In this chapter, two different planar UWB antennas (Planar Inverted Cone Antenna and Tapered Slot Antenna) have been presented, and their spectral and transient performance have been illustrated in free space and when body-mounted. Both antennas have shown acceptable radiation performances in terms of impedance matching, radiation pattern, gain and ability to preserve the shape of the pulse.

The two aforementioned antennas have been used to characterize the on-body radio propagation channel in an anechoic chamber, and in indoor environment, and both antennas proposed promise to be a suitable candidate for UWB-BCWC systems.

In particular the TSA, besides a significative size reduction, has shown better performances in terms of delay spread, due to its slightly more directional radiation.

The effect of the body movements on the UWB on-body radio channel have been also analyzed in the chapter. To enable prediction and modeling, the variation of path loss and time delay parameters with the body movements, have been compared to empirical statistical models, and it was deduced that the lognormal distribution provides the best fit for the time delay parameters, while the normal is the best for modeling of the path loss. From the analysis of several on-body radio links, it was deduced that amplitude and delay spread of the received signal can vary significatively with the changes in posture of the body. Especially in the case of a wrist-worn unit, the relative distance and orientation of the two antennas is drastically changing, thus leading to high variation on the level of the received signal.

References

[1] *FCC First Report and Order, Revision of the Part 15 Commission's Rules Regarding Ultra-Wideband Transmission Systems*, pp. 98–153, April 22, 2003.

[2] J. Bernardhard, P. Nagel, J. Hupp, W. Strauss, and T. von der Grun, "BAN – body area network for wearable computing," *9th Wireless World Research Forum Meeting, Zurich*, July 2003.

[3] C. Kunze, U. Grossmann, W. Stork, and K. Muller-Glaser, "Application of ubiquitous computing in personal health monitoring systems," *Biomedizinische Technik: 36th Annual meeting of the German Society for Biomedical Engineering*, pp. 360–362, 2002.

[4] P. S. Hall and Y. Hao, *Antennas and Propagation for Body-Centric Wireless Communications*. Artech House, 2006.

[5] W. Soergel, C. Waldschmidt, and W. Wiesbeck, "Antenna characterization for ultra wideband communications," *IWUWBS, Oulu, Finland*, June 2003.

[6] S. Licul, J. A. N. Noronha, W. A. Davis, D. G. Sweeney, C. R. Anderson, and T. M. Bielawa, "A parametric study of time-domain characteristics of possible UWB antenna architectures," *2003 IEEE 58th Vehicular Technology Conference, Fall 2003*, vol. 5, pp. 3110–3114, October 2003.

[7] T. Yang, S.-Y. Suh, R. Nealy, W. Davis, and W. L. Stutzman, "Compact antennas for UWB applications," *2003 IEEE Ultra Wideband Systems and Technologies*, pp. 205–208, November 2003.

[8] Z. N. Chen, "Novel bi-arm rolled monopole for UWB applications," *IEEE Transactions on Antennas and Propagation*, vol. 53, no. 2, pp. 672–677, February 2005.

[9] S.-Y. Suh, W. Stutzman, W. Davis, A. Waltho, and J. Schiffer, "A novel CPW-fed disc antenna," *2004 IEEE Antennas and Propagation Society Symposium*, vol. 3, pp. 2919–2922, June 2004.

[10] S.-Y. Suh, W. L. Stutzman, and W. A. Davis, "A new ultrawideband printed monopole antenna: The planar inverted cone antenna (PICA)," *IEEE Transaction on Antennas and Propagation*, vol. 52, no. 5, pp. 1361–1364, May 2004.

[11] A. Rahman, A. Alomainy, and Y. Hao, "Compact body-worn coplanar waveguide fed antenna for UWB body-centric wireless-networks," *European Conference on Antennas and Propagation (EUCAP 07), Edimburgh, UK*, November 2007.

[12] A. Alomainy, A. Sani, J. Santas, A. Rahman, and Y. Hao, "Transient characteristics of wearable antennas and radio propagation channels for ultra wideband body-centric wireless communications," *IEEE Transactions in Antenna and Propagation*, vol. 57, no. 4, pp. 875–884, 2009.

[13] D. Lamensdorf and L. Susman, "Baseband-pulse-antenna techniques," *IEEE Antennas and Propagation Magazine*, vol. 36, no. 1, February 1994.

[14] M. Klemm, I. Z. Kovacs, F. G. Pedersen, and G. Troester, "Novel small-size directional antenna for UWB WBAN/WPAN applications," *IEEE Transactions on Antennas and Propagation*, vol. 53, no. 12, pp. 3884–3896, 2005.

[15] J. McLean, H. Foltz, and R. Sutton, "Pattern descriptors for UWB antennas," *IEEE transactions on antennas and propagation*, vol. 53, no. 1 Part 2, pp. 553–559, 2005.

[16] T. Dissanayake and K. Esselle, "Correlation-based pattern stability analysis and a figure of merit for UWB antennas," *IEEE Transactions on Antennas and Propagation*, vol. 54, no. 11 Part 1, pp. 3184–3191, 2006.

[17] A. Alomainy and Y. Hao, "Radio channels model for UWB body-centric wireless-networks with compact planar antennas," *2006, IEEE AP-S International Symposium on Antennas and Propagation, Albuquerque, New Mexico*, vol. 152, no. 6, 9-14 July 2006.

[18] A. Alomainy, Y. Hao, and C. G. Parini, "Transient and small scale analysis of ultra wide-band on-body radio channel," *North American Radio Science Meeting URSI 2007, Ottawa, Canada*, 22-26 July 2007.

[19] T.-G. Ma and C.-H. Tseng, "An ultra wideband coplanar waveguide-fed tapered slot ring antenna," *IEEE Transactions on Antenna and Propagation*, vol. 54, no. 4, April 2006.

[20] M. Kanda, "A relatively short cylindrical broadband antenna with tapered resistive loading for picosecond pulse measurements," *IEEE Transactions on Antennas and Propagation*, vol. 26, no. 3, pp. 439–447, 1978.

[21] T. Zasowski, F. Althaus, M. Stager, A. Wittneben, and G. Troster, "UWB for noninvasive wireless body area networks: channel measurements and results," *IEEE Conference on Ultra Wideband Systems and Technologies*, November 2003.

[22] W. Ciccognani, A. Durantini, and D. Cassioli, "Time domain propagation measurements of the UWB indoor channel using PN sequence in the FCC-compliant band 3.66 GHz," *IEEE Transactions on Antenna and Propagation*, vol. 53, no. 4, April 2005.

[23] K. P. Burnham and D. R. Anderson, *Model Selection and Multimodel Inference: A Practical Information-Theoretic Approach*. New York: Springer-Verlag, 2002.

[24] T. S. Rappaport, *Wireless Communications: Principle and Practice*. Prentice-Hall, 1999.

[25] J. A. Dabin, N. Ni, A. M. Haimovich, E. Niver, and H. Grebel, "The effects of antenna directivity on path loss and multipath propagation in UWB indoor wireless channels," *in Proc. IEEE Conf. Ultra Wideband Systems and Technologies, Newark, NJ,*, pp. 305–309, 2003.

[26] A. Alomainy, "Antennas and radio propagation for body-centric wireless networks," Ph.D. dissertation, Queen Mary, University of London, 2007.

Chapter 7

Wireless Telemetry for Medical Implants

Implantable devices have a wide range of promising novel biomedical applications that would play vital and important roles in building comprehensive telemedical networks [1, 2]. In [3] a global overview of implanted microsystems, and their clinical application is presented, and it is shown that at the state-of-the-art implanted devices can be located almost everywhere inside the human body. To ensure wireless connectivity of implanted systems with external base stations, physical understanding of in-body and off-body radio propagation channels with implanted antennas is needed.

The chapter, presents the numerical analysis of subject-specific geometric and electrical properties on the performance of wireless implants located in different parts of the body. Furthermore, a link budget study for a cardiac implanted antenna is proposed, and different propagation scenarios (free space and indoor environment) are considered. The derived channel characteristics are used to evaluate the system performance as a function of specific parameters, such as communication range, transmitted power and the required data-rate.

7.1 Radiation Characteristics of Wireless Sources Considering Different Digital Phantoms

Over the past few years, many studies and investigations on radio propagation from implanted sources, and the design of tissue implanted antennas, have been presented in the open literature [4–12]. In [13, 14], Scanlon *et al.* demonstrated numerically and experimentally the characteristics of a vagina implant at 418 and 916.5 MHz. In [13], the results obtained adopting homogeneous and inhomogeneous phantoms were compared, and it was concluded that segmentation of the phantom in the region surrounding the source is critical for analysing the performance of an implant. Radiation characteristics of ingested sources in the human gastro-intestinal tract placed at different locations were numerically investigated in [15] at VHF and UHF bands. Chirwa *et al.* [15] demonstrated that there is a Gaussian-like relationship between the radiation intensity outside the body and the operating frequency.

The aim of this study is to characterise the radiation from implanted wireless sources considering the impact of different tissue types and body compositions. Three inhomogeneous male phantoms are compared: two males and one female phantom. In the investigation presented, three different locations of the wireless implant are considered, namely: the stomach, the bladder, and the heart (inside the left ventricle).

Wirelessly controlled valves in the urinary tract operating on-demand by the patients have been developed for restoring bladder control, [16, 17]. Ingested capsules operating in the digestive apparatus have been developed for diagnosing gastro-intestinal disorders [18]. Context aware implanted pacemakers, cardiac defibrillators and pressure sensors have been developed to monitor the heart activity and diagnose critical heart failures. [19–21]. In particular, the pressure in the left ventricle is a critical parameter to monitor, since some heart failure may be due to a dysfunction of the left ventricle [22]. The aforementioned applications and medical scenarios emphasise the need of comprehensive study on wireless implants in various subjects and locations inside the body.

7.1.1 Computational Models

The proposed numerical investigations are performed using the finite-difference time-domain (FDTD) technique. Two different frequency bands are considered, the medical implanted communication services (MICS) radio band (402-405 MHz) [23], and the frequency band 868.0-868.6 MHz, which is unlicensed for scientific and medical applications in Europe [24]. The three dimensional FDTD simulations are carried out using a uniform grid with cell size $dx = dy = dz = 4$ mm, and a near to far field transformation [25] has been applied to evaluate the total radiated power and the radiation patterns. A near to far field transformation [25] has been applied to evaluate the total radiated power and the radiation patterns.

As the dimensions of practical implanted antennas are electrically small, it is considered a safe assumption to represent them using a single-cell point source and to excite the electric field component along the z-axis. In the simulations, an insulation thickness of one cell (4 mm) was used between the source and the tissues.

Three different inhomogeneous digital phantoms (see Fig. 4.4) are considered in the simulations: a male (height 172 cm, weight 65 kg, body mass index 22.0) and a female (height 160 cm, weight 53 kg, body mass index 20.7) Japanese model developed by the National Institute of Information and Communication Technology (NICT) [26], and the HUGO model (height 186 cm, weight 90 kg, body mass index 26.0), which is based on the data provided by the Visible Human Project of the National Library of Medicine [27]. Table 7.1 lists conductivity and permittivity values of the human tissues at 402 and 868 MHz.

Figure 7.2 shows the permittivity of the tissues at 402 MHz sliced horizontally on the plane where the excitation sources are imposed. For the case of a cardiac implant, the source is placed inside the left ventricle. The stomach is modeled as a semi-full cavity containing large amounts of fluid (see Fig 7.2(a)), while bladder and heart are assumed as cavities with muscular walls filled with urine and blood respectively. It is important to note that, for all the models, it has been estimated that the contents of bladder and heart (respectively urine and blood) have the same electric properties; and they exhibit higher losses than the stomach contents (see Table 7.1).

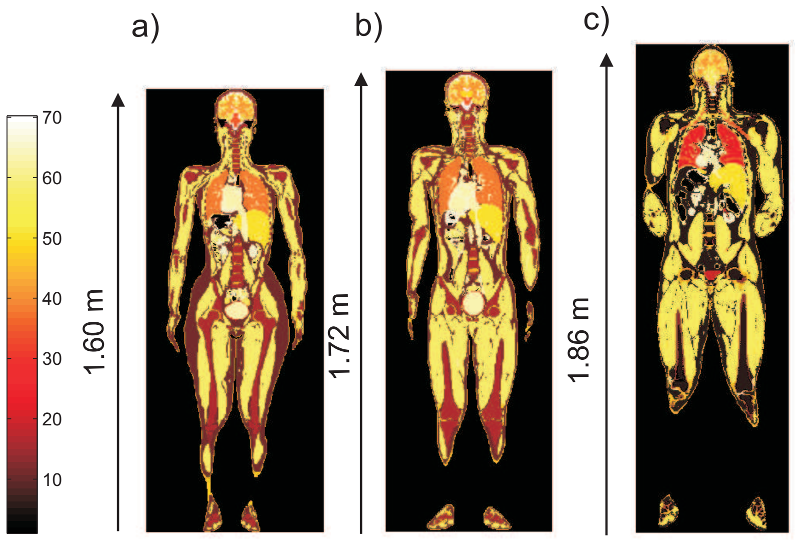

Figure 7.1: Permittivity of the digital phantoms at 868 MHz sliced vertically: (a) Japanese female; (b) Japanese male; (c) HUGO model.

	402 MHz		868 MHz	
Tissue	σ (S/m)	ϵ_r	σ (S/m)	ϵ_r
Bladder	0.32	19.7	0.38	18.97
Blood	1.35	64.16	1.52	61.46
Grey Matter	0.74	57.39	0.93	52.88
White Matter	0.45	42.05	0.58	40.00
Breast Fat	0.03	5.51	0.05	5.43
Fat	0.08	11.62	0.11	11.35
Gall Bladder	1.14	61.20	1.25	59.19
Gland	0.88	61.53	1.03	59.76
Heart	0.97	66.05	1.21	60.10
Kidney	1.10	66.36	1.37	58.93
Liver	0.65	51.2	0.84	46.99
Lung Deflated	0.68	54.66	0.85	51.54
Lung Inflated	0.37	23.80	0.45	22.06
Muscle	0.82	57.96	0.96	56.03
Pancreas	0.82	57.96	0.96	56.03
Prostate	1.03	63.35	1.20	60.66
Skin Dry	0.69	46.74	0.86	41.58
Skin Wet	0.67	49.87	0.83	46.21
Spleen	1.03	63.17	1.26	57.38
Stomach	1.00	67.47	1.17	65.15
Stomach Content	0.82	57.96	0.96	56.03
Tendon	0.56	47.28	0.71	45.89
Testis	0.82	57.96	0.96	56.03
Urine	1.35	64.16	1.52	61.46

Table 7.1: Electric properties of specific human tissues used within the visible man model at 402 MHz and 868 MHz [28] (σ is the tissue conductivity, ϵ_r is the dielectric constant).

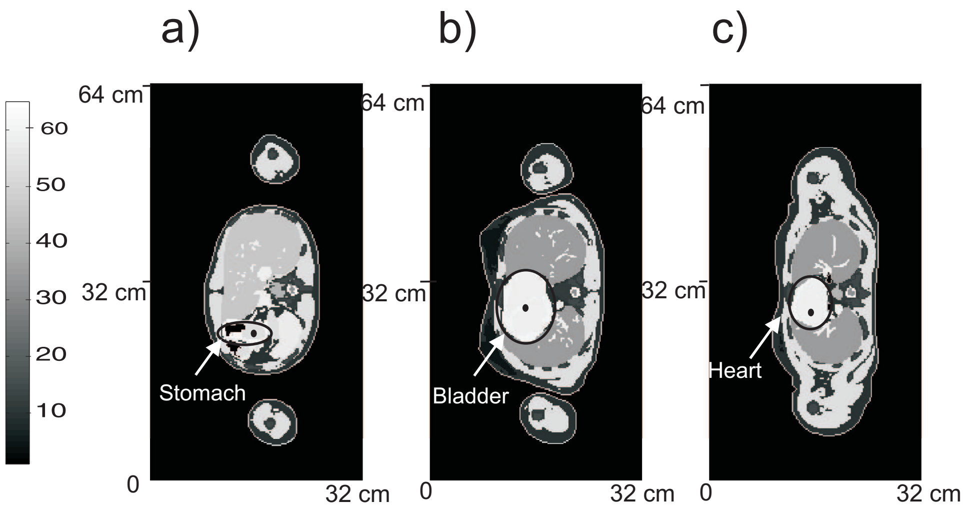

Figure 7.2: Permittivity of the human body sliced horizontally on the plane where the excitation sources are imposed. Data in this figure are referred to the Japanese male case; (a) the model is sliced at a height of 113.4 cm, (b) the model is sliced at a height of 88.8 cm, (c) the model is sliced at a height of 140.8 cm.

7.1.2 Radiation Characterization

Azimuthal Radiation Pattern

The far-field has been calculated with a 3D near-to-far field transformation [25]. Since the main aim of presenting the patterns is to examine the spatial radiation performance of the wireless implants, they have been normalised to the maximum radiated power for each case.

Figure 7.3 shows the radiation pattern for the wireless source in the stomach. The maximum radiation is towards the front part of the body for all three human phantoms, and this is due to the fact that the source is closer to the front of the body. Besides, the dorsal part of the body has a high presence of lossy tissues (such as muscle), leading to significant attenuation. The radiation pattern for the female case is less directive than the male cases, and this is because the female body composition contains low conductivity tissues (less presence of muscles) than the male model. Moreover, considering the location of the stomach implant, the female body has a smaller circumference at the waist leading to less attenuation. The HUGO model presents the most directive radiation pattern and shows a front-to-back ratio of 20 and 30 dB at 402

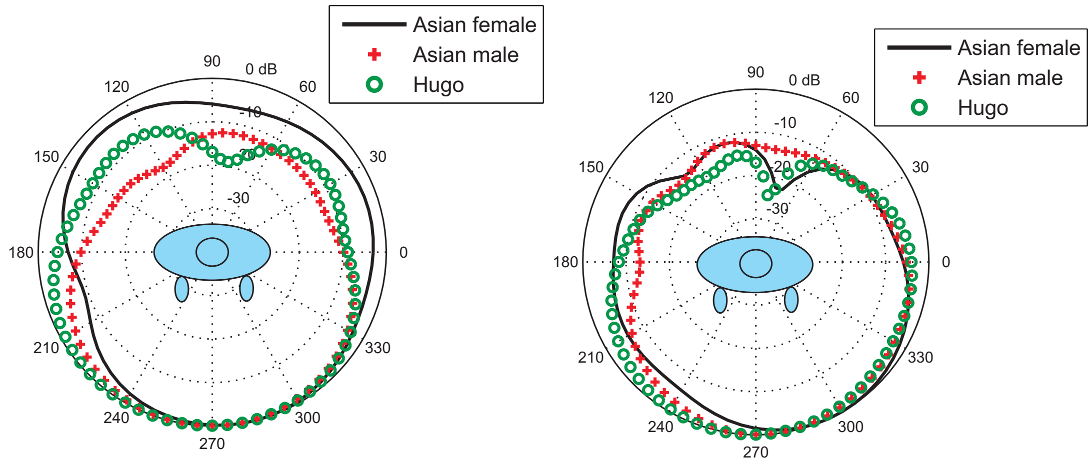

(a) 402 MHz (b) 868 MHz

Figure 7.3: Comparison between the normalised azimuthal radiation pattern obtained for the three digital phantoms for the stomach implanted source at (a) 402 MHz and (b) 868 MHz. The front of the body is towards 270 degrees.

and 868 MHz respectively. This is due to the fact that the HUGO body has the biggest size and the largest body curvature around the waist.

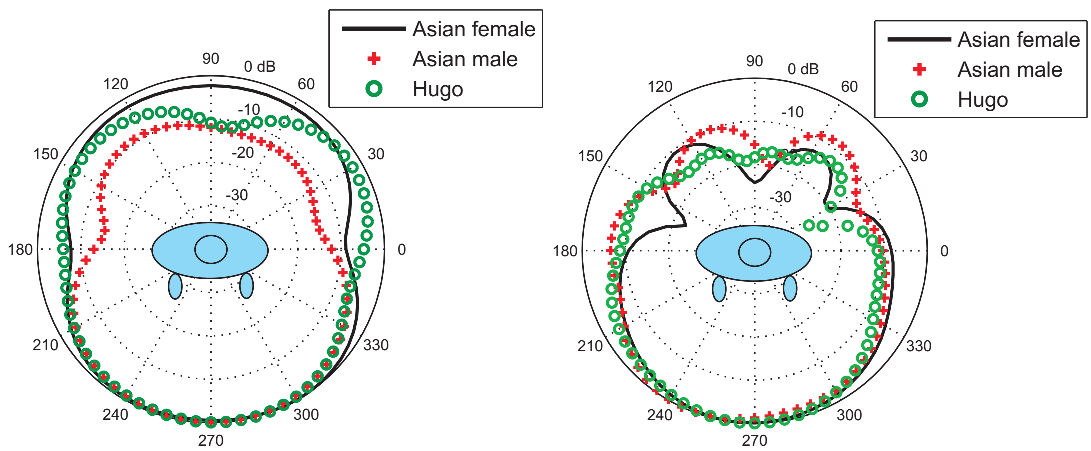

(a) 402 MHz (b) 868 MHz

Figure 7.4: Comparison between the normalised azimuthal radiation pattern obtained for the three digital phantoms for the bladder implanted source at (a) 402 MHz and (b) 868 MHz. The front of the body is towards 270 degrees.

Figure 7.4 shows the radiation pattern for the bladder implanted source. In contrast to the stomach case, the shape of the radiation pattern is very different at the two frequencies. At 402 MHz, the pattern is not significantly directive, and the front-to-back ratio is approximately 10 dB for the three phantoms. At 868 MHz the patterns are more directive, and they present some nulls on the back side (see Fig. 7.4(b)).

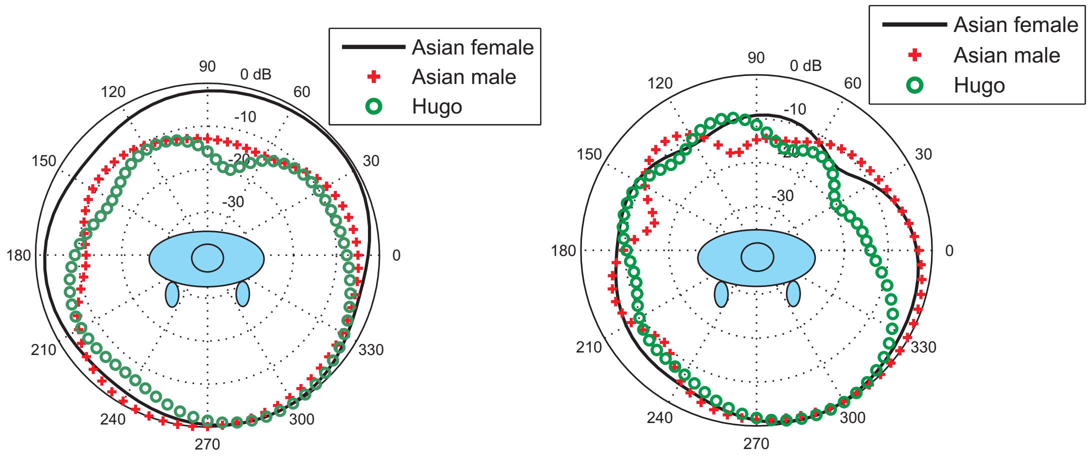

(a) 402 MHz (b) 868 MHz

Figure 7.5: Comparison between the normalised azimuthal radiation pattern obtained for the three digital phantoms for the cardiac implanted source at (a) 402 MHz and (b) 868 MHz. The front of the body is towards 270 degrees.

Figure 7.5 illustrates the radiation pattern for the cardiac implant. The direction of maximum radiation is slightly tilted towards the left part of the body due to the natural location of this organ. At 402 MHz, the radiation pattern for the female case is almost omni-directional on the azimuth plane, while for the male cases a front-to-back ratio of 10 and 15 dB (for the Asian and the HUGO model respectively) is experienced. The maximum radiation, in all the three cases, is towards the front of the body. This is due to the location of the sources (they are closer to the front of the body), and to the high presence of muscle tissue on the dorsal part. The wave can reach the back of the body through direct penetration inside the body, as well as through combination of penetration inside the tissues and creeping wave around the body. In the two male models cases, considering the highest presence of lossy tissues (muscle), and the bigger size of the body, it is possible to note deeper null on the back side of the body.

If the communication of wireless implants with an off-body base station is required, the lower band (402 MHz) is preferable. In this case, the radiation patterns are much more omni-directional, and hence the RF link is less sensitive to the orientation between transmitter and receiver.

Net Body Losses and Gain

It has been widely known that electrically small antennas used in wireless implants are often very inefficient. When the antenna is placed inside the body, there is a significant absorption from the lossy tissues, which can be partially compensated by the increased electrical size of the antenna, caused by the dielectric loading of human tissues [13]. In the previous studies, the effect of electrically small antennas deployed in the implants and the losses of human tissues on in-body/off-body radio channels were not decoupled. In the following, we intend to calculate the percentage of power absorbed while the wave propagates inside the body tissues, regardless of the antenna used in the wireless implant.

In the simulations, an insulation thickness of one cell (4 mm) between the Hertzian dipole source and the tissues was considered. The insulation was introduced in order to consider only the dissipation of the energy while the wave propagates in the tissues, and not the losses in the very near field of the source (as explained in Chapter 9 of [29]). Some analytical results on the effect of the insulation layer on the losses, were presented in [30] considering a simple hertzian dipole in a lossy sphere, and in [10], the effect of a silicone insulation layer on the antenna characteristics was studied.

In a real implanted antenna, the introduction of insulation reduces the losses, but on the other hand, the antenna becomes electrically smaller because it decreases the effect of the dielectric loading. The effect of such trade-off on the performance of the implanted antenna is an under-going study, and it is out of scope in this thesis. To obtain the net body loss in a in-body radio channel, the radiated power from the source is calculated in free space (P_{fs}), and when implanted (P_{body}). Because of the air insulation between antenna source and body tissues, the change in the input impedance between free space cases and implanted cases, was found to be very small, and the differences in terms of delivered power are less than 1dB, therefore the power loss can be calculated as [13]

$$\eta = \frac{P_{body}}{P_{fs}}. \tag{7.1}$$

Table 7.2 lists the amount of power dissipated inside the body. The highest percentage radiated power is found for the empty stomach case. Even when the stomach

402 MHz	Stomach (Empty)	Stomach (Full)	Bladder	Heart
Asian Female	-10.8	-13.4	-17.8	-18.4
Asian Male	-11.4	-15.3	-18.2	-19.8
HUGO	-11.8	-16.8	-22.5	-24.2
868 MHz	**Stomach (Empty)**	**Stomach (Full)**	**Bladder**	**Heart**
Asian Female	-14.4	-17.8	-19.2	-27.0
Asian Male	-15.1	-19.5	-23.5	-27.2
HUGO	-15.8	-21.4	-27.0	-33.0

Table 7.2: Net body losses in dB at 402 MHz and 868 MHz for the three different phantoms.

is filled with fluid, more power is radiated than from the bladder and the heart. This can be explained with the fact that the losses inside the bladder and the heart are higher than the ones inside the stomach cavity (as indicated in Table 7.1, at 402 MHz the conductivity inside the bladder and the heart is $\sigma = 1.35$ S/m, while inside the stomach is $\sigma = 0.8$ S/m). Comparing the three different phantoms, it is possible to note that, in general, the power radiated from the implants inside the female body is higher. This is due to the smaller size of the female phantom with respect to its male equivalents. Furthermore, the female body contains more low loss tissues (such as fat tissues, $\sigma = 0.08$ S/m at 402 MHz) in comparison to the male body which contains more muscle tissues ($\sigma = 0.8$ S/m at 402 MHz). The Hugo model, due to its larger size, presents the highest losses among the three cases. At 402 MHz, the minimum body loss is about -10.8 dB for the gastric implanted source inside the female body, while the maximum is -24.2 dB when the source is placed inside the heart of the Hugo phantom. At 868 MHz, an increase in its electrical size of the body, and losses of the tissues, lead to large net body losses, and a maximum loss of -33.0 dB is observed for the cardiac implant in the Hugo model.

Table 7.3 lists the values of antenna gain obtained as follows

$$G = \eta D \tag{7.2}$$

where η is the net body loss, and D is the directivity.

402 MHz	Stomach (Empty)	Stomach (Full)	Bladder	Heart
Asian Female	-6.1	-7.8	-13.6	-14.0
Asian Male	-6.9	-8.9	-13.3	-14.9
HUGO	-8.2	-10.5	-19.0	-20.7
868 MHz	**Stomach (Empty)**	**Stomach (Full)**	**Bladder**	**Heart**
Asian Female	-9.1	-11.2	-13.3	-21.8
Asian Male	-9.3	-12.0	-18.2	-22.2
HUGO	-10.6	-13.3	-19.9	-25.9

Table 7.3: Gain in dBi at 402 MHz and 868 MHz for the three different phantoms.

7.2 Cardiac Implanted Loop Antennas

In the previous section, it was highlighted that the highest loss is found from the cardiac implanted source inside the Hugo model. However, a simplified point source insulated from the tissues was considered as radiation source. In a true implant environment, there are strong ohmic and radiation losses in a physical antenna structure, such as loop antenna in cardiac implants [29]. In this analysis, two loops with a circumference of one, and a half wavelength are considered, and no insulation layer between antenna and tissue is considered. The wavelength inside the heart at 402 MHz is found to be 93.6 mm, and can be calculated from the following formula,

$$\lambda_m = \frac{\lambda_0}{Re\left[\sqrt{\varepsilon_r - \frac{j\,\sigma}{\omega\varepsilon_0}}\right]}. \tag{7.3}$$

In both cases, because of the losses in the body tissues, the antenna is well matched at the frequency of interest, and the return loss is found to be -13.6 dB and -14.8 dB respectively for the bigger and the smaller loop. A one-cell-gap source with an input impedance of 50 Ω is located at the two extremes of the loop [31].

Figure 7.6 shows the radiation patterns of the implanted loops. Because of the location of the antennas, the maximum radiation is towards the front part of the body slightly tilted on the left, and the front-to-back ratio is approximately 10 dB. The maximum value of radiation efficiency is found when the loop is placed vertically on the z-x plane. Radiation efficiency and peak gain for the bigger loop are η is -35.4 dB and -30.9 respectively, while for the smaller loop, the peak gain is -35.9 dB and the radiation

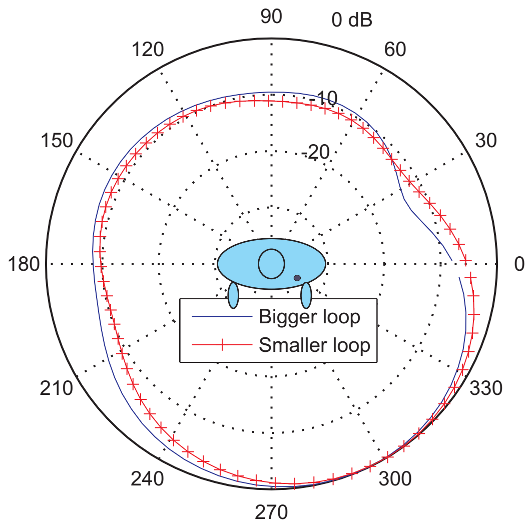

Figure 7.6: Normalised azimuthal radiation pattern (x-y plane) of the loop antennas implanted in the left ventricle.

efficiency is -40.6 dB.

Radius [mm]	$\mathbf{G_{Max}}$**[dB]**	$\mathbf{G_{99\%}}$**[dB]**	$\mathbf{G_{90\%}}$**[dB]**	η**[dB]**
14.9 ($l = \lambda$)	-30.9	-44.5	-40.7	-35.4
7.5($l = \lambda/2$)	-35.9	-48.7	-46.2	-40.6

Table 7.4: Gain values of the two loop antennas implanted in the left ventricle for different percentage of angular coverage

To overcome eventual errors of mis-alignment between the implant and the off-body base station, in addition to the peak gain, more pessimistic values of gain must be considered. Table 7.4 lists the gain value for different percentage of spatial coverage, namely 90 and 99%.

7.3 Link Budget Calculation for MICS Standard

The European Telecommunications Standard Institute [32] indicates two different application scenarios for the MICS standard; the first is the communication between implanted device and an external base station, and the second is the communication between the implant and other on-body equipments. In this work, the link budget between a cardiac implant, and an external base station is studied and analysed for two different scenarios: propagation in free space and propagation in indoor environment. Particular emphasis is given to the up-link, (from the implant to the base station).

The bandwidth, in the MICS standard is limited to 300 KHz for the complete session (up and down links). To maximize the data rate for each link (up-link and down-link), a half-duplex solution can be adopted: transmitter and receiver work one at a time using the full bandwidth. However, since a higher data rate is usually required in the up-link (from the implant to the base station), this solution is not convenient. In [33] an example of link budget calculation was presented, and a bandwidth of 200 and 25 KHz were allocated for up-link and down-link respectively. The thermal contribution to the background noise density can be calculated as

$$N_0 = k_b T, \tag{7.4}$$

where k_b is the Boltzman constant and it is equal to 1.38×10^{-23}, T is the temperature in Kelvin which is set to 310 Kelvin (37 Celsius). The noise density is -173.6 dBm/Hz. However, in [34] the noise power level at the base station is estimated to be around 20 dB above the thermal noise level (due to interferences from other equipment, and natural disturbances), and in [33] it was indicated a noise figure of the receiver of 4 dB, therefore the total noise power density for the up-link is -149.6 dBm/Hz.

In the case of down-link communication, the body tissues attenuate the signal, and the receiver is less sensitive to interferences from other equipments, therefore, the only contribution to the noise power is the thermal one. In [33] the noise figure of the implanted receiver was 9 dB, thus leading to a total spectral noise power density of -164.6 dBm/Hz.

In this study a system adopting a binary-phase shift keying (BPSK) modulation is considered, the required carrier-to-noise density ratio ($C/N0$) [35]

$$C/N_0[dBHz] = E_b/N_0[dB] + 10\log(B_r) \tag{7.5}$$

where E_b is the energy per bit, N_0 is the noise power density, and B_r is the bit-rate. The parameters for the proposed link budget are listed in Table 7.5.

N_0	-149.6 dBm/Hz
BER	10^{-5}
E_b/N_0	9.6 dB

Table 7.5: Parameters of the proposed link budget

To guarantee a value of BER below 10^{-5}, the ratio E_b/N_0 has to be at least 9.6 dB [35].

Link budget for Propagation in Free Space.

In case of far-field communication, the received power at the base station is calculated using the Friis formula for a free-space link [10].

$$C = P_t\,(1 - |S_{11}|^2)\,G_{imp}\left(\frac{\lambda}{4\pi d}\right)^2 G_r(1 - |S_{22}|^2) \tag{7.6}$$

where P_t is the transmitter's available power, G_{imp} is the gain of the implanted antenna, G_r is the gain of the receiver, λ is the free-space wavelength (0.75 m), and d is the distance between transmitter and receiver.

The minimum distance considered in the study is 1m, in order to guarantee that the receiver is in far-field zone. The power level at the receiver, depends on the orientation of the body with respect to the base station, as the implanted antenna does not have an omni-directional radiation pattern. In particular, between the maximum and the minimum gain, there is a decrease in the SNR of around 12-14 dB for both cases considered. To highlight the worst case scenario for radiated power coverage and its effect on the overall system performance, G_{imp} is considered to be the gain for a 99% of angular coverage ($G_{99\%}$). In [33], a power of -2 dBm was supplied to the antenna, however, in order to decrease the size and increase the lifetime of the sensor's battery, it is important to minimize the transmitted power. Three different values of input power were considered in this analysis, namely -2, -10, and -20 dBm, all assuring an EIRP below -16 dBm as imposed in [34]. The gain of the receiving antenna (G_r) is set to 2 dBi (approximately that of a typical free space dipole antenna). The two terms $1 - |S_{ii}|^2$ are the mis-match factors, and they can be neglected considering the good impedance matching of the loop antennas considered.

As indicated in (7.5), the required C/N_0 is a function of the desired bit-rate. Figure 7.7 shows the parameter C/N_0 as a function of the communication distance. Considering an input power of -2 dBm, a communication at a data-rate of 100 kbps could be sustained within a range of 10 m if the wavelength loop is adopted, and within 5 m

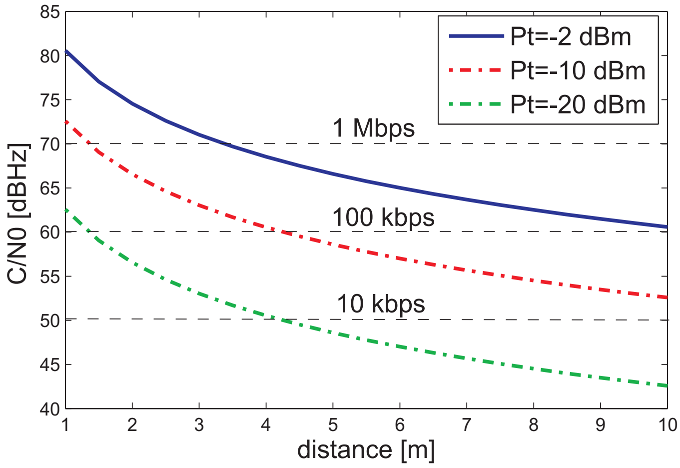

(a) loop with circumference of one wavelength

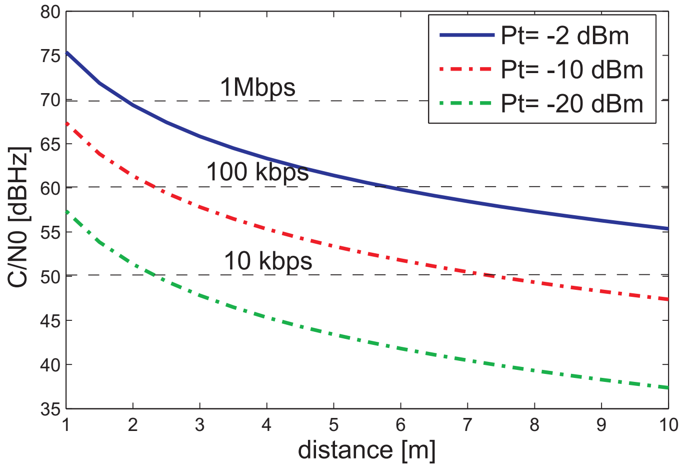

(b) loop with circumference of half wavelength

Figure 7.7: Signal-to-noise ratio as a function of distance considering an input power of -10 and -20 dBm.

using the half wavelength loop. With an input power of -10 dBm, such range is decreasing to 4, and 2 m respectively for the bigger, and the smaller loop. Finally applying an input power of -20 dBm, a data-rate of 100 kbps can not be sustained. However a lower data-rate of 10 kbps could be achieved within a range of 4, and 2 m respectively for the bigger, and the smaller loop. These results can be used to predict the operational range of wireless telemetry. The constant connectivity between the wireless implant and the base station could be possible within a room, but cannot be sustained within the entire floor of a building, even assuming a free space propagation.

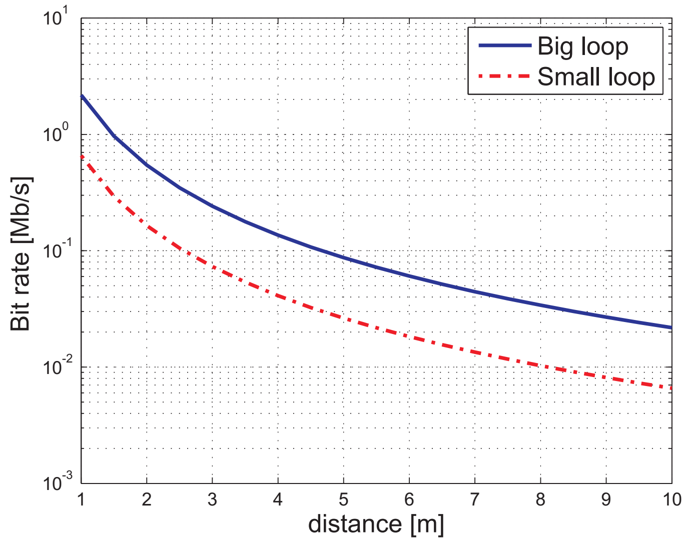

Figure 7.8: Bit-rate as a function of the communication distance, an input power of -10 dBm has been considered.

Figure 7.8 shows the bit-rate as a function of the communication distance considering an input power of -10 dBm. The bit-rate is inversely proportional to the square of the distance d. For the wavelength loop case, the maximum bit-rate is equal to 0.5 Mbps at a distance of 2 m, while for the half wavelength loop it is less than 0.3 Mbps. However, most of implanted systems, such as electro cardiogram (ECG), and pressure sensors, requires data rate in the order of 10 kbps and communication distances not greater than 2-3 m.

Figure 7.9 illustrates the bit-rate achievable as a function of the power supplied to the antenna. Results indicates that in the case of the wavelength loop, a bit-rate of 10 kbps could be sustained with an input power of -33,-28, and -24 dBm within a distance of 1,2, and 3 m respectively . In the case of the half wavelength loop, the values of power are respectively -28,-23, and -19 dBm.

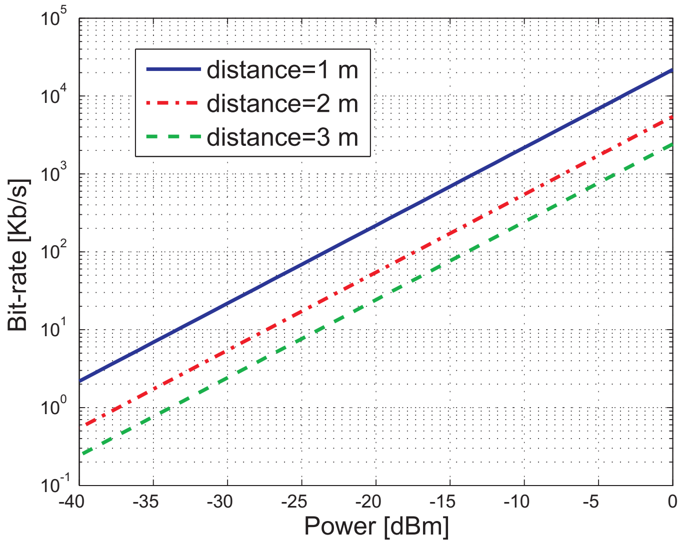

(a) loop with circumference of one wavelength

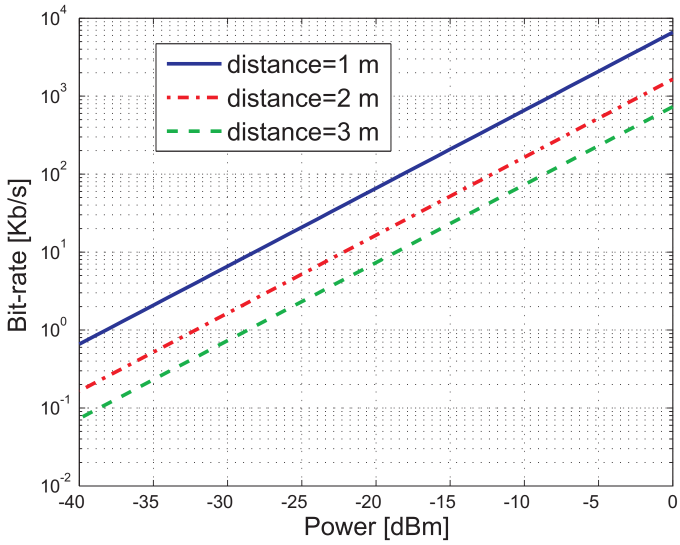

(b) loop with circumference of half wavelength

Figure 7.9: Bit-rate as a function of the power supplied to the antenna.

In case of a down-link communication, considering an antenna gain of 2 dBi, and no mismatch loss, the maximum input power (P_t) is

$$EIRP = G_{ant} + P_t \Rightarrow P_t = -16dBm - 2dBi = -18dBm. \tag{7.7}$$

However, as previously mentioned, the down-link is less sensitive to the external interferences, and the noise spectral density is equal to -165.0 dBm/Hz.

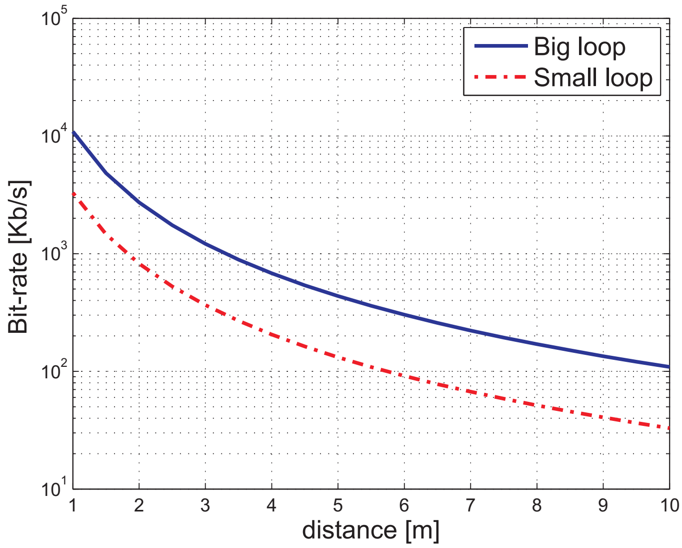

Figure 7.10: Bit-rate as a function of the communication distance, the power in input to the antenna is -18 dBm, which is the maximum allowed by the standard [34].

Figure 7.10 shows the bit-rate as a function of the communication distance for the down-link. The input power has been set to the maximum allowed by the standard (-18 dBm), and results demonstrated that the data rate achievable at a distance of 3m adopting the smaller loop is 200 kbps, therefore, for low-rate communications, the transmitted power can be further reduced.

Link Budget for Propagation in a Room

Due to reflections, diffraction and scattering of electromagnetic waves in the indoor environment, the transmitted signal reaches the receiver via more than one path.

In order to characterize the path loss in an indoor environment, a set of simulations were performed considering a simplified version of the layout of the body-centric wireless sensor lab [36] at Queen Mary, University of London. The received power at the base station is calculated as

$$S[dBm] = Pt[dBm] + G_{imp}[dB] - PL_{dB}(d) + G_r[dB]. \tag{7.8}$$

where PL_{dB} indicates the calculated path loss. In multipath propagation scenarios, the system is less affected by the nulls in the antenna radiation pattern. However, to highlight the worst case scenario for overall coverage, the gain of the implanted loop for 99% of angle coverage is used for the calculations.

The distribution of the path loss in the body-centric sensor lab is calculated adopting the FDTD technique. The simulations are performed at 402 MHz, and two different positions of the base station antenna are considered (see Fig. 7.11). Both transmitters are placed at an height of 1.5. The base station 1 is placed next to the bed, and hence part of the room is in a condition of non line of sight respect to the base station.

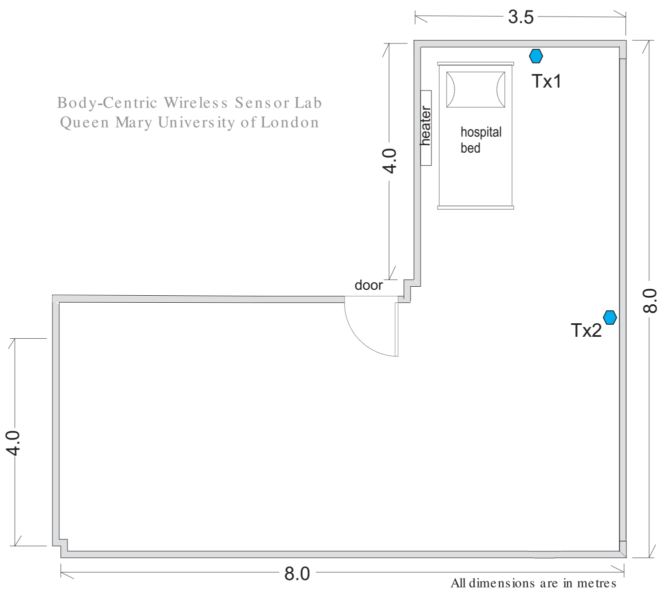

Figure 7.11: Layout of the room considered in the simulations

Figure 7.11 shows the layout of the room considered in the simulations. The walls, the floor and the ceiling were modeled as a 9 cm layer of concrete, while the bed frame and the heater were considered as made of perfect electric conductor. A cell size of 3 cm, corresponding to 25 free space wavelength is adopted.

Figure 7.12 shows the distribution of the electric field sliced at a height of 1.5 m. Such results can be used to calculate the percentage of area where C/N_0 is above the required level. In this calculation, the up-link case is considered, and the input power

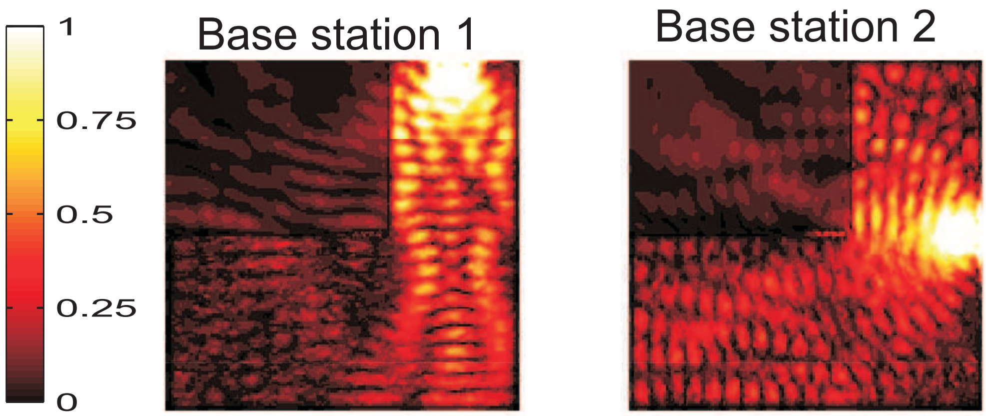

Figure 7.12: Normalised amplitude of the electric field at a height of 1.5 m.

to the antenna is set to -10 dBm. As indicated in Fig. 7.7, to sustain a data-rate of 10 kbps, the required C/N_0 is 49.6 dBHz.

Figure 7.13 shows the distribution of C/N_0 in the up-link case considering an input power of -10 dBm. Such a parameter, was evaluated at a height of 1.5 m, which is approximately the height of the implant in case that the subject is standing, and at 0.5 m, corresponding to the height of the implant in case that the candidate is sitting down.

In Figure 7.14 the red color indicates those locations where C/N_0 is above the required level of 49.6 dBHz, and hence a communication at a bit-rate of 10 kbps can be sustained. If the base station is located in the position 1, the percentage of coverage at a height of 1.5 m is 76.0% using the wavelength loop, and 43.2% adopting the smaller loop. At a height of 0.5 m, the percentages of coverage are slightly decreasing to 62.7 % and 33.1 % respectively. If we consider the base station 2, there is always line of sight between transmitter and receiver, and hence a higher coverage can be guaranteed. At a height of 1.5 m the percentage of coverage is 90.3% adopting the bigger implanted loop, and 46.9 % adopting the smaller one. These results can be used to predict the coverage range of a wireless implant in a realistic operational scenario, and to optimize the input power with respect to certain system requirements.

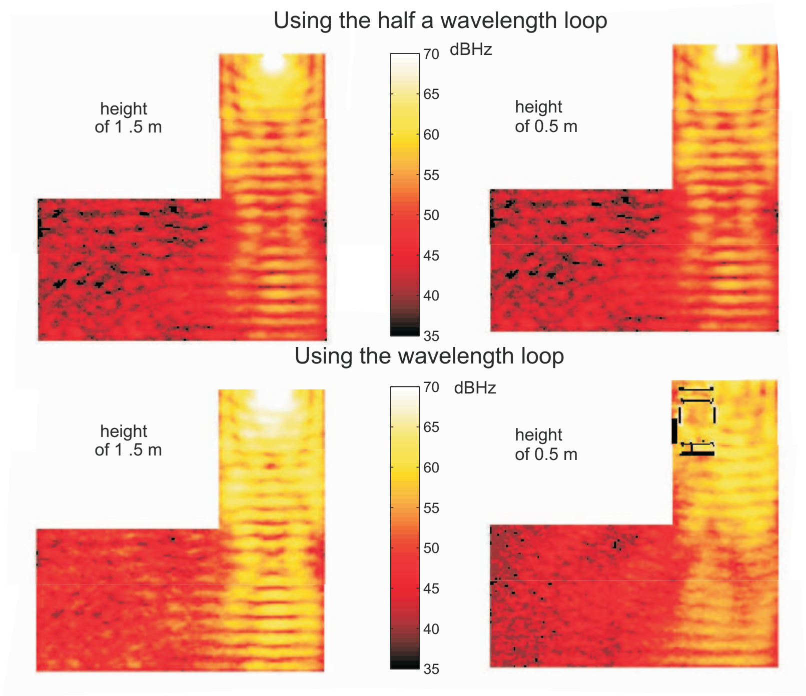

(a) Transmitter no. 1

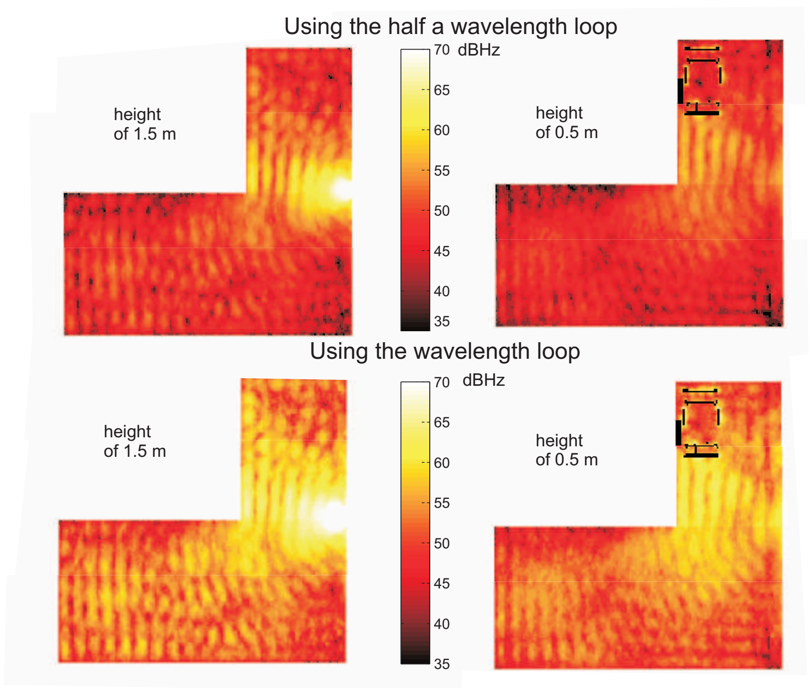

(b) Transmitter no. 2

Figure 7.13: Signal-to-noise ratio for propagation in indoor environment with an input power of -10 dBm

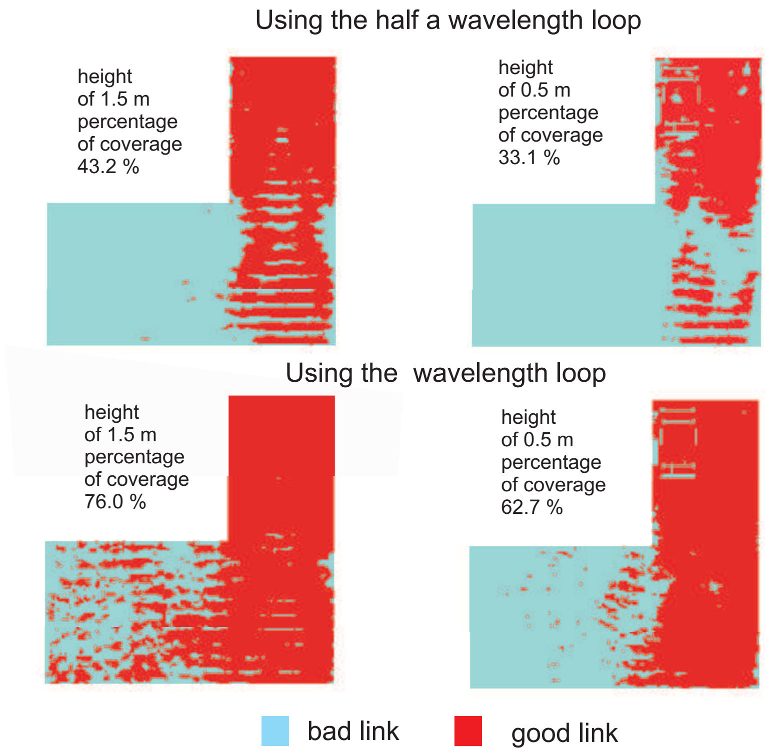

(a) Transmitter no. 1

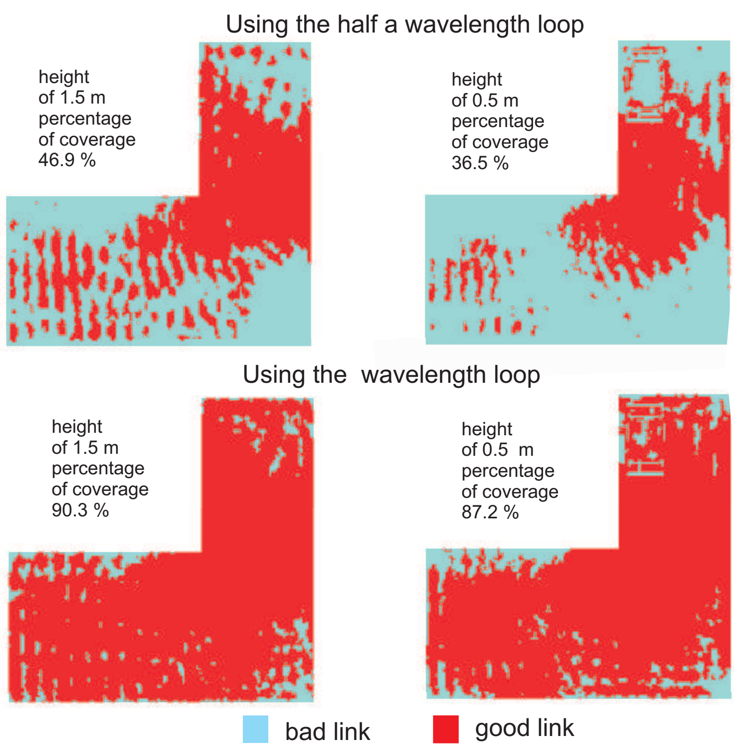

(b) Transmitter no. 2

Figure 7.14: Signal-to-noise ratio for propagation in indoor environment with an input power of -10 dBm

7.4 Summary

Medical implants are of extreme importance for building comprehensive telemedical networks and they form a growing application field for body-centric wireless communications. Implanted devices have to be made of bio-compatible material, and since they operate embedded in the body tissues, the impedance matching of the antenna is more problematic than in conventional antennas. Besides, the lossy nature of the body tissues and the relatively low level of power available (the battery has to be small and the lifetime of the implant long), create the need for an accurate study of the wireless link.

The first part of the chapter presented the radiation characteristics of wireless sources located in stomach, bladder and heart. The numerical analysis was performed adopting the FDTD technique at the Medical Implanted Communication Systems (MICS) frequency band of 402 MHz, and at the unlicensed frequency band of 868 MHz. Three different inhomogeneous digital phantoms (two male and one female) were considered to compare the effects of various body shapes and compositions on the radiation characteristics of the wireless implants. The numerical analysis indicated that the radiation characteristics of wireless implants are subject-specific, and strongly related to the location of the sensor. In particular, wireless sensors inside the female body demonstrated higher radiation efficiency, due to the smaller size, and anatomical features of the female body.

The second part of the chapter presented a link budget study for the communication between a cardiac implanted wireless source and an external base station. In the proposed link budget, a BPSK modulation scheme was adopted, and the trade-off between antenna size, data rate, input power and communication distance was discussed. The analysis was performed considering a free space path loss model, as well as considering the propagation in indoor environment. Full-wave FDTD simulations of the distribution of the path loss in the body-centric sensor lab, at Queen Mary, University of London, were used to determine the signal-to-noise ratio for different positions of the external base station, and to determine the percentage of coverage of a wireless implant in a realistic operational scenario.

References

[1] B. M. Steinhaus, R. E. Smith, and P. Crosby, "The role of telecommunications in future implantable device systems," *IEEE EMBS Conference*, pp. 1013–1014, 1994.

[2] B. C. Towe, "Passive biotelemetry by frequency keying," *IEEE Transactions on Biomedical Engineering*, vol. BME-26, pp. 905–909, February 1979.

[3] R. A. M. Receveur, F. W. Lindemans, and N. F. D. Rooij, "Microsystem technologies for implantable applications," *Journal of Micromechanics and Microengineering*, vol. 17, no. 5, pp. R50–R80, May 2007.

[4] P. Soontornpipit, C. M. Furse, and Y. Chung Chung, "Design of implantable microstrip antenna for communication with medical implants," *IEEE Transactions on Microwave Theory and Techniques*, vol. 52, no. 8, pp. 1944–1951, August 2004.

[5] J. Kim and Y. Rahmat-Samii, "Implanted antennas inside a human body: Simulations, designs, and characterizations," *IEEE Transactions on Microwave Theory and Techniques*, vol. 52, no. 8, pp. 1934–1943, August 2004.

[6] T. Karacolak, A. Z. Hood, and E. Topsakal, "Design of a dual-band implantable antenna and development of skin mimicking gels for continuous glucose monitoring," *IEEE Transactions on Microwave Theory and Technique*, vol. 56, no. 4, pp. 1001–1008, April 2008.

[7] M. S. Soora, K. Gosalia, M. S. Humayun, and G. Lazzi, "A comparison of two and three dimensional dipole antennas for an implantable retinal prosthesis," *IEEE Transactions on Antenna and Propagation*, vol. 56, no. 3, pp. 622–629, March 2008.

[8] T. Houzen, M. Takahashi, K. Saito, and K. Ito, "Implanted planar inverted f-antenna for cardiac pacemaker system," in *International Workshop on Antenna Technology: Small Antennas and Novel Metamaterials, IWAT 2008.*, March 2008, pp. 346–349.

[9] A. Sani, A. Alomainy, and Y. Hao, "Numerical characterization of the radiation from implanted wireless source considering different digital phantoms," in *European Conference on Antennas and Propagation (EUCAP 2009)*, March 2009, pp. 459–461.

[10] R. Warty, M. Tofighi, U. Kawoos, and A. Rosen, "Characterization of implantable antennas for intracranial pressure monitoring: Reflection by and transmission through a scalp phantom," *IEEE Transactions on Microwave Theory and Techniques*, vol. 56, no. 10, pp. 2366–2376, 2008.

[11] P. M. Izdebski, H. Rajagopalan, and Y. Rahmat-Samii, "Conformal ingestible capsule antenna: a novel chandelier meandered design," *IEEE Transactions on Antennas and Propagation*, vol. 57, no. 4, pp. 900–909, 2009.

[12] N. Haga, K. Saito, M. Takahashi, and K. Ito, "Characteristics of cavity slot antennas for body-area networks," *IEEE Transactions on Antennas and Propagation*, vol. 57, no. 4, pp. 837–843, 2009.

[13] W. G. Scanlon, J. B. Burns, and N. E. Evans, "Radiowave propagtion from a tissue implanted source at 418 MHz and 916.5 MHz," *IEEE Transactions on Biomedical Engineering*, vol. 47, no. 4, pp. 527–534, April 2000.

[14] W. G. Scanlon, N. E. Evans, and Z. McCresh, "RF performance of a 418 MHz radio telemeter packaged for human vaginal placement," *IEEE Transactions on Biomedical Engineering*, vol. 44, no. 5, pp. 427–430, May 1997.

[15] L. C. Chiwra, P. A. Hammond, S. Roy, and D. R. S. Cumming, "Electromagnetic radiation from ingested sources in the human intestine between 150 MHz and 1.2 GHz," *IEEE Transactions on Biomedical Engineering*, vol. 50, no. 4, pp. 484–492, April 2003.

[16] W. Sansen, B. Puers, and R. Veerecken, "Realization of a pressure telemetry capsule for cystometry," *IEEE Engineering in Medicine and Biology Annual Conference*, pp. 711–714, September 1984.

[17] E. Siwapornsathain, A. Lal, and J. Binard, "Telemetry and sensor platform for ambulatory urodynamics," *IEEE-EMBS Special Topics Conference on Microtechnologies and Biology*, pp. 283–287, 2002.

[18] G. Iddan, G. Meron, A. Glukhovsky, and P. Swain, "Wireless capsule endoscopy," *Nature*, vol. 405, no. 6785, May 2000.

[19] A. S. Walton and H. Krum, "The heartpod implantable heart failure therapy system," pp. S31–33, November 2005.

[20] A. Magalski, P. Adamson, F. Gadler, M. Boehm, D. Steinhaus, D. Reynolds, K. Vlach, C. Linde, B. Cremers, B. Sparks, *et al.*, "Continuous ambulatory right heart pressure measurements with an implantable hemodynamic monitor: a multicenter, 12-month follow-up study of patients with chronic heart failure," *Journal of Cardiac failure*, vol. 8, no. 2, pp. 63–70, 2002.

[21] S. Bush, "Imperial heart implant pulses RF piezo oscillator, available online at http://www.electronicsweekly.com/articles/2008/07/01/44043/imperial-heart-implant-pulses-rf-piezo-oscillator.htm."

[22] J. Schreuder, F. Van der Veen, E. Van Der Velde, F. Delahaye, O. Alfieri, O. Jegaden, R. Lorusso, J. Jansen, S. Hoeksel, G. Finet, *et al.*, "Left ventricular pressure-volume relationships before and after cardiomyoplasty in patients with heart failure," *Circulation*, vol. 96, no. 9, pp. 2978–2986, 1997.

[23] "Federal communications commission (FCC), code of federal regulations (CFR), title 47 part 95, MCIS band plan," *URL: http://www.fcc.gov*, March'03.

[24] "International telecommunications union-radiocommunications (ITU-R), radio regulations, section 5.138 and 5.150," *URL: http://www.itu.int/home*.

[25] A. Taflove, *Computational Electrodynamics: The Finite Difference Time Domain Method*. Norwood, MA: Artech House, 1995.

[26] T. Nagaoka, S. Watanabe, K. Sakurai, E. Kunieda, S. Watanabe, M. Taki, and Y. Yamanaka, "Development of realistic high-resolution whole-body voxel models of japanese adult males and females of average height and weight, and application of models to radio-frequency electromagnetic-field dosimetry," *Phys. Med. Biol.*, vol. 49, no. 4, pp. 1–15, December 2003.

[27] M. J. Ackerman, "Viewpoint: The visible human project," *J. Biocomm*, vol. 18, no. 4, p. 14, 1991.

[28] "Calculation of the dielectric properties of body tissues," *Institute for Applied Physics, Italian National Research Council, http://niremf.ifac.cnr.it/tissprop/*.

[29] P. S. Hall and Y. Hao, *Antennas and Propagation for Body-Centric Wireless Communications*. Artech House, 2006.

[30] F. Merli, B. Fuchs, and A. K. Skrivervik, "Influence of insulation for implanted antennas," *European Conference on Antennas and Propagation*, pp. 196–199, 2009.

[31] R. Luebbers and J. Beggs, "FDTD calculation of wide-band antenna gain and efficiency," *IEEE Transactions on Antennas and Propagation*, vol. 40, no. 11, pp. 1403–1407, 1992.

[32] European Telecommunications Standards Institute, "Electromagnetic compatibility and radio spectrum matters (ERM); radio equipment in the frequency range 402 MHz to 405 MHz for ultra low power active medical implants and accessories; part 1: Technical characteristics, including electromagnetic compatibility requirements, and test methods." *European Telecommunications Standards Institute, ETSI EN 301 839-1*, 2002.

[33] A. C. Authority, "Planning for medical implant communications systems (MICS) & related devices proposals paper."

[34] *International Telecommunication Union, Recommendation ITU-R SA.1346, 1998*, 1998.

[35] J. Proakis and M. Salehi, *Digital communications*. McGraw-hill New York, 1995.

[36] A. Alomainy, A. Sani, J. Santas, A. Rahman, and Y. Hao, "Transient characteristics of wearable antennas and radio propagation channels for ultra wideband body-centric wireless communications," *IEEE Transactions in Antenna and Propagation*, vol. 57, no. 4, pp. 875–884, 2009.

Chapter 8

Conclusions and Future Work

8.1 Summary

This thesis presented significant advancements in characterisation and modelling of antenna and propagation for body-centric wireless communications. In particular, it was highlighted the importance of developing powerful and reliable numerical modeling to be used in conjunction with measurement campaigns for a comprehensive understanding of the propagation mechanism in BCWC. The numerical analysis of the radio channel was conducted by importing realistic-shaped digital phantoms in the FDTD code. Analysing the on-body radio channel at 2.4 GHz, it was concluded that, since the skin depth is small, the internal composition of the body does not play a major role, and hence a homogeneous phantom (made of muscle tissue) can be used for representing the human body.

The subject-specificity of the on-body radio channel was also investigated by considering nine body models of different size and gender, and it was concluded that parameter such as the height of the subject, and the curvature radius at the trunk affect the path loss. The effect of the body posture on the on-body radio links was numerically studied, and it was demonstrated that for certain on-body links (e.g. belt-to-head) the changes in the position of the arms can lead to a significant variation (up to 25 dB) in the received power.

Over the past few years, the attention towards the UWB technology for wearable applications has experienced considerable growth. Two planar UWB antennas for wearable applications were proposed and characterised as a part of the on-body radio channel. A novel miniaturised TSA antenna was presented, and it was shown that in addition to a significant size reduction (it is four times smaller than a conventional UWB planar monopole), it does not lead to a degradation in the on-body radio channel characteristics, thus making it an ideal candidate for UWB-WBANs.

The characteristics of the UWB on-body radio channel were experimentally investigated in relation to different antennas, and considering the effect of the body movements on the channel parameters. To enable prediction and modelling, a statistical analysis on the spectral and transient parameters of the channel was performed.

The last part of this work is devoted to the analysis of the telemetry link for medical implants. In this case the internal composition of the body affects the performance of the radio link, and hence the numerical analysis was performed by adopting inhomogeneous digital phantoms, each of them classifying over fifty different tissues. The radiation characteristics of wireless implants at different locations were investigated at 402 and 868 MHz, and the impact of various body shapes and compositions were analysed by considering two male and one female digital phantoms. The results indicated that the radiation characteristics of wireless implants are strongly related to the location of the source and are subject-specific. In particular lower losses were found for the female phantom, and this is due to the smaller size and anatomical features of the female body.

A link budget study for MICS application was also proposed for communication between implant and off-body base station. The trade-off between communication range, bit-rate, input power, and antenna size was studied. In addition to a free space path loss propagation, the study was carried out by considering the propagation in a room. Full-wave FDTD simulations of the path loss distribution in the body-centric wireless sensor lab, at Queen Mary, University of London, were used to determine the performance of the wireless telemetry system in a realistic environment.

8.2 Key Contributions

The major contributions of this thesis are:

- Investigation of the subject-specificity of the radio channel at 2.4 GHz. The numerical analysis was conducted by considering nine homogeneous digital phantoms, and the results demonstrated that different body size and shapes can lead to a variation in path loss, and hence to different system performances. The effect of the body posture on the radio channel was also studied, and the results demonstrated that the changes in posture can lead to a significant variations on the received power.

- Development of a numerical technique based on the equivalence principle for including the radiation characteristics of practical antennas in the characterisation of the on-body radio channel. In the proposed technique, the physical antenna is replaced by equivalent currents representing its radiation characteristics.

- Spectrum and transient characteristics of ultra wide-band antennas for body-centric communications, and analysis of their behavior as a part of the on-body radio channel

- Analysis of the spectral and transient characteristics of the on-body ultra wide-band radio channel. The impact of different antennas, and the effect of changes in body posture were considered. To enable prediction and modelling, statistical models based on measured data were derived.

- Study of the radiation characteristics of medical implants at different locations, and considering three different inhomogeneous digital phantoms. The numerical analysis indicated that the radiation properties of wireless implants are subject-specific and they depend on the location of the implant.

- Study of the link budget for MICS applications. The communication between a cardiac implanted antenna and an external base station was analysed. Full-wave FDTD simulations of the path loss distribution in a room were used to determine the percentage of coverage in relation to certain system parameters.

8.3 Future Work

Based on the conclusions drawn and the limitations of the work presented, the following research aspects and issues would provide potential and natural progression to the accomplished work in the thesis:

Numerical Modelling Aspects

- Extension of the equivalence principle based FDTD technique. One of the drawbacks in the existing approach is that it is restricted to a single frequency analysis. A time-domain equivalence principle could be developed to deal with broadband wearable antennas. In addition, the antenna resonance detuning needs can be characterised adopting the proposed time-domain equivalence principle.
- Modelling of UWB on-body propagation channel using the dispersive FDTD technique. Such method has been introduced in this thesis and can be used to analyse the UWB on-body radio channel.
- Numerical modelling of the dynamic on-body radio channels. The thesis presented initial results on the effect of changes in posture on the radio channel. Such results can be further extended in order to model realistic body movements, and their effect on the channel characteristics.
- Analysis of the subject-specificity of the in-body radio channel including a broader range of inhomogeneous phantoms.

Radio Channel and System-Level Characterisation of WBAN

- Performing UWB measurements with a time-domain channel sounder to provide a cross-reference for a comprehensive understanding of the channel characteristics.
- Use of wireless sensors for realistic channel measurements. So far, measurement campaigns have been done by connecting two stand-alone antennas to the VNA through coaxial cables. However, cables do not allow freedom of movement to the user, and, it has been proven that, when connected to small antennas, they

may radiate and hence produce measurements errors. This can be avoided by using wireless sensors relying information on the received signal strength.

- System-level modelling of UWB-WBANs. The derived channel models can be used to analyse the performance of the on-body system in relation to different modulation schemes and receiver architectures.

- Investigation of the use of diversity techniques for improving the power efficiency of UWB-WBAN.

Antennas for Body-Centric Communications

- Identification of the best body-worn antenna. Previous studies have demonstrated that body-worn antennas suffer of reduced efficiency, impedance mismatch, and frequency detuning. The nature of these drawbacks depends on the frequency of operation, the polarisation, and the physical constraints of the antenna itself. A parametrical and statistical analysis of these effects, can help in selecting the best antenna for a certain application, and enable the development of a guideline useful for the antenna designers.

- Design of novel antennas for guiding surface waves along the body. In a on-body scenario, confining the radiated power in proximity of the body surface reduces the risk of interference, improves the security, and makes the system more power efficient.

- Design of novel antennas for reducing the body tissues absorption. Metamaterials techniques (e.g. electromagnetic bandgap) can be used to reduce the backward radiation, thus leading to an improved radiation efficiency of wearable antennas.

- Design of textile and fabric antennas to be integrated in everyday's clothing. Different combinations substrate/conductor need to be investigated for providing optimised antennas with constant radiation characteristics.

- Studying smart antenna systems as a solution for optimising the radio link. Since on-body systems are required to communicate with other body-worn equipments, off-body base station, and with other WBAN's, intelligent self-adapting antenna systems can be adopted for directing the energy in the desired direction, therefore improving the power efficiency of the end-to-end radio link.

- Design of optimised small antennas for medical implants. In particular, previous studies have proven that the introduction of a bio-compatible low-permittivity protective packaging leads to an improved radiation efficiency. Different combinations of material and thickness for the protective packaging need to be investigated, and the antenna design optimised for having a good impedance matching.

Appendix A

Implementation of the Parallel FDTD

The FDTD method is a versatile numerical technique. However, similarly to other numerical methods, it is computationally intensive. For large EM problems such as the modeling of WBANs, the requirement for system resources is beyond the capability of personal computers (PCs). One way to resolve this problem is to divide the whole problem domain into smaller sub-domains, and each sub-domain can be handled by a cluster of PCs. By linking the PCs together with a proper synchronization procedure, the original large problem can be decomposed and solved efficiently.

One of the most attractive features of the FDTD method is that it can be easily parallelized with very little modifications to the algorithm. Since it solves Maxwell equations in the time-space domain, the parallel FDTD algorithm is based on the space decomposition technique. The data transfer functionality between processors (PCs) is provided by the message passing interface (MPI) library. Data exchange is required only for the adjacent cells at the interface between different sub-domains and is performed at each time step, hence the parallel FDTD algorithm is a self-synchronized process. Figure A.1 shows the arrangement of the field components in different sub-domains in parallel FDTD simulations. Gray arrows are the transferred field components from the neighboring sub-domain during the data communication process. At the end of parallel FDTD simulations, the results calculated at each node needs to be

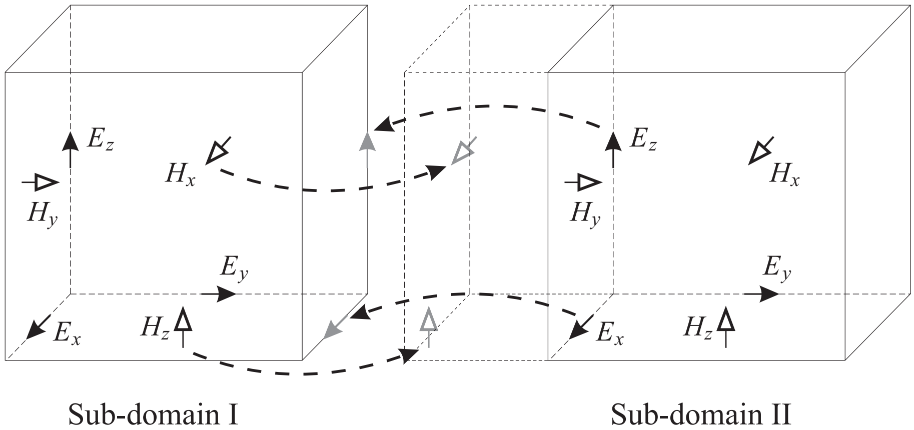

Figure A.1: The arrangement of the field components in different sub-domains in parallel FDTD simulations. Gray arrows indicate the field components which are transferred from the neighboring domain during the communication process and used to update the field components on the boundary of the current sub-domain.

combined to obtain the overall simulation result.

The PC cluster within the Body-Centric Wireless Sensor Lab, Queen Mary, University of London consists of one head node for monitoring purposes and fourteen compute nodes for performing calculation tasks. Each node has Dual Intel Xeon E5405 (Quad Core 2.0 GHz) central processing units (CPUs) which gives 120 cores and 480 GB memory in total. The nodes are connected by a 24-port gigabit switch. The GCC compiler and a free version of MPI, are used to compile the parallel FDTD code and to handle the inter-node communications, respectively.

To evaluate the performance of the cluster, different scenarios have been tested and the speed-up factor (the ratio of the computation time running a task on one core (T_1), to the time running the same task on N cores (T_N)) have been calculated to compare with the ideal case. The test results are shown in Fig. A.2. For the ideal case, the computation time reduces with the number of processors (cores) in a linear scale. However since additional time is required for data communications, the actual computation time deviates from the ideal linear case and especially when the number of processors increases, the deviation becomes more obvious, as shown in Fig. A.2. It is therefore recommended to divide the whole computation domain along the longest dimension of the 3-D matrices to reduce data communication load. During the test, the task has been distributed to run on one core per node, in order to maximize the memory usage. The overall computation time can be slightly reduced when running

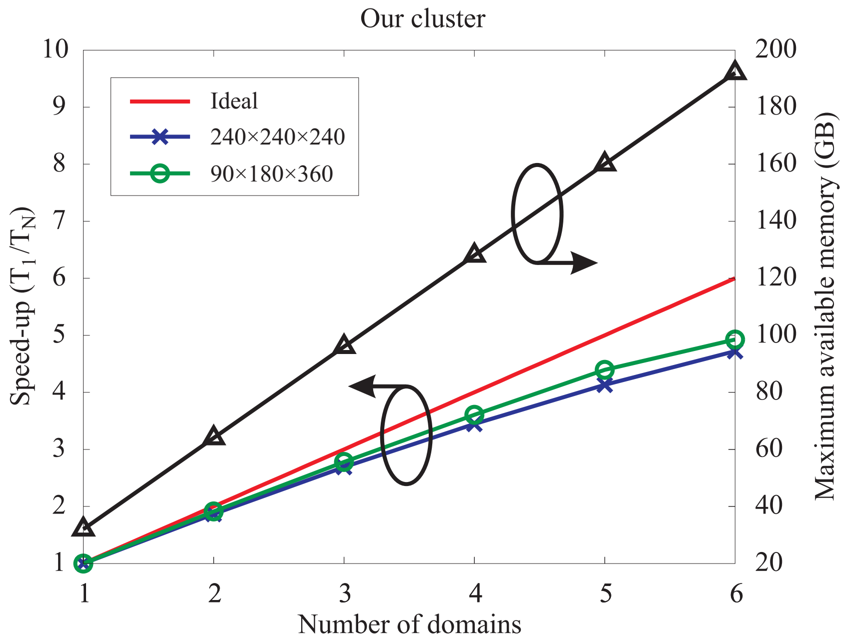

Figure A.2: The speed-up factor of the cluster for different cases (matrix dimensions $240 \times 240 \times 240$ and $90 \times 180 \times 360$) and its comparison with the ideal case (linear). The task is distributed to one core per node to maximize the memory usage.

the task on more than one core (up to eight) per node, since the data communication is accomplished within the same CPU and is not required to pass through the switch.

To validate the parallel FDTD simulations, the scenario of a human body standing in the free space is considered in simulations, where the sensor antenna is mounted on the right wrist of the human body. The whole domain is calculated by dividing it into two, four and eight sub-domains then compared with the results from the simulation on a single processor without dividing the domain. It is shown that the comparison in Fig. A.3 validates and demonstrates the efficiency of the parallel FDTD method.

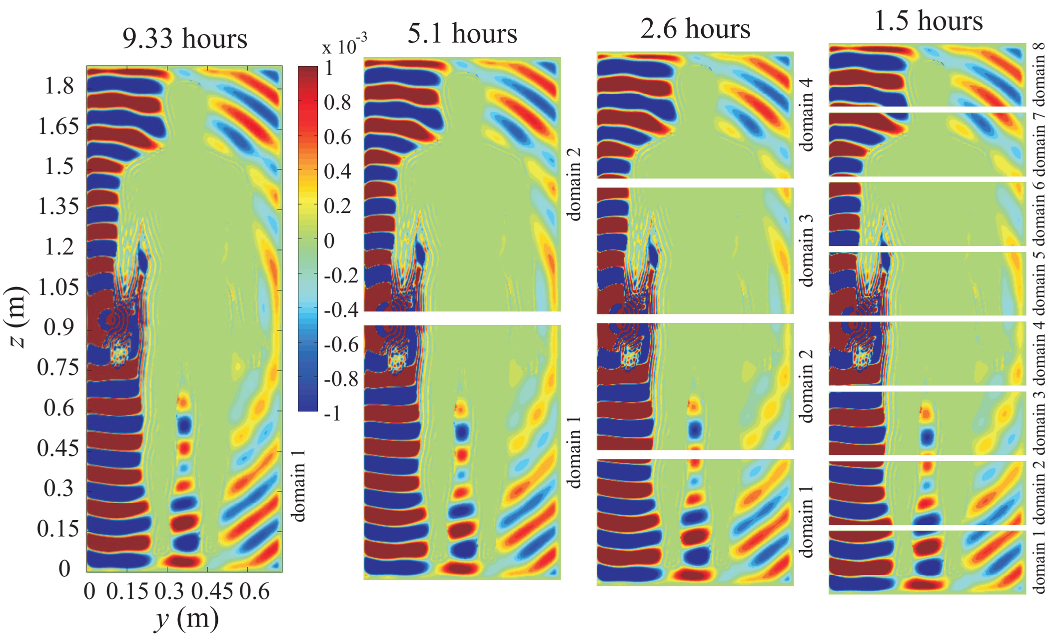

Figure A.3: The validation of the parallel FDTD method. The scenario is considered as a human body standing still in the free space with the sensor antenna mounted on the right wrist.

Appendix B

Impedance Matching of the Presented Narrowband Planar Antennas

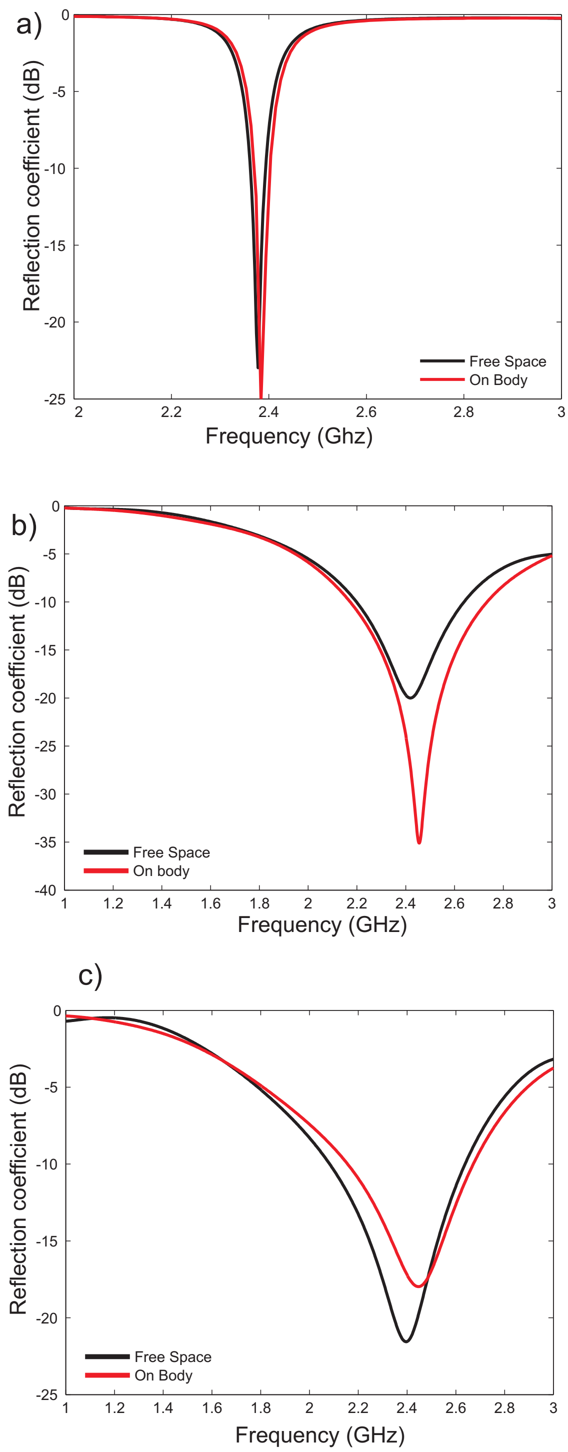

Figure B.1: Impedance matching of the narrowband microstrip antennas presented in section 5.5. Measurements were performed with the antennas placed off and on the body at 3 mm away from the human chest; (a) Patch; (b) Planar Monopole; (c) Inverted L.

Appendix C

Post-Processing of Measured Channel Data

The frequency domain measurement data is transformed to time domain. This is performed as following:

- UWB signals are carrierless and use pulse based transmit and receive techniques that do not use a complex baseband receiver. For a real passband (PB) approach, the spectrum is zero padded from 0 to 3 GHz. Due to the extension of the spectral domain to the band -9GHz to +9GHz, the obtained pass-band representation of the radio channel impulse response is over sampled to 4801 samples for the produced response.

- The complex conjugate of the spectrum is flipped to give the negative frequency portion of the spectrum, guaranteeing the inverse Fourier transform would be real. Figure C.1 shows an example of real channel frequency transfer function obtained by real pass-band technique.

- The passband signal has timing resolution of 55.6ps per sample, while the complex baseband has resolution of 166.7ps per sample (1/18 GHz compared to 1/6 GHz).

- Time resolution (binning) can be applied to obtain better time resolution.

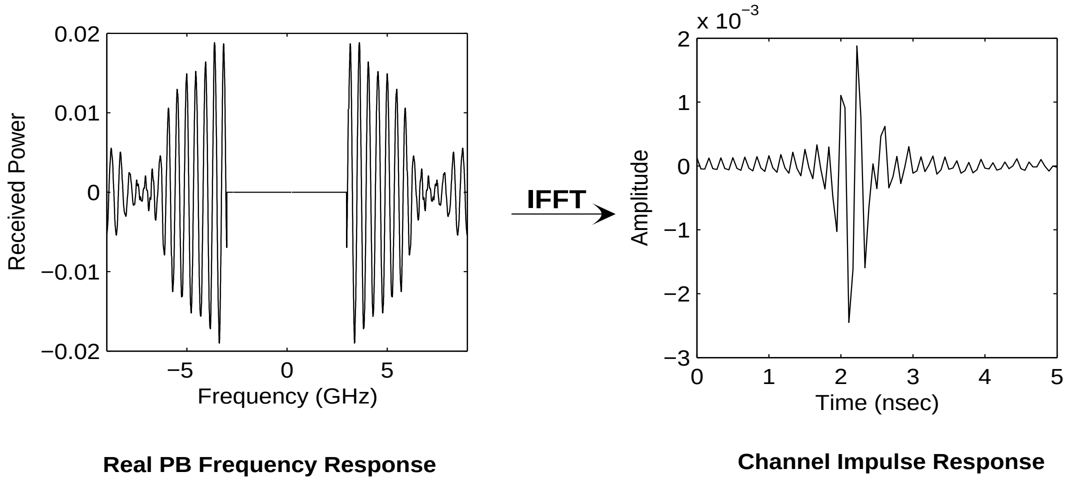

Figure C.1: Real pass-band measured frequency transfer function of on-body channel

- The pass-band impulse response representation is used for the time delay analysis.

Appendix D

Statistics Distributions

For a comprehensive understanding of the radio propagation, and to enable prediction and modelling of the channel parameters, statistical analysis is needed. In wireless communications, several statistics distributions have been used to model the characteristics of the received signal (such as amplitude, phase, time of arrival etc.). Some well known distribution will be described in this appendix.

Lognormal Distribution This distribution has been used to describe large scale variation of the signal amplitude in multipath environment. The pdf is given by

$$Pr(x) = \frac{1}{\sqrt{2\pi}\sigma x} \exp\left[\frac{-(\ln x - \mu)^2}{2\sigma^2}\right], \quad x \geq 0 \tag{D.1}$$

Mean and variance of the distribution are given by

$$mean = \exp(\mu + \sigma^2/2) \tag{D.2}$$

$$variance = \exp(2\mu + \sigma^2)\left(\exp(\sigma^2) - 1\right) \tag{D.3}$$

Weibull Distribution The pdf is given by

$$Pr(x) = b\, a^{-b}\, x^{b-1} \exp\left[-(x/a)^b\right], \quad x \geq 0 \tag{D.4}$$

Mean and varaiance can be expressed as follows:

$$mean = a\Gamma(1 + 1/b) \tag{D.5}$$

$$variance = a^2 \left[\Gamma(1 + 2/b) - \Gamma(1 + 1/b)\right] \tag{D.6}$$

where $\Gamma(x)$ is the gamma function, a is a shape parameter and b is a scale parameter of the distribution.

Rayaleigh Distribution This distribution has been widely used for modeling the small-scale fading in absence of a dominant component (such as LOS). The pdf is given by

$$Pr(x) = -\frac{x}{b^2}\exp\left(-\frac{x^2}{2b^2}\right), \quad x \geq 0 \tag{D.7}$$

Mean and variance can be expressed as follows:

$$mean = \sqrt{\pi/2}b \tag{D.8}$$

$$variance = (2 - \pi/2)b^2 \tag{D.9}$$

Nakagami Distribution The pdf is given by

$$Pr(x) = \frac{2m^m x^{2m-1}}{\Gamma(m)\Omega^m}\exp\left[-\frac{mx^2}{\Omega}\right], \quad x \geq 0 \tag{D.10}$$

$$\Omega = E[x^2] \tag{D.11}$$

$$m = \{E[x^2]\}^2/Var[x^2] \tag{D.12}$$

Mean and variance can be expressed as follows:

$$mean = \frac{\Gamma(m + 1/2)}{\Gamma(m)}\left(\frac{\Omega}{m}^1/2\right) \tag{D.13}$$

$$variance = \Omega\left(1 - \frac{1}{m}\left(\frac{\Gamma(m + 1/2)}{\Gamma(m)}\right)^2\right) \tag{D.14}$$